Superconducting Tunnel Junctions as Direct Detectors for Submillimeter Astronomy

A Dissertation
Presented to the Faculty of the Graduate School
of
Yale University
in Candidacy for the Degree of
Doctor of Philosophy

by
John Daniel Teufel

Dissertation Director: Professor Robert J. Schoelkopf

May 2008

Abstract

Superconducting Tunnel Junctions as Direct Detectors for Submillimeter Astronomy

John Daniel Teufel

2008

This thesis presents measurements on the of performance of superconducting tunnel junctions (STJ) as direct detectors for submillimeter radiation. Over the past several decades, STJ's have been successfully implemented as energy-resolving detectors of X-ray and optical photons. This work extends their application to ultra-sensitive direct detection of photons near 100 GHz. The focus of this research is to integrate the detector with a readout that is sensitive, fast, and able to be scaled for use in large format arrays. We demonstrate the performance of a radio frequency single electron transistor (RF-SET) configured as a transimpedance current amplifier as one such readout. Unlike traditional semiconductor amplifiers, the RF-SET is compatible with cryogenic operation and naturally lends itself to frequency domain multiplexing. This research progressed to the invention of RF-STJ, whereby the same RF reflectometry as used in the RF-SET is applied directly to the detector junction. This results in a greatly simplified design that preserves many of the advantages of the RF-SET while achieving comparable sensitivity. These experiments culminate in calibration of the detector with an on-chip, mesoscopic noise source. Millimeter wave Johnson noise from a gold microbridge illuminates the detector *in situ*. This allows for direct measurement of the "optical" properties of the detector and its RF readout, including the response time, responsivity and sensitivity.

Acknowledgements

I would like to take these few paragraphs to recognize some of the people who were instrumental in both the completion of this thesis as well as my progress as a scientist. To begin, I would like to thank my parents for always encouraging my love of science. This includes my father teaching me the importance of asking the right questions and my mother making sure I worked hard at whatever it was I decided to pursue.

While I learned most of the facts and equations as an undergraduate, it was as a graduate student at Yale that I learned what it means to be a physicist. Most importantly I would like to thank my advisor, Rob Schoelkopf. His example has had a great influence on how I think about physics, the way in which I approach an experiment, and how to debug it when things are not working as they should. Never underestimate a man who can smell a ground loop from ten feet away. Dan Prober has served as my second advisor. I appreciate his open door and willingness to discuss the details of a past, present or future experiment. This includes both tracking down the last factor of two in an equation and providing perspective of where our daily research fits into the bigger picture. I have also learned a great deal from Michel Devoret. I am constantly rediscovering all the levels in which his simple, yet precise analogies, aptly explain even the most complicated physics.

In general, it has been a pleasure to work on the 4th floor of Becton Center; the Schoelkopf, Prober, and Devoret labs demonstrate that innovative research is the natural byproduct of an active and inspiring scientific environment. This is the direct result of the many postdocs and graduate students in these labs. Specifically, I want to thank Luigi Frunzio, Bertrand Reulet, Etienne Boaknin, Irfan Siddiqi, Chris Wilson, Andreas Wallraff, Hannes Majer, and Andrew Houck. Just as important, I am indebted to my fellow graduate students with whom I overlapped to most: Lafe Spietz, Minghao Shen, Ben Turek, Dave Schuster, Julie Love, Matt Reese, Vijay, and Veronica Savu. I especially need to thank Konrad Lehnert for his role both at the start and finish of this work. It was his example that shaped much of who I am as an experimentalist; and his support that allowed me to see it through to fruition.

Lastly, I want to thank my wife, Rachael. She has been nothing but supportive and understanding over the entire process of my graduate education. I would not be where I am, or who I am, today without her.

Contents

List of Figures

List of Tables

List of Symbols and Abbreviations

B	Bandwidth
c	Speed of light
C	Capacitance
C_g	Gate capacitance
C_Σ	Sum capacitance
D	Diffusion constant
DC	Direct current
δ	Skin depth
Δ	Superconducting gap
e	Charge on the electron, $1.60217653(14) \times 10^{-19}$ C
E	Energy
E_C	Charging Energy
ϵ_0	Permittivity of free space
f	Frequency
f(E)	Fermi function
η	Fano factor
η_0	Impedance of free space
G	Gain or thermal conductance
GPIB	General Purpose Interface Bus
γ	Propagation constant

Γ	Reflection coefficient
h	Plank's constant
$\hbar$	Plank's constant divided by 2π
HEMT	High Electron Mobility Transistor
I	Current
I_c	Critical current
J_n	Nth Bessel function of the first kind
k_B	Boltzmann constant, $1.3806505(24) \times 10^{-23}$ J/K
κ	Thermal conductivity
L	Inductance
$\mathscr{L}$	Lorenz number $\pi^2 k_B^2/3e^2$
L_{e-e}	Electron-electron inelastic scattering length
L_{e-ph}	Electron-phonon scattering length
μ_0	Permeability of free space
NIST	National Institute of Standards and Technology
NEP	Noise Equivalent Power
NRAO	National Radio Astronomy Observatory
ν	Frequency
OFHC	Oxygen Free High Conductivity
ω	Angular frequency
Q	Quality factor
$\mathcal{R}$	Responsivity
R_n	Normal state resistance
$R_\square$	Sheet Resistance
RF	Radio frequency

RF-SET	Radio Frequency Single Electron Transistor
RF-STJ	Radio Frequency Superconducting Tunnel Junction
R_K	Resistance quantum h/e^2
S	Scattering matrix
S_I	Current spectral density (measured in A^2/Hz)
S_V	Voltage spectral density (measured in V^2/Hz)
SEM	Scanning Electron Microscope
SET	Single Electron Transistor
SQUID	Superconducting Quantum Interference Device
σ	Conductivity
STJ	Superconducting Tunnel Junction
T	Temperature
T_c	Critical temperature
T_n	Noise temperature
τ	Integration time
V	Voltage
x	Normalized voltage eV/k_BT
Z	Impedance

Chapter 1

Introduction

"Physics is like sex. Sure, it may give some practical results, but that's not why we do it."

–Richard P. Feynman

Detection of light is one of the most fundamental ways in which a scientist can acquire information. As light is nothing more than electromagnetic mode, the method of detection is varies widely depending of the frequency of the radiation and the size of the signal. An ideal detector would transduce or amplify the signal in a way that not only adds the least amount of additional noise, but is also fast, efficient, and feasibly scaled to a many-pixel camera. One such candidate detector is the superconducting tunnel junction (STJ). The goal of thesis work is to experimentally verify the performance of the STJ as a detector of submillimeter wave radiation. Furthermore, this work integrates the detector for the first time with RF readout techniques that are both sensitive and amenable to simultaneous readout of many pixels at once. This introductory chapter motivates the need for such a detector and discusses how the STJ compares in operation and potential performance to other types of detectors.

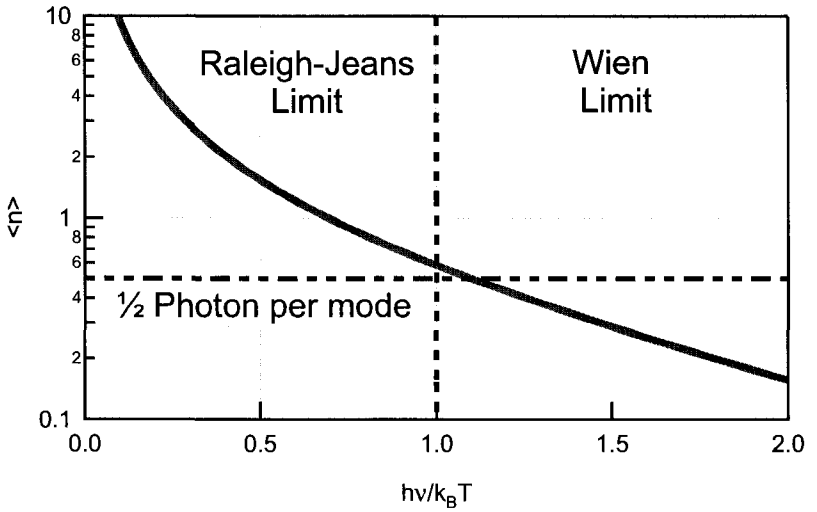

Figure 1.1: The Bose-Einstein distribution dictates the average occupancy per mode for photons from a thermal source. Any coherent detector must add at least 1/2 quantum of noise in the process of measurement. This added noise is unimportant in the Raleigh-Jeans limit ($h\nu$ <k_BT), where there are many photons per mode. In the Wien limit, however, the average occupancy per mode quickly become less than 1, and the noise from even a quantum limited coherent detector represents an unacceptably large amount of added noise. Thus, once $h\nu$ >k_BT, a direct detector is strongly preferred. For a 3 K blackbody, this transition occurs at $\sim$ 60 GHz

1.1 Overall Motivation

Submillimeter and millimeter waves represent a range of the electromagnetic spectrum that is in rich cosmological information, yet not fully explored due to the need for better detectors. Specifically, there is a need for an ultra-sensitive direct detector that can be background limited even in the the lowest noise space environment (Mather et al., 1996). The submillimeter spectrum is rife with spectral information from many sources such as radiation from highly red-shifted galaxies. Furthermore, the overwhelming success of cosmic microwave background (CMB) studies has shown that in addition to the vast array of spectral lines, the universe is radiating as a nearly-ideal blackbody with an average temperature of 2.725 K (Fixsen et al., 1996). The accuracy of this work has allowed for determinations of very small temperature fluctuation about this average depending on the direction of observation and the polarization of the light (Hinshaw et al., 2007). These anisotropies contain valuable information about the early universe and its formation (Spergel et al., 2007). In order to fully explore these subtle, but extremely important, variations, future space missions will require large arrays of sensitive detectors.

For any thermally radiating source, the average energy of each emitted photon is determined by the Bose-Einstein distribution function. Thus, as shown in Equation 1.1, the average energy per mode begins to decrease exponentially at frequencies greater than k_BT/h.

$$< E >= \frac{h\nu}{\exp\left(\frac{h\nu}{k_B T}\right) - 1} = \begin{cases} k_B T & \text{if } h\nu \ll k_B T \text{ (Raleigh-Jeans Limit)} \\ \exp\left(-\frac{h\nu}{k_B T}\right) & \text{if } k_B T \ll h\nu \text{ (Wien Limit)} \end{cases} \tag{1.1}$$

At low frequencies ($h\nu < k_B T$), the energy per mode is simply k_BT. This is the Raleigh-Jeans limit, and it is here that average occupancy per mode is very large. As shown in Figure 1.1, as $h\nu$ becomes greater than $k_B T$ this occupancy quickly decreases. This is the Wien limit, where the non-classical nature of the photons becomes apparent. Here, the average energy per mode decreases exponentially with frequency. If one were going to detect photons in the Wien limit with a coherent detector (one that simultaneously measure the amplitude and phase of the signal), quantum mechanics dictates that measurement process must necessarily add at least $h\nu/2$ of energy per mode (Caves, 1982). This is in addition to the $h\nu/2$ of vacuum noise that will also be detected. A direct detector, that only measures photon number, is not subject to this "quantum limit." In the end, it is only the photon shot noise that determines the limit on the sensitivity of the detector. The goal of this work is to realize a direct detector that would be limited by this photon shot noise, even in the extremely low background environment of space.

Figure 1.2 shows one way in which detectors may be classified as well as an example of a cryogenic detector of each type. First are coherent detectors that provide information on both the amplitude and phase of the signal. The sensitivity is often quoted in terms of noise temperature. This is the equivalent temperature a load resistor would have to have in order to account for the noise added by amplifier. The quantum limit implies that the minimum possible noise temperature of an amplifier is set by the frequency of detection.

$$T_n \geq T_Q = \frac{h\nu}{2k_B} \tag{1.2}$$

For submillimeter and millimeter wave radiation, amplifiers come quite close to this limit. HEMT amplifiers similar to the ones used in this work at RF frequencies provide sensitive amplification to frequencies greater than 100 GHz with noise temperatures less than a factor of ten above the quantum limit (Gaier et al., 2003). SIS mixers actually achieve this quantum limit and work well up to frequencies of order 1 THz (Face et al., 1986). For higher frequencies, hot electron bolometers mixers continue to operate within an order of magnitude of the quantum limit (Hajenius et al., 2007). While these detectors are ideally suited for some applications, the noise from even a quantum limited coherent detector is unacceptable for detecting photons from a thermal source in the Wien limit.

One of the simplest examples of a direct detector is a bolometer. The incoming radiation power is determined by measuring how the photons increase the temperature of thermally isolated sample. Thus, the bolometer acts as a square-law detector, or power meter, acquiring no information about the phase of the incoming signal. The intrinsic limit of the sensitivity is the statistics of the phonons

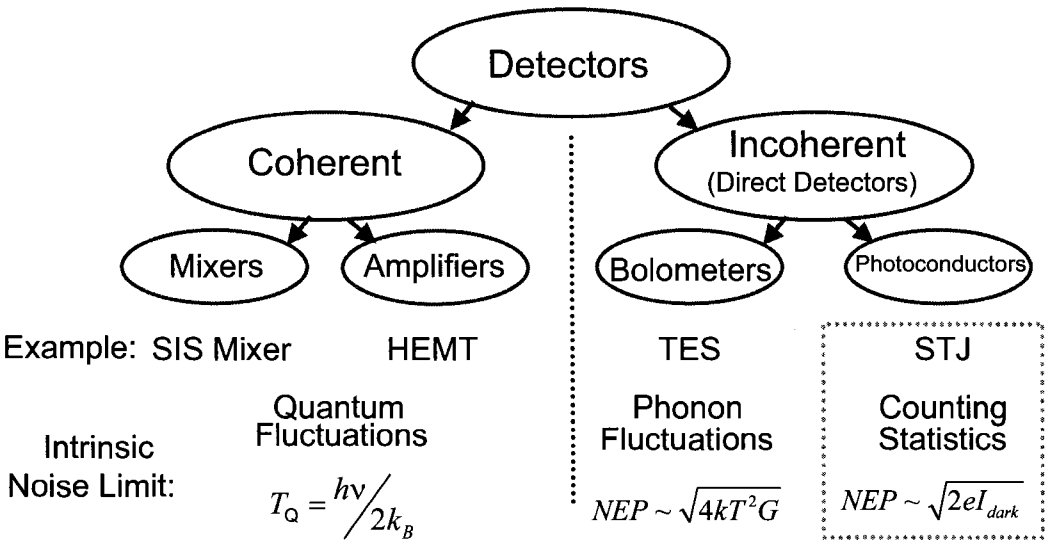

Figure 1.2: This diagram shows the general hierarchy of detector classifications as well as the fundamental limits on their sensitivity. While superconducting tunnel junctions can be used as either a coherent or incoherent detector of light, this work focuses on its use as a direct detector. As with any photoconductor, the ultimate limit on the intrinsic sensitivity is the statistics of the tunneling currents.

in the bolometer.

$$NEP_{bolometer} = \sqrt{4k_B T^2 G} \tag{1.3}$$

Here G is the thermal conductance with which the bolometer is coupled to the bath. As shown in Equation 1.3, this fundamental limit on the sensitivity scales linearly with the temperature. One of the most sensitive and widely used form of bolometer is the transition edge sensor (TES) (Irwin and Hilton, 2005). These devices exploit the dramatic change in the DC resistance of a superconductor at the critical temperature, T_c. In practice, the devices are engineered to have a T_c just above their operating temperature. A proper voltage bias then self-heats the bolometer to the most sensitive temperature. The resistance of the device is measured by inductively coupling the its current to a SQUID amplifier. This technique represents the current state of the art. For submillimeter applications, NEPs as low as 10^{-19} W/$\sqrt{\text{Hz}}$ have been demonstrated (Kenyon et al., 2006). Furthermore, time division multiplexing schemes allow for readout of detector arrays as large as 1280 pixels (Woodcraft et al., 2007).

Another form of bolometer is the so-called NIS bolometer (Nahum and Martinis, 1993). This is analogous to the STJ except that the absorber is made with a normal metal. As incident photons heat the electrons in the absorber, the subgap tunneling current through a detector junction is increases. Recently, this detector has been integrated with an RF readout exactly analogous with

radio frequency readout implemented in this work (Schmidt et al., 2003; Schmidt et al., 2005).

The STJ is not a bolometer, but rather is a non-equilibrium photoconductor. Just as in a photodiode, the detector creates charge carriers proportional to the number of incident photons, not their energy. This has several important advantages over bolometric schemes. First, the fundamental limit on the sensitivity is the shot noise of the leakage or dark current. For an SIS junction, this current scales exponentially with the operating temperature. Thus, the dark current can ideally be made negligible simply by operating at lower temperature. Furthermore, these lower temperatures do not decrease the speed of the detector. The response time of the STJ is independent of the temperature of operation. This is in stark contrast to a bolometer where low temperature operation dictates a slow thermal time constant.

One last type of detector is the microwave kinetic inductance detector (MKID) (Day et al., 2003; Mazin, 2004). It relies on photons breaking Cooper pairs, just as with the STJ. Instead of using a tunnel junction to measure the quasiparticle density, it uses a high Q resonant circuit. The excess quasiparticles lead to small changes in both the real and imaginary parts of the surface impedance of the superconducting film and hence the Q and center frequency of the resonator. The advantages of this technique are the natural frequency domain multiplexing and the simplicity of fabrication. While this detector will always have a slower response time than a comparable STJ because it relies solely on recombination to reset the detector, this is not an issue for many applications. In the original design the sensitivity was limited by the intrinsic phase noise of the resonators. In recent work, however, the NEP has improved to 3×10^{-18} W/$\sqrt{\text{Hz}}$(Baselmans et al., 2008).

While there are many other varieties of cryogenic detectors, these examples represent the current state of the art with which the STJ should be compared. The next section will detail the exact operation of the STJ as well as the expectation for the performance.

1.2 General Operating Principle for the STJ

Superconducting tunnel junctions (STJs) have been used for decades to measure x-ray photons (Twerenbold, 1996; Lerch and Zehnder, 2005). As a photon of this frequency has enough energy to break $\sim10^6$ Cooper pairs, the STJ provides not only a photon counter, but also resolves the energy of each photon. These same techniques were then extended to ultraviolet and optical detection, where single photon resolution is still possible and many pixel array have been demonstrated. This work is the natural extension to the lowest possible photon energies, where a single photon breaks a single Cooper pair. As the binding energy of typical low temperature superconductors is of order milli-electron volt, this limit corresponds to light with a wavelength of order a millimeter. Specifically for aluminum junctions, like the ones used in this work, the minimum frequency is roughly 100 GHz. Thus a steady flux of incoming light will lead to an increase in the current through the detector. This response is quantified as the current responsivity, $\mathcal{R}$.

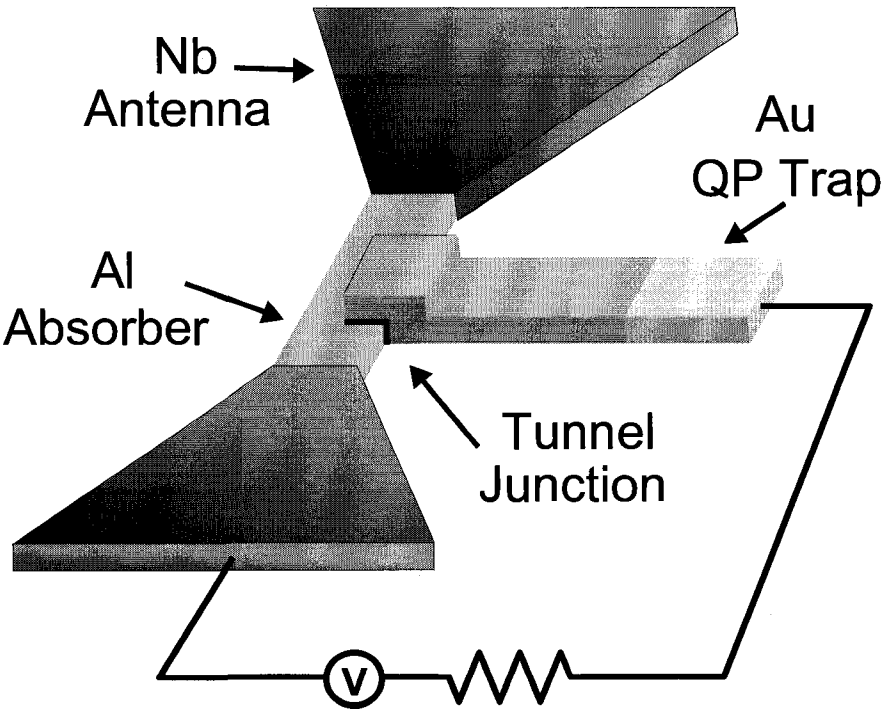

Figure 1.3: This cartoon illustrates the basic operating principle behind the detector. A superconducting antenna couples radiation into a small aluminum absorber where photons with $h\nu > 2\Delta$ break Cooper pairs and create excess quasiparticles. Because the superconducting gap of the niobium antenna is larger than that of aluminum, these excitations are confined to the absorber until they tunnel across the detector junction. Thus, the STJ become a photoconductor, whereby the incident photon flux produces an increased tunneling current through the STJ.

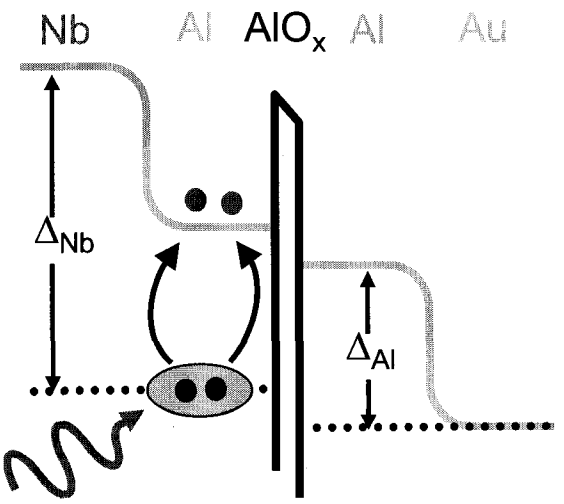

Figure 1.4: This diagram demonstrates the relevant energy scales of the detector. A superconductor with a gap much larger than the radiation of interest is used to couple the radiation into a small volume of aluminum. Thus, photons with $2\Delta_{Al} > h\nu > 2\Delta_{Nb}$ will create quasiparticles in the aluminum that lack the energy to escape into the niobium. When a voltage bias is placed across the junction, these excitations result in a net increase in tunneling current. A normal metal (in this case gold) contacts the counter electrode to serve as a quasiparticle trap. This ensures that the excess energy of the tunneling quasiparticles is dissipated away from the junction and that each quasiparticles only tunnels once.

$$\mathcal{R} = \frac{2e}{h\nu} \approx \frac{2e}{2\Delta} \sim 5000 \text{ A/W} \tag{1.4}$$

As each absorbed photon creates two quasiparticle excitations from the annihilation of a single Cooper pair, the ideal responsivity is shown in Equation 1.4.

To be more specific, a general detection scheme is shown in Figure 1.3. In this cartoon, a planar antenna focuses submillimeter wave radiation into a small aluminum absorber where it creates excess quasiparticles. These excitations are detected by placing a small voltage bias ($V < \Delta/e$) across the detector junction, and monitoring the resulting increase in tunneling current. This antenna is comprised of metal with a larger superconducting gap, such as niobium. This serves two purposes. First, it implies that the antenna will have negligible losses as no Cooper pairs in the niobium will be broken. Second, and more importantly, the quasiparticles that are created in the small volume absorber cannot escape into the antenna as they will be Andreev reflected at the aluminum-niobium interface. This quasiparticle confinement is crucial for ensuring that the excitations will quickly tunnel through the junction resulting in a detector that is both fast and efficient. The counter electrode of the junction is contacted by a normal metal to create a quasiparticle trap. As shown in Figure 1.4, the normal metal allows the energy of the excitations to be dissipated away from the junction and prevents any of the quasiparticles from reentering the aluminum or tunneling back into

the absorber.

For efficient detection, the impedance of the absorber and the radiation impedances of the antenna should both be matched to that of the radiation source. It should be noted that the photon absorption does not take place across the junction, but solely in one electrode. Thus, the radiation impedance of the detector is independent of the the resistance of the detector junction. For example, a bowtie antenna on a dielectric half space of silicon will have an impedance of order 100 Ω. This implies that the absorber should have a real impedance at 100 GHz that is close to this value. As the frequency of radiation is above the superconducting gap of aluminum, the impedance of the absorber will be close to its value in the normal state. So while the absorber maintains its zero DC resistance, it serves as a resistive termination for the antenna. Once the light is coupled into the absorber, the quasiparticle density may be monitored with a detector junction of arbitrarily large resistance. As smaller area junctions should have proportionally smaller leakage currents, the ability to separately optimize the absorption and the detection is one of the many advantages of this scheme. The only constraint on the resistance of the detector junction is that the excitations must tunnel on a timescale that is fast compared to their recombination. As this tunneling time is determined by the product of the absorber volume and the normal state resistance of the detector junction, a fast and efficient detector may be maintained by inversely scaling these quantities. So while the wavelength of the radiation is of order one millimeter, it is only the antenna, not the absorber that must be comparable to this length. The absorber volume can be much less than one cubic micron. This small volume implies that fast ($\sim \mu$s) tunneling times can be achieved even for detector junctions with normal state resistances of order kΩ. The dynamic resistance of the detector in the subgap region where it is biased is increased by another factor of order 10^4, so the STJ is a very high impedance detector that is well suited for extremely low current noise detection.

As the tunneling current is a fundamentally random process, the unavoidable fluctuations in the current correspond to apparent fluctuations in the incoming photon power. Ultimately, it is the shot noise of the tunneling current in the absence of any photons that sets the intrinsic limit of the sensitivity of the photon detector. The figure of merit for the sensitivity of a direct detector is the noise equivalent power (NEP). This is the photon power that may be resolved in one second of integration time with a signal to noise ratio of one. The NEP of the readout may be calculated by dividing the current noise, i_n, by the responsivity, $\mathcal{R}$. If the current noise of the readout could be made arbitrarily small, the shot noise of the detector current would set this sensitivity.

$$\mathrm{NEP} = \frac{i_n}{\mathcal{R}} = \frac{\sqrt{2eI}}{\mathcal{R}} \tag{1.5}$$

For example, detector currents of order 1 pA would imply a shot noise of less than 1 fA/$\sqrt{\mathrm{Hz}}$. Assuming a responsivity of 5000 A/W, this yields a shot noise limited NEP of 10^{-19} W/$\sqrt{\mathrm{Hz}}$. As mentioned earlier, this type of ultra-low NEP is exactly what will be required for future space

missions. To fully exploit this inherently low noise detector, it must be coupled to a readout that is equally low noise.

1.3 Readout Techniques

As the STJ itself is a photoconductor, a sensitive readout is one that corresponds to having the lowest possible current noise. The field effect transistor (FET) is the workhorse of the high impedance detector community, providing extremely low current noise, large dynamic range and a readout bandwidth of order 100 kHz. Unfortunately, most semiconductor-based technologies are not suitable for cryogenic operation. The heat load from the FETs to the cold stage of the cryostat puts a stringent practical limit on the size of the detector arrays that could be readout this way. Furthermore, the increased physical distance between the detector and the amplifier reduces the useable bandwidth and makes the measurements susceptible to other sources of technical noise.

Many other cryogenic detectors use superconducting tunnel junctions in the form of SQUIDS, the amplify the readout signal. While the extremely low voltage noise of SQUID makes it ideally suited for inductively coupling to a low impedance detector, its large current noise would completely dominate the readout noise of a detector with large dynamic resistance. The natural solution would be to use the high impedance analogue of the SQUID, the single electron transistor (SET). By capacitively coupling to an SET, one creates a voltage amplifier with an extremely high input and optimal noise impedance. Furthermore, the advent of the radio frequency single electron transistor (RF-SET) makes the SET fast, sensitive, and naturally lends itself to frequency domain multiplexing (Schoelkopf et al., 1998). While the input impedance of the SET is the nearly infinite impedance of the coupling capacitor, its output impedance (given by the dynamic resistance of the tunneling currents) is greatly reduced to of order 100 kΩ. In the RF-SET, an RF resonant circuit then further transforms this output impedance to roughly 50 Ω so that the SET can be read out with RF reflectometry. As it is the natural advantages of these RF techniques that are responsible for many of the desirable characteristics of the RF-SET, this work also pioneered the idea of applying similar techniques to readout the detector junction directly. This concept of the RF-STJ uses a scheme completely analogous to the RF-SET to measure the state of the detector simply by monitoring how it damps an RF resonant circuit. Such a readout is applicable to the STJ in general, for submillimeter, optical or X-ray applications.

1.4 Thesis Overview

While the ultimate goal of this research is create a sensitive submillimeter camera suitable for space-based astronomy, this preliminary work seeks to demonstrate the single pixel performance in the laboratory setting. The experiments in this thesis are separated into three basic categories. The first measurements focus on exploring the superconducting properties and leakage currents in small-area,

aluminum tunnel junctions. As it is the shot noise of the subgap current that sets the fundamental limit on the sensitivity of the detector, it is important to understand whether the junction behavior may be predicted from theory or if there are important practical considerations that would limit the performance. The next research thrust is to integrate the detector with a sensitive readout. In this work, two such options are tested. The first is using a RF-SET configured as a transimpedance amplifier, while the second uses similar RF techniques to monitor the detector junction directly. These measurements leverage the natural advantages of RF readouts to realize a detection scheme that is not only sensitive, but is amenable to multiplexing into large arrays. The last experiments combine the detector and readout with an on-chip photon source in order to measure the "optical" properties of the detector. The 100 GHz Johnson noise of a mesoscopic resistor illuminates the detector with a calculable photon flux similar to the cosmic radiation which the detector is ultimately designed to detect. This *in situ* source allows for direct measurement of many of the figures of merit for the STJ, including the speed, responsivity, sensitivity, and saturation levels.

Chapter 2

Theory of Superconducting Tunnel Junctions

"Door meten tot weten."

–Motto of H. Kamerlingh Onnes, which translates from Dutch to mean "From measurement to knowledge."

In this chapter, I will provide the theoretical foundations for the superconducting physics used in this work. This includes the electromagnetic properties of superconductors as well as the transport properties of tunnel junctions.

2.1 Introduction to BCS Theory

While superconductivity was first experimentally discovered in 1911 by Kamerlingh Onnes, it was more than 50 years later that a theory was developed to explain the phenomenon (Onnes, 1911). This theoretical framework (BCS theory) arose out of the combined efforts of Bardeen, Cooper and Schreiffer (Bardeen et al., 1957). At temperatures below the critical temperature, T_c, the ground state of a superconducting metal is for the electrons to form bosonic pairs, known as Cooper pairs. At zero temperature, all free electrons would be bound in these pairs and the resulting condensate

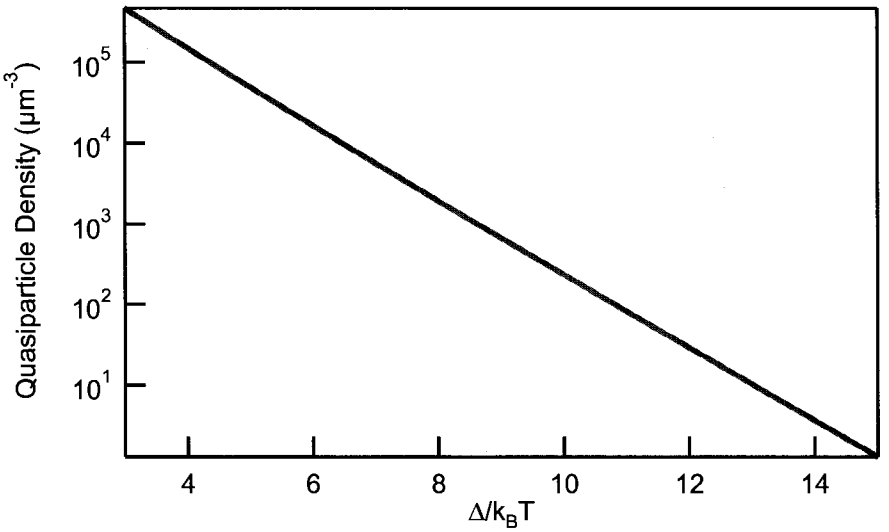

Figure 2.1: Plot of the density of thermal quasiparticles for aluminum. In the detectors used in this thesis work, the typical absorber volume is $\sim 0.5\ \mu m^3$. This implies that at temperatures obtainable with a pumped ^{3}He cryostat, the number of thermal quasiparticles in the absorber is less than 500.

would be describable by a single wave function. Any unpaired electrons are excitations from this ground state. These quasiparticles are fermions whose charge has the magnitude of $|e|$. The binding energy of the Cooper pairs is characterized by the gap parameter. In BCS theory, this is related to the critical temperature by:

$$2\Delta = 3.52 k_B T_c \tag{2.1}$$

While Δ is a temperature dependent quantity, the value in the above equation is the zero-temperature value. The full temperature dependence of the gap may be solved for self-consistently within the BCS framework. It is identically zero at T_c and very quickly increases to its low-temperature asymptote once $T \ll T_c$. The existence of a superconducting gap for excitations has many important consequences. As will be discussed, it results in gap in the quasiparticle density of states as well as in electromagnetic absorption spectrum.

For direct detector applications, it is the quasiparticles, not the Cooper pairs that carry to important information. At temperatures below T_c, the onset of superconductivity gives rise to a gap in the quasiparticle density of states (DOS). In the superconducting state, the quasiparticle density of states is strictly zero for $|E| < \Delta$. For $|E| \geq \Delta$, it is given by:

$$N_s(E) = \frac{2N_0 E}{\sqrt{E^2 - \Delta^2}} \tag{2.2}$$

The number of thermal quasiparticles at a given temperature may be calculated by assuming occupation probability at a given energy is given by a fermi distribution, $f(E)$.

$$f(E) = \frac{1}{1+\exp\left(\frac{E}{k_B T}\right)} \tag{2.3}$$

Thus, the total quasiparticle density can be found by integrating the the product of the DOS and the fermi distribution over all energies.

$$n_{qp}(T) = \int_0^\infty \frac{N_s(E)}{1+\exp\left(\frac{E}{k_B T}\right)} dE \approx 2N_0\sqrt{2\pi k_B T\Delta}\exp\left(-\frac{\Delta}{k_B T}\right) \tag{2.4}$$

where N_0 is the single spin density of states at the Fermi energy. For aluminum, the phonon-enhanced density of states is: N_0=1.72 10^{10} $\mu m^{-3} eV^{-1}$ (McMillan, 1968).

The number of thermal quasiparticles in a given volume of metal is an exponential function of temperature. Figure 2.1 shows this quasiparticle density for aluminum. If high frequency radiation with $h\nu > 2\Delta$ is absorbed by the metal, this will break Cooper pairs and increase the number of quasiparticles. For a small volume of metal at low temperature, the total number of thermal quasiparticles can be quite small, hence the radiation can lead to an appreciable fractional change in the number of quasiparticles. In this way, the quasiparticle density is a direct probe of the number of incident photons. At low temperatures, however, most of the electrical properties of a superconductor are completely dominated by the supercurrent. For example, the DC resistance of the superconductor is strictly zero at all temperatures below T_c, independent of the number of quasiparticles. In a tunnel junction, however, once the critical current is exceeded, the current must be carried by the quasiparticles. Thus, the current voltage characteristic contains information about the quasiparticle density. The next sections will describe the detailed IV curve of a superconducting tunnel junction, as well as how it is affected by the number of excess quasiparticles.

2.2 Josephson Tunneling Currents

One way to exploit many of the useful properties of a superconducting metal is to create a Josephson junction. First explained theoretically by Brian Josephson, a Josephson junction is created by separating two superconductors by small insulating barrier (Josephson, 1962). If the insulator is thin enough current can still flow across the device by quantum mechanically tunneling. For small currents ($I<I_c$), the charge flow is carried entirely by the Cooper pairs. The tunneling of Cooper pairs leads Josephson equations.

$$I = I_c \sin(\phi) \tag{2.5}$$

$$\frac{\partial\phi}{\partial t} = \frac{2eV}{\hbar} \tag{2.6}$$

Here ϕ is the phase difference across the junction. These equations have several implications. First, the critical current of a junction can be modulated with the presence of a magnetic field (the DC Josephson effect). Secondly, a DC bias voltage will cause the current to oscillate at the Josephson frequency with an amplitude of I_c (AC Josephson effect).

This Josephson current has a maximum value predicted by Ambegaokar and Baratoff to be (Ambegaokar and Baratoff, 1963):

$$I_c = \frac{\pi}{4}\frac{2\Delta(T)}{eR_n}\tanh\left(\frac{\Delta(T)}{2k_BT}\right) \tag{2.7}$$

For low temperatures ($T \ll T_c$), the gap becomes independent of temperature and this equation reduces to:

$$I_c = \frac{\pi}{4}\frac{2\Delta}{eR_n} \tag{2.8}$$

In this application, these Cooper pair currents serve only to obscure the measurement of the quasiparticle currents. It is only with the supercurrent fully suppressed that the IV curve is a direct probe of the quasiparticle density. The Josephson current may be suppressed by applying a magnetic field. Applying a parallel magnetic field will modulate the critical current as integer number of flux quanta are enclosed in the cross section of the junction. For small area junctions, the field required to apply one flux quantum becomes so large that the field may begin to affect the T_c. In this case, the solution is to partition the junction into two junctions in parallel in order to form a DC SQUID (Clarke and Braginski, 2004). Now a magnetic field applied perpendicular to the surface will modulate the supercurrent with a periodicity related to the loop area of the SQUID, not the size of the junction.

For a general SQUID comprised of two Josephson junctions with critical currents I_1 and I_2, the critical current is periodic in the applied flux as given by 2.9.

$$I_c(\Phi) = \sqrt{(I_1 - I_2)^2 + 4I_1I_2\cos^2\left(\pi\frac{\Phi}{\Phi_0}\right)} \tag{2.9}$$

If the junctions are identical, then $I_1 = I_2 \equiv I_0$ and this equation reduces to:

$$I_c(\Phi) = 2I_0\left|\cos\left(\pi\frac{\Phi}{\Phi_0}\right)\right| \tag{2.10}$$

Neglecting the self-inductance of the SQUID, this shows that at $\Phi = \Phi_0/2$, the critical current can be made arbitrarily small. Figure 2.2 shows the normalized critical current as a function of applied flux for perfectly symmetric SQUID and one with a 10% junction asymmetry. In this work, suppression by a factor of more than 1000 is typically observed. In practice, small supercurrents can be suppressed by noise of the environment. The relevant energy scale for tunneling currents is given by the Josephson energy.

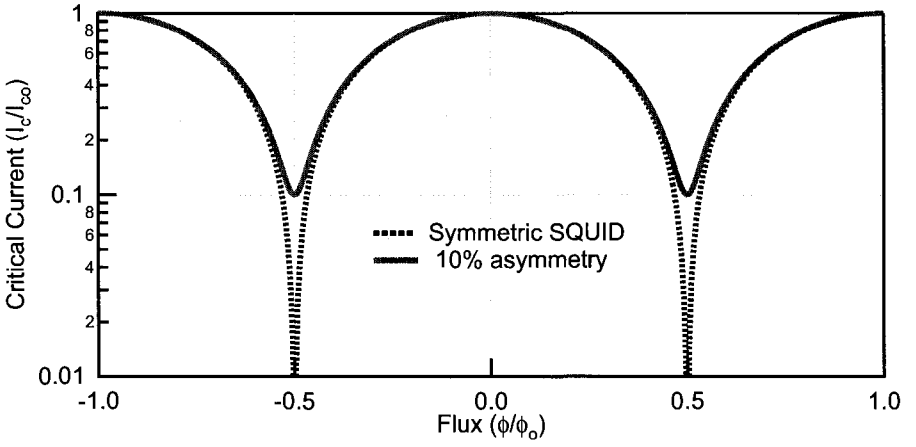

Figure 2.2: The supercurrent of a SQUID is a periodic function of applied flux. The first minimum occurs at $\Phi_0/2$. If the two junctions of the SQUID have any asymmetry in their critical currents, the this will lead to incomplete suppression at this minimum. The two curves above show the modulation of the critical current for a SQUID comprised of two identical junctions and for a SQUID whose junctions have a 10% difference in critical current.

$$E_J = \frac{\Phi_0 I_c}{2\pi} = \frac{\hbar I_c}{2e} \tag{2.11}$$

As E_J becomes less than $k_B T$, the thermal noise of the environment affects the measured supercurrent. In fact, for small critical currents the current peak at zero bias becomes rounded and has finite dynamic resistance due to phase diffusion[ref phase-diffusion].

2.3 Quasiparticle Tunneling Currents

With the supercurrent suppressed, the remaining structure in the IV curve is shown in Figure 2.3. This resulting tunneling current clearly reflects the gap in the DOS for the quasiparticles. At zero temperature, the current is strictly zero for all voltages less than $2\Delta/e$. At finite temperatures, there is some current that flows in this subgap region due to the thermal quasiparticles. The current may be calculated by integrating the DOS in the two electrodes, taking into account the occupied and unoccupied states in each.

$$I_{SIS}(V) = \frac{1}{eR_n}\int_{-\infty}^{\infty} N_{s1}(E'-eV)\,N_{s2}(E')\,[f_1(E'-eV) - f_2(E')]\,dE' \tag{2.12}$$

$$= \frac{1}{eR_n}\int_{-\infty}^{\infty} \frac{|E'-eV|}{\sqrt{(E'-eV)^2-\Delta_1^2}}\frac{|E'|}{\sqrt{(E')^2-\Delta_2^2}}\,[f_1(E'-eV) - f_2(E')]\,dE' \tag{2.13}$$

where the subscripts 1, 2 denote the properties of the each of the two superconducting electrodes.

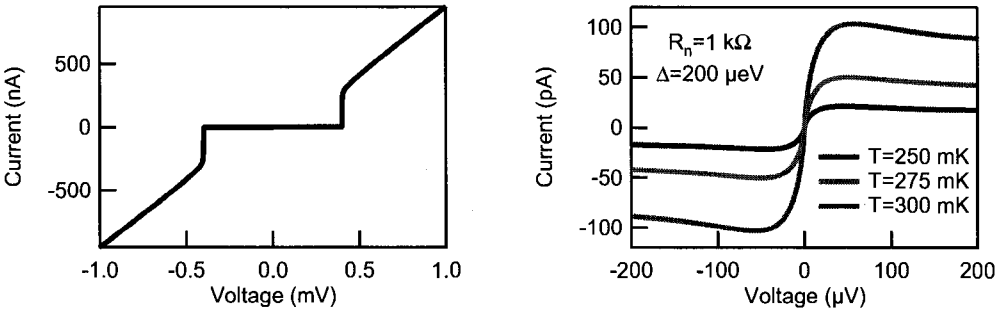

Figure 2.3: These graphs shows the quasiparticle tunneling current predicted by BCS theory for an SIS tunnel junction. The right hand graph shows the subgap currents predicted by equation 2.14 for a junction with a normal state resistance of 1 kΩ and a superconducting gap of 200 μeV in both electrodes. The overall scale of the subgap current scales exponentially with temperature and is plotted for three different quasiparticle temperatures of 250, 275, and 300 mK. From a detector standpoint, the thermal quasiparticle current represents the lower baseline above which a photocurrent must be measured. As submillimeter radiation creates excess quasiparticles in the absorber, the resulting subgap tunneling current increases as if the junction were at a higher temperature. For example, the curve at 300 mK is a good approximation of the effect of 15 fW of 100 GHz radiation on a detector held at 250 mK. It is important to note that the effect of the incident photons can be measured either by monitoring the current at finite bias voltage or by measuring the differential resistance near zero bias.

There are several features of tunneling current to note. At temperatures greater than T_c of both electrodes, the current-voltage relation is completely ohmic with a slope given by R_n. As the temperature is lowered past T_c, the differential conductance, $\frac{dI}{dV}$, begins to reflect the gap in the density of states of the superconducting metal. The gap used in the equation 2.12 is the temperature dependent gap, $\Delta(T)$. Once the temperature is much lower than T_c, the gap becomes essentially independent of temperature.

In general, equations 2.12, do not require that the two electrode have the same superconducting gap. For an SIS′ junction, there are two distinct features in the IV curve when the bias voltage equals the sum and difference of the two gaps. When $eV=|\Delta_1 - \Delta_2|$, there is a peak in the subgap current (followed by a region of negative differential resistance) as the singularities in the density of states in the two superconductors align. Once $eV=\Delta_1+\Delta_2$, there is a sharp increase in the tunneling current. On the gaprise, the current abruptly increases by several orders of magnitude. When the bias voltage is much greater than sum of the two gaps, ($eV \gg \Delta_1+\Delta_2$), the superconducting density of states approaches its value in the normal state, and the differential resistance again becomes ohmic with a value of R_n. This highly non-linear IV characteristic exhibits a dynamic resistance that can be orders of magnitude less than or greater than R_n, or even negative. In fact, in the non-equilibrium case where the two electrodes have both a different temperature and a different gap value, the junction can exhibit absolute negative resistance. Here the current near zero bias

decreases for increasing bias voltage (Krauss et al., 1996).

A more typical case for the subgap current is when the electrodes are comprised of the same metal (with the same T_c and Δ) and are held as the same temperature. Now the gaprise, occurs at $V=2\Delta/e$ and there is no difference feature. The current for $V<2\Delta/e$, *i.e.* the subgap region, can be calculated analytically for low temperatures (Van Duzer and Turner, 1998). Assuming that $T \ll T_c$ the subgap current given by the tunneling integral in equation 2.12 is well approximated by:

$$I_{SIS}(V) = \frac{2}{eR_n}\sqrt{\frac{2\Delta}{eV+2\Delta}}(eV+\Delta)\sinh\left(\frac{eV}{2k_BT}\right)K_0\left(\frac{eV}{2k_BT}\right)\exp\left(-\frac{\Delta}{k_BT}\right) \tag{2.14}$$

where K_0 is the zeroth-order modified Bessel function.

The quasiparticles possess both an electron-like and hole-like nature, but is only in the process of tunneling that these are distinguished. At zero bias voltage across the junction, there is no net electrical current because just as many quasiparticles tunnel as electrons (with charge $+|e|$) as holes (with charge $-|e|$). As a bias voltage is applied, this symmetry is broken and net charge is transferred. As seen in Figure 2.3, the current monotonically increases with voltage, until the bias voltage is $\sim k_BT/e$. Beyond this point, the current no longer increases because at this energy, there are no longer empty states into which to tunnel. In fact for voltages greater than k_BT/e, the current actually decreases as the superconducting density of states slowly reduces to its asymptotic value. Ideally, the current would follow this functional form until the sharp current increase at the gaprise when $V=2\Delta/e$. Practically, equation 2.14 fits the measured tunneling current very well (in situations where the supercurrent can be fully suppressed) only for voltages up to $\sim \Delta/e$. Beyond this voltage, the subgap current tends to increase due to other effects such as self-heating or higher order tunneling processes. The important feature of the subgap current is that it is directly proportional to the quasiparticle density and that the number of thermal quasiparticles scales exponentially with temperature. For a typical aluminum film with $\Delta=200$ μeV at 250 mK, there are only 500 thermal quasiparticles in a cubic micron volume of metal. The subgap current at a bias voltage of 100 μV is reduced by a factor of 5000 from its value in the normal state. If the temperature is further lowered to 200 mK, both the number of thermal quasiparticles and the corresponding subgap current are reduced by another order of magnitude. The changing current level also results in change in the differential resistance near zero bias voltage. This effect will be exploited in this work by using RF reflectometry to sense this change in the RF impedance and infer the incident photon power.

2.4 Other Tunnel Junction Physics

The discussion in the previous section accounts only for the currents due to the presence of thermal quasiparticles. There are many other effects that can markedly change the measured IV curves. This section will discuss some of these effects and their importance in this application.

The first non-ideality is related to excess quasiparticle current. As seen in the last section, this current is an exponentially sensitive thermometer. Thus, if the electrodes are not properly heat sunk or if the filtering in not adequate, the subgap current will still fit to the same functional form as in equation 2.14, but with a temperature greater than that of the cryostat. This effect is readily diagnosed by mapping out the full temperature dependence of the subgap current. Incomplete cooling would be indicated by a decoupling of the quasiparticle temperature from the cryostat temperature at low temperatures. The excess heating can also be related to the Joule power dissipated near the junction by the measurement current. At typical bias voltages less than Δ/e, this is not an issue do to the small currents and voltages. At the gaprise, the Joule power greatly increases and the quasiparticle density can actually become large enough to reduce the gap of the superconductor. The reduced gap in turn, reduces the heating giving rise to a complicated gaprise structure. The measurement of this "backbending" depends on the load line of the bias as well as the detailed cooling dynamics of the quasiparticles. While this self heating does not affect the performance of the detector, it does make it more difficult to determine the exact value of the superconducting gap from the IV curve.

While the tunnel junction is a resistive element, the dissipation does not actually occur in the junction. On the contrary, the power is dissipated in the reservoirs of the electrodes when the high energy quasiparticles emit phonons. If the geometry does not allow these energetic quasiparticles to diffuse away from the junction, there can be backtunneling. In this process, a single excitation can tunnel several times before it eventually recombines with another quasiparticle. This effect can be exploited to increase the size of the detector signal, but it does not improve the intrinsic signal to noise of the detection (Wilson, 2002; Savu, 2007). In this work, the geometry is designed to avoid backtunneling by contacting the counter electrode with a normal metal. Once the energy is transferred to the electrons in the normal metal, the electrons quickly scatter to lower energy and cannot re-enter the aluminum as quasiparticles.

Another non-ideality of tunnel junctions is simple leakage. This occurs if there is any alternate current path across the junction. In some experiments in this work subgap currents as low as 1 fA were seen at a bias point of 100 μV. Thus, a leakage resistance of 1 TΩ would affect the measurement. An ohmic leakage contribution was not seen in this work, but is known to be more prevalent in very high current density junctions. The quality of aluminum oxide as an insulator is one of the many reasons it is the dielectric of choice in most tunnel junction realizations.

The most prevalent non-ideality in SQUID junctions used in this work is inability to fully suppress the supercurrent. Naively, one would assume that residual supercurrent would only affect the IV curve at the zero bias voltage point. The complex dynamics of the Cooper pair currents, however, can also lead to excess current throughout the subgap region. One mechanism is referred to as inelastic Cooper pair tunneling (Holst et al., 1994). The AC Josephson effect dictates that when the junction is biased at a finite voltage, an AC supercurrent is created. It has an amplitude given by the

DC critical current and is at the Josephson frequency ($f_J = 2eV/h$). Conversely, if an AC voltage is applied across a junction, the Cooper pair currents are displaced from their zero bias location to a finite voltage corresponding to the Josephson frequency. These Shapiro steps were first measured by Shapiro in 1963 (Shapiro, 1963). The inelastic Cooper pair tunneling occurs when a Josephson junction has an environment with a real impedance at the Josephson frequencies. As the junction is biased, it emits an AC current into its environment. This AC current across a real impedance gives rise to an AC voltage. But this AC voltage, in turn, creates a Shapiro-like step in the subgap current. This effect can be thought of as a self-induced Shapiro step. The subgap current from this effect may be calculated simply by equating the AC power with the DC Joule power of the bias point.

$$I_{iect} = \frac{I_c^2 Re[Z(\omega_J)]}{2V} \tag{2.15}$$

It is important to emphasize that relevant frequencies for bias voltages of 20 to 200 μV are 10 to 100 GHz. Thus, it is difficult to fully engineer the local environment to avoid any resonances. This effect is less important for large area junctions, because the large capacitance of the junction shunts the environmental impedance. For small area junctions, the subgap structure due to the uncontrolled resonances in the environmental impedance can give rise to currents that are orders of magnitude larger that the thermal quasiparticle currents.

An analogous effect that is often seen in STJ detector work is that of Fiske modes (Fiske, 1964). A Fiske mode occurs when the junction itself is large enough to form an electromagnetic resonator at the Josephson frequencies. The two electrodes of the junction form a parallel plate transmission line, that can support a TEM mode. The edges of the junction put boundary conditions on this transmission line to form a resonant cavity. Thus, this electromagnetic resonance will give rise to a sharp peak in the IV curve whenever the bias voltage excites one of these cavity modes. While this effect is prevalent STJ detectors used for the detection of X-rays, (Li, 2003), the junctions used in this work are too small to support Fiske modes.

2.5 Complex Conductivity of a Superconductor

In order to understand how the submillimeter wave radiation is absorbed by a superconducting metal, the complex frequency-dependent impedance must be analyzed. The first observed hallmark of superconductivity was the onset of perfect DC conductivity at low temperatures. At high enough frequencies, however, the impedance of the superconductor returns to that of a normal metal, even at temperatures below T_c. In work that actually predates BCS theory, Mattis and Bardeen developed a theory that describes the impedance of a superconductor at all frequencies (Mattis and Bardeen, 1958).

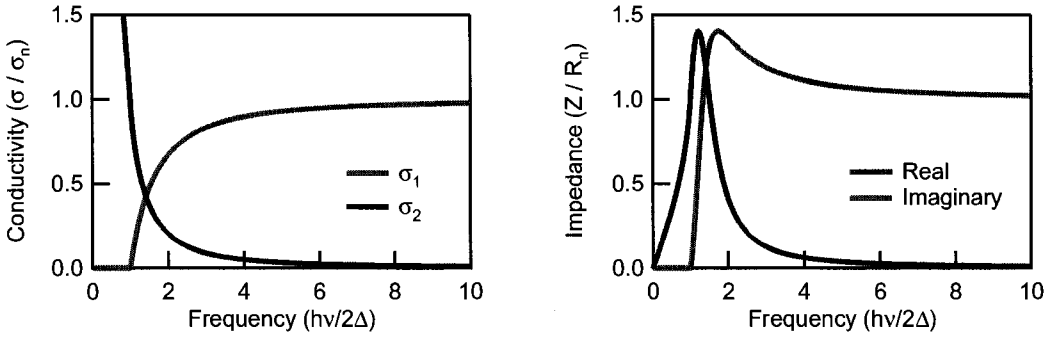

Figure 2.4: These graphs show the real and imaginary parts of the conductivity and impedance of a superconductor at zero temperature. Each graph is normalized to the value just above T_c. For frequencies below $2\Delta/h$, the superconductor looks purely inductive. At frequencies much greater than $2\Delta/h$, the conductivity and the impedance asymptotically approach their value in the normal state.

The complex conductivity of a superconducting metal is both frequency and temperature dependent. Following the convention of Glover and Tinkham, it is parameterized as (Glover and Tinkham, 1957; Tinkham, 1965)

$$\sigma = \sigma_1 - i\sigma_2 \tag{2.16}$$

In a 1958 paper, Mattis and Bardeen calculated these quantities (Mattis and Bardeen, 1958). These integrals give the ratio of the σ_1 and σ_2 to σ_n, which is the conductivity just above T_n.

$$\frac{\sigma_1}{\sigma_n} = \frac{2}{h\nu}\int_{\Delta}^{\infty} [f(E) - f(E+h\nu)]\, g(E)\, dE + \frac{1}{h\nu}\int_{\Delta-h\nu}^{-\Delta} [1 - f(E+h\nu)]\, g(E)\, dE \tag{2.17}$$

$$\frac{\sigma_2}{\sigma_n} = \frac{1}{h\nu}\int_{\Delta-h\nu,-\Delta}^{\Delta} [1 - 2f(E+h\nu)]\, g(E)\, dE \tag{2.18}$$

where

$$g(E) = \frac{E^2 + \Delta^2 + Eh\nu}{\sqrt{(E^2 - \Delta^2)\left[(E+h\nu)^2 - \Delta^2\right]}} \tag{2.19}$$

and $f(E)$ is the Fermi function defined by Equation 2.3.

The first integral in equation 2.17 accounts for the effect of thermally excited quasiparticles. The second integral accounts for the fact that the radiation with $h\nu > 2\Delta$ will break Cooper pairs and create more quasiparticles. The imaginary conductivity, given by equation 2.18, is due strictly to the Cooper pairs. The lower limit of integration is understood to be $\Delta - h\nu$ for $h\nu < 2\Delta$ and $-\Delta$ for $h\nu < 2\Delta$.

Assuming T=0, the fermi functions become unit step functions, and these equations can be integrated analytically. The resulting expressions are:

$$\frac{\sigma_1}{\sigma_n} = \left(\frac{2\Delta}{h\nu} + 1\right) E(k) - 2\left(\frac{2\Delta}{h\nu}\right) K(k) \tag{2.20}$$

$$\frac{\sigma_2}{\sigma_n} = \frac{1}{2}\left(\frac{2\Delta}{h\nu} + 1\right) E(k') + \frac{1}{2}\left(\frac{2\Delta}{h\nu} - 1\right) K(k') \tag{2.21}$$

where $E(k)$ and $K(k)$ are the complete elliptic integrals of the 1st and 2nd kind, respectively.[1] The arguments are defined as: $k = \left|\frac{2\Delta - h\nu}{2\Delta + h\nu}\right|$ and $k' = \sqrt{1-k^2}$. Equation 2.20 is valid for $h\nu > 2\Delta$. When $h\nu \leq 2\Delta$, $\sigma_1 = 0$.

Figure 2.4 shows the zero temperature results of Mattis-Bardeen theory. Roughly speaking, the gap frequency ($\nu = 2\Delta/h$), represents the threshold, above which the metal no longer looks like superconductor. For frequencies below the gap, the real part of the conductivity is strictly zero except for a delta function at DC. The height of this delta function accounts for the "missing" area in the conductivity-frequency product as compared to the normal state. At these low frequencies, the impedance is purely inductive. At the gap frequency there is a sharp increase in the real part of the conductivity as the radiation can be absorbed by breaking Cooper pairs. As must be expected from Kramers-Kronig relations, this sudden change in the real part of the conductivity with frequency must be accompanied by a change in the imaginary part as well. Indeed, there is a discontinuity in slope of σ_2 at the gap frequency. The magnitude of the imaginary conductivity at this frequency is equal magnitude of the conductivity in the normal state.

This conductivity may then be used to calculate the impedance of the metal. Because the radiation only penetrates a finite distance into the metal, the useful quantity is the surface impedance. While in a normal metal, this length scale is given by the skin depth; in a superconductor it is given by the London penetration depth, λ_L. As the thin films used in this work have a thickness that is $\lesssim \lambda_L$, the surface impedance is simply given by the film thickness. The right-hand graph in Figure 2.4 shows this impedance. As expected, at frequencies below the gap, the incident radiation will be reflected. Well above the gap, the impedance of the film approaches the value in the normal state. Thus, in order to couple radiation into the film, the absorber is designed to be a resistor with a real impedance in the normal state that matches the radiation impedance. This impedance is purely that of the absorber and is independent of the resistance of the tunnel junction used to detect the excess quasiparticles in the absorber. For each photon that is absorbed by the film, one Cooper pair is broken. Under a steady stream of incident photons, the current responsivity of the detector, $\mathcal{R}=2e/h\nu$. For 100 GHz photons, this is roughly 5000 A/W. Unlike a bolometer, this responsivity depends on the number of incident photons just above the gap, not the energy of the photons.

[1] If evaluating these expressions in Mathematica, the argument of all elliptic functions is m or m', where $m = k^2$ and $m' = k'^2$.

2.6 Quasiparticle Dynamics

This last section calculates the relevant timescales in the photon detection process. These timescales set the overall speed of the STJ detector as well as determine the efficiency with which absorbed photons result in increased current through the detector.

The first important timescale is the tunneling time. In a normal metal tunnel junction, the tunneling time is defined as the average time for an electron in one electrode to tunnel into the other. This depends on the volume of the electrode, the number of transmission channels, and the average transparency of the channels. The product of the two latter quantities is simply the inverse of the normal state resistance of the junction.

$$\tau_{tun} = e^2 N_0(0) R_n Vol \tag{2.22}$$

In the superconducting state, there is an analogous expression for the tunneling time, but it now has a voltage dependence due to the energy dependence in the superconducting quasiparticle DOS.

$$\tau_{tun} = 2e^2 N_0(0) R_n Vol \frac{\sqrt{(E \pm eV)^2 - \Delta^2}}{E \pm eV} \tag{2.23}$$

This expression is the average time for a quasiparticle with energy, E, in an absorber of volume, Vol, and gap, Δ, to tunnel into the counter electrode at energy, $E \pm eV$. Thus, a fast detector can be created by having a small absorber volume or by having a small normal state resistance of the STJ. As high resistance junction have the smallest dark currents, one would optimize for sensitivity by making the junction a small as possible. Unfortunately, this implies a small absorber volume, and hence a detector that will saturate sooner. Like any detector, there is a fundamental tradeoff between sensitivity and saturation. For the detectors in this thesis work, the absorber volume is made as small as possible and the junction resistance is chosen such that the tunneling time is roughly 1 μs.

The microsecond timescale is important for two reasons. First, it allows for several hundred kilohertz of readout bandwidth. Depending on the exact application, this bandwidth may or may not be required. More importantly, the second reason for this short tunneling time is that it must be fast compared to any other timescales for quasiparticle loss in the system. One such mechanism is quasiparticle recombination. If two quasiparticle excitations can recombine into a Cooper pair, then no excess tunneling current is ever detected. The rate of recombination increases with increasing number of quasiparticles. In fact, as the probability of finding another quasiparticle is proportional to the number of different pair that can be created, the rate goes as the square of number of quasiparticles.

$$\frac{\partial N}{\partial t} = -N(N-1)\frac{R}{Vol} \equiv -\frac{N}{\tau_{rec}} \tag{2.24}$$

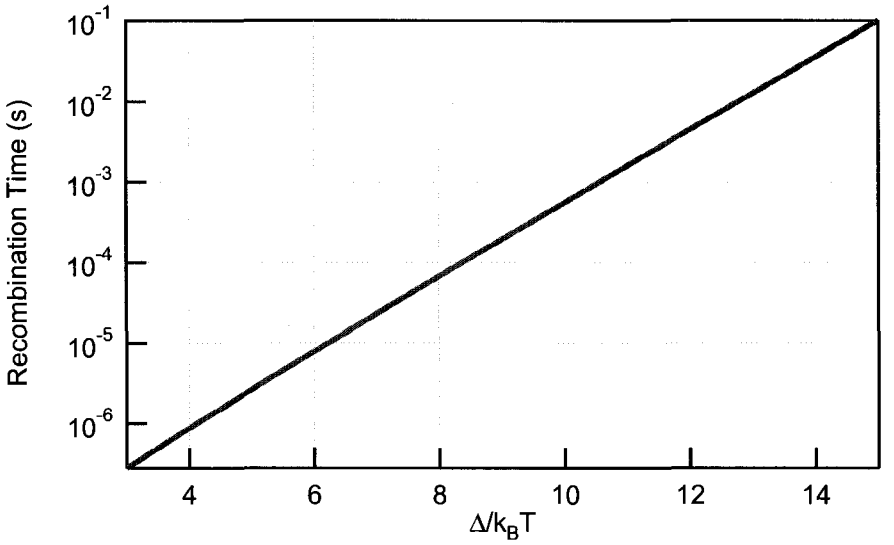

Figure 2.5: The theoretical prediction for the recombination time in an aluminum absorber as a function of temperature. This timescale is inversely proportional the the quasiparticle density with proportionality constant of 0.1 s/μm^3. Saturation in the detector occurs once the quasiparticle density is high enough that the recombination time is comparable to the tunneling time of the STJ.

Here R is the recombination rate per unit density of quasiparticles and N/Vol is the quasiparticle density, n_{qp}. Thus, at both high temperature or high incident photon powers, the quasiparticle density is high and hence the recombination rate is fast. It is the ration of this time to the tunneling time that determines the maximum operation temperature for the detector. The recombination rate per unit density can be calculated analytically assuming the system is close to equilibrium and the quasiparticle density is given by the thermal density from Equation 2.4 (Kaplan et al., 1976).

$$R = \left(\frac{2\Delta}{k_B T_c}\right)^3 \frac{1}{4N_0\tau_0\Delta} \tag{2.25}$$

Here, τ_0 is a material-dependent quantity that characterizes the strength of the electron-phonon interaction. It is found to be 438 ns for aluminum (Kaplan et al., 1976). Thus, R$\approx$10 μm^3/s. The temperature dependence of the recombination time is plotted in Figure 2.5. Thus for aluminum at 300 mK, the theoretical recombination time is $\sim$30 μs. This agrees with well with experimental measurements (Wilson, 2002). It is only once incident photons raise the quasiparticle density to an effective temperature of 500 mK that the recombination time should fall below 1 μs.

Chapter 3

Radio Frequency Techniques

"Radio has no future."

–Lord Kelvin

Maxwell's equations dictate the behavior of all electromagnetic waves whether they are at 5 Hz, 5 MHz, or 5 THz. But from an engineering standpoint, there are vastly differing frameworks developed to deal with each frequency range. The reason is that the wavelength of the light sets the characteristic length scale for manipulating these waves. In DC electronics and at audio frequencies, the wavelength is always much larger than circuits or the devices they are measuring, and the language is that of lumped circuit elements. Above the terahertz, one enters the range of optics where the wavelength is almost always less than the objects with which the light is interacting. This thesis addresses the ranges in the electromagnetic spectrum in between. The goal of this work is to measure light at frequencies just below the far infrared, known as submillimeter wave radiation. This will be accomplished by monitoring the response of the detectors in the RF, at frequencies between 200 and 600 MHz. Thus, this work uses the upper and lower extremes of the microwave spectrum for detection and readout, respectively. In both cases, one can exploit methods from both DC electronics and optics. Furthermore, it is precisely the ability to do nano-lithography that allows for the creation of lumped circuit elements even up to terahertz frequencies.

This thesis work, as well as all other experiments in the Schoelkopf lab, takes advantage of the ability to use radio frequency and microwave techniques to study cryogenic phenomena that were traditionally only accessible through DC transport measurements. This experimental niche not only allows access to timescales that were previously unattainable, but in many cases, it can be used to increase the sensitivity of the measurement. For experiments in which the noise is the signal of interest, larger measurement bandwidth directly correlates to shorter integration times and hence greater sensitivity. In contrast, reflectometry is a way to use an RF carrier signal to monitor the DC properties of system. It is important to emphasize the specific choice of an RF band does not correspond to frequencies unique to any particular mesoscopic measurement. On the contrary, whether the experimental setup is at 300 MHz or 3 GHz is usually inconsequential; it merely provides a convenient window in the frequency domain into which the signals of interest can be mixed. Audio frequency, lock-in techniques have been the workhorse of "DC" measurements for decades because of their ability to avoid low frequency noise and control the effective noise bandwidth of the measurement. In the same way, RF reflectometry may be seen as the extreme extension of these methods that allow for simultaneous DC and RF measurements. Unlike the case of noise thermometry, with reflectometry larger measurement bandwidth is only advantageous if one wishes to study faster dynamics. In practice, even "narrow band" RF measurements will still greatly exceed the speed of "fast" DC measurements. So in many cases it is possible to tradeoff this excess bandwidth for increased sensitivity (bigger transformers) or increased number of measurements (multiplexing). Both of these properties are of great interest in the detector community, where one could use the large frequency window to monitor the response of many individual detectors. This frequency domain multiplexing would reduce the number of amplifiers, wires, and complexity of the overall system, while still preserving many of the benefits of working at RF frequencies. These methods will become crucial as 4 x 4 arrays of detectors are scaled toward megapixel cameras. One final advantage of RF measurements has come with the advent of increasing commercial microwave technology. This provides a rich and mature infrastructure from which to draw both techniques and technology. A prime example is High Electron Mobility Transistors, or HEMT amplifiers, which can operate at cryogenic temperatures and are unsurpassed in their combination of sensitivity, gain, and dynamic range (Bradley, 1999). It is for all of these reasons that this research seeks to exploit these qualities not only to carry out novel measurements, but to improve the performance of existing methods.

With all of these benefits in mind, there are also many reasons that such measurements can be difficult. Simply stated, the problem is that requirements for getting devices to cryogenic temperatures is inherently contradictory to how one would design for maximal bandwidth. The cryostats need long, resistive wires in order to provide thermal isolation between stages at vastly differing temperatures. An RF engineer would cringe at the capacitance this adds, in addition to making experimental setup large compared to wavelengths of interest. Furthermore, as will be discussed

in detail in chapter 5, there are strict filtering requirements necessary to ensure that the cryogenic environment of the sample is completely devoid of any photons with energy greater than the temperature of the sample. Not only does this imply even greater parasitic capacitance of the measurement leads, but also should make one paranoid about opening a measurement window to room temperature at these higher frequencies. The final issue is that the devices of interest rarely have constant resistance, let alone ones that match the input impedance of RF amplifiers or cables. If unaddressed, this will lead to both degradation in overall sensitivity and the properties of the system will vary greatly over the frequency band of interest. As will be shown, there are experimental techniques to overcome all of these issues. This chapter will develop the language of microwave techniques and show how they have been successfully integrated into cryogenic experiments.

3.1 Impedance and Reflection

Impedance matching is an important consideration in the design of any measurement setup. It is the impedance that characterizes how electromagnetic waves will be absorbed or reflected by a given load. An unmatched load will not only create standing waves but will necessarily diminish the signal to noise ratio of the measurement. This becomes especially relevant at radio frequencies and above, where the wavelengths involved become on the order of or shorter than the measurement circuit. At these frequencies, parasitic capacitances and inductances are no longer negligible, but can have dramatic effects that distort and degrade the signal. The characteristic impedance is a property of any electromagnetic mode. It is defined by the geometry of the surrounding conductors and dielectrics. It specifies the relative strengths of the electric and magnetic fields as the wave propagates. For example, a plane wave propagating in a vacuum is a TEM mode which has characteristic impedance of free space, $\eta_o \approx 377\Omega$. In order to define a transmission line for a TEM mode, it requires two conductors and the resulting characteristic impedance of the line will be on the order of η_o (Pozar, 2005). While the exact geometry and dielectric constants can make this vary from a few ohms to a few hundred ohms, the overall scale is set by η_o. This impedance is real, which means that currents and voltages in the conductors will be in phase. In some measurements, one has the freedom to design the experiment to naturally match this impedance; however, if the devices of interest have a resistance that is very different from the impedance of the transmission lines, then some form of transformation will be required in order to efficiently couple to the radiation. The voltage reflection coefficient, Γ quantifies how waves will be reflected from a given impedance discontinuity.

$$\Gamma(\omega) = \frac{Z(\omega) - Z_o}{Z(\omega) + Z_o} \tag{3.1}$$

where Z_o is the characteristic impedance of the line and $Z(\omega)$ is the frequency dependent impedance of the load.

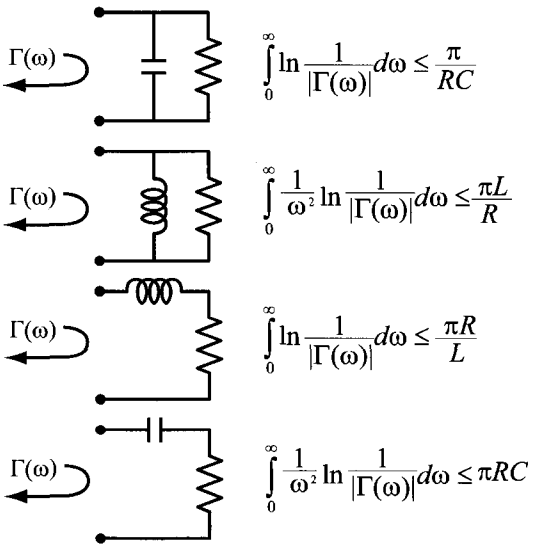

Figure 3.1: Theoretically, any two real impedances can be matched over an arbitrarily large bandwidth. However, if the load has a reactive component, then the Bode-Fano limit places an upper bound on the bandwidth of the impedance match. This figure shows the result of the Bode-Fano theorem for four types of complex loads.

From this, it is apparent that there will be no reflection from a line terminated in its characteristic impedance. The reflection coefficient, like the impedances, is a complex quantity that specifies both the magnitude and phase of the reflected wave. A load consisting of a short or open circuit will result in complete reflection, but the former will be 180 degrees out of phase. In the case that the source has an imaginary component, the condition for complete power transfer is that the load has an impedance that is the complex conjugate of the source, $Z_s = Z_L^*$. The magnitude of reflection can be quantified in several other ways as well. The return loss (RL) is the magnitude of the reflection in units of dB, RL=20 log $|\Gamma|$. The voltage standing wave ratio (VSWR) is defined as VSWR=$\frac{1+|\Gamma|}{1-|\Gamma|}$. As the name implies, it quantifies the ratio of the amplitude of the standing wave created by the impedance mismatch. As such, it ranges from 1 for a matched load to ∞ for a short or open. For example, in matching to a 50 Ω line, any impedance between 40 Ω and 60 Ω would have a return loss of better than 20 dB or a VSWR of less than 1.22.

In practice, conjugate matching can only be accomplished at particular, resonant frequencies of the system. As will be shown in the next section, this limits the total bandwidth over which power transfer can occur. The rest of this chapter will then focus on how one can best make a large impedance look like the 50 Ω characteristic impedance of the transmission lines and amplifiers that will be used.

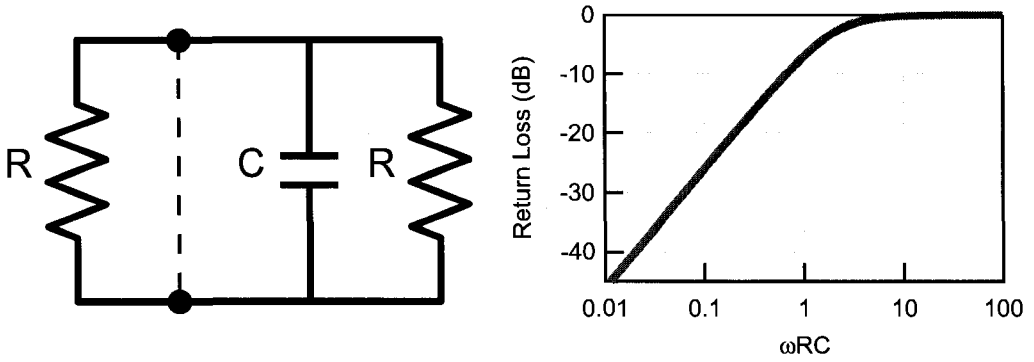

Figure 3.2: Example of a circuit where the load can be said to be conjugately matched at DC and a plot of its return loss as a function of frequency. The RF matching techniques used in this work use an inductor to simply move this conjugate match away from DC to RF frequencies, ideally without any loss of intrinsic bandwidth.

3.2 Bode-Fano Limit

In general, any impedance can be matched to any other impedance using a lossless (purely reactive) matching network. The bandwidth over which this match can occur is, however, limited. In 1945, Bode showed that for the case of a resistance shunted by a capacitance, the bandwidth of the match is inversely proportional to the RC product of the system (Bode, 1945). Later, Fano extended this work to show that the reactance of the load (inductive or capacitive, in series or in parallel) will always set the fundamental limit for the bandwidth (Fano, 1950). This is know as the Bode-Fano criterion. Figure 3.1 shows four configurations for complex load impedances and their corresponding Bode-Fano limits (Pozar, 2005).

The implications of this theorem are twofold. First, while one can use resonant techniques to work at higher frequencies, the amount of usable bandwidth is fixed and independent of the center frequency of the match. The second important implication is that one should not waste any of the bandwidth by inadvertently matching at frequencies outside the region of interest.

In order to illustrate this principle, one can examine the simple case of a resistance that matches the source resistance but is shunted by a finite capacitance as in figure 3.2. In this case, there is no matching network necessary since the source and load are naturally matched at DC. This is relevant for the shot noise thermometer (Spietz, 2005), where a 50 Ω tunnel junction has an intrinsic capacitance on the order of several hundred femtofarads. Integrating the log of the inverse of the resulting reflection coefficient, the bandwidth of this system can be compared to the Bode-Fano limit.

$$\Delta\omega_{BF} = \int_0^\infty ln\left[\frac{1}{|\Gamma(\omega)|}\right] d\omega = \frac{1}{2}\int_0^\infty ln\left[\frac{4+(\omega RC)^2}{(\omega RC)^2}\right] d\omega = \frac{\pi}{RC} \tag{3.2}$$

This configuration, in fact, reaches the maximum possible bandwidth allowed by its intrinsic reactance. This bandwidth is on the order of 10 GHz for typical tunnel junctions. It could be moved away from DC to higher frequencies by shunting the load with the appropriate inductor, but as required by the theorem, this could not increase the total bandwidth.

3.3 The L Section Transformer

This section will derive in detail the requirements for matching to a large, real impedance that is shunted by some amount of capacitance. The simplest transformer is to place an inductor in series with the parallel resistor and capacitor. This "L section" matching circuit has been increasingly used within the past decade to study both 2 DEG devices, such as quantum dots (Qin and Williams, 2006; Cassidy et al., 2007; Fujisawa and Hirayama, 2000), atomic point contacts (Flowers-Jacobs et al., 2007), as well as tunnel junction devices, like SETs (Schoelkopf et al., 1998), SQUIDs (Irwin and Lehnert, 2004), NIS bolometers (Schmidt et al., 2003; Schmidt et al., 2005), or now STJ photon detectors.

Conceptually, the behavior of this tank circuit is straight-forward. The positive imaginary impedance of the inductor not only compensates for the negative imaginary component of the load impedance, but also lowers the real part of the impedance as seen from the input of the circuit on resonance. More precisely, the input impedance for this circuit is:

$$Z(\omega) = \imath\omega L + \frac{R}{1 + \imath\omega RC} \tag{3.3}$$

Resonance occurs at the frequency where the positive imaginary part of the input impedance cancels the negative part. Thus, $Im[Z(\omega_o)] = 0 \Longrightarrow$

$$\omega_o = \sqrt{\frac{1}{LC} - \frac{1}{(RC)^2}} = \frac{1}{\sqrt{LC}}\left(1 + \frac{1}{Q^2}\right) \tag{3.4}$$

where is $Q = R/Z_{LC}$. For the tank circuits used in this work, the resonance frequencies range from 300 to 600 MHz and the Q's from 20 to 200.

Putting this resonance frequency back into equation 3.3:

$$Z(\omega_o) = \frac{L}{RC} = \frac{(Z_{LC})^2}{R} \tag{3.5}$$

where $Z_{LC} \equiv \sqrt{\frac{L}{C}}$ is the magnitude of imaginary impedance of the inductor or capacitor on resonance.

There will be a real solution as long as $Z_{LC} < R$. Furthermore, if $Z_{LC} \ll R$, then $\omega_o \approx \sqrt{\frac{1}{LC}}$ independent of R. So, on resonance, the input impedance of this circuit is real and is inversely proportional to the resistance of the device. In can be easily shown that this equation also holds for

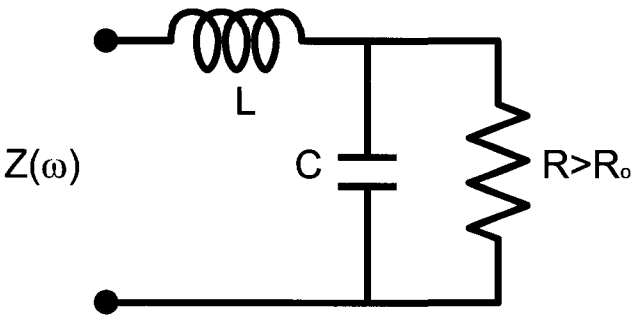

Figure 3.3: Circuit diagram for an L section matching network. This resonant circuit transforms the the large resistance, R, to $Z(\omega)$. On resonance, $Z(\omega)$ is purely real and has a magnitude of L/RC.

a quarter-wave transmission line terminated in a real resistance, R. In this case, Z_{LC} is replaced by the characteristic impedance of the line.

When discussing transformers, it is useful to think about this in terms of the quality factor, or Q. Formally, the Q of a resonance is the ratio of the energy stored to the energy lost in a give cycle. An ideal transformer will still have a finite Q, because the resonant circuit has intentionally been coupled to the resistive load. One must be careful to distinguish between the bare quality factor, Q, of the LC resonance coupled solely to the 50 Ω line and the loaded quality factor, Q_L, which is additionally damped by the resistance of the device.

$$Q = \frac{Z_{LC}}{R_o} \tag{3.6}$$

$$Q_L = \left(\frac{R_o}{Z_{LC}} + \frac{Z_{LC}}{R}\right)^{-1} \tag{3.7}$$

where R_o is the 50 Ω impedance of the lines or amplifiers.

The transformer will step up the voltage and step down the current, each by a factor of Q. Thus, the optimum impedance will be a factor of Q^2 higher than R_o as seen by equation 3.5. In other words, the L and C should be chosen such that Z_{LC} is the geometric mean of the line impedance and the device resistance.

To look at the frequency dependence, one can Taylor expand the input impedance about the resonant frequency. To lowest order, the real part of the impedance can be approximated as independent of frequency. By design, the imaginary part of the impedance is zero on resonance; so to lowest order, it varies linearly as the frequency detunes from the resonance .

$$Re[Z(\omega)] = \frac{R}{1+(\omega RC)^2} \approx \frac{(Z_{LC})^2}{R} \tag{3.8}$$

$$Im[Z(\omega)] = \omega L - \frac{\omega R^2 C}{1+(\omega RC)^2} \approx 2Z_{LC}\left(1-\frac{1}{Q^2}\right)\left(\frac{\omega-\omega_o}{\omega_o}\right) \approx 2Z_{LC}\left(\frac{\omega-\omega_o}{\omega_o}\right) \tag{3.9}$$

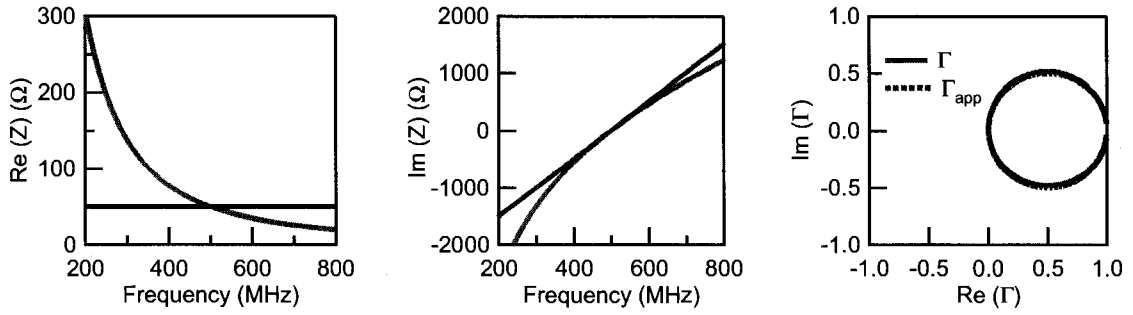

Figure 3.4: Plot of input impedance and reflection coefficient for a typical tank circuit. The two traces show the actual value as well as the Lorentzian approximation in which only the lowest order frequency dependence is considered. The values plotted above assume L=400 nH, C=255 fF and R=31 kΩ.

Using a network analyzer, what one measures is not $Z(\omega)$ directly, but rather how the change in impedance modulates the reflected signal (i.e. S_{11}, or Γ).

Now, using the impedance approximated above:

$$\Gamma(\omega) = \frac{Z(\omega) - Z_o}{Z(\omega) + Z_o} \approx \frac{\frac{(Z_{LC})^2}{R} + 2\imath Z_{LC}\left(\frac{\omega-\omega_o}{\omega_o}\right) - R_o}{\frac{(Z_{LC})^2}{R} + 2\imath Z_{LC}\left(\frac{\omega-\omega_o}{\omega_o}\right) + R_o} \tag{3.10}$$

On match, $Z_{LC} = \frac{R}{Q} = \frac{Q}{R_o}$, which implies:

$$\Gamma(\omega) \approx \frac{\imath\left(\frac{\omega-\omega_o}{\omega_o}\right)}{\imath\left(\frac{\omega-\omega_o}{\omega_o}\right) + \frac{1}{Q}} \tag{3.11}$$

This is the characteristic Lorentzian line shape, whose width is determined by the Q of the resonance. When the circuit is critically coupled, the resonance is equally damped by the line and the device so that Q_L=Q/2. One way to quantify the usable bandwidth of the match is the 3 dB point. This is, by definition, the half-width at half maximum of the reflection coefficient squared.

$$\Delta f_{3dB} = \frac{1}{2}\frac{\omega_o}{2\pi Q_L} = \frac{\omega_o}{2\pi Q} \tag{3.12}$$

Now, one can examine how this compares to the Bode-Fano Limit for the system.

$$\Delta\omega_{BF} = \int_0^\infty ln\left[\frac{1}{|\Gamma(\omega)|}\right] d\omega = -\int_0^\infty ln\left|\frac{\imath\left(\frac{\omega-\omega_o}{\omega_o}\right)}{\imath\left(\frac{\omega-\omega_o}{\omega_o}\right) + \frac{Z_{LC}}{R}}\right| d\omega = \frac{\omega_o}{Q}\left(\frac{\pi}{2} + \tan^{-1}(Q)\right) \tag{3.13}$$

As Q becomes large, the arctangent will approach $\frac{\pi}{2}$.

$$\Delta\omega_{BF} \approx \frac{\pi\omega_o}{Q} \approx \frac{\pi}{R}\frac{1}{\sqrt{LC}}\sqrt{\frac{L}{C}} = \frac{\pi}{RC} \tag{3.14}$$

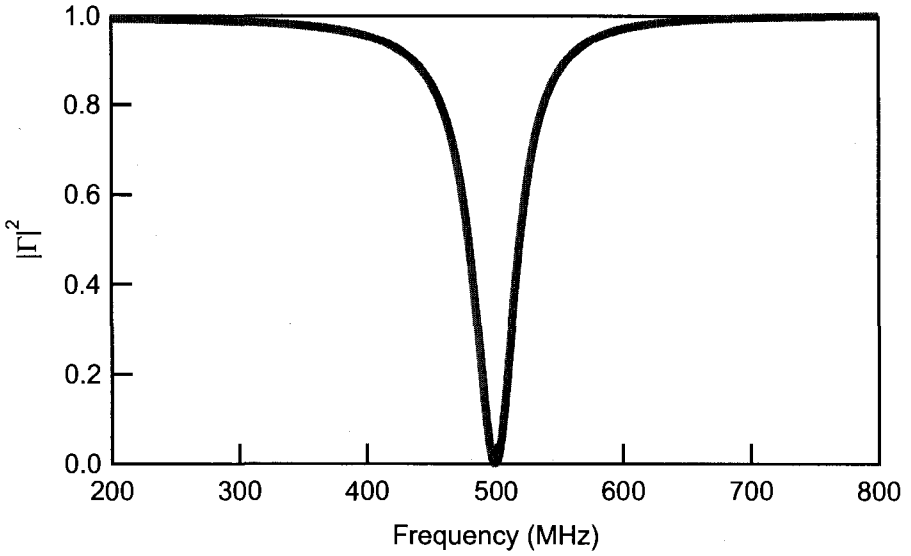

Figure 3.5: The reflection coefficient squared is a Lorentzian curve whose full width half maximum is a direct measure of the loaded Q, Q_L, of the circuit. This graphs shows a tank circuit that matches to R=31 kΩ.

Thus, within the approximations above, this tank circuit reaches the maximum possible bandwidth that is theoretically possible for this choice of R and C. This capacitance no longer includes the hundreds of picofarads of the cables that is seen at DC. At these frequencies, the cables are a good transmission line that has its capacitance compensated for by the inductance of the line. This does, however, include a small amount of capacitance on the device side of the inductor. Good layout design can keep this parasitic capacitance from dominating the total capacitance of the circuit, and it is in this sense that the intrinsic bandwidth of the device has been reached.

The dual of this circuit can be used to match to an impedance much less than 50 Ω. By reversing the order of the inductor and capacitor, the transformer will act in the opposite direction. This is the circuit of choice for matching to low-impedance devices with a small amount of series inductance, such as a SQUID. The algebra for analyzing this circuit is analogous to before.

Again, solving for input impedance:

$$Z(\omega) = \left(\imath\omega C + \frac{1}{R + \imath\omega L}\right)^{-1} \tag{3.15}$$

$$\Rightarrow \omega_o = \sqrt{\frac{1}{LC} - \frac{R^2}{L^2}} \tag{3.16}$$

$$\Rightarrow Z(\omega_o) = \frac{L}{RC} = \frac{(Z_{LC})^2}{R} \tag{3.17}$$

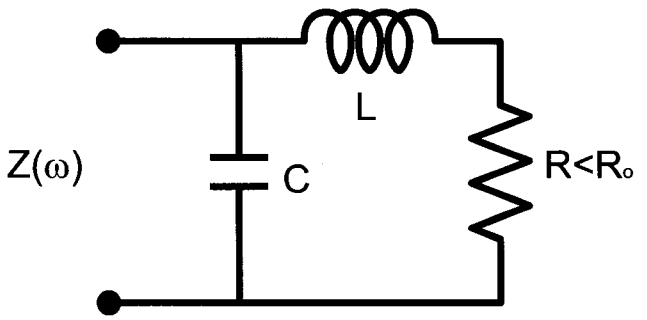

Figure 3.6: Circuit diagram for a resonant circuit that transforms a low resistance up to 50 Ω.

As might be expected, this transform behaves just as its converse. On resonance, it is an impedance inverter where the Z_{LC} should again be chosen as the geometric mean of 50 Ω and the lower impedance to be matched. While this thesis work involves exclusively high-impedance devices, this circuit can be used to correct for over transformation.

One essential characteristic of both transforms discussed in this section is that the matching network has DC continuity. This is important because it will allow simultaneous measurement of both the RF and DC properties. While future applications may not require any DC measurement, it provides an invaluable tool for characterization and verification in the laboratory setting.

3.4 Practical Considerations

At RF frequencies, one could implement either lumped circuit element or transmission line resonators, but this work has used almost exclusively lumped circuit elements. While transmission line techniques, like a quarter-wave transformer, are easier to design *a priori* and to scale to arbitrarily high frequencies, the lumped elements offer the versatility to change a single component without redesigning the entire layout. Furthermore, lumped elements are physically much smaller and readily achieve more extreme matching conditions. For example, designing a transmission line with a characteristic impedance of 5 kΩ is completely unfeasible. This impedance is so different from the impedance of free space that the TEM mode for which it is designed is no longer the dominant mode. On the contrary, lumped inductors and capacitors with imaginary impedances of greater than 5 kΩ are achieved with standard surface mount components throughout this work. It is mainly for these reasons that this work has focused on a lumped circuit approach.

While it was shown above that the L section transform provides a simple and elegant solution to the problem of impedance matching, there are several practical limits that might prevent its application in all situations. An inductor, for example, only look inductive at sufficiently low frequencies. This is because there will always be some capacitance that shunts the inductor. The result is that this inductor now has a self-resonance, at frequencies above which the element looks capacitive.

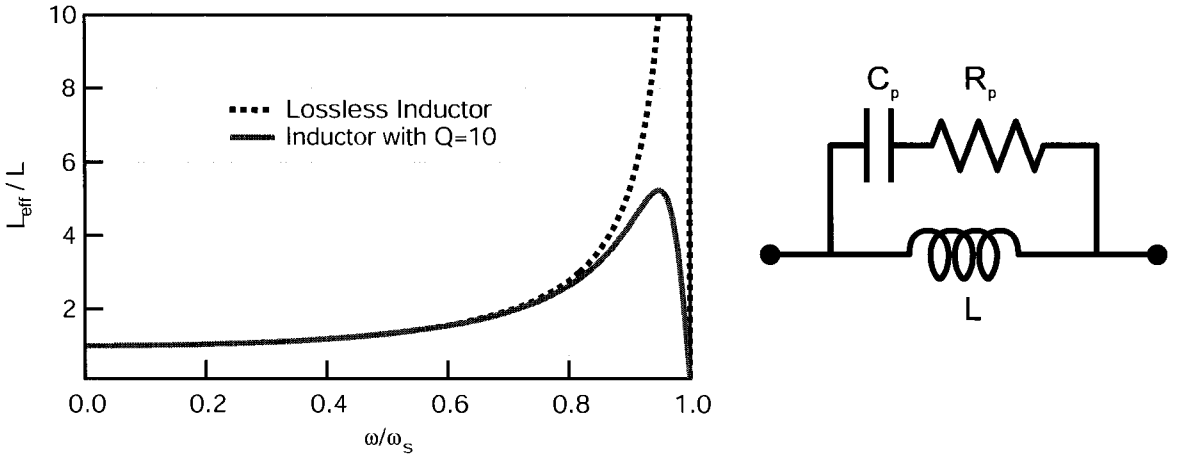

Figure 3.7: A realistic model for the impedance of an inductor includes the effects of the parasitic capacitance and resistance. This graph shows the effective inductance as a function of frequency for the circuit model above. For all tank circuits in this thesis, the inductors are used very close to their self resonance frequency and hence have an effective inductance much greater than their nominal value.

When trying to achieve large inductance values at high frequencies, even small shunt capacitances become important. In fact, this effect can be exploited in that just below the self-resonance, the inductance is greatly enhanced. The impedance of a parallel L and C_s is:

$$Z = \frac{i\omega L}{1 - \omega^2 L C_p} \tag{3.18}$$

The self-resonance frequency is given by, $\omega_s = \frac{1}{\sqrt{LC_p}}$. The effect inductance of the LC combination is:

$$L_{eff} = \frac{Z}{i\omega} = \frac{L}{1 - \left(\frac{\omega}{\omega_s}\right)^2} \tag{3.19}$$

It is the sum of this capacitance that shunts the inductor and that which shunts the load that together will determine the overall resonance frequency. It is only in minimizing the latter that will achieve the highest possible impedance match. It is in that sense that it is convenient to consider the shunted inductor as a mildly frequency-dependent, effective inductor. The practical limitation on this approach is that the inductor will also have some amount of dissipation. This will limit the internal Q and hence the degree to which the effective inductance can be amplified. In general, it is the internal Q of the reactive elements used in the matching network will ultimately limit how much the impedances can be transformed.

For commercial surface mount inductors, it is conductor losses that will limit the internal quality factor. The wire is clean copper whose DC resistance is much less than an ohm at low temperatures. At radio frequencies, the skin depth of the copper becomes relevant and this limits the internal Q to several hundred. Superconducting circuits, in contrast, have demonstrated internal quality factors of over one million (Mazin, 2004). The use of superconducting inductors and quality dielectrics will be a straightforward, but necessary, improvement in order to realize transformers with Q >1000.

To give some typical values for these quantities, a Q=25 would impedance match 50 Ω to a device resistance of R≈30 kΩ. This implies that Z_{LC}=1.25 kΩ. A typical center frequency of 500 MHz implies that L=400 nH and C=255 fF. The 3 dB bandwidth of this match is Δf=20 MHz. If one wanted to match this impedance over a broader range in frequency, the only way would be to reduce C by minimizing the parasitic capacitance. While this will also change the optimum impedance of the transformer, this effect can be undone by adding additional stages of transformation. These parameters are those generally used for SET's. For direct readout of photon detectors, one would desire the largest possible transformation (i.e. higher Q). This implies realizing microhenry inductors, and limiting the load capacitance to tens of femtofarads. In this way, the Q can be increased to ~150, which implies matching to an impedance of over 1 MΩ. If one cannot realize either the large reactive components or components with high enough internal Q's, the option exists to add successive stages of transformation to lower the burden on any one stage. While this adds complexity and can diminish the bandwidth of the match, there are many situations in which multistage transforms are the only solution that is feasible.

3.5 Multistage Transformers

In section 3.4, it was shown how to make high impedances match to 50 Ω. Ideally, for a single stage transform, the Z_{LC} of the tank circuit will be the geometric mean of the two resistances that one is attempting to match. But in practice, one is usually confronted with having a fixed resonance frequency (to match the band of the amplifier), a fixed line impedance (50 Ω), and a fixed load capacitance (given by the device and the layout). This completely determines all the parameters of the tank circuit, so that if one tried to choose the optimum device resistance, the problem would be over constrained. By adding a second stage of transformation, one now has the freedom to optimize either the bandwidth or the matching impedance for the given circuit. Furthermore, in many situations, it is more practical to first transform to an intermediate impedance and then apply a second stage to reach 50 Ω. This intermediary impedance can be either above or below 50 Ω, resulting in under or over transformation, respectively. The former provides a way to keep each stage of the transform relatively low Q. This implies insensitivity to losses in reactive components and maximal bandwidth. Conversely, over-transforming will necessarily increase the Q of the first stage. This will allow one to match to much higher impedances, but at the cost of bandwidth.

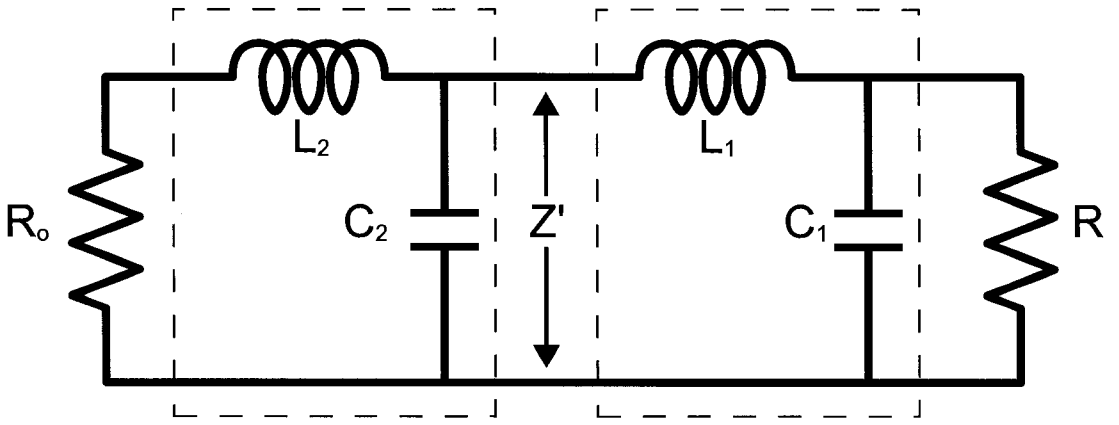

Figure 3.8: Circuit diagram for a two-stage transformer where the first stage has under transformed (i.e. $R_0 < Z' < R$). While it may be difficult to realize the small capacitances and large inductances necessary for this type of circuit, it puts little demand on the internal quality factor of each the lumped element. This technique of under transforming maximizing the bandwidth of the matching circuit.

This section will quantify the advantages and drawbacks of both methods, while emphasizing the practical implementations of each circuit.

Using the results, from section 4.3, it is straightforward to examine what would happen if the first stage matched to a few hundred ohms and then a second stage matched that to 50 Ω. As shown in equation 3.5, the impedance after the first stage will be:

$$Z(\omega_o) = \frac{(Z_1)^2}{R} \tag{3.20}$$

where Z_1 is the Z_{LC} of the first stage.

Adding a second stage implies we can reapply this formula with the new impedance:

$$Z(\omega_o) = \frac{(Z_2)^2}{\left(\frac{(Z_1)^2}{R}\right)} = \left(\frac{Z_2}{Z_1}\right)^2 R \tag{3.21}$$

Unlike the single stage, the transformed impedance is directly, not inversely, proportional to the device resistance. The overall bandwidth will be limited by the narrower of the two resonances, just as with two bandpass filter in series. For maximal bandwidth, one would choose the Q of each stage to be equal. This means that the intermediary impedance, Z', should be the geometric mean of the device resistance and 50 Ω. Because this impedance transform has been partitioned into two stages, there is much less burden on each individual stage. For example, instead of one stage with Q=25, one could use two Q=5 stages. Because both stages are transforming in the same direction, the effective Q in terms of overall impedance transformation is the product of the Q of each stage. Thus, the same impedance match is achieved, but with a factor Q increase in bandwidth. This may seem counterintuitive, given the result that a single stage transform already met the Bode-Fano

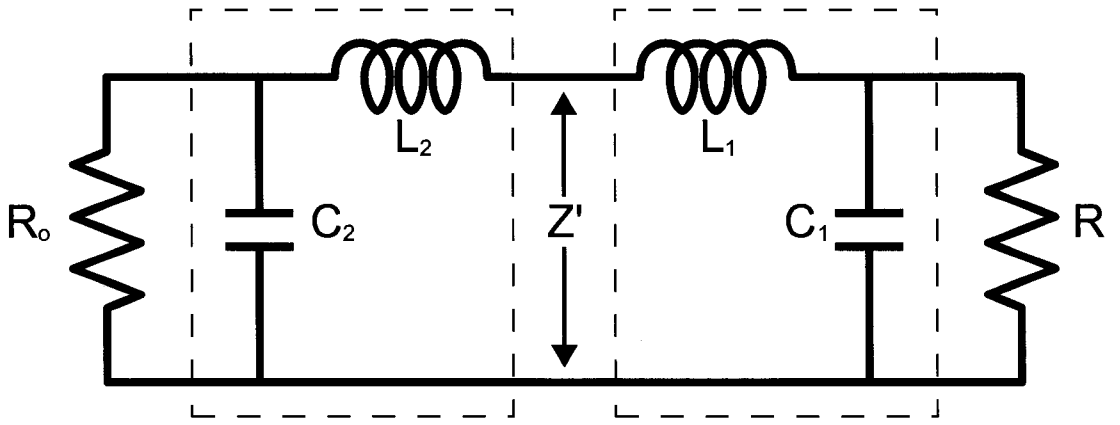

Figure 3.9: Circuit diagram for a two-stage transformer where the first stage has over transformed (i.e. Z′ <R_0 <R). While this circuit puts a larger demand on the internal quality factor of the elements, it allows one to match to high impedances even in the presence of a large shunt capacitance. For multiplexing applications where many resonances must fit in a given frequency window, this method can be used to narrow the width of the resonance without matching to a higher impedance.

criterion. However, implicit in the two stage transform is the requirement that the load capacitance be reduced. This is the only way to realize the impedances necessary for the transformation. But given that this can be accomplished, one can show this two stage transform meets the Bode-Fano limit for these values of R and the new C. The practical difficulty is in realizing the large imaginary impedances required for the first stage. This implies both reducing the capacitance, as stated above, and simultaneously increasing the inductance to keep the resonance frequency fixed. Such inductances can only be realized by working very near to the inductor's self-resonance. An on-chip planar inductor, as opposed to a surface mount component, would minimize the stray capacitance even further. Ideally, the planar inductor would be fabricated directly connected to the device, without the additional capacitance of a bond pad for wirebonding. While this adds complexity to device fabrication, the reward is a large increase in bandwidth for devices whose intrinsic capacitance is small (such as an SET).

In this previous example, it was shown that under-transforming with the first stage is a way to maximize the usable bandwidth. Conversely, one can over-transform to a low impedance and then back up to 50 Ω. This allows one to trade-off some of the bandwidth for the ability to match to a much higher impedance. In order to do this, the second stage of the transform is accomplished with the capacitor on the 50 Ω side of the inductor. Using this as a second stage, the resulting transform is again governed by equation 3.5.

$$Z(\omega_o) = \left(\frac{Z_2}{Z_1}\right)^2 R = \left(\frac{C_1}{C_2}\right)^2 R \tag{3.22}$$

The optimum resistance for this circuit is determined by the square of the ratio of the capaci-

	Single Stage	Under Transform	Over Transform
Z_1 [Ω]	1250	6250	1250
L_1 [nH]	400	2000	400
C_1 [fF]	255	51	255
Q_1	25	5	625
Δf_1 [MHz]	20	100	0.8
Z' [Ω]	—	1250	2
Z_2 [Ω]	—	250	10
L_2 [nH]	—	80	3.2
C_2 [fF]	—	1270	31800
Q_2	—	5	625
Δf_2 [MHz]	—	100	100
R_{match}[Ω]	31250	31250	781250
Δf_{tot} [MHz]	20	100	0.8

Table 3.1: Example tank circuit values for the three types of matching networks. The parameters above are for resonances centered at f_o=500 MHz. In multistage transformers there is the additional freedom to optimize the bandwidth or the impedances. As shown in column 2, by under transforming with the first stage, one can increase the bandwidth of the match. Conversely, by over transforming, the resistance to which the circuit is matched may be increased.

tances. This has been increased by a factor of $(Q_2)^2$. Furthermore, as is evident from the circuit diagram, the two inductors need not be separate components. It is merely useful from a pedagogical standpoint to analyze this "π" (C-L-C) circuit as two disparate stages. Unlike before, Q_1, the quality factor of the first stage, has been increased by the square of Q_2, the Q of the second stage. It is this first stage that will always limit the overall bandwidth of the circuit. Because this node of the circuit is such high Q, one might become limited by the internal losses in the inductor or capacitor. The engineering benefit is that capacitances need not be small, nor the inductances large. In some situations, like when multiplexing, the reduction in bandwidth may actually be desirable. In these cases, over transforming provides a way to narrow each resonance without necessarily changing the impedance match (Stevenson et al., 2002).

In conclusion, multistage transforms allow the user an extra degree of freedom in the design of the circuit. From a performance stand point, making the first stage with as large of Z_{LC} as possible, by minimizing the capacitance, will always result in a better transform—either in terms of impedance or bandwidth, depending on the second stage. Because it is the first stage that has the stringent requirements on both losses and impedances, it would ideally be accomplished with an on-chip, superconducting circuit. The second stage need only be low Q (5 or less) and can be done with surface mount components. This low Q makes it trivial to match the resonance frequencies of the two stages and keeps the demand on the internal quality factor of the surface mount elements within reason. In some applications, like frequency domain multiplexing, over transformation can be used to narrow the width of resonances without changing the impedance match. This would allow

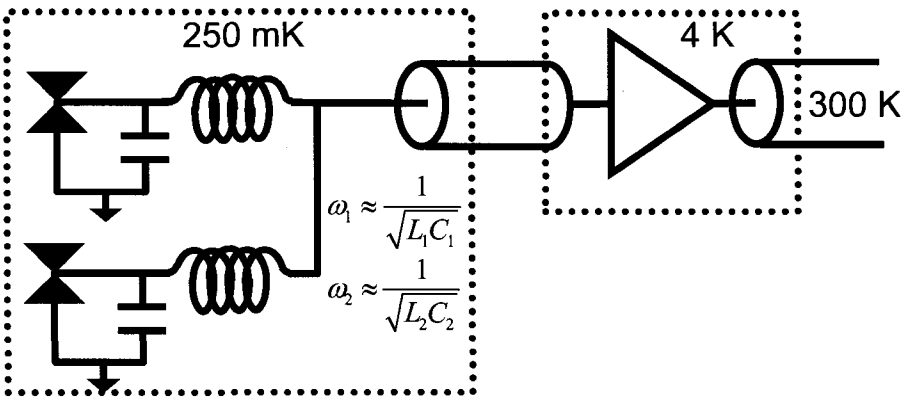

Figure 3.10: Frequency domain multiplexing may be achieved simply by designing each detector to have its own resonance frequency. A single broadband amplifier can be used to monitor the response of the entire array to a comb of RF tones. As long as the resonances are spaced many linewidths apart in frequency, each pixel will uniquely modulate only the tone at its resonance frequency.

for simultaneous readout of more devices in a given bandwidth.

3.6 Frequency Domain Multiplexing

While the explicit goal of this thesis work is to develop a sensitive submillimeter photon detector, this is merely a stepping stone toward the ultimate goal—a submillimeter photon camera. Ideally, large arrays of detectors can be readout simultaneously. Brute force methods where each pixel has its own wiring and preamplifier become prohibitive under the stringent constraints of a cryogenic environment. Multiplexing is a way in which one set of readout electronics can be used to monitor the response of several detectors. The readout may be partitioned in either the time or frequency domain. In time domain multiplexing, each pixel is sampled only during a short interval. In contrast, with frequency domain multiplexing, each pixel is monitored at all times, but only in a small frequency window. The resonant nature of RF readout naturally lends itself to the latter method.

The idea is each detector has a matching network that has a slightly different resonant frequency. These are all connected in parallel to a single transmission line leading to a single amplifier. A signal generator is used to create a waveform that is a comb of delta functions in the frequency domain. Each peak is tuned to the resonance frequency of a single detector. These carriers are reflected off the parallel combination of all of the detectors. Because each detector is only impedance matched over its narrow range in frequency, only the tone tuned to its resonance will be amplitude modulated by the detector. The reflected signal (containing the information about the entire array) is then amplified by a single broadband, cryogenic RF amplifier so that it may then be demodulated at room temperature. Thus, the performance of each detector is constantly measured despite the fact that there is only one amplifier. All the complexity of the readout is in the room temperature

electronics for signal generation and demodulation; the wiring at the detector level has been greatly simplified. This frequency domain multiplexing has been demonstrated in the lab for both RF-SET (Stevenson et al., 2002) and RF readout of SQUIDS (Irwin and Lehnert, 2004).

One concern of this scheme is the level to which a signal in one pixel can spuriously affect other pixels. If two detectors are not spaced sufficiently far apart in frequency, a signal in one pixel will result in amplitude modulation not only of its carrier, but also that of its neighbor's. By ensuring that each resonance is several linewidths away in frequency, the carriers that are off resonance will be so strongly attenuated that they will be unaffected by the detector. The tradeoff for this high degree of isolation is a reduction in overall usable bandwidth. Although sparsely spacing the resonances will minimize crosstalk, this wastes bandwidth that could be used either to increase the readout speed of each detector or to pack more detectors into the band of the amplifier.

Another issue is overall loading of the circuit by the parallel combination of all of the LC resonances. When a pixel is off resonance the inductor makes the circuit look like a very high impedance. This impedance is not infinite, so that the parallel combination of many of these can load the circuit with an impedance that is no longer negligibly large. In practice, this effect, may be the limiting factor that determines how many pixels are sent to any one amplifier.

In light of the earlier discussion of multistage transforms, one can now see how narrower resonances can actually be an advantage. As discussed in the last section, over transforming each pixel is the best way to fit many resonances in a given measurement window. These low impedances can then be transformed back to 50 Ω by a single broadband transformer just before the amplifier. The only caveat is that the transmission line between the two stages must maintain that low characteristic impedance if the signals are going to travel distances comparable to or larger than the wavelength before transformation.

3.7 Noise and Sensitivity

So far in this chapter the emphasis has been on the bandwidth of the measurement. This section will analyze the noise and sensitivity of the various RF techniques. In general, any amplification must necessarily result in an increase in the noise of the measurement. Ideally, this noise can be made small enough so that when referred to the input of the amplifier, the additional noise is negligible compared to the intrinsic noise of the system. One way to quantify this noise is to compare it to the Johnson noise of a resistor on the input. In this way, the noise temperature of an amplifier is a measure of the noise power and is defined as the temperature of an input resistor required to double the amount of noise power at the output. Because the amplifier's noise is composed of both voltage and current noise, there will be optimum impedance on the input that will minimize the amplifier's noise temperature. Assuming that the two noise sources are uncorrelated:

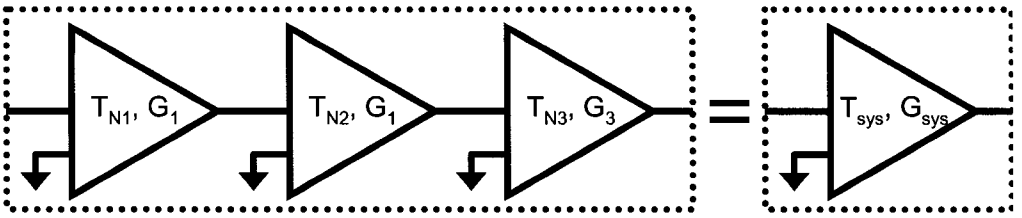

Figure 3.11: The noise temperature of a chain of amplifiers may be calculated by referring each amplifier's noise to the input of the entire chain as seen in Equation 3.25.

$$T_n = \frac{1}{4k_B R}\left(S_V + S_I R^2\right) \tag{3.23}$$

where S_I and S_V are the current and voltage spectral density and are measured in units of $\frac{A^2}{Hz}$ and $\frac{V^2}{Hz}$, respectively. This assumption that current and voltage noises are uncorrelated implies the optimum impedance will be purely real and given by the ratio of the two noise sources.

$$R_{opt} = \sqrt{\frac{S_V}{S_I}} \tag{3.24}$$

The RF amplifiers used in this work are designed to have input and output impedances that match standard, 50 Ω, coaxial cables. This is accomplished with matching networks, internal to the amplifier, that transform the optimal noise impedance within the specified band of the amplifier. With this fixed noise impedance, the noise temperature as a function of frequency completely characterizes the noise properties of the amplifier. If there are several amplifiers in series, the system noise temperature is calculated by referring each noise temperature to the input of the amplifier chain. This is done by dividing by power gain, G.

$$T_{sys} = T_{n1} + \frac{T_{n2}}{G_1} + \frac{T_{n3}}{G_1 G_2} + ... \tag{3.25}$$

From this equation, one can see that the first stage of amplification is the most critical from a noise perspective. Ideally, its gain will be large enough to make the system noise temperature insensitive to the noise temperature of the following amplifiers. This analysis can also be used to evaluate the effect of attenuation by considering it to be an "amplifier" with a gain of less than one. Again, this attenuation has the largest effect between the device under test and the first amplifier, and will directly increase the system noise temperature.

One common application of low noise, RF amplifiers is radiometry. This is also referred to as noise thermometry because, in equilibrium, the noise power is directly proportional to the temperature. The Dicke radiometer formula reveals that the optimal sensitivity occurs with the lowest possible amplifier noise temperature over the largest possible bandwidth (Dicke et al., 1946; Dicke, 1946).

$$\frac{\delta P}{P} = \frac{1}{\sqrt{B\tau}} \tag{3.26}$$

where τ is the integration time and B is the equivalent noise bandwidth.

This implies that the temperature sensitivity, t_n, (in units of $K/\sqrt{Hz}$) is:

$$t_n = \frac{T + T_N}{\sqrt{B}} \tag{3.27}$$

Thus, a HEMT with a noise temperature of 10 K coupled over 100 MHz has a temperature sensitivity equal to a DC SQUID with 100 mK noise temperature and only 10 kHz of bandwidth. This assumes the temperature of the sample is much less than the noise temperature, which is not always the case for extremely low noise amplifiers.

The equivalent noise bandwidth is related, but not equal to, the 3 dB bandwidth. It represents the frequency width of an ideal bandpass filter with unity gain inside and no gain elsewhere. Formally, it is defined as (Kittel, 1977):

$$B = \frac{\left[\int_0^\infty G(\omega)d\omega\right]^2}{4\pi \int_0^\infty G(\omega)^2 d\omega} \tag{3.28}$$

where G is the power gain of the system.

As an example, a Lorentzian line shape that matches on resonance has a gain of:

$$G(\omega) = 1 - |\Gamma(\omega)|^2 = \frac{1}{1 + Q^2\left[\frac{\omega - \omega_o}{\omega_o}\right]^2} \tag{3.29}$$

This implies an equivalent noise bandwidth of:

$$B = \frac{\left[\int_0^\infty (1 - |\Gamma(\omega)|^2)d\omega\right]^2}{4\pi \int_0^\infty (1 - |\Gamma(\omega)|^2)^2 d\omega} = \frac{\omega_o}{4Q} \tag{3.30}$$

This noise radiometry is used in this work to characterize the noise power emitted by the gold microbridge. By directly measuring the noise power at 500 MHz, the noise power at 100 GHz can be inferred. Direct radiometry also serves as a useful diagnostic technique for determining the noise temperature and matching properties of the amplifier when measuring a high impedance device. It is the measurement of high impedance devices that constitutes the bulk of this thesis work. For this reflectometry is used.

Reflectometry refers to monitoring the response of a device by reflecting an RF signal off of it. As the impedance of the device changes, so does the reflection coefficient. Thus, the carrier signal is amplitude modulated by the changing impedance. In this way, the reflected signal contains all the same information as the DC current-voltage characteristic, but with a bandwidth only limited by that of the matching network. Without the matching network, the readout of a high-impedance device with a 50 Ω HEMT amplifier would be disappointingly insensitive. There would not only be

a large impedance mismatch resulting in a high effective noise temperature, but the current noise of the amplifier would dominate the measurement. A 50 Ω amplifier with a noise temperature of 4 K has a current noise of:

$$i_{no} = \sqrt{S_I} = \sqrt{\frac{4k_B T_N}{R_o}} = 2\frac{pA}{\sqrt{Hz}} \tag{3.31}$$

Using the techniques of a lossless matching circuit, the devices can be impedance matched and the current noise can be greatly reduced. In terms of power, or noise temperature, the tank circuit cannot improve the system. Ideally, it can only preserve the noise temperature for a new characteristic impedance. The result is that the current noise, i_n, is reduced by a factor of Q, at the cost of proportionally higher voltage noise, v_n. But as the noise temperature is proportional to the product of the current and voltage noise, it remains unchanged.

If the resistance of the device is not exactly equal to the optimum matching resistance of the tank circuit, there will be an increase in the effective noise temperature of the system. This is because not all of the available power is coupled between the source and the amplifier.

$$T_{eff} = \frac{T_n}{1 - |\Gamma|^2} \tag{3.32}$$

Using the Lorentzian approximation for the reflection coefficient of a single section resonant circuit, this effective noise temperature is plotted in Figure 3.12. These graphs are plotted for the three different coupling regimes of over-, under-, and critically coupled. When the device is over coupled, the bandwidth is increased because the loading of the circuit is dominated by the device. Conversely, if the transformed impedance is greater than 50 Ω, the device is under coupled and the bandwidth is set almost entirely by the damping from the input of the amplifier.

To analyze the sensitivity of the reflectometry, one can convert the voltage noise of the amplifier to an effective current noise of the reflected RF carrier.

$$i_n = v_n \frac{d\Gamma}{dv_{RF}} \frac{dR}{d\Gamma} \frac{dI}{dR} \tag{3.33}$$

where v_n is the voltage noise of the amplifier, v_{RF} is the RMS RF carrier voltage, Γ is the voltage reflection coefficient, R is the dynamic resistance of the device seen by the RF carrier, and I is the DC current through the device.

Using the Lorentzian approximation for the tank circuit, and assuming the dynamic resistance of the device is ohmic over the range that the carrier samples, the current noise becomes:

$$i_n = \frac{i_{no} R_o}{v_o} \frac{\left(Q^2 R_o + R\right)^2}{Q^2 R_o} \frac{v_d \sqrt{2}}{R^2} \tag{3.34}$$

The factor of $\sqrt{2}$ comes from the conversion of a peak-to-peak voltage used in the determination of the dynamic resistance to an RMS value necessary for the noise analysis. This assumes that the real

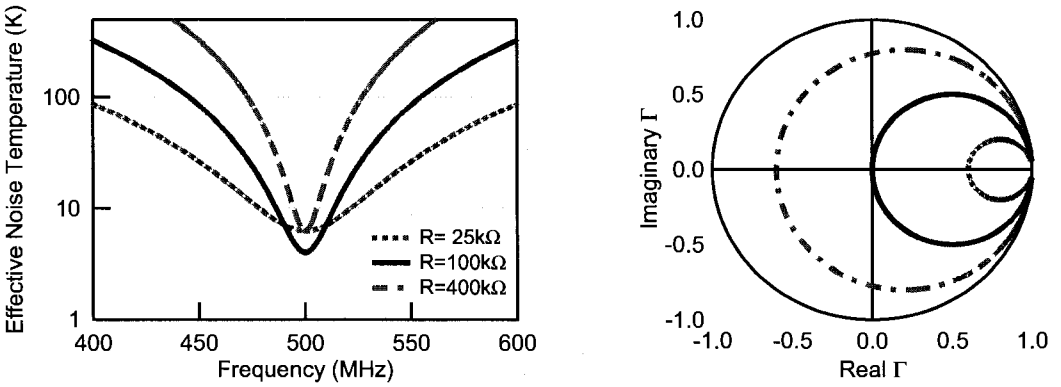

Figure 3.12: Effective noise temperature and Smith chart for a Q=45 tank circuit coupled to T_n= 4 K amplifier for three different device resistances. Both the under and over coupled impedances suffer from an increased noise temperature, even on resonance. It is only when the device is critically coupled, that the intrinsic noise temperature is preserved.

part of the impedance seen by the RF carrier may be inferred from the measured DC resistance. Experimental comparisons demonstrate that the DC resistance is a valid approximation for the RF resistance.

Assuming that the matching network is lossless, the power coupling can be used to determine the ratio of RF carrier voltage before and after transformation. As mentioned earlier, if the impedances are matched their ratio is Q. In general,

$$\frac{v_o^2}{2R_o}\left(1-|\Gamma|^2\right)=\frac{v_d^2}{2R_d} \tag{3.35}$$

where the subscript 'o' denotes the 50 Ω side of the transformer and 'd' denotes the device side.

Substituting this into the above equation,

$$i_n=\frac{i_{no}\sqrt{2}}{Q}\left(1+\frac{Q^2R_o}{R}\right) \tag{3.36}$$

In order to minimize this current noise, one can take the derivative with respect to Q. Not surprisingly, the optimum occurs when Q= $\sqrt{RR_o}$, i.e. matched impedances. Thus within the numerical factor of $2\sqrt{2}$, the effective current noise of the reflection technique on match is the current noise of the amplifier divided by the Q. It is important to note that the Q in this analysis is $\frac{Z_{LC}}{R_o}$ and is independent of the device resistance. Because the reflection method does not have any intrinsic gain, its noise temperature cannot improve upon that of the RF amplifier. Cryogenic HEMT amplifiers can have noise temperatures as low as 2 K for frequencies in the 500 MHz range (Bradley, 1999). Further developments in microwave squid amplifiers have demonstrated amplification in this range with a noise temperature of less than 100 mK (Muck et al., 1998; Muck et al., 1999; Muck et al., 2001; Bradley et al., 2003). Successfully integrating these with the RF-STJ or RF-SET would further

improve the performance to intrinsic limits of the device. For an application such as the RF-STJ, preserving even HEMT's noise temperature for impedances greater than 1 MΩ provides a current noise of $\sim$ 10 fA/$\sqrt{\text{Hz}}$. While this is still not as sensitive as low frequency JFETs, it avoids many of the disadvantages associated with traditional high impedance measurements. These include extraneous noise sources such as 1/f noise of the device or amplifier, microphonic pickup, and excess noise from large bias resistors. Combined with the ability to multiplex and to measure fast dynamics, RF reflectometry offers a unique alternative to low current DC measurements.

Chapter 4

Device Fabrication

"An experiment is a question which science poses to Nature, and a measurement is the recording of Nature's answer."

–Max Planck

The fabrication of the devices measured in this thesis work was initially performed at NASA Goddard Space Flight Center. This collaboration with Thomas Stevenson, Wen-Ting Hsieh and coworkers produced the original antenna-coupled STJ's with on-chip RF-SET circuits. For all measurements after 2004, the devices were fabricated here at Yale. This fabrication was primarily performed by Luigi Frunzio and Minghao Shen. The original design and fabrication of the on-chip source was performed by Chris Wilson and Luigi Frunzio. In this chapter, I will give a brief overview of the general lithographic techniques and equipment used in the fabrication of the superconducting tunnel junctions.

4.1 Overview of E-Beam Lithography

The tunnel junctions measured in this thesis are $Al/AlO_x/Al$ SIS junctions fabricated with electron beam lithography. While optical lithography provide the ability for wafer level processing, the sub-micron features required for our devices dictate e-beam techniques. The tunnel junctions are

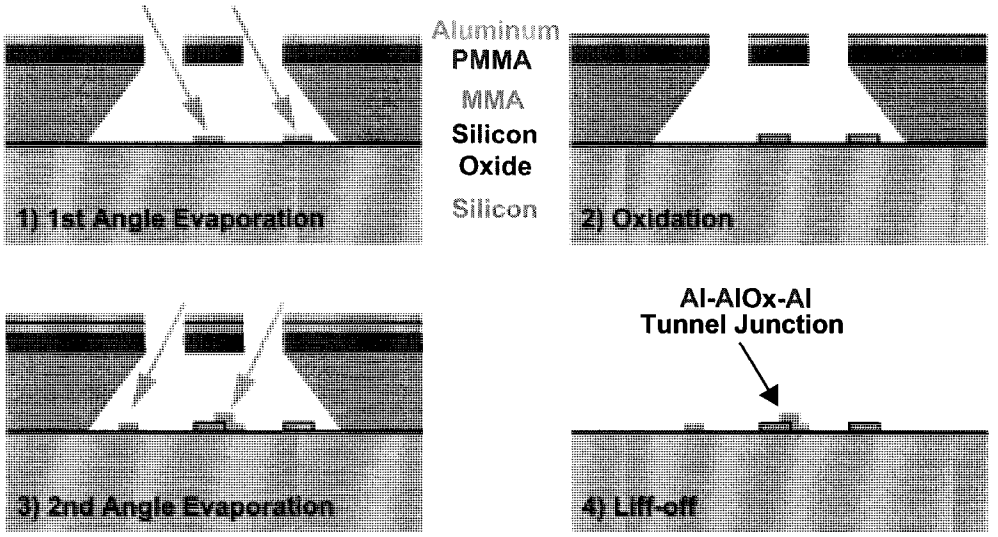

Figure 4.1: Dolan bridge technique. A silicon chip with a thermally grown oxide is spun with a bilayer of MMA/PMMA resist. The pattern is written with a scanning electron microscope, exposed and developed to create the suspended pattern shown in cross section. A first layer of aluminum is evaporated at an angle to create the bottom electrode of the tunnel junction. Then oxygen is introduced into the evaporation chamber so a that an aluminum oxide forms. Next, a second layer of aluminum is evaporated to form the counter electrode. Finally, the resist pattern is lifted off to leaving the finish tunnel junction and wiring.

fabricated using a Dolan bridge technique first using to fabricate the ultra-small area junctions necessary to form single electron transistors (Dolan, 1977; Fulton and Dolan, 1987). With this method, a resist layer is undercut to create a suspended bridge. This gives an evaporation mask that is displaced from the surface. By evaporating at two different angles and allowing an appropriately thick oxide to form in between, the region of overlap results in a tunnel junction. A diagram of this process is shown in Figure 4.1. One advantages of this technique is that it is self-aligning and requires only one written mask pattern. Equally important is that the sample remains under vacuum during the entire evaporation process, avoiding the possibility of contamination in junction.

A layer of polymethyl methacrylate (PMMA) is spun atop a layer of methyl methacrylate (MMA) to form the resist bilayer necessary create the suspended structures. The e-beam dosage required to expose the MMA is less than that of the PMMA. Thus, the bottom layer of MMA is essentially overexposed so that the written lines are larger in than in the top layer. This results in structures in the top layer of resist that are completely suspended. The directionality inherent in evaporation is then exploited by evaporating the at two different angles (as shown in Figure 4.1) in order to form the overlap junctions. One side effect of this technique is that all final structures on the chip are essentially tunnel junctions, in that they are comprised of a trilayer of $Al/AlO_x/Al$. For most applications this is irrelevant because the large surface area ensures that the two layers are short

circuited by tunneling current at low frequencies and by the large capacitance at high frequencies.

4.2 Tunnel Junction Fabrication at Yale

The fabrication process starts with a 300 μm thick silicon wafer, which will serve as the substrate. This wafer is single crystal, ultrahigh purity silicon to ensure a quality loss tangent for the RF measurements. A thin ($\sim$1 μm) oxide is thermally grown so that devices can be measured at room temperature without leakage through the substrate. The wafer is thoroughly cleaned with acetone methanol and ultrasonic agitation before depositing the resist. First, a thick ($\sim$1300 nm) layer of MMA is spun onto the entire wafer and baked on a hot plate at 170°C for 1 minute. A second, thinner (750 nm) layer of PMMA is spun and baked at the same temperature for 30 minutes. At this point, the diced into individual 1 cm^2 chips.

The desired patten is written into the resist using a scanning electron microscope. Our system is a FEI XL30 SEM. The electron beam is generated with a field emission filament and accelerated to 30 keV. This system has a writing resolution of $\sim$20 nm and an imaging resolution of $\sim$5 nm. In order to control the SEM for writing, Nabilty Nanmometer Pattern Lithography System (NPGS) software is used. The geometry of the desired structure is drawn with CAD software and the NPGS uses this to raster the electron beam and expose the pattern in the resist. Once all features are written, the resist is then developed in a 1:3 solution of methyl isobutyl ketone (MIBK) and isopropanol (IPA) to remove the resist from the exposed regions.

At this point, the chip is ready for deposition of the metal. The electron beam evaporator is a load-locked system made by Plassys. The chip is loaded (with the correct orientation for the double angle evaporation) and the chamber is pumped down to a pressure of 3×10^{-7} Torr. With a shutter protecting the chip, a brief evaporation of titanium acts as a getter, further lowering the pressure to 3×10^{-7} Torr. In order to evaporate the aluminum, a 20 keV electron beam locally melts the target metal held in a graphite crucible. The first layer of aluminum is evaporated perpendicular to the sample at a rate of 1 nm/s. Once the sample cools, oxygen is introduced into the chamber to form the aluminum oxide insulator of the junction. The sample is then tilted by 37° and a second aluminum layer is evaporated (also at 1 nm/s). Again, the sample is allowed to cool for 2 minutes and then the chamber is vented. The final step is to remove the resist. This lift off process is accomplished by soaking the chip in heated (65°C) acetone for two hours, followed by 60 second of ultrasonic agitation, completing the junction fabrication process.

4.3 Junction Properties

Once fabrication is completed, the junctions are probed at room temperature to ensure that the resistances are as expected. This is accomplished with probe station equipped with the same measurement configuration as used in the cryogenic experiments. Practically, this is the point at which

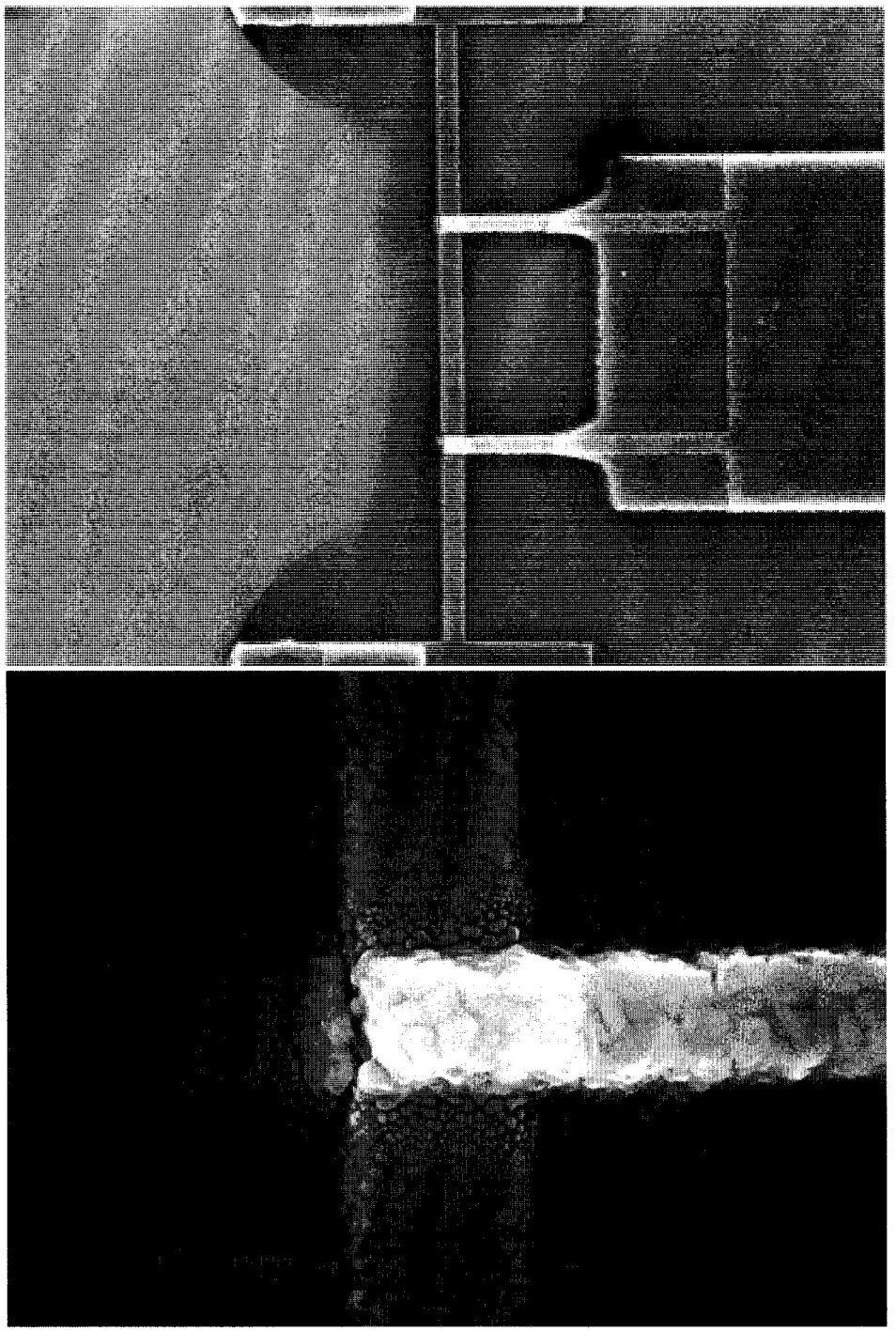

Figure 4.2: The SEM image shows a SQUID detector fabricated by Minghao Shen. The large shift between evaporation of the two layers ($\sim$1 mum) allows the absorber (the 200 nm wide vertical line) to be only a single layer. In the second evaporation, image of the absorber is cast onto the side of the resist so that it is removed upon liftoff. The lower image is a close-up of one of the junctions. It shows the excellent resolution of the FEI scanning electron microscope both in terms of writing patterns and imaging.

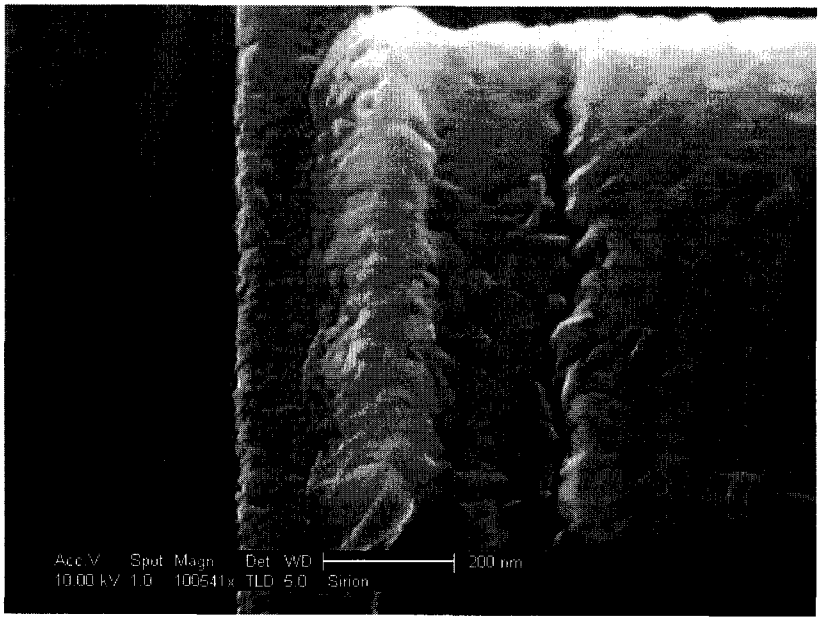

Figure 4.3: Taken at a 35 degree angle, this SEM image shows a typical $Al/AlO_x/Al$ junction. The bottom layer is only 20 nm thick in order to realize an absorber that is both 50 Ω and as small volume as possible. The apparent break seen on the right is a side effect of the angle evaporation, but this is in fact a continuous contact.

the devices are most susceptible to electro-static discharge. A ground strap is always worn and the probe needles are grounded prior to contacting each device. A bias resistor larger than or comparable to the expected device resistance is used and the bias voltage is limited to less than 1 mV. If the resistance is measured multiple times, some device aging is observed. Typically, the resistance of the device tends to increase over time. For most junctions, the effect is only ~20% and seems to reach its an asymptotic value after a few days. This effect is mitigated by storing the chip in a vacuum chamber when not in use. A 60 nm thick aluminum film has measured sheet resistance of 0.22 $\Omega/\square$ just above T_c. The T_c is approximately 1.3 K, and the superconducting gap is consistently seen to be 190 μeV. As for the junction properties, the resistance-area product varies depending on the exact recipe but tends to have a value around 500 $\Omega\mu m^2$. The specific capacitance is estimated to be 50 $fF/\mu m^2$. For larger junctions, it it this capacitance that sets the limit on the Q and bandwidth of a matching circuit. These parameters determine several junction properties that are independent of the junction area. The current density is:

$$J_c = \frac{\pi\Delta}{2eR_nA} \approx 60 \text{ A/cm}^2 \tag{4.1}$$

The intrinsic junction RC time is 25 ps. This, for example, determines the ultimate limit on the bandwidth over which noise thermometry could be performed (Spietz, 2005). It is also related to the plasma frequency of the junction in the superconducting state. This is the frequency at which

the Josephson inductance resonates with the junction capacitance.

$$\omega_J = \sqrt{\frac{1}{L_J C_J}} = \sqrt{\frac{\pi\Delta}{\hbar RC}} \approx 2\pi \times 30 \text{ GHz} \tag{4.2}$$

It should also be noted that the superconducting gap of aluminum can be increased by introducing oxygen into the chamber during evaporation. Unlike other materials, the T_c of aluminum tends to increase as with a "dirtier" film. Here "dirty" is used to describe an increase resistivity of the film metal. For example, a dirty 40 nm thick film was measured to have a sheet resistance of 3.5 $\Omega/\square$ at room temperature and a Δ of 270 μeV. In principle, this technique can be used to engineer the gap of aluminum depending on the needs of the particular application (Savu, 2007).

4.4 Design Considerations

These superconducting tunnel junctions have two application in this work. The first is to form the junction or SQUID that detects the photons. The second is to create a SET to readout of the detector. In the SET, the junction must necessarily be small in order to have a charging energy of order or greater than 1 K. The implies that each junction must have a capacitance less than 500 aF. Given the specific capacitance assumed above, each junction should be roughly 100 nm by 100 nm. The resistance must also be greater than a resistance quantum. In practice, it is the capacitance requirements that dictate the R_n of the junctions. As the total power gain of the SET scales with the current flowing through the device, total resistance should be kept as small as possible. If the R_n is much larger than 100 kΩ, it will become difficult to impedance match the RF-SET to 50 Ω and the bandwidth of the measurement will be reduced. For these reasons, higher current densities would allow large charging energies without the added cost of having a device that is too high impedance.

For the detector junctions, the most relevant parameter is R_n, not the current density. The product of the R_n and the total absorber volume determine the tunneling time of the detector. This not only sets the overall speed of the detector, but also determines at what temperature or photon power the detector will begin to saturate. As the number of quasiparticles increases, so does the rate of the quasiparticle loss due to recombination. It is the ratio of the tunneling time to this recombination time that determines the efficiency with which created quasiparticle are measured by the detector. The number of thermal quasiparticles also determines the dark current that flows in the absence of any photons. As this scales exponentially with the ratio of Δ/k_BT, a 50% increase in the superconducting gap would result in almost of factor of five reduction in the thermal subgap current.

$$\tau_{tun} \propto R_n \cdot Volume \tag{4.3}$$

$$\tau_{rec} \propto \frac{1}{n_{qp}} \propto \exp\left(\frac{\Delta}{k_B T}\right) \tag{4.4}$$

$$I_{subgap} \propto n_{qp} \propto \exp\left(-\frac{\Delta}{k_B T}\right) \tag{4.5}$$

The superconducting gap also determines the frequency at which photons can begin to break pairs in the aluminum. A film with a gap of 190 μeV with detect photons at or above 92 GHz. Since the STJ creates two quasiparticles for each photon, whether it is at 95 GHz or 150 GHz, the smaller the gap, the larger the responsivity. For the same reason, in X-ray or optical photon detection a smaller gap device gives the most tunneling current per photon. These competing considerations imply that exact choices of the R_n and T_c of the aluminum detectors depend on the particular application as well as the intended temperature of operation.

One final consideration for detector junctions is the ideality of the subgap current. The ability to measure a subgap current that matches with BCS theory demonstrates a control over several fabrication issues. The junction must have quality oxide barrier that does not show any ohmic leakage in the subgap region. Furthermore, it also implies that the critical current can be fully suppressed. As seen in Chapter 2, this suppression relies on precise symmetry in the size of the two junctions of the SQUID. In practice, smaller junctions always seem to show better suppression. This is presumably because the smaller critical currents of high impedance junctions are naturally reduced by noise. The measurements in this thesis work seem to indicate that an R_n of $\sim$5 kΩ represents a practical resistance threshold. Junctions with a resistance below this tend to show residual supercurrent below 300 mK. In contrast, almost all junctions with a resistance higher than this have shown complete suppression down the the 255 mk base temperature of the ^{3}He cryostat. This seems to indicate that the ideal situation would be to fabricate an absorber with a small enough volume that a junction with an $R_n \geq 5$ kΩ would still have tunneling time less than 1 μs.

This chapter has given an overview of processes used to fabricate superconducting tunnel junctions as well as the design considerations. For further fabrication details, the reader is referred to a journal article for devices made at NASA Goddard (Stevenson et al., 2003) and to Minghao Shen's thesis for Yale devices (Shen, 2005).

Chapter 5

Experimental Setup

"Cold! If the thermometer had been an inch longer we'd have frozen to death."

–Samuel L. Clemens

As this thesis work investigates the properties of superconducting tunnel junctions, all experiments must take place at temperatures well below the critical temperature of aluminum. While commercial cryostats can readily cool the devices under test, there are many other important considerations for successful measurements of cryogenic devices. Some of these issues include implementation of RF and DC bias wiring, filtering, vibration isolation and heat sinking. This chapter describes the the important practical issues and actual implementation of the experimental setup used in this thesis work.

5.1 General Filtering Requirements

Filtering is an integral part of any cryogenic experiment. Just as resistive wires must be used to minimize the conductive thermal heat load on the on the sample, electromagnetic radiation can equally drive the experiment from thermal equilibrium. While heat shields and light-tight enclosures can shield the general environment, the electrical leads provide a path for electromagnetic modes to couple from room temperature directly to the electrons in the mesoscopic experiment. Ideally,

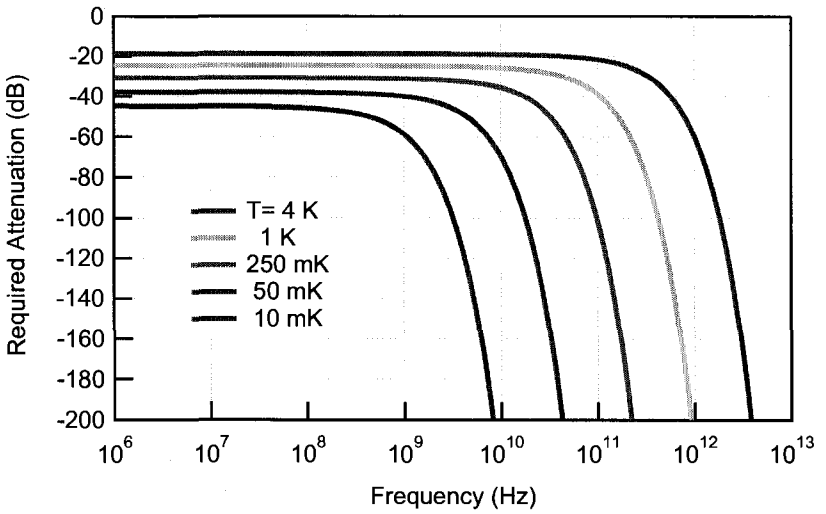

Figure 5.1: Filtering required to reduce room temperature thermal radiation to that of cryogenic temperatures.

the number of photons seen by the sample at a particular energy should be given by the Bose-Einstein distribution for the base temperature experiment. For low frequencies, where $h\nu \ll k_B T$, the total radiative power in a one-dimensional mode is directly proportional to the temperature. Thus, in this Rayleigh-Jeans limit, room temperature radiation would need only to be attenuated by a factor of ~1000 for an experiment at 300 mK. Above frequencies of ~5 GHz, however, the filtering requirements become exponentially more important. The necessary filtering is the ratio of the blackbody spectra at the two temperatures (Glattli et al., 1997). So the required attenuation, in dB, is:

$$A(\nu) = -10 \log \left(\frac{\exp\left(\frac{h\nu}{k_B T_1}\right) - 1}{\exp\left(\frac{h\nu}{k_B T_2}\right) - 1} \right) \tag{5.1}$$

where T_1 is the cryogenic temperature to be achieved and T_2 is the environmental temperature before filtering.

As seen in figure 5.1, an experiment at 10 mK would need 50 dB of attenuation for low frequencies, but more than 200 dB by 10 GHz. This only considers the effects of thermal radiation. As anyone with a cell phone can attest, the electromagnetic environment is far from a thermal bath. Thus, beyond attenuating thermal noise, the experimental setup must sufficiently isolate the device under test from all forms of electromagnetic radiation including radio stations, 60 Hz pickup, *etc.* This will put stringent requirements on shielding and filtering in the lower RF spectrum as well. In general, attenuation and filtering should be chosen such that the device is well-coupled only at frequencies necessary for measurements.

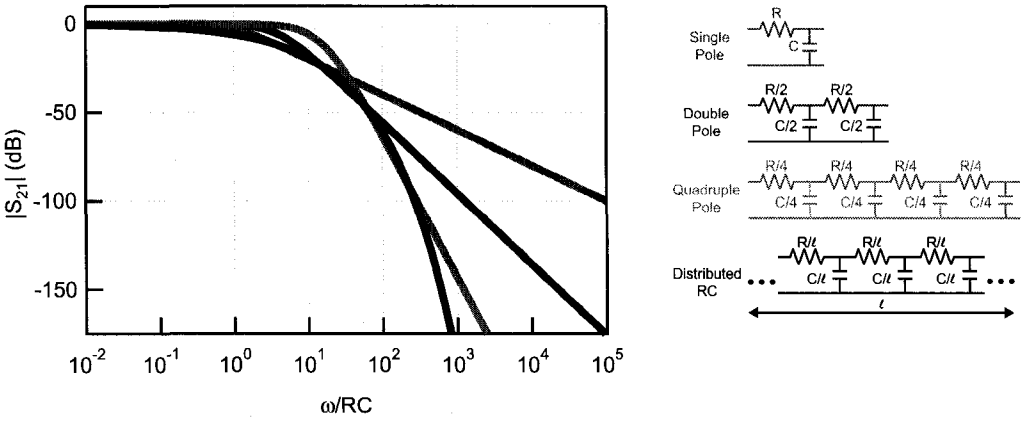

Figure 5.2: For a simple-pole RC filter, the attenuation above the 3 dB point increases by 20 dB per decade. By partitioning the resistance and capacitance into N sections, the corner frequency is increased as well as the attenuation in the stopband. For a given total capacitance and resistance, the most attenuation is achieved in the limit of a distributed (transmission line) RC filter. In this case, the attenuation increases exponentially with frequency as shown above.

While lumped-element low pass filters can provide very sharp cutoffs and excellent transmission in band, at sufficiently high frequencies their performance suffers. Unavoidable parasitic capacitance and self-resonances in the lumped elements imply that there will be frequencies in the stopband with unacceptably high transmission. One natural solution is to implement transmission line filters. A lossy transmission line behaves as a distributed RC filter. For a transmission line with large series resistance and shunt capacitance, the propagation constant(γ) is complex and has equal real (α) and imaginary (β) parts. Thus, the attenuation per unit length increases exponentially with frequency.

$$|S_{21}| = \exp(-\alpha\ell) = \exp\left(-\sqrt{\frac{\omega RC}{2}}\right) \tag{5.2}$$

Here R is the total series resistance over the length of the line and C is the total capacitance to ground. For a given total series resistance and shunt capacitance, an RC transmission line gives the maximum attenuation. This is illustrated in Figure 5.2. This analysis only treats the TEM mode for which the filter is designed. In reality, at high enough frequencies, a coaxial line will become overmoded. This means it can support TE or TM modes that are not strongly attenuated as calculated above. For this reason, the gap between the center conductor and ground should be made as small as possible. This both increases the attenuation per unit length of the TEM modes and increases the frequency at which non-TEM modes could propagate.

There are two types of transmission line filters that are used in this work. The first is a powder filter. These filters consist of a long (~1 m) copper wire that is coiled and immersed in a mixture of epoxy and copper powder. This structure is housed in a copper box and fitted with SMA connectors. In these filters, the high frequency loss comes from the powder itself, not from the resistance

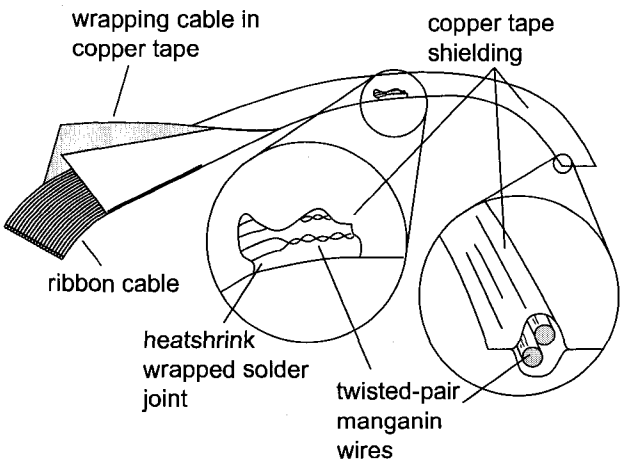

Figure 5.3: This illustration shows the general assembly of the tapeworm filter. A transmission line lowpass filter is created by using resistive, shielded twisted pair lines. The wires are comprised of fine gauge, manganin wire. The copper tape forms the shield as well as provides additional capacitance to ground for maximal attenuation per unit length. (Figure courtesy of Lafe Spietz)

of the center conductor. This small DC resistance (<1 Ω) allows for single-ended transport measurements and minimal DC Joule power dissipated at the cold stage of the cryostat. As the dense powder is in close contact with the wire, these filters provide a large surface area over which the phonons in the center conductor of the bias line can thermalize with the cryostat. Furthermore, unlike a coaxial cable, there is not a large gap between the inner and outer conductors that could support higher order modes. The overall filtering characteristic is shown in Figure 5.5. There is unity transmission at low frequencies, and greater than 100 dB of attenuation by 2 GHz. The ripple in the rolloff varies from filter to filter presumably due to variations in exact fabrication. A detailed description of filtering requirements and the fabrication and performance of powder filters can be found in the following references (Martinis et al., 1987; Vion et al., 1995; Bladh et al., 2003; Fukushima et al., 1997; Zorin, 1995).

While powder filters provide an effective means for filtering lines, it is becomes difficult to implement for non-coaxial lines. In order to make use of the 10 sets of twisted pair lines in the cryostat, it is necessary to have an analogous filter that is conducive to twisted-pair geometry and could filter many lines at once. This is the impetus behind the creation of the "tapeworm" filter. The general design is depicted in Figure 5.3. It uses resistive, insulated wire (38 gauge manganin wire) that is shielded by copper tape. In this way, it is a lossy transmission line that provides the exponential attenuation of high frequency signals. As a transmission line, it has a resistance, capacitance and inductance per unit length of 50 Ω/m, 200 pF/m, and 200 nH/m. In order to match the filter characteristics of a traditional powder filter, a length of roughly 2 meters is required. Ten sets of twisted pair lines are mass terminated in a commercial connector and the shield is integrated directly

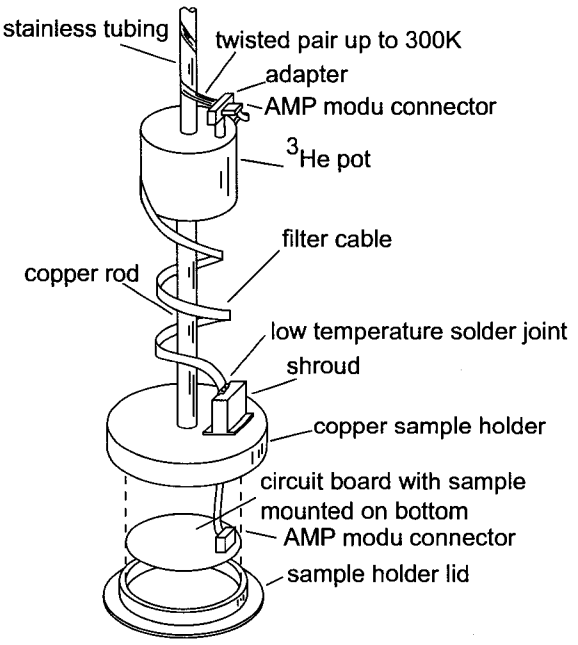

Figure 5.4: The tapeworm filter is integrated into the ^{3}He cryostat as shown above. A commercial micro-D connector attaches the filter to the existing Oxford wiring at the ^{3}He stage. The other end is terminated in an AMP-MODU connector and a copper shroud is soldered directly to the copper tape. This shroud is then screwed into the sample holder so that a shielded environment is maintained from the filter to the device. (Figure courtesy of Lafe Spietz)

into the sample holder as shown in Figure 5.4. The current design is only to filter lines which are already at the base temperature of the cryostat. A similar filter could be used to bridge temperature gradients in the cryostat if the copper shield is replaced by resistive or superconducting metal to minimize the overall thermal conductance.

As seen in Figure 5.5, the attenuation is as expected. Unlike the powder filter, there is 6 dB of loss at low frequency simply from the resistive division. As this filter is used on lines that already have an significant DC resistance, the additional loss in not a significant drawback. One nice feature is the smooth, monotonic rolloff with frequency. This implies minimal distortion of pulses and a filter that is characterized by a single time constant. The filter also has minimal temperature dependence, as most of the loss arises from the resistive manganin wire with a small residual resistance ratio. For further details on fabrication and modelling of the tapeworm filter the reader is referred to the following references (Spietz et al., 2004; Spietz, 2005).

In practice, a combination of a lossy transmission line filter and a lumped element filter gives the best overall performance. The lumped element filter, such as a Mini-Circuits SLP-1.9, gives a sharp multi-pole rolloff at 2 MHz with almost no DC resistance. While its performance begins to degrade above 200 MHz (as shown in Figure 5.5), this is precisely where the powder or tapeworm

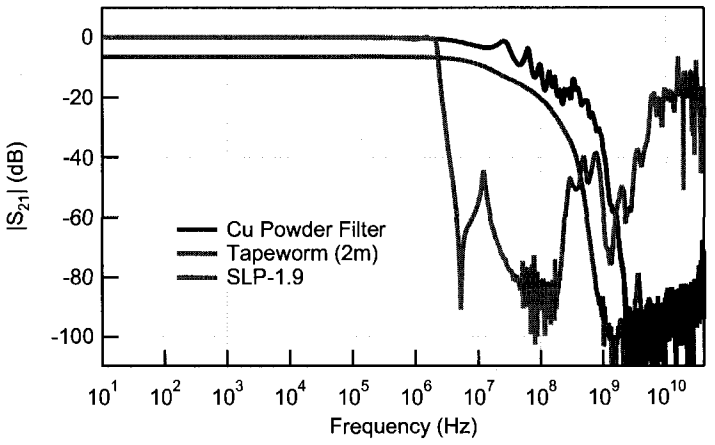

Figure 5.5: This transmission data shows the attenuation of the three types of low-pass filters from 10 Hz to 40 GHz. The commercial SLP filter provides a sharp cutoff at 2 MHz, but shows increased transmission above ~1200 MHz. In contrast, both the copper powder filter and the tapeworm filter provide strong attenuation without any spurious transmission peaks in the stopband. The tapeworm provides the smoothest filtering characteristic, but also has 6 dB of loss at low frequencies due to the DC resistance ($\sim$ 100 Ω). The series combination of a lumped-element filter and lossy transmission line filter provides the necessary frequency dependent attenuation for cryogenic measurements. While this data is taken at room temperature, there is only a slight change in the filter characteristic when used at cryogenic temperatures.

filter will provide the necessary attenuation. For the twisted pair lines, a commercial 20-pin filter is used instead of the SLP to provide the low frequency filtering.

5.2 Cryostat Overview

The bulk of the measurements were performed in a pumped ^{3}He cryostat. This a commercial "Heliox" cryostat from Oxford Instruments. The standard design uses a closed volume of ^{3}He with a charcoal sorption pump to obtain tens of microwatts of cooling power at 300 mK. This type of cryostat offers an excellent balance between the additional cost and complexity of a dilution refrigerator and the limited cooling power and hold time of a adiabatic demagnitization refrigerator (ADR). The advent of high-vaccuum SMA feedthroughs that work at cryogenic temperatures allows the RF components and cabling to be immersed in the liquid ^{4}He bath before passing into the inner vacuum chamber (IVC). This general design is used in all cryostats in the Schoelkopf lab to take advantage of the extremely low noise temperature RF amplifiers that operate at 4 K.

Figure 5.6 shows several pictures of the ^{3}He cryostat. The design of the IVC and baffling was significantly modified from the original Oxford design to accommodate the necessary RF components. The cryostat is outfitted with 10 sets of twisted-pairs lines as well as 5 semi-rigid coaxial lines for DC and RF measurements. With these modifications, the system has minimum base temperature

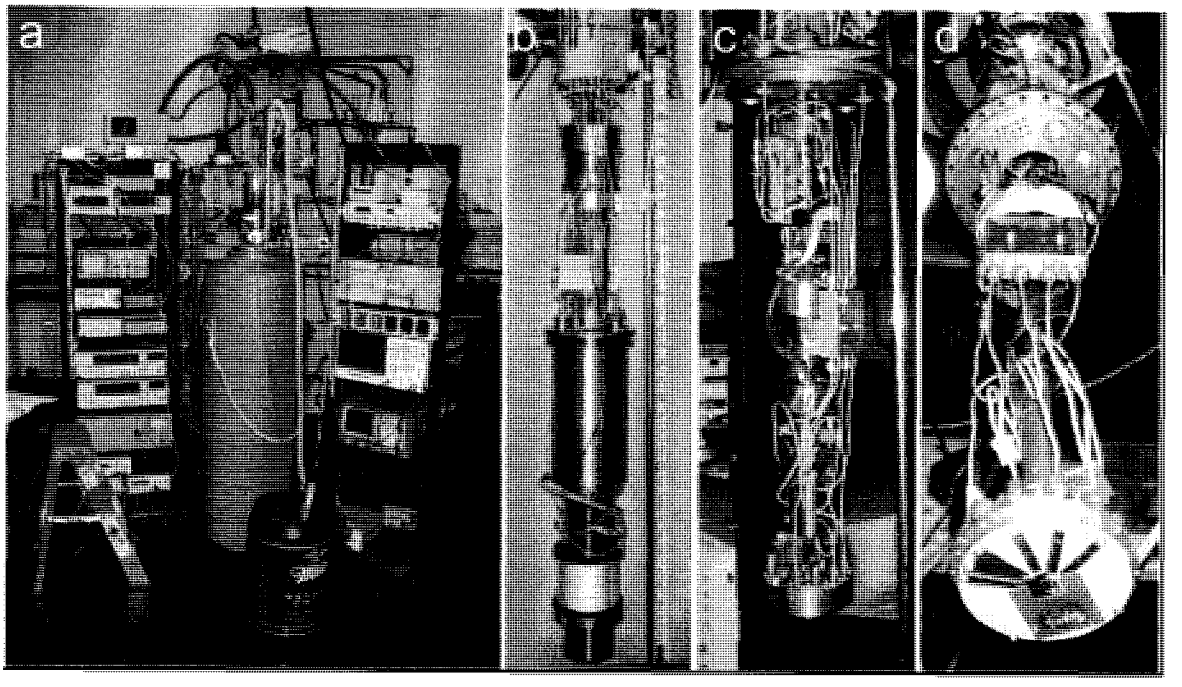

Figure 5.6: The ^{3}He cryostat is a commercial Heliox from Oxford Instruments. (a) The cryostat in the dewar with a typical measurement setup. (b) The insert with the IVC closed. This shows the superconducting magnetic at the bottom and the NRAO amplifier just above the IVC. (c) Inside the IVC. The sample holder at the bottom is connected to 4 SMA cables and 10 twisted-pair lines. These line are filtered by powder filters and the tapeworm filter, respectively. (d) Inside the sample holder. The lid of the jellyhog is removed and the picture is taken from below to show the device and circuit board *in situ*.

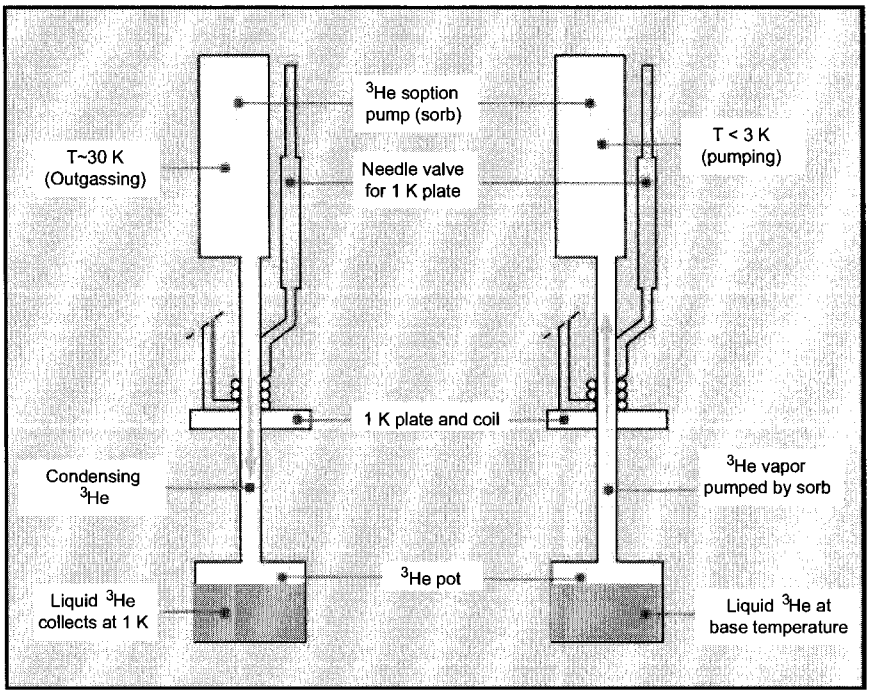

Figure 5.7: This schematic diagram shows the general operating principle of a ^{3}He cryostat. A sorption pump is cooled by the 1 K plate to pump on a closed volume of ^{3}He. The pictures on the left and right show the operation during condensation and pumping, respectively.

of 251 mK and a hold time of approximately 48 hours. The dewar holds approximately 40 liters of liquid He in the belly above the IVC. With a typical He boil off of 25 liters per day, the system can be run for roughly two days at base temperature before transferring liquid He and recondensing the ^{3}He. The modified IVC allows the sample to sit at the center of a commercial (American Magnetics) superconducting magnet. This NB-Ti magnet has a maximum field of 0.5 T at the center of its bore. While this is a large enough magnetic field to keep aluminum devices from superconducting at low temperature, it is typically used in this work simply to provide the few hundred microTelsa necessary to suppress the critical current of the SQUID detector junctions. The advantage of the superconducting magnet is that the field can be persisted with a superconducting switch. This keeps the field extremely stable and implies no Joule heating from the current in the magnet.

There are several important temperature stages inside the IVC of the cryostat. The IVC itself is immersed in liquid He and is held at 4.2 K. The next stage is the "1 K pot." While in this cryostat it is not actually a pot, but simply a coiled tube through which liquid ^{4}He may be pumped from the bath. The pumping is performed with a rotary rough pump and the flow is controlled with a manually-adjusted needle valve. While the temperature of the stage depends on the exact position of the needle valve, under normal operation the pressure is few millibar and the temperature is less than 1.5 K. All cables are thermally anchored at the 1 K plate before passing to the cold stage.

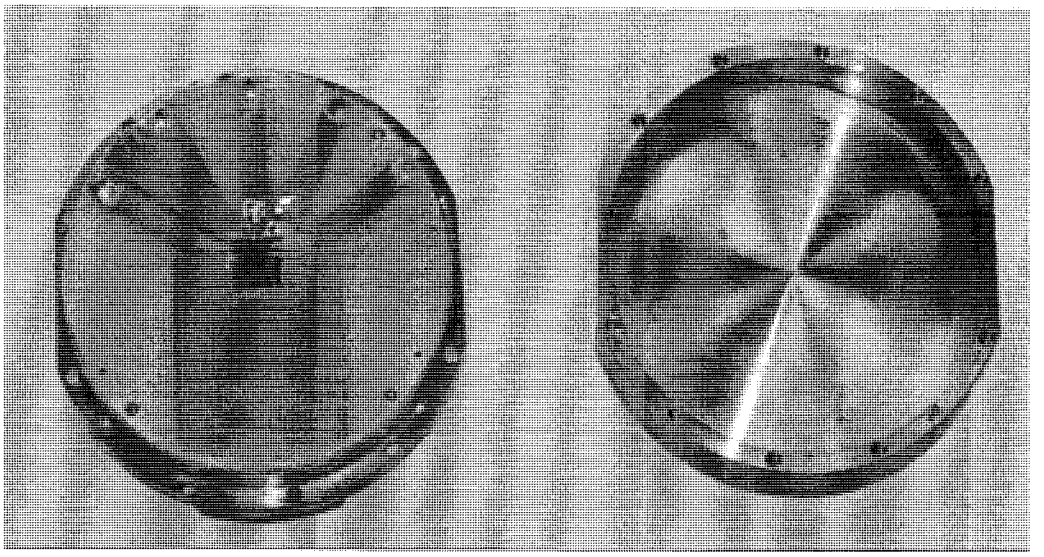

Figure 5.8: The sample holder is a light-tight enclosure machined from oxygen free copper for maximal thermal conductivity. The circuit board has 4 microstrip lines that connect to SMA cables and 20 DC lines. A surface mount inductor is soldered on the one of the RF lines to form the tank circuit. The chip is adhered to the board with vacuum grease and is electrically connected with aluminum wirebonds.

The cold stage consists of a ^{3}He pot in which a closed volume of liquid ^{3}He is pumped on by a sorb near the 1 K plate. In order to condense the liquid ^{3}He the sorb is heated to 25 K while the needle valve is opened to keep the 1 K pot below 3 K. As the condensation temperature of ^{3}He is 3.2 K, this allows the ^{3}He gas expelled from the warm sorb to condense on the 1 K plate and fill the ^{3}He pot. Once all the ^{3}He is liquified, one simply stops applying heat the the sorb and reduces the flow through the needle valve. The sorb now begins to pump on the liquid ^{3}He. After about a half hour, the sorb temperature cools to around 3 K and the temperature of cold stage equilibrates typically to 255 mK. This cycle is depicted in Figure 5.7.

The temperature is measured with resistive thermometers that were installed and calibrated by Oxford. The temperature of the cold stage is measured with two separate thermometers: a Cernox thermometer that is calibrated from 1.4 to 300 K and a ruthenium oxide (RuOx) thermometer which is calibrated from 0.2 to 7 K. There are also thermometers on the 1 K pot and the ^{3}He sorb. Heaters at each of these stages allow the temperature to be regulated with a PID loop at a broad range of temperatures. For more detail on the cryostat thermometers and their accuracies, the reader is referred to Lafe Spietz thesis (Spietz, 2005).

5.3 Sample Holder

The sample holder is a gold-plated copper enclosure that maintains a shielded environment around the device under test as well as the circuit board to which it is wirebonded. The holder is affectionately known as a "jellyhog" due to its ambiguous likeness to several different animals. As shown in Figures 5.8 and 5.6, it has seven SMA connectors and one 20-pin connector for the DC wiring. A custom circuit board plugs into the holder to bring the wiring directly to the chip. For most measurements, the board consisted of an FR-4 dielectric with a single layer copper patterned on it. The SMA connections transition to 50 Ω microstrip transmission lines on the board. A surface mount inductor may be soldered in series to create the tank circuit for the high impedance RF measurements. As discussed in Chapter 3, minimizing the parasitic capacitance after the inductor is the key to obtaining the highest impedance resonant circuit. Thus, for situations where a high Q tank circuit is required, the chip and inductor are mounted on an additional teflon dielectric layer. The chip is adhered to the surface by either cryogenic vacuum grease (Apeizon "N') or rubber cement. The inductor may be wire bonded to the sample to avoid the additional capacitance of a solder pad.

5.4 Cables and Wiring

There are two types of bias lines in the cryostat. The first is referred to as the "DC" wiring and consists of resistive leads. This wiring is a braided loom of ten sets of twisted-pairs. The filtering consists of a 2 MHz lowpass filter at room temperature and the tapeworm filter at the cold stage. The primary use of these lines is characterization of DC IV characteristics of tunnel junctions. As the total series resistance of these lines (including the filter) is 200 Ω a four wire measurement is typically used. While this type of wiring is not conducive to RF measurements, it provides an invaluable method for testing many devices in a single cryogenic run.

For most measurements the semi-rigid coax bias lines are used. By maintaining a 50 Ω characteristic impedance from room temperature directly into the sample holder, these leads allow for well controlled measurements at both DC and the RF frequencies used in this work. The cables are 0.085" diameter coaxial lines with a teflon dielectric and are terminated with SMA connectors. The inner and outer conductors are either copper or stainless steel depending on the location in the cryostat. While the large electrical conductivity of copper offers the least attenuation per unit length, the thermal conductivity gives an unacceptably large heat load to the cold stage. Thus, stainless steel cables are used to span the significant the temperature gradients in the cryostat. Across the main baffle stack that goes from room temperature into the liquid helium bath, a cable with a stainless steel outer conductor and a silver-plated copper weld (SPCW) inner conductor offers as good balance of thermal and electrical characteristics. As most of the metallic cross section of the cable is in the outer conductor, replacing this with stainless steel greatly reduces thermal conductivity and hence the liquid helium boil off. The copper center conductor gives a DC resistance of less than

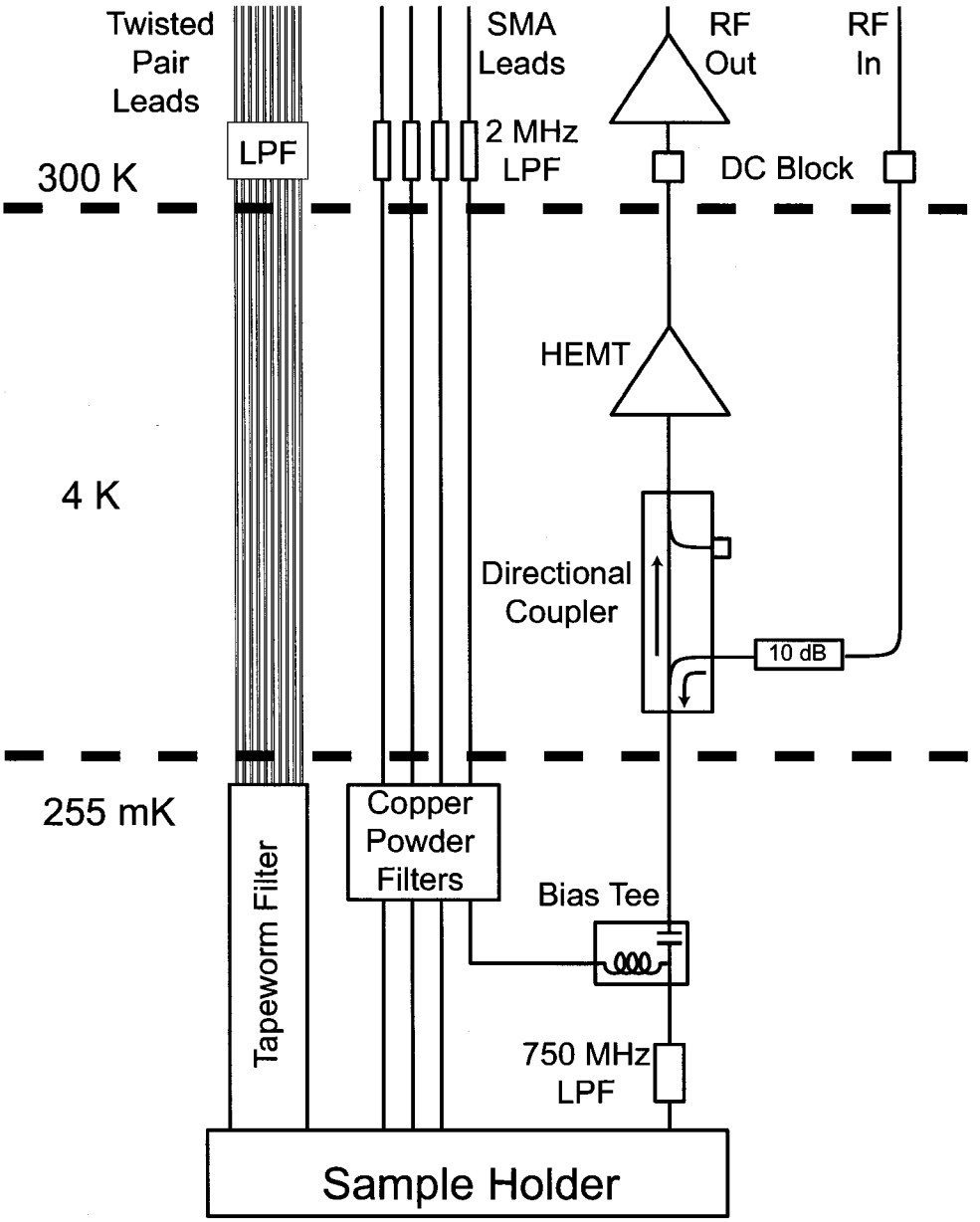

Figure 5.9: The experimental setup for the ^{3}He cryostat. Five SMA coaxial cables are brought into the IVC with cryogenic feed-throughs. These lines connect to copper power filters at the base temperature in order to provide strong attenuation of high frequency signals and good thermalization for the center pin of the conductors. There are also an additional 10 twisted-pair lines that are filtered using the tapeworm filter. The bias tee configuration allows for simultaneous DC and RF measurements.

1 Ω and little RF attenuation at 500 MHz. Once in the helium bath, the cables with copper inner and outer conductors connect to the feedthroughs into the IVC. Again, a cable with SPCW inner and stainless outer is used from the 4 K plate to the 1 K plate. Then, only in the last section from 1 K to the cold stage are cables with stainless steel inner and outer conductors used. This provides the lowest possible heat load to the cold stage and maintains the lowest possible base temperature. Copper powder filters at the cold stage ensure that the center pin is fully thermalized. One of the lines that is used for the RF measurements goes directly from 4 K to a bias tee at the cold stage with a single stainless/stainless cable. The outer conductor is anchored to the 1 K pot the minimize the total heat load. This line does not have a powder filter as it is used to both applied the 500 MHz carrier and monitor the reflected signal. The overall wiring is shown in Figure 5.9.

5.5 RF Measurement Setup

As seen in Figure 5.9, the bias tee configuration allows one to simultaneously measure the DC IV characteristic and monitor the reflected RF signal. While the RF reflection technique could work equally well at 5 MHz or 5 GHz, the 500 MHz band is chosen as a balance of several factors. At 5 GHz, the parasitic capacitance of the device will result in a much lower impedance tank circuit. In the end, the important figure of merit is the effective current noise of the reflection technique. This is optimized with high Q resonant circuits and lowest noise amplifiers. As the noise temperature of cryogenic HEMT amplifiers tends to remain a fixed factor above the quantum limit as a function of frequency, the absolute noise temperature tends to be lower at lower frequencies. However, for frequencies below roughly 300 MHz, the intrinsic 1/f noise of the transistors begins to dominate the noise performance (Bradley, 1999). Thus, there is little improvement in noise temperature by going below this frequency until one reaches audio frequencies. The 300 to 600 MHz range represents a range where the lowest noise temperature RF amplifiers are available. This frequency is also high enough so that a tank circuit with Q~100 still has more than 1 MHz of bandwidth.

As the RF line cannot be filtered in the same way as the DC leads, this lead requires broadband attenuation. A signal of order -30 dBm is made using a signal generator or vector network analyzer. This is attenuated at room temperature by 40 dB and connected to the cryostat using an Inmet inside-outside DC block to prevent a ground loop. The signal is attenuated again in the liquid helium bath by a cryogenic 10 dB attenuator and by the -20 dB arm of a broadband directional coupler (MAC Technology Inc). The signal then continues into the IVC and to the RF port of a microwave bias tee (Anritzu). The RF+DC port of the bias tee is then connected to the sample holder. Within the sample holder the tank circuit transforms the impedance of the device under test near 50 Ω. As this impedance changes, the amount of the RF carrier that is reflected is modulated. The reflected signal then travel through the directional coupler to the cryogenic HEMT amplifier in the helium bath. The signal is DC blocked again at room temperature and further amplified by a

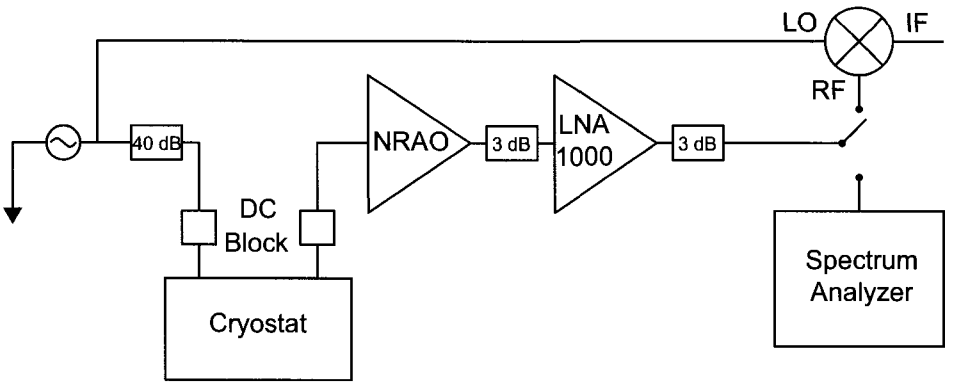

Figure 5.10: The reflected RF signal can be demodulated in two ways. Using a spectrum analyzer (HP E4407) in zero span mode allows for convenient measurement of the carrier power. The analyzer has adjustable input attenuation, reference level, video and resolution bandwidth. If the carrier power is small or the tank circuit is very close to match, a vector measurement is preferred. Then an RF mixer is used to measure the amplitude and sign of the signal.

custom low noise amplifier and two broadband Mini-Circuits amplifiers (LNA-1000). Demodulating this reflected signal can be performed in several different ways. Initially, when characterizing the center frequency and Q of the tank circuit, the RF signal is simply fed back into the vector network analyzer. Once the resonance frequency is found, only a CW tone is applied and the reflected power is measured either with an RF diode or a spectrum analyzer. Either of these devices can output a voltage that may recorded with a Keithley DVM or digitized with an Aquiris card. If the reflected signal is comparable to the noise then simply measuring the power is not a good method for demodulation. This can occur either because the applied carrier is small or because the circuit is close to match. In fact, if only measuring the RF power, the technique becomes first order insensitive to changes in dynamic resistance near match. In this case, a vector measurement is the solution. Using a mixer determines not only the amplitude, but also the sign of the reflected signal. Thus, the reflected RF voltage is a monotonic function of resistance.

One concern with this technique is the lack of filtering near the band of amplification. From the standpoint of the device, the tank circuit acts as a bandpass filter. But within this band, the device is extremely well coupled (by design) to amplifier. Simply specifying the noise temperature of an amplifier does not necessarily determine the noise power emitted back to the device. The solution is use a circulator to break the symmetry between signals travelling to and from the device. Thus, the noise seen by the device would ideally only be the Johnson noise of the 50 Ω termination on the third port of the circulator. While octave bandwidth cryogenic circulator are available (Pamtech), they were not necessary for the measurements made in this thesis work. In general, only a 750 MHz lowpass filter was placed between the sample holder and the amplifier to limit any radiation above the amplification band. When properly biased, the HEMT amplifier showed no adverse affects on

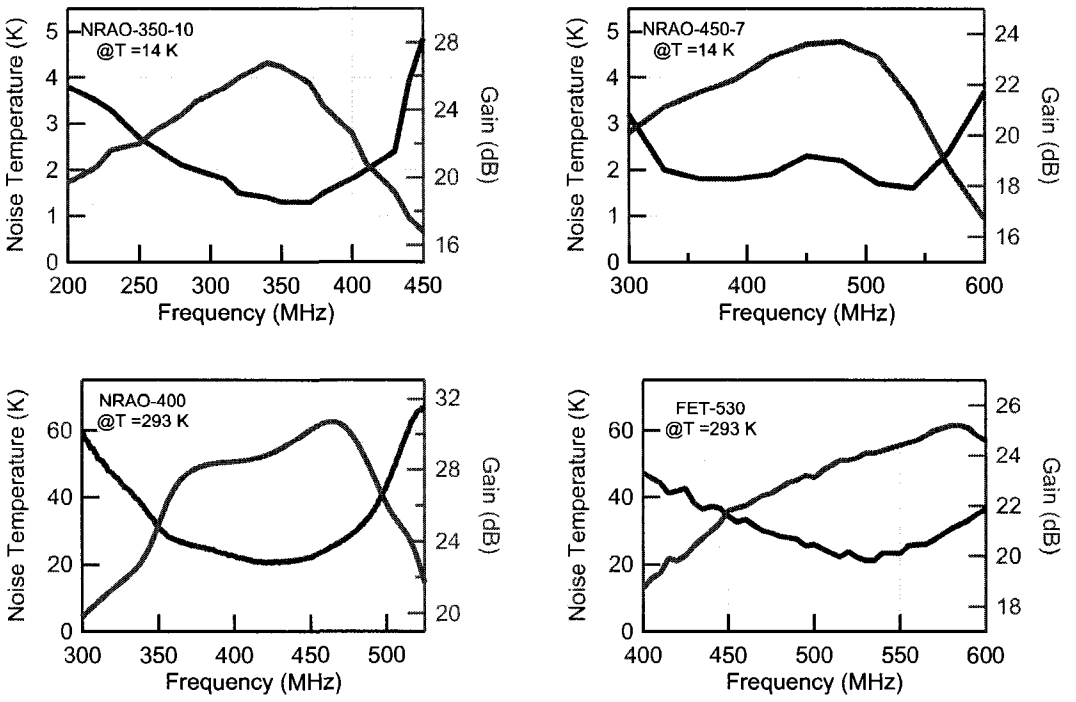

Figure 5.11: The ultra low noise amplifiers used are custom build by NRAO. The two cryogenic HEMT amplifiers are octave bandwidth, balanced amplifiers centered at 350 MHz and 450 MHz. The top graphs show the gain and noise temperature measured at NRAO at 14 K. The lower graphs show the characteristics of the two room temperature amplifiers used to increase the system gain while preserving the low system noise temperature.

the detector junctions.

5.6 Cryogenic Amplifiers

The heart of this thesis work is to exploit the exceptional noise performance, versatility, and dynamic range of cryogenic amplifiers. While HEMT amplifiers are commercially available, the ones used in this work are custom build by NRAO (Bradley, 1999). These are octave-bandwidth balanced amplifiers centered at either 350 or 450 MHz. Figure 5.11 shows the gain and noise temperature for our specific amplifiers. These measurements were performed at NRAO at 14 K. A 2 K noise temperature at 500 MHz implies a total voltage noise of 75 pV/$\sqrt{\text{Hz}}$ or a total current noise of 1.5 pA/$\sqrt{\text{Hz}}$ for a 50 Ω load to which they are matched. When combined with a tank circuit, this current noise is further reduced by a factor of Q. These cryogenic amplifiers have a power gain of a few hundred so the noise temperature of the next amplifier is important, but not critical. The room temperature amplifiers from NRAO have a noise temperature of 20 K and add a negligible tens of millikelvin to the overall system noise temperature. From this point, the output noise temperature

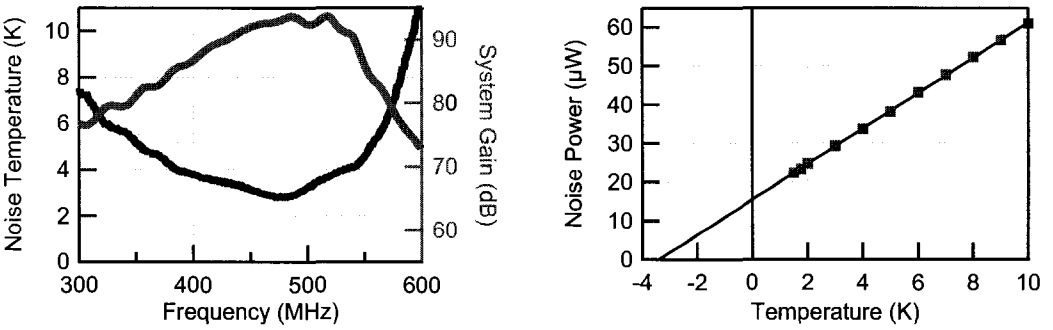

Figure 5.12: These data show the measured system gain and noise temperature for the amplifier chain used in this thesis work. The amplification chain consists of a cryogenic HEMT amplifier at 4 K follow by three more amplifiers at room temperature. The measurements were performed in the ^{3}He cryostat while varying the temperature of a 50 Ω termination from 1 to 10 K. At 475 MHz, the system noise temperature is 2.8 K. The right graph shows the total output noise power from 300 to 600 MHz as a function of load temperature yielding a system noise temperature of 3.4 K over 110 MHz of equivalent noise bandwidth.

is large enough that any components that follow will not readily affect the system noise temperature.

Figure 5.12 show the system gain and noise temperature as measured in our setup. A Y-factor measurement is performed by using the cryostat to vary the temperature of a 50 Ω termination. As a function of frequency, the system has large gain and low noise over the entire 300 to 600 MHz band. A minimum system noise temperature of 2.8 K is seen at 475 MHz. For noise thermometry, the bandwidth is almost as important as the noise temperature. The righthand graph shows the broadband noise as a function of load temperature. This shows a system noise temperature of 3.4 K over 110 MHz of equivalent noise bandwidth. Applying the Dicke radiometer formula, this implies a load temperature sensitivity of 300 $\mu K/\sqrt{Hz}$.

5.7 DC Measurement Setup

The DC measurements is shown in Figure 5.13. All measurements made with the SMA leads are single-ended. The device is wirebonded to the cryostat ground inside the sample holder. The current-voltage characteristics are measured by monitoring the voltage drop across a series bias resistor at room temperature. A Yokogawa 7651 DC voltage source is supplies a floating bias voltage. This voltage is attenuated with resistive division and applied to a decade variable bias resistor in series with the device. Low noise instrumentation amplifiers with gain of 500 simultaneously measure the voltage across the device and the bias resistor for real-time measurement of the IV curve. The output of these amplifiers is recorded with floating digital voltage meters (Keithley) and downloaded to the computer via GPIB. A copy of the output is sent through unity-gain isolation amplifiers and

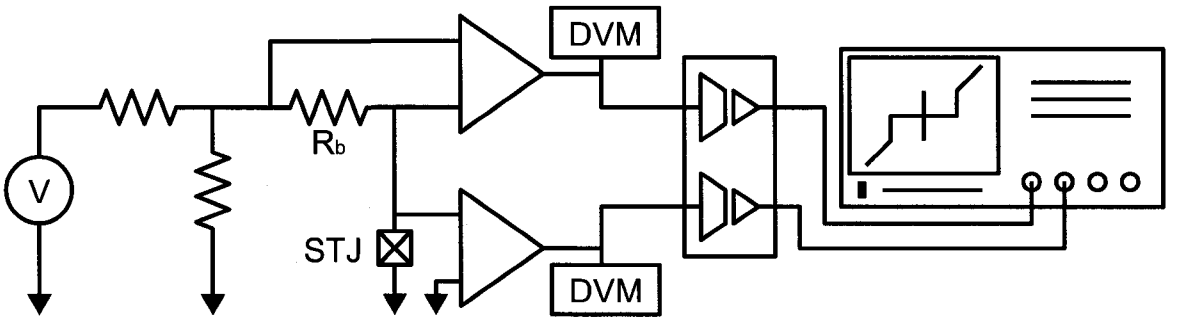

Figure 5.13: This diagram shows the measurement configuration for DC transport measurements. A floating voltage source is resistively attenuated then connected to the device under test via a series bias resistor. The voltages across the bias resistor and the device are amplified with low noise instrumentation amplifiers (INA-110) for simultaneous measurement of the current and voltage. These signals are then split so that they may be recorded with floating digital voltage meters and also monitored in real time on the oscilloscope. Unity-gain, isolation amplifiers are used to prevent a ground-loop between the oscilloscope and the cryostat.

monitored on the oscilloscope.

The instrumentation amplifiers are Brown-Burr INA-110. They are rated to have a voltage noise of 10 nv/$\sqrt{\text{Hz}}$ and a current noise of 1.8 fA/$\sqrt{\text{Hz}}$. Thus, with a 10 MΩ bias resistor, the total current noise of the amplifier is 2 fA/$\sqrt{\text{Hz}}$. This is negligible compared to the Johnson noise of the room temperature bias resistor (40 fA/$\sqrt{\text{Hz}}$). While the bias resistor could easily be placed in the cryostat to reduce this Johnson noise, the ability to change the bias resistor during the experiment far outweighs this slight increase in sensitivity. The main drawback of the DC measurement setup is the large capacitance from the semi-rigid cables and extensive filtering. The total capacitance of ~10 nF limits the DC measurement bandwidth to less than 10 Hz for a 10 MΩ bias resistor. Not only does this imply that the measurements are necessarily slow, but it also means that the setup is very sensitive to vibration (microphonics) at audio frequencies. This affect was minimized by placing the entire cryostat on rubber pads. These drawbacks in the DC measurement setup highlight many of the advantages of using RF techniques.

Chapter 6

DC Characterization of Tunnel Junctions

"Weather forecast for tonight: dark."

–George Carlin

The goal of the first measurements is to characterize the "dark" properties of the tunnel junctions without illumination with any photons. This chapter will present the experimental results of the DC current-voltage measurements of the tunnel junctions used throughout this work. The goal of these measurements was the verify the degree to which the junctions fabricated for this work could be predicted by simple BCS theory. Unlike previous STJ detectors where the large area junctions are required to handle the photocurrents from optical or X-ray photons, this work relies on the ability to use small area junctions in order to achieve extremely low quasiparticle currents. Because it is this subgap current that flows in the absence of an illumination that sets the fundamental limit on the sensitivity of the detector, these measurements are critical in understanding the potential for the STJ as a submillimeter direct detector. Ideally, this dark current will be completely determined by the small number of quasiparticles that BCS theory predicts must be there given the finite temperature of the experiment. This assumes not only that the quasiparticles are in thermal equilibrium with the

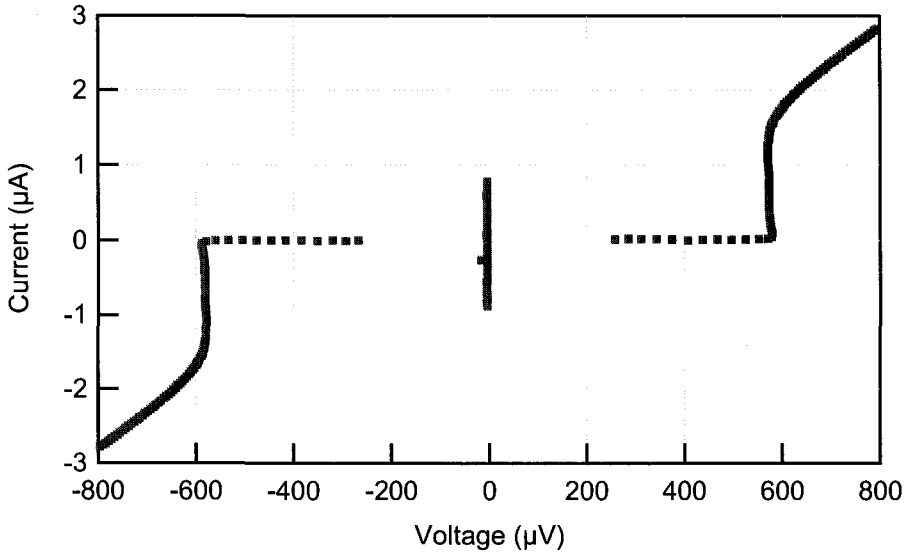

Figure 6.1: An aluminum SIS junction before suppressing the supercurrent. This particular junction was evaporated in the presence of oxygen to give an exceptionally large gap value of Δ=290 μV.

cryostat, but also that all other mechanisms of current flow have been suppressed. There are several well-known processes that can limit subgap current in tunnel junctions; many of which only become important only in high impedance junctions. This chapter shows the experimental verification that these alternate mechanisms of tunnelling current can be explained by well-understood physics and will not be the limiting factor in the ultimate performance of the the detector. Furthermore, the near-ideality of the measured quasiparticle currents has important implications for many applications of Josephson junctions.

6.1 General Characteristics of an SIS Tunnel Junction

This section outlines the transport characteristics of a generic Josephson junction at temperatures well below it transition temperature. Figure 6.1 shows a typical current-voltage characteristic, or IV curve, of a superconducting tunnel junction. As is apparent from the graph, there are essentially three distinct regimes: V=0, 0<V< $\frac{2\Delta}{e}$ and V> $\frac{2\Delta}{e}$. The first region represents the dissipationless supercurrent due to tunnelling of Cooper pairs. At small but finite voltages, the current dramatically drops by many orders of magnitude. In this "subgap " region, there is no more direct tunnelling of Cooper pairs and it is ideally only the quasiparticles that can carry the current. The dynamic resistance of the junction has changed from a true short circuit on the supercurrent branch to essentially an open circuit in the subgap. As the voltage bias reaches $\frac{2\Delta}{e}$, there is enough energy provided by the battery that the quasiparticle tunnelling is no longer suppressed by the gap in

the density of states in the superconducting electrodes. The dynamic resistance asymptotically approaches the normal state resistance that the junction would have at a temperature above T_c. As a detector, the subgap is the only region of interest. The broad IV curve, however, provides a direct measurement of the two main parameters for characterizing a junction, R_n and Δ. The primary importance of the gap in this work is twofold. It determines the minimum frequency at which the detector can absorb/detect radiation. It also is what sets the scale in the exponential for the number of thermal quasiparticles at a given temperature and hence the dark current.

All devices are SIS junctions where the superconductor is aluminum and the insulator is aluminum oxide. The exact T_c (and zero temperature gap) is dependent on the cleanliness of the aluminum. Unlike most materials, the transition temperature for aluminum is actually increased for a dirtier film. So while the bulk value for the gap of aluminum is 170 μeV, the measured gap ranges from 180 μeV for nominally clean films to 290 μeV for aluminum intensionally evaporated in the presence of oxygen. The normal state resistance, which is determined by the area of the junction, also determines the scaling for many effects important to the overall detector performance. Over the course of this work, a broad range of junction types were measured. Their R_n's ranged from 100 Ω to 100 kΩ. This corresponds to a junction overlap area ranging from 5 to 0.005 μm^2.

It is important to note that even this basic measurement is nontrivial for several reasons. The extreme nonlinearity of the junction implies that it has sharp features in the IV curve that are very susceptible to noise over a broad range of frequencies. The supercurrent itself is an extremely sensitive threshold detector, where by any uncontrolled source of energy can cause it to prematurely switch to the dissipative state. Likewise, the gaprise also represents a sharp feature that can easily be rounded or even displaced in voltage with excess noise. Furthermore, improper geometric design of the junction electrodes can lead the self-heating of the junction due solely to the Joule power dissipated by the bias current. This will manifest itself in a structured gaprise that can "backbend" due to excess quasiparticles locally reducing the gap. Lastly, the subgap region relies on there being truly no states for quasiparticles to tunnel into in the superconductor. A single pin-hole in the insulator or any ohmic leakage path will dramatically increase the current in this region. It is the subgap that provides the most rigorous test for the intrinsic quality of aluminum as a superconductor and aluminium oxide as an insulator. That all of these effects can be overcome to measure even the basic IV characteristics already shows quality junction design and fabrication as well as a sufficiently filtered and thermalized experimental setup.

6.2 Cooper Pair Tunnelling Currents

In many applications, the interesting transport properties of a Josephson junction are determined the Cooper pair currents. On the contrary, in this work, the entire goal is to probe the number of quasiparticles directly by monitoring only its current. The junction serves as a method to measure

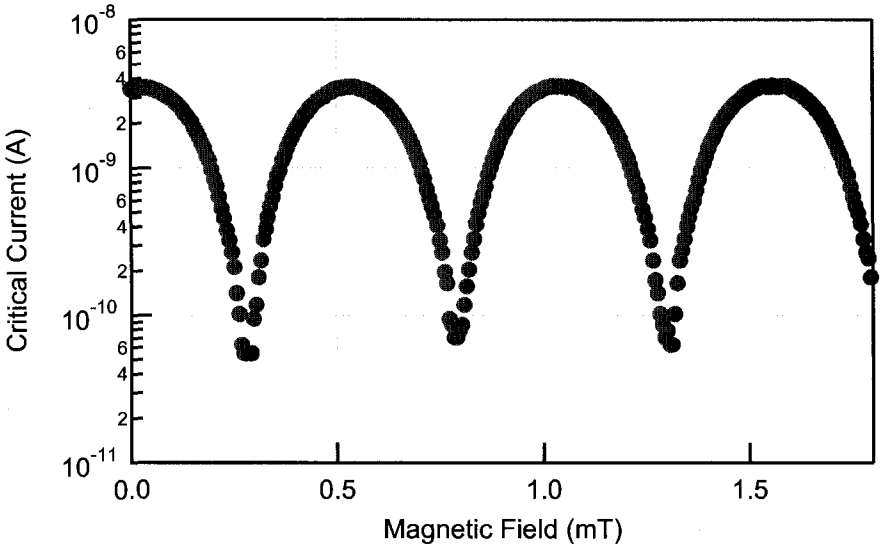

Figure 6.2: Plot of critical current of a SQUID junction with applied magnetic field. The loop area of roughly 10 μm^2 allows the supercurrent of the SQUID to be suppressed with a fraction of a milliTesla of applied field.

at finite voltage bias, separating the Cooper pair and quasiparticle currents. In order to ensure the detector current is solely due to the latter, the supercurrent must be suppressed. This section describes the measurements of various way in which unsuppressed Cooper pair currents can spoil the subgap currents of the junction.

The maximum current, I_c, is ideally given by (Ambegaokar and Baratoff, 1963):

$$I_c = \frac{\pi}{4}\frac{2\Delta}{eR_N} \tag{6.1}$$

I_c represents a threshold, above which the current must be carried by quasiparticles. The energy scale related to this Josephson current is the Josephson energy. It is given by:

$$E_J = \frac{\Phi_o I_c}{2\pi} = \frac{h\Delta}{8e^2 R_n} \tag{6.2}$$

For aluminum junctions with $R_n \gtrsim 1$ kΩ, the Josephson energy is small enough that the measured critical current is rarely the full predicted height. This is certainly true for IV curves traced out in a way where each bias point on the curve is integrated for a large fraction of a second. In general, this work only benefits from the extra suppression due to the small Josephson energy scale for high impedance junctions. It is, however, important to distinguish between the actual height of the supercurrent and that which is measured. As is seen in 6.1, the abrupt reduction in current as the voltage increases from zero to a few microvolts makes it hard to access small voltage points. Ideally, the measurement is conducted so that the junction in voltage biased, but it is impossible

to voltage bias a short circuit. In general, the load line of measurement will determine exactly how close to the supercurrent one can stably bias. What is more important for this work, is that even if one could stably bias, the current can be orders of magnitude larger than the thermal quasiparticle current. As explained in Chapter 2, inelastic Cooper pair tunnelling provides a mechanism whereby unsuppressed supercurrent can give rise excess current away from zero bias (Holst et al., 1994). The AC Josephson current produced when a junction is voltage biased can find resonances real part of the impedance of the circuit at the Josephson frequencies. This in turn, looks like AC voltage bias of the junction, which gives rises to a current analogous to a Shapiro step. While this effect is present at some level in all junctions, it is especially important in small area junctions. This is because small area junctions are intrinsically small capacitance junctions. A large capacitive shunt would prevent the junction from radiating into the uncontrolled impedances of the leads. Of course, large area junctions can suffer from electromagnetic resonance within the junction itself. These Fiske modes are well known to give large features in the subgap current (Fiske, 1964). Both of these effects emphasize the fact that the DC characteristics of a Josephson junction are the direct result of the environment seen by the junction at a broad range of frequencies. In this way, it is essential for high impedance junctions that the supercurrent be fully suppressed in order to directly probe only the quasiparticles.

In much of the previous STJ detector work, the junctions used were large enough in area that the supercurrent could be suppressed by applying a magnetic field parallel to the junction. The single valued nature of the wave function in the superconductor implies that the supercurrent will be periodic in this parallel field. The geometry of the junction will determine the applied field necessary to thread a flux quantum in the cross-section of the junction and hence the periodicity of the supercurrent. As the size of the junction becomes small ($\lesssim$ 1 μm on a side), this necessary field can become so large that it begins to suppress the gap of the material. In this case, the solution is to split the detector junction into two smaller area junction in parallel. This forms a traditional SQUID in which the supercurrent can be modulated by applying a perpendicular field. This now decouples the field required to reach the first minimum in I_c from the size of the junction itself. For symmetric junctions with negligible self-inductance the critical current is given by (Tinkham, 1996):

$$I_c = I_o \cos(\pi \frac{\Phi}{\Phi_o}) \tag{6.3}$$

The only downside to the SQUID geometry is that any asymmetry in the junction areas will lead to incomplete suppression of the supercurrent even at exactly one half flux quantum. In general the supercurrent suppression was always better for higher impedance junctions. This is almost certainly due to the lower E_J and not that the junction fabrication is somehow more symmetric. For junctions with $R_n \lesssim 3$ kΩ, the suppression tended to be noticeably incomplete at 250 mK, but still was reduced by better than a part in a thousand.

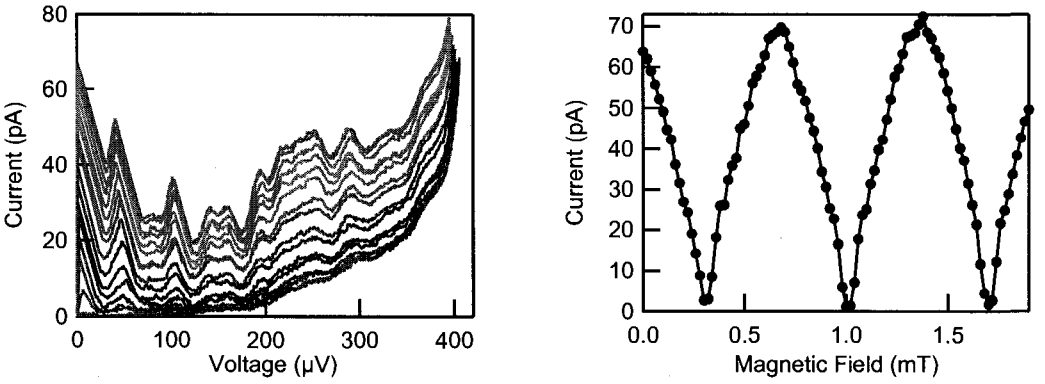

Figure 6.3: These graphs show the subgap current as a function of applied magnetic field. Any residual Josephson current can greatly increase the subgap current of the junction do to inelastic Cooper pair tunneling. The peaks seen in the IV curve correspond to resonances in the electromagnetic environment at the Josephson frequencies. The righthand graph show the current at a voltage bias point of 20 μV demonstrating the expected periodic I_c dependence.

In order to demonstrate the true importance of supercurrent suppression for detector performance, it is necessary to look at current, not just at zero voltage, but at finite voltage. Figure refiecpt shows the measured currents for a SQUID with R_n=45 kΩ while varying the applied magnetic field. In this case, the uncontrolled electromagnetic environment of the junction gives sharp current spikes in the subgap region. Each peak corresponds to a resonance seen by the junction at that particular Josephson frequency. This inelastic Cooper pair tunnelling shows the characteristic 1/V dependence predicted by the simple power balance of AC and DC currents (Holst et al., 1994).

$$I_{DC} = \frac{I_c^2 Re\left[Z\left(\omega\right)\right]}{2V} \tag{6.4}$$

One can also clearly see that it is periodic with I_c as predicted. Once again, it is important to emphasize that all of these curves were taken at the same temperature (T=250 mK), and that it is only when I_c is fully suppressed the subgap current is a good measure of the quasiparticle number. With the effects of the supercurrent understood, the temperature dependence may now be examined.

6.3 Quasiparticle Currents

With Cooper currents completely suppressed, the remaining mechanism for transport in only the quasiparticles. Assuming that aluminum electrodes are in thermal equilibrium with the heavily filtered cryostat the quasiparticle density, and hence quasiparticle current, should be directly calculable from BCS theory. Below is an approximation for the subgap current as a function of voltage for an SIS junction well below T_c (Van Duzer and Turner, 1998):

p

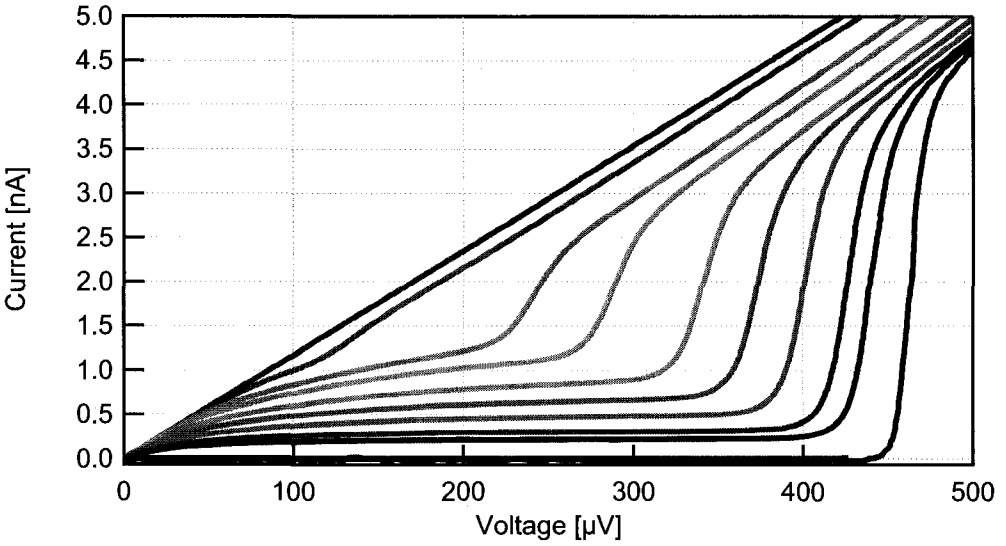

Figure 6.4: Measurements of temperature dependence of the IV curve from 250 mK to 1.6 K. At temperatures above roughly 500 mK, the temperature dependence of the superconducting gap becomes apparent.

$$I = \frac{2}{eR_n}\sqrt{\frac{2\Delta}{eV+2\Delta}}\,(eV+\Delta)\sinh\left(\frac{eV}{2k_BT}\right)K_0\left(\frac{eV}{2k_BT}\right)\exp\left(-\frac{\Delta}{k_BT}\right) \tag{6.5}$$

These currents scale inversely with the normal state resistance of the junction and exponentially with temperature. Thus, the subgap current represents a thermometer of the quasiparticle temperature (Giazotto et al., 2006). As with all exponential scaling, the relevant question are at what level will this continue to be true. At T=340 mK, the current should be reduced by a factor of 10^3 from the normal state. By 250 mK, the standard base temperature of our pumped ^{3}He cryostat, the currents should be reduced by 10^4. This temperature represents a convenient balance between cryogenic temperatures cold enough to make the thermal currents well below expected photocurrent, yet not requiring the added complexity of a dilution refrigerator. Figure 6.4 shows the general temperature dependence of a typical junction measured in the Heliox after suppressing the supercurrent. Above 600 mK there is a noticeable reduction in the gap. For all temperatures, the overall shape and current scale fits well with the BCS formula.

In order to understand the limitations to this scaling, the next step was to test IV curves at even colder temperatures. For laboratory purposes, the dilution refrigerator provides an way to see what the ultimate detector limitation might be, should the project warrant the added complexity and expense of such a system. The detailed temperature dependence of the subgap currents of high resistance tunnel junctions is a subject important to many applications of Josephson junctions,

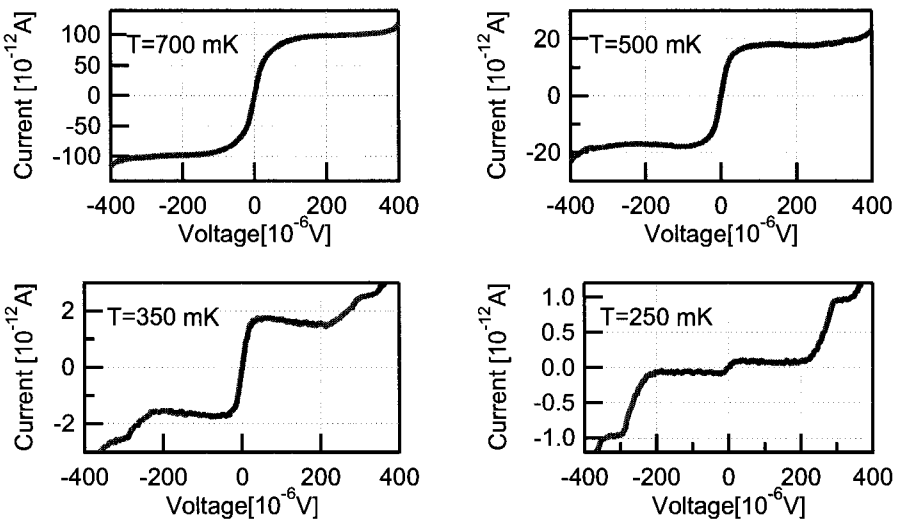

Figure 6.5: Measured IV curves shown with BCS theory plots showing excellent agreement in both magnitude and shape.

including thermometry, current standards, quantum computing and photon detectors. Quantitative agreement with BCS theory is the definitive way to demonstrate the necessary filtering, supercurrent suppression, and ideality of the overall junction parameters requisite to many of the above applications. The graphs below show the current-voltage characteristic of a small SQUID junction. It was fabricated at NASA Goddard with all the components necessary for photon detection. The junction was coupled to a niobium antenna as well as a gold quasiparticle trap on the counter electrode to prevent back-tunnelling. The SQUID loop area was 4 μm^2, which implies that the first supercurrent null should occur with a magnetic field of 300 μT applied perpendicular to the the device.

Figures 6.5 and 6.6 show the measured subgap current for a particular detector junction that was measured in the Kelvinox dilution refrigerator. The normal state resistance was 92 kΩ and the measured gap was 225 μV. Figure 6.5 shows fits to BCS theory for the quasiparticle current measured with the supercurrent fully suppressed. There are, in general, three free parameters for the fit, R_n, Δ, and temperature. Because both R_n and Δ can be measured directly from the broad IV characteristic, the only fit parameter was temperature. The fit temperature reproduced the cryostat's thermometry reading at few percent level, demonstrating both ideality of the junctions as well as the intrinsic accuracy of subgap currents for determining the quasiparticle temperatures. For temperatures above 500 mK, the fit gap began to reduce slightly in a manner consistent with the temperature dependence of the gap also predicted by BCS theory. The range of the fit was from $\pm$200 μV. A generic feature of all tunnel junctions measured in this work is a marked increase in subgap current about 1 Δ. While this structure is not contained in the BCS theory fit, a likely

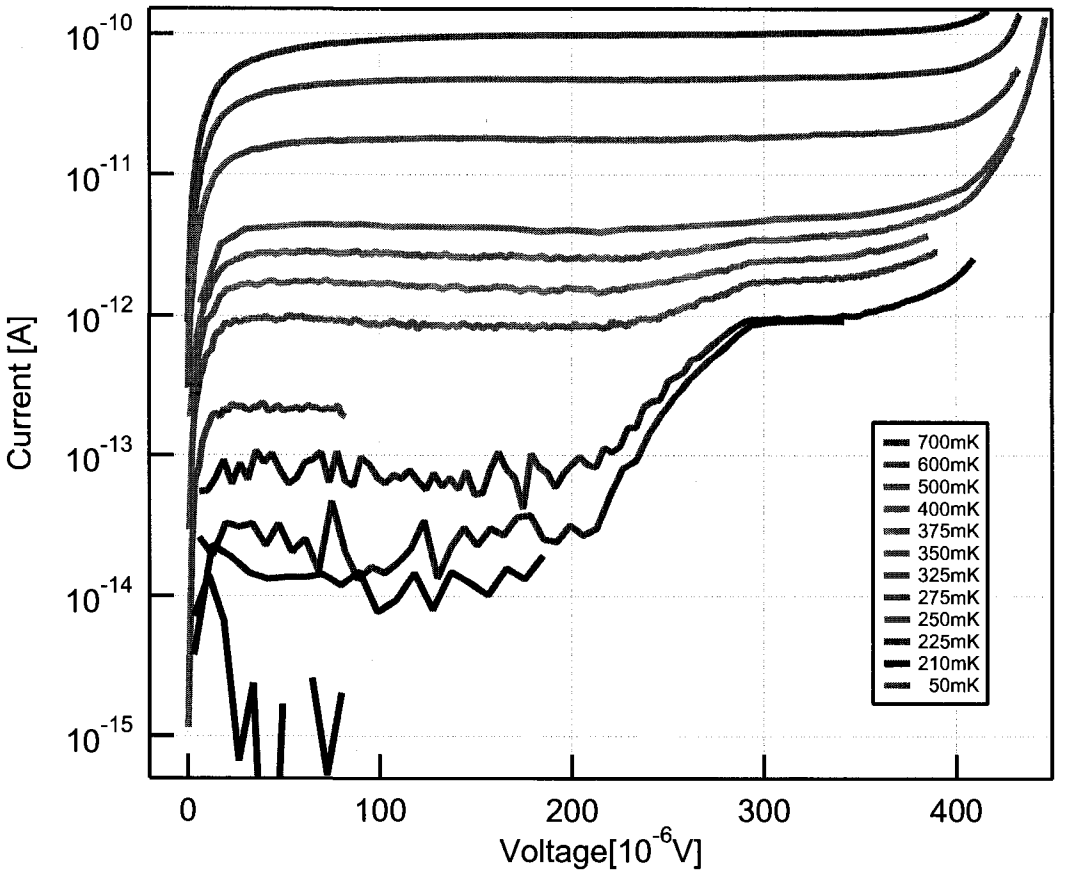

Figure 6.6: Temperature dependence of the quasiparticle current in SIS junction with Δ=225 μV and R_n=92 kΩ.

explanation is higher order processes within the junction that allow quasiparticle currents to flow despite insufficient bias voltage to exceed the $2\Delta/e$. For example, electron-like quasiparticle currents at voltages less than $2\Delta/e$ can be reflected as a hole-like quasiparticle current. This tunnelling process is 2nd order in the tunnelling probability, but can explain the temperature independent current plateau. In fact, just as the normal state resistance gives information about the average tunnelling probability per channel, this current is proportional to the average of the probability squared. The current below 1 δ continues to scale with the temperature perfectly to the degree that the current is still measurable. With considerable averaging it was possible to put a 1 fA bound on the current at 50 mK. This bound continued to drop with longer averaging, but had proven that the dark current could be made arbitrarily small. There was no apparent limitation on the ability to suppress I_c, again the only limitation was averaging longer enough to see if if it was well suppressed.

These dilution refrigerator measurements are definitive proof that the dark current can be reduced

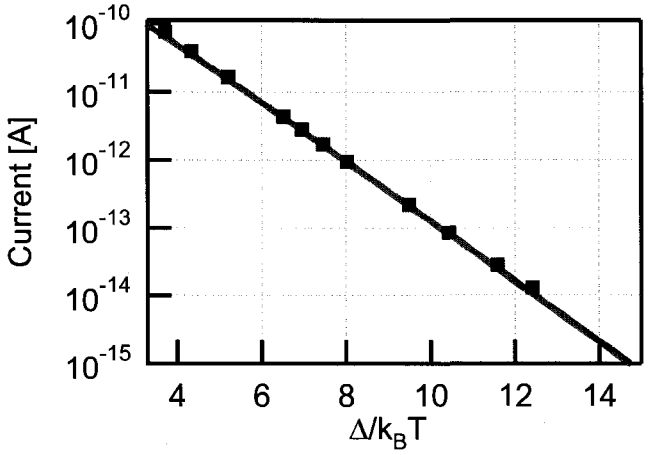

Figure 6.7: The subgap current measured at V=50 μV as a function of temperature. Data agrees with BCS predictions over more than four orders of magnitude in current.

by over six orders of magnitude from the critical current. This excludes nonidealities such as ohmic leakage at the GΩ level. As this dark current is a direct probe of the quasiparticle temperature, it represents primary thermometry on electrons in the detector. This demonstrates the ability to effectively cool well below ^{3}He temperatures, without excess self-heating or thermal decoupling from the cryostat. While this behavior certainly benefits from the very high normal state resistance of the junction, it shows a proof-of-principle for extremely low leakage currents in aluminum tunnel junctions.

6.4 Conclusion

In conclusion this work has measured the subgap currents in a wide variety of aluminum tunnel junctions. The junctions measured throughout this thesis work varied in resistance, gap, and geometry. Several conclusions may be drawn from the data. While the smallest junctions give the most ideal supercurrent suppression and lowest current noise, their large R_n would imply both slow tunnelling times and an earlier onset of of saturation in the photoresponse. Conversely, the largest area junctions were prone to incomplete supercurrent suppression in both the SQUID and single junction geometries. This leads to excess dark current above their already-large thermal current. These junctions, however, offer the ability to handle much larger photocurrents. Lastly, the larger junction are not nearly as fragile as their smaller counterparts, which can be extremely sensitive to electrostatic discharge. All of these factors imply that the optimum junction size would depend on the specific detector requirements for a given application. Overall, all aspects of the tunnelling currents are well-understood and thermal quasiparticle currents can remain the only contributing

factor even in the extreme limit of ultra-small area junctions and dilution refrigerator temperatures.

Chapter 7

Single Electron Transistors as Current Amplifiers

"The engineer who embarks on the design of a feedback amplifier must be a creature of mixed emotions."

–Hendrik W. Bode

This chapter will present the theoretical background and experimental results for measurements conducted on single electron transistors and their use as current amplifiers. The overall goal of this thesis work is to demonstrate an extremely sensitive photon detector. This detection is comprised of two important parts. First, there is the transduction, where the STJ converts incident photon power into excess current through the junction. The second, equally important, step is to amplify and measure that current with as little additional noise as possible. Ideally, this current amplifier would be optimized for the impedance of the detector, have low noise, low input capacitance, large bandwidth, and be able to multiplex in a way that would allow for readout of many pixels at once. In principle, a properly configured RF-SET can simultaneously meet all of these requirements (Schoelkopf et al., 1999).

The single electron transistor is the world's most sensitive charge amplifier, but it was only with

the advent of the RF-SET that this electrometer possessed the bandwidth necessary to achieve the best sensitivity (Schoelkopf et al., 1998; Aassime et al., 2001; Brenning et al., 2006). The radio frequency readout simultaneously provided a straightforward way in which to multiplex the readout of many devices in the frequency domain (Stevenson et al., 2002). The nearly infinite input impedance of the SET means that it can be capacitively coupled, on chip, to monitor the voltage drop across the STJ. When combined with a large bias resistor, this voltage can be used to infer the current through the junction. Because the SET uses the same aluminum tunnel junctions as the detector, there is little added complexity to making both detector and readout with the same e-beam lithography on the same chip. In this way, this method avoids the large number of wires, large input capacitance, and limited bandwidth of FET amplifiers. In the end, the resonant, "tank," circuits of many RF-SETs could be coupled to a single, broadband, HEMT amplifier sitting at 4 K. While the multiplexing is certainly one of the biggest advantages of the RF-SET readout, this work focuses on demonstrating the single pixel performance. In order for an RF-SET to be a good current amplifier is should have the following characteristics: a normal state resistance greater than a resistance quantum, a large charging energy, and good RF impedance matching in order to ensure that it will be a sensitive electrometer. For this charge sensitivity to correspond to a low current noise, there must also be a large, cryogenic bias resistor and large capacitive coupling between the SET and the detector. Lastly, because the SET, like the SQUID, has a periodic response function, stable feedback will be necessary to increase the linearity, dynamic range, and stability of the measurement.

In addition to discussing the physics behind the SET, this chapter will motivate why it is ideally suited to measure the photocurrent of an STJ. It will detail how an SET can be configured as an RF-SET in order to exploit the full bandwidth and sensitivity intrinsic to SET (Schoelkopf et al., 1998). Experimentally, this work begins by characterizing the DC performance of many different SETs in a pumped ^{3}He system, in both the superconducting and normal state. Some of these SETs were then configured as RF-SETs in order to directly verify their high frequency sensitivity. Unlike many applications of the SET such as charge qubits (Lehnert et al., 2003) or electron counting (Love, 2007), the emphasis in not on the charge sensitivity, but rather the voltage sensitivity. Thus, much of the characterization was to verify that increasing the gate capacitance did not adversely affect the overall performance of the SET. With successful demonstration of good voltage sensitivity, the goal became to continue work started in the Schoelkopf lab by a previous postdoc Ken Segall to integrate the SET in stable feedback to form a transimpedance amplifier (Segall et al., 2002). Ultimately, this portion of the thesis work culminated in measurements of a fully integrated RF-SET as an on-chip current amplifier, used in feedback, to faithfully readout the subgap current of a detector junction. The quantitative results for the figures of merit, such noise temperature, current sensitivity and rise time, are shown to be competitive semiconductor technology, but without several of the performance drawbacks that make large format arrays with FET readouts prohibitive.

7.1 Current Amplifier Technology

As discussed in Chapter 4, the noise temperature of an amplifier is optimized for a particular impedance at its input. Only this special value for the impedance of the load optimally balances the imprecision in the measurement of the quantity of interest and backaction of the amplifier on the device. This optimum noise impedance of the amplifier is one of many important factors when choosing how to readout the signal from the detector. For example, in traditional semiconductor amplifiers, bipolar transistors are suited for low impedances up to of order 100 kΩ, while junction gated field effect transistors (JFETs) can have noise impedances from 100 kΩ to well over 100 MΩ at low frequencies. Typical semiconducting instrumentation amplifiers are cheap, reliable, and readily achieve noise temperatures less than 1 K, even when operated at room temperature (ref for example Burr-Brown INA110). A carefully optimized JFET can be used to readout a high impedance cryogenic detector with a noise temperature of less than 100 mK. For example, microcalorimeter groups report using a commercial JFET (Interfet NJ14AL) to readout 10 MΩ X-ray microcalorimeters with an amplifier voltage noise of 3 nV/$\sqrt{Hz}$ and current noise of <50 aA/$\sqrt{Hz}$ (Porter et al., 1999). For the cryogenic detector applications, it is not the sensitivity nor the noise temperature that is the issue; it is the fact that these FETs cannot operated at temperatures less than 100 K. Because each detector pixel needs to be connected to its own amplifier, the heat load on the cold stage due to the wiring limits the number of pixels for the entire experiment. Furthermore, the added capacitance of the wiring limits the bandwidth and makes the measurement susceptible to vibrational, or microphonic, noise. While most application do not necessarily require fast response time, this limited bandwidth would make it difficult to multiplex in either the frequency or time domain. For space-based applications, the power dissipation of the FETs also becomes a serious issue. It is for all of these reasons that cryogenically compatible amplifiers like the SET or SQUID are a natural choice for the detector community.

The SET and SQUID are two types of "quantum" amplifiers. They are quantum in the sense that their properties drastically changed by the influence of a single electron or single flux quantum, respectively. In this way, they are electromagnetic dual of each other (Devoret and Schoelkopf, 2000). The former is intrinsically suited for high impedance applications and the latter for low impedances. While both require cryogenic temperatures to achieve their optimal performance, as discussed above, this requirement is actually one of their most sought-after features. For detectors that already require low temperatures and nano-lithography, these kind of amplifiers offer a natural way that the detector and readout can be fully integrated on the microchip level. SQUID amplifiers have rapidly matured to become a standard readout technology for many types of detectors (Clarke and Braginski, 2004). They routinely achieve μK noise temperatures at audio frequencies with closed-loop feedback operation to give large dynamic range and excellent stability. Time domain multiplexing has been demonstrated for arrays of TES bolometers and integrated with detector arrays with as many as

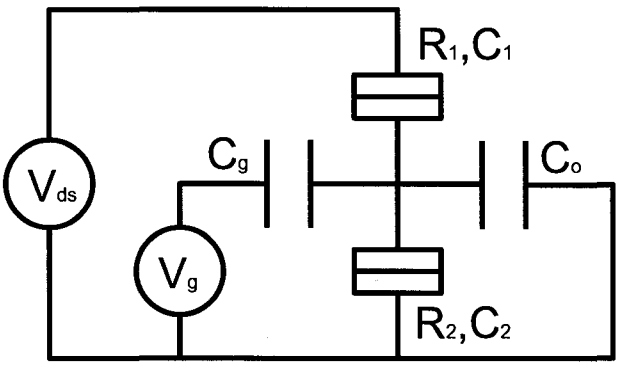

Figure 7.1: Circuit diagram of a single electron transistor. The rectangular symbols denote two small capacitance tunnel junctions in the normal state, which are characterized by capacitances (C_1,C_2) and resistances (R_1,R_2). C_o represents the unavoidable parasitic capacitance to ground.

1280 pixels (Woodcraft et al., 2007). Microwave frequency domain multiplexing schemes for SQUIDs are also current being pursued (Irwin and Lehnert, 2004; Lehnert et al., 2007; Mates et al., 2008). Despite all these attributes, the current noise of a SQUID would be completely unacceptable for coupling to a high impedance detector such as an STJ. It is exactly this niche in which the SET is the natural choice. Unfortunately, the elegant electromagnetic duality between SQUIDs and SETs does not necessarily imply equal ease of use or engineering feasibility. Many of the same benefits that have been demonstrated for SQUIDs can, in principle, be achieved with SETs. The reality is that SETs as a detector readout technology has not enjoyed the same popularity or advanced to the same engineering sophistication. While part of the reason for this disparity is due to the manpower and money pursing each of these options, there are practical difference between these two quantum sensors that affect their performance. For example, 1/f noise that tends to plague charge measurements up to MHz frequencies, only appears in the sub-Hz regime for SQUIDs. Furthermore, the natural energy scale for a SQUID, the Josephson energy, can easily be made arbitrarily large; while the corresponding scale for an SET, the charging energy, requires ultra-cold temperatures or extreme lithography for it to be larger than the operating temperature. Even with these issues in mind, the SET remains a not only viable, but attractive option; as will be demonstrated by many of the experimental results of this chapter.

7.2 SET Physics

At the heart of all single electron devices is the effect known as Coulomb blockade. This refers to the fact that the transport properties of a system will be modified when one node of the circuit has small enough capacitance that electrostatic energy for adding an additional electron is no longer negligible. While this effect has been studied in many different system as early as the 1950's (Gorter, 1951), this work deals exclusively SETs fabricating by placing two aluminum tunnel junctions in series to

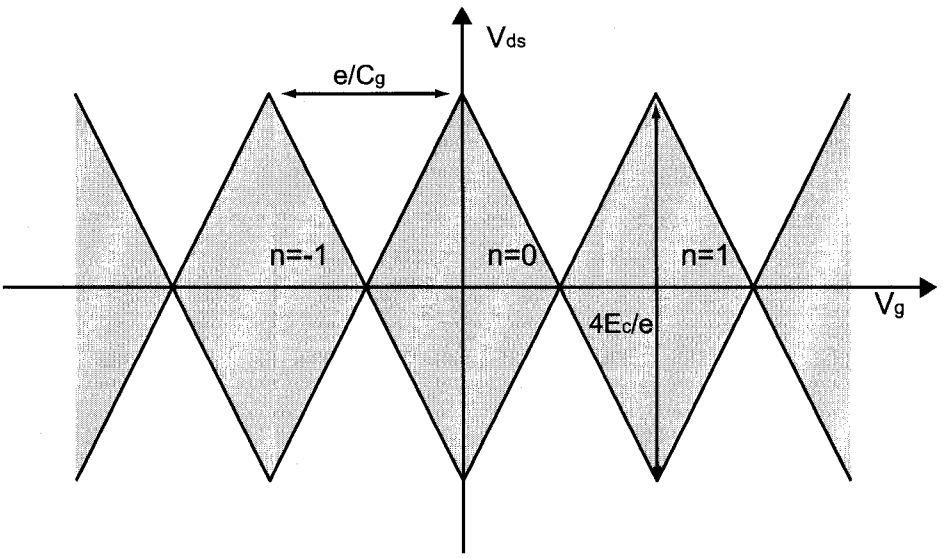

Figure 7.2: Energy diagram, or charging diamond, for a single electron transistor in the normal state.

form a small capacitance island between them (Fulton and Dolan, 1987). The current through the junctions is modulated by the potential of a third, gate electrode that is capacitively coupled to this center island. In this way, it forms a fundamental version of a transistor in which the gate charge necessary to turn on or off the drain-source current is merely a small fraction of an electron. In order for this to occur, there are several requirements that must be met. To begin, the energy scale for adding or subtracting a single electron to or from the island must be greater than all other sources of fluctuations in the system. This is the charging energy, E_C, and it is determined solely by the total capacitance of the island to the rest of the world, C_Σ.

$$E_C = \frac{e^2}{2C_\Sigma} \tag{7.1}$$

Because the tunnel junctions that isolate the island also have a very high specific capacitance, lithographic limitation on the size of the junctions will set the limit on how large this charging energy can be. While standard e-beam lithography can readily produce junctions with an area of $(100\ \text{nm})^2$, the capacitance of these junctions alone tend to limit the C_Σ to 1 fF, which implies an E_C of about 1 K. Thus, cryogenic temperatures will be necessary to ensure that $E_C \gg k_B T$ so that thermal fluctuations do not completely degrade the charge localization. Likewise, if the quantum fluctuations of charge are larger than the charging energy, these charging effects would not be observable at any temperature. This requirement sets a limit on the resistance of the tunnel junctions.

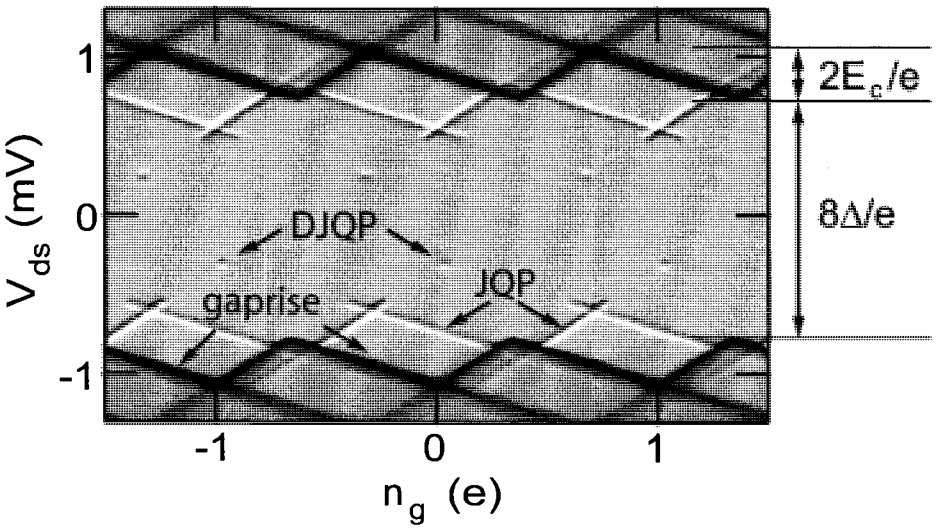

Figure 7.3: This is a superconducting charge diamond. The grey scale is reflected RF voltage, which is monotonically related to the differential resistance of the SET. This graph was adapted from Benjamin Turek's thesis (Turek, 2007) in order to clearly show the prominent features and energy scales of the SET.

$$R \gg R_K = \frac{h}{e^2} \simeq 25.8\ k\Omega \tag{7.2}$$

Conceptually, this is a result of requiring that the RC time of the junction is much longer than the timescale given by the uncertainty principle and the charging energy. With these requirements in place, the conductance through the drain-source lead of the SET can be periodically modulated with the gate voltage as an addition electron is pulled onto or off of the center island. To be more precise, one can write down the electrostatic energy cost of an electron tunneling through either junction. To begin, we will consider an SET in the normal state at zero temperature. In this case, the only energy available to the system is from the two bias voltages: the drain-source voltage, V_{ds}, across the two junctions and the gate voltage, V_g, applied to the capacitively coupled gate electrode. Thus, in order for it to be energetically allowed for electrons to tunnel, the potential across each junction much exceed the charging energy. Following Figure 7.1, the region of blockade is bounded by the following equations:

$$e\left(n-\frac{1}{2}\right) < C_1 V_{ds} + C_g V_g < e\left(n+\frac{1}{2}\right) \tag{7.3}$$

$$e\left(n-\frac{1}{2}\right) < \left(C_2 + C_o + C_g\right) V_{ds} - C_g V_g + < e\left(n+\frac{1}{2}\right) \tag{7.4}$$

where C_1 and C_2 are the capacitance of the first and second junctions and n is the integer number of electrons on the island. The fact that these equations are not symmetric with respect two the two junction is simply an artifact of the single-ended bias scheme that is typical for our measurements.

Plotting these equations as a function of the two voltages produces the "charging diamonds" where there will be zero conductance at zero temperature as sketched in figure 7.2. The diamond represents a threshold beyond which current can flow. By measuring this charge diamond, one can determine several of the parameters of the transistor. The periodicity in gate voltage is a direct measure of the gate capacitance: C_g=e/V_g. The height of the diamond is a measure of the charging energy: E_C=2eV_{ds}. The slope of the two sides of the diamond measures the ratios C_1/C_g and $(C_2+C_o+C_g)/C_g$.

The full transport properties of the SET at finite temperature can be calculated using orthodox theory. Briefly stated, orthodox theory uses first order perturbation theory to calculate the tunneling rates through each junction taking into account the appropriate number of charge states given the bias and temperature. This theory neglects the ability for charges to simultaneously tunnel across both junction leaving the overall energy configuration unchanged. This "cotunneling" becomes more suppressed as the resistance of the junctions become much greater than a resistance quantum. A much more detailed and rigorous description of orthodox theory is given in the following references (Grabert and Devoret, 1992; Averin and Likharev, 1990).

So far this description is for non-superconducting tunnel junctions. While superconductors are not required in order make single electron transistors, it has been found that superconducting single electron transistors offer improved charge sensitivity (Schoelkopf et al., 1998). Just as tunneling currents through SIS junctions were calculated in chapter 2, similar calculations can be used to predict the IV characteristic of the superconducting SET. The gap in the density of states of the superconducting electrodes will prevent any pure quasiparticle currents from flowing until the bias voltage exceeds 4Δ/e. The sharp onset of gaprise currents due to the singularity in the density of states in modulated periodically with the gate voltage. Thus, this threshold varies from occurring at V_{ds}=4Δ/e (for minimum blockade) to $V_{ds} = (4\Delta + 2E_C)$/e (for maximum blockade). This feature is often one of the most sensitive bias points for the SET. While there are many other processes that give rise to structure in the superconducting charge diamond, there are two particularly important bias points which are worth mentioning here. They occur at bias voltages less than 4Δ/e and are processes that involve the exchange of Cooper pairs in addition to quasiparticles. The first prominent feature is known as the Josephson quasiparticle current or JQP feature (Fulton and Dolan, 1987; Pohlen, 1999). This is a cyclic process whereby a Cooper pair resonantly tunnels across one of the junctions, then two quasiparticles separately tunnel to return the island to the original electrostatic configuration. The other process is known as the double Josephson quasiparticle current, or DJQP. It occurs only if $E_C > 2\Delta/3$. In this case, there will be a doubly resonant process allowed in which a Cooper pair and a single quasiparticle tunnel across each junction. Both of these subgap features can have very large gain due to their abrupt onset in the IV characteristic. However, for the SETs used in this work, the large gate capacitors limited the charging energy such that most did not possess a DJQP feature. In the end, the gaprise was almost always used as a bias point because it allowed

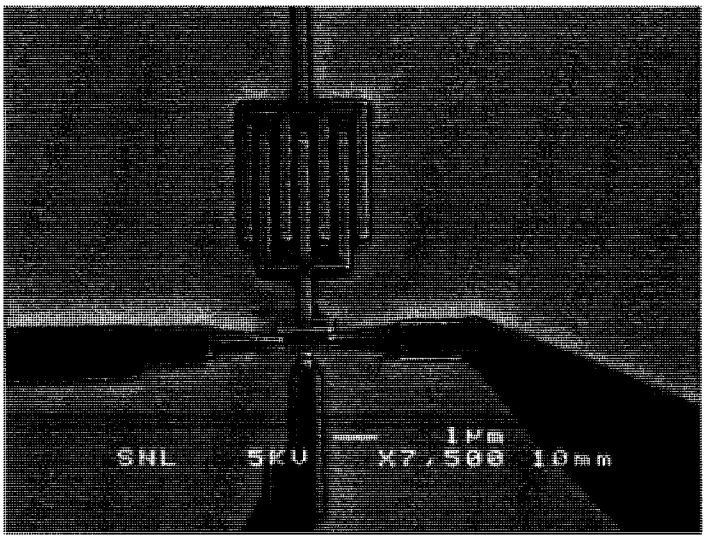

Figure 7.4: SEM image of SET fabricated at NASA Goddard with an interdigitated-finger gate capacitor of 450 aF.

for a larger dynamic range and increased sensitivity due to larger carrier in an RF measurement.

7.3 SET Design and Layout

As outlined above, there are many requirements for making an optimal SET. Unfortunately, many of these requirements are actually conflicting. For example, large resistance is required to ensure the quantization of charge. But if this resistance is unnecessarily high it will lead to a small absolute change in drain-source current of the SET. In other words, the charge to current transduction will be smaller. Furthermore, this resistance is what sets the output impedance of the SET as an amplifier. High impedances will always imply slower response times (in both DC and RF-SETs). In the case of the RF-SET, there will also be greater difficulty in impedance matching to 50 Ω. Another trade-off in the design of the SET is in the capacitance. One obviously wants to minimize the total capacitance of the island so that the charging energy is as high as possible. However, the gate capacitor should be made large in order to maximize the fraction of the charge detected by the SET. The voltage sensitivity of the SET is given by:

$$v_n = \frac{q_n e}{C_g} \tag{7.5}$$

where q_n is the charge sensitivity in units of $[e/\sqrt{Hz}]$. So one might readily give up some charging energy for better voltage sensitivity. As an amplifier, it is not hard for the SET to have power gain simply because the input impedance (through the gate capacitor) is much larger than the output impedance (through the drain-source lead). However, it is only with a gate capacitor that is larger

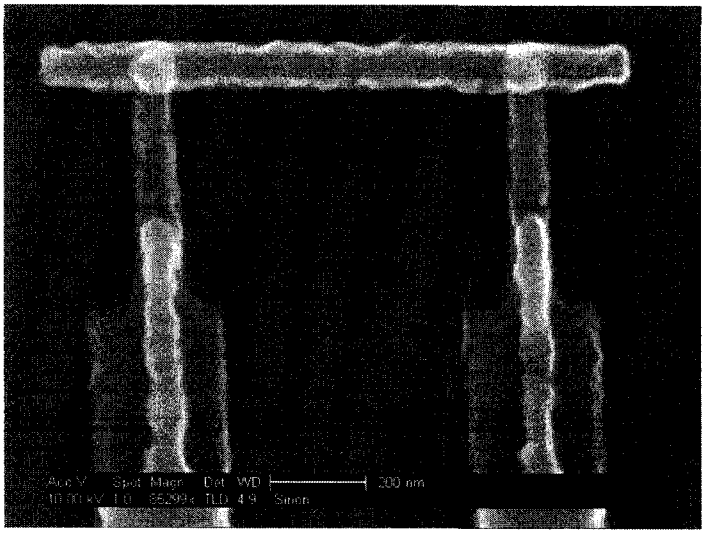

Figure 7.5: SEM image of SET fabricated at Yale. A double angle evaporation is used to create two $Al/AlO_x/Al$ tunnel junctions in series. These junctions have a designed area of 80 nm by 80 nm.

than the junction capacitance that the SET can have true voltage gain. Such SETs have been studied using both overlap and interdigitated-finger capacitors at NIST (Zimmerli et al., 1992) and Delft (Visscher et al., 1995), and SETs in this work are of similar design. In the extreme limit, very strong coupling between the STJ and the SET could lead to unwanted backaction from the SET breaking excess quasiparticles in the STJ. A final consideration is the overall reproducibility of the fabrication. Extremely small junctions made at the resolution limits of the lithography will be unacceptable if the resulting junction sizes are unpredictable. All these factors must be taken under consideration in the final design of the SET.

Because the STJ itself will require temperatures of order 250 mK or below, this implies that the charging energy should be of order 1 K, but does not need to be much more than that. This immediately limits the size of the gate capacitor to 1 fF if the parasitics and the junction capacitance were in fact negligible. In reality, a feasible design is to have junctions with an area of less than 0.01 μm^2 so that two junctions contribute about one quarter to one half of the total capacitance. It is also important to realize that as the size of the island is increased in order to achieve large gate capacitances the parasitics will also directly increase. For our layout, it was found that the parasitic capacitance to ground was of order 50% of the large gate capacitor with interdigitated fingers. This could be improved by using overlap capacitors, but these parasitics did not warrant this added complexity in fabrication. Thus, the final design that was fabricated by our collaborators at NASA Goddard add arrays of SET's with varying gate capacitor sizes and hence charging energies. The junctions were 80 nm by 60 nm each and contributed a total of about 200 aF to C_Σ. In general, the normal state resistances were intended to be 100 kΩ per junction, but varied from chip to chip from

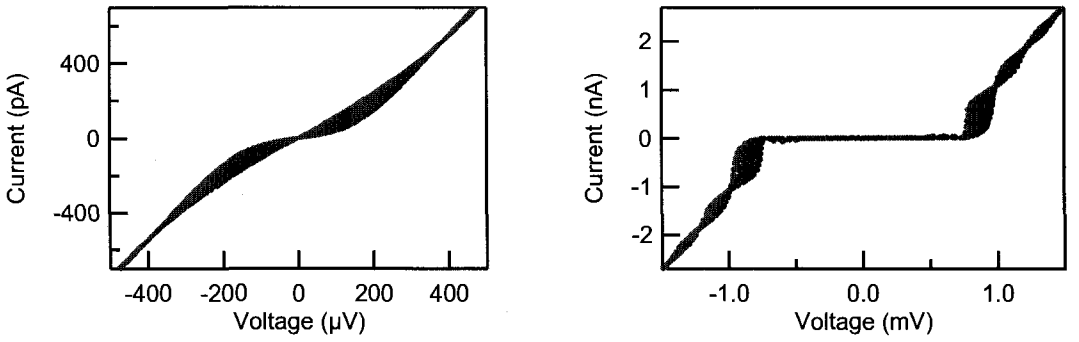

Figure 7.6: IV characteristic of SET19, in the normal (left) and superconducting (right) state at T=260 mK. The gate voltage was modulated during each trace so that the areas with gate dependence can be seen. This SET had R_N=425 kΩ, Δ=191 μV and E_C=1.2 K.

100 kΩ to 1 MΩ depending on both the junction size and the exact current density. These SETs were then measured in the pumped ^{3}He cryostat in order to determine how results compared to expectations as well as to experimentally find the optimum balance of these design considerations.

7.4 DC Characterization of SETs

Before trying to couple an SET to an STJ, it is important to ensure that the designed SET's have the desired parameters. At room temperature, the only quantity that can be measured with any accuracy is the normal state resistance; the determination of the charging energy, coupling capacitance and superconducting gap can easily be determined at ^{3}He temperatures. This section summarizes the measured values for these parameters as determined from the DC IV curves of the SET's. These measurements test SETs fabricated at NASA Goddard as well as ones made here at Yale.

The left hand side of figure 7.6 shows a typical IV of an SET in the normal state at T=260 mK. A magnetic field of 0.5 T was used to suppress the superconductivity. In order to see the region that modulates with gate charge, the gate voltage was swept at a rate of 2 Hz while the curve was taken. This method will be used throughout this chapter in order to characterize SETs. From the IV curve one can see that the conductance at V_{ds}=0 is modulated from a value of order $1/R_N$ to about 5 time lower. One can clearly distinguish the blockaded region as well as its thermal rounding. In the maximally blockaded state, the voltage intercept of the large bias asymptote of the IV curve is a direct measure of the charging energy (Grabert and Devoret, 1992). Specifically, this offset is equal to $2E_C/e$. While theoretically, this offset should also be present at room temperature, one would need to bias to a voltage larger than k_BT (~25 mV) in order to see it. In general, in order to avoid inadvertently damaging the SETs only voltages of order 1 mV were applied to the junctions at room temperature.

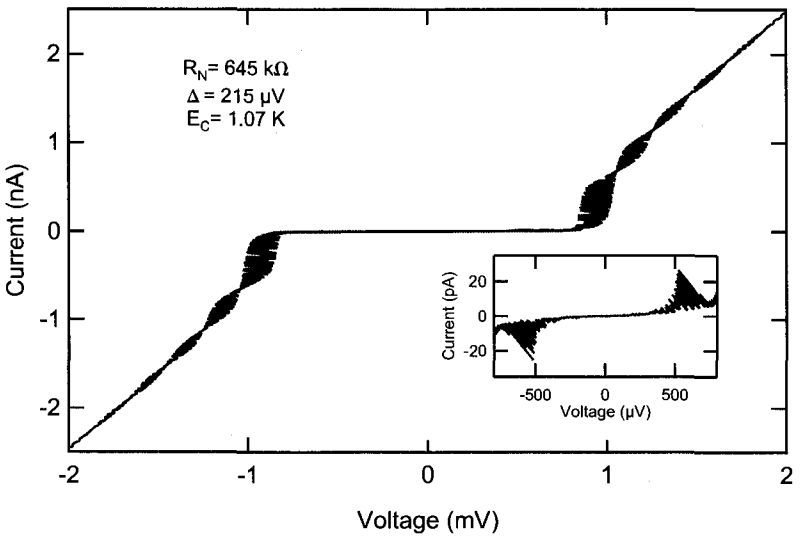

Figure 7.7: IV characteristic of SET02 measured in the superconducting state at 270 mK taken while modulating the gate voltage. The well-defined nodes in the modulation demonstrate the excellent resistance symmetry of the two SET junctions. Their persistence to voltages many times E_C shows that higher-order, cotunneling processes are greatly suppressed as expected for $R_N \gg R_Q$. The inset shows the region of modulation known as the JQP.

If the large magnetic field is removed, and the aluminum tunnel junctions are allowed to superconduct, the effects of the Coulomb blockade are now convolved with familiar SIS tunnel junction characteristics. The right side of figure 7.6 shows the same SET in the superconducting state. The large-scale regions of modulation begin at $V=4\Delta/e$ and their width in voltage corresponds to $2E_C/e$. Figure 7.7 shows a different SET measured in the superconducting state. There is no identifiable supercurrent as expected for this slow DC measurement and such extremely small value for E_J. The largest rise in current occurs at $V=4\Delta/e$ because it is only then that the bias voltage is enough to exceed the gap of both junctions. The voltage of this gaprise is modulated with gate as the threshold is increased from $4\Delta/e$ to a maximum of $(4\Delta+2E_C)/e$. Thus, the location of gaprise gives a direct measurement of the superconducting gap and the width of modulation gives the charging energy. In fact, there will be higher voltage regions of modulation at increasing multiples of the charging energy corresponding to the addition of an integer number of electrons. The degree to which regions of modulation come to precise nodes is a measure of the resistance symmetry of the of the two junctions. Eventually, these regions will fade due to the fact that higher order processes can make the width of the charge states comparable to the charging energy. The degree to which these cotunneling processes will affect the modulation is given by the parameter α as defined by Averin (Averin et al., 1997; Stevenson et al., 2001).

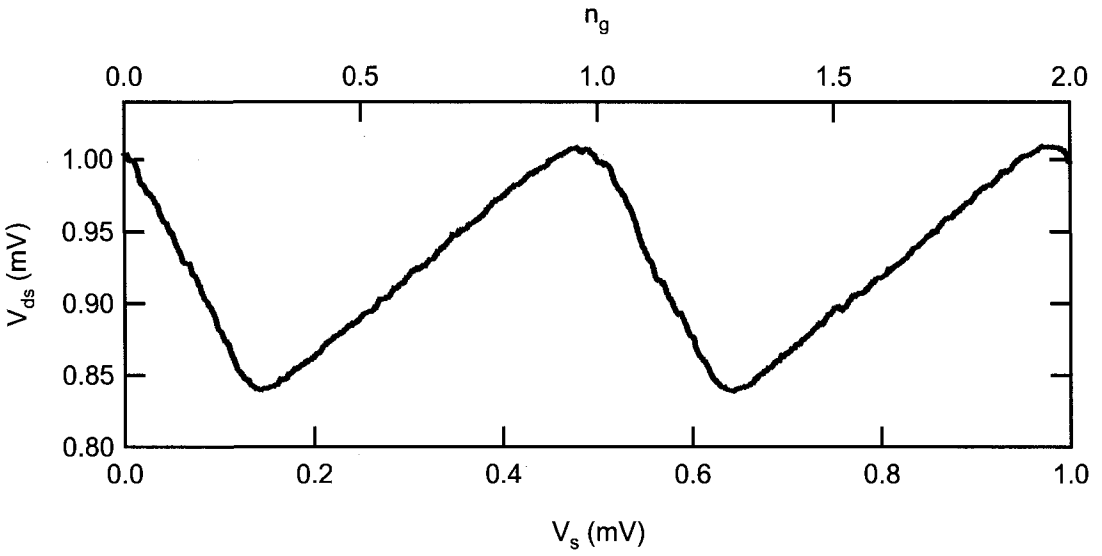

Figure 7.8: This is the DC transfer function of a current biased SET. The periodicity implies a gate capacitance of 320 aF.

$$\alpha = \frac{\Delta}{E_C}\frac{h}{2e^2}\left(\frac{1}{R_1}+\frac{1}{R_2}\right) \tag{7.6}$$

Thus, because of the dependence of α on E_C and R_N, the smallest junctions tend to give the smallest value for α, and hence cotunneling is correspondingly less important.

In order to determine the exact gate capacitance, the SET was current biased at a particular value and the drain-source voltage was measured as a function of gate voltage. The periodicity of this transfer function in gate voltage corresponds to the addition of one more electron to the island of the SET. Thus, one can define $n_g = CgV_g/e$ as the number of additional electrons on this center island. Figure 7.8 shows a typical transfer function for a superconducting SET biased on its gaprise. The slope of the transfer function is the gain of SET. This also demonstrates the need for feedback if one wanted to measure a signal that was larger than a small fraction of an electron on the SET.

The devices showed great uniformity over an entire chip, but did tend to vary between chips. Subsequent SEM imaging after fabrication did not kill the junctions, however an increase the resistance by ~10% was seen. These devices are extremely sensitive to electrostatic discharge. Not surprisingly, they tended to be most vulnerable after wirebonding but before mounting in the cryostat. With these issues aside, the results of this DC characterization were very encouraging. They demonstrated that it is in fact possible to make SET's with large coupling capacitors ($\leq$ 450 aF) while maintaining reasonable charging energies (~1 K). In the next section, it will be discusses how to configure the SET as RF-SET and directly measure their most important property–the sensitivity.

Date	Device	Chip	Made by	$R_N(k\Omega)$	$\Delta(\mu eV)$	$E_C(K)$	$C_g(aF)$	α
05/02	SET01	SQPC-D1-24	NASA	950	219	1.85	–	0.04
05/02	SET02	SQPC-D1-27	NASA	645	215	1.07	327	0.09
06/02	SET03	SQPC-D1-27	NASA	227	215	0.67	320	0.42
03/03	SET04	SQPC-23-C11	NASA	1570	225	3.50	180	0.01
07/03	SET05	RSL001	Yale	139	191	0.93	21	0.44
	SET06	RSL001	Yale	77	191	1.10	17	0.67
09/03	SET07	LF030827	Yale	94	190	0.17	13	3.56
	SET08	LF030827	Yale	97	190	0.17	–	3.45
	SET09	LF030827	Yale	90	190	0.20	–	3.16
	SET10	LF030827	Yale	81	190	0.15	–	4.68
	SET11	LF030827	Yale	89	190	0.20	–	3.19
	SET12	LF030827	Yale	106	190	0.18	–	2.98
10/03	SET13	RSL019	Yale	307	191	0.64	36	0.29
	SET14	RSL019	Yale	331	191	0.72	15	0.24
	SET15	RSL022	Yale	179	191	0.35	–	0.91
	SET16	RSL019	Yale	282	191	0.52	–	0.39
	SET17	RSL022	Yale	278	191	0.52	–	0.40
	SET18	RSL019	Yale	228	191	0.43	–	0.58
12/03	SET19	RSL037	Yale	425	191	1.20	–	0.11
	SET20	RSL037	Yale	575	191	1.60	–	0.06
	SET21	RSL037	Yale	3400	191	3.10	–	0.01

Table 7.1: This table summarizes the DC characteristics of the SETs measured in this thesis.

7.5 RF-SET Charactrerization

One unifying theme of this thesis is that while DC measurements are the traditional method for exploring the transport properties of tunnel junction devices, incorporating radio frequency or microwave measurements can provide much of the same information with many added benefits. The RF-SET is a prime example. This section will introduce how a SET can be configured as an RF-SET. It will also present representative measurements that are necessary in order to characterize the overall performance.

At its heart the RF-SET is the integration of radio frequency reflectometry with a tradition single electron transistor. As seen from the DC characterization, the current through the SET (and hence dynamic resistance) is a sensitive function of the gate charge. So there are many ways in which this can be biased in order to form an electrometer. The simplest way is current bias the SET through a large bias resistor and measure the voltage change as gate charge modulates the feature of interest. Conversely, the SET can, instead, be voltage biased and the current becomes the quantity that is measured. This is accomplished with a transimpedance amplifier where the measured voltage drop across the device is fedback to the bias voltage. In the limit of large gain, this feedback loop will provide a voltage bias even in the case of a large bias resistor. In order to avoid the effects of low frequency noise and drift, one often applies a lock-in style measurement where a small AC signal

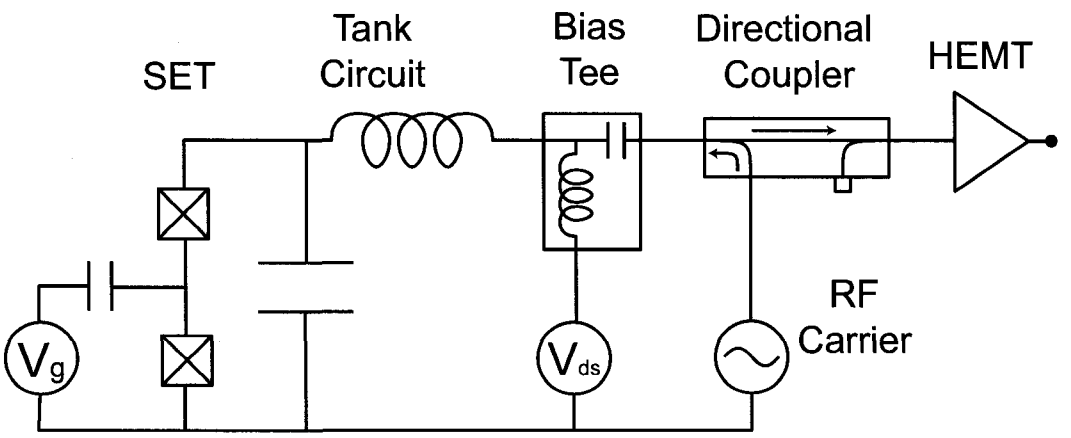

Figure 7.9: Circuit diagram for an RF-SET measurement. The SET is embedded as the damping element in a RF resonant circuit. An RF carrier tone is coupled to this tank circuit and the reflected signal is amplified at 4 K by a state of the art HEMT amplifier. A cryogenic bias tee allows for simultaneous RF and DC measurements.

is applied at audio frequencies and the output is measured synchronously in a narrow band around the chosen AC frequency. In this way, the quantity that is now measured is differential resistance instead of current or voltage. This contains all of the same information as the DC IV characteristic up to an overall shift in current or voltage. RF reflectometry may be seen in a completely analogous way. A small bias is applied at radio frequencies and, as seen in chapter 4, the degree to which this signal is reflected or absorbed by the device is a sensitive measurement of it dynamic resistance. This is because from the standpoint of the tunnel junction, this RF bias is still very slow compared to all the relevant time scales in the problem. This implies that the impedance at DC or audio frequencies is essentially the same as what the microwaves "see."

In order to maximize the coupling and measurement of the high frequency probe it is necessary to impedance match the SET to the input impedance of standard microwave cables and amplifies. Unlike the active impedance transformation of an FET (where the output impedance can be made much less than the input impedance), the transformer takes the form of a passive LC resonance. This ensures that power matching occurs and that information is not wasted. Now the "bias" resistor in the problem is not a physical $\sim$1 MΩ resistor, but the 50 Ω input resistance of the amplifier. Using a bias-T, the RF and DC signals can be separately applied and measured so that one can perform all the same measurements as a DC SET concurrently with RF techniques. This also implies that an RF-SET can be perfectly voltage biased at DC while maintaining an impedance match at the relevant RF frequencies.

As a charge signal is capacitively coupled to the SET, its differential resistance at a sensitive bias point varies from well below to well above its normal state resistance. This will in turn directly influence the loading of the resonance resulting in amplitude modulation of the carrier. So now the

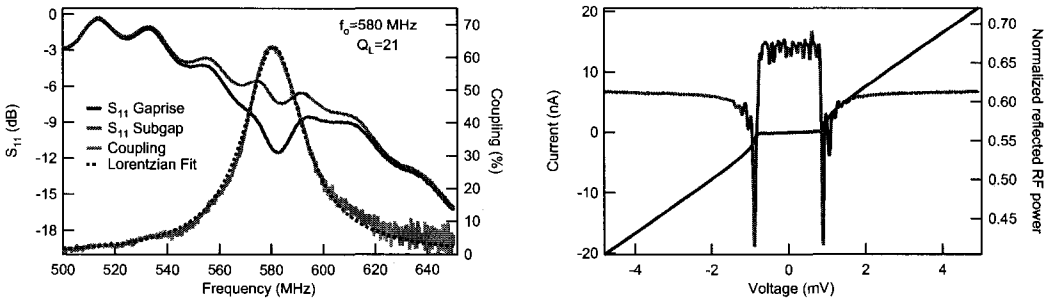

Figure 7.10: The left graph shows the result of a network analyzer measurement for SET03. The SET is well coupled to the HEMT amplifier over 30 MHz of bandwidth. The righthand graph shows the bias voltage dependence of the the reflected power on resonance. This shows that the SET is best coupled (smallest reflected power) on the gaprise, where the SET has the lowest dynamic resistance.

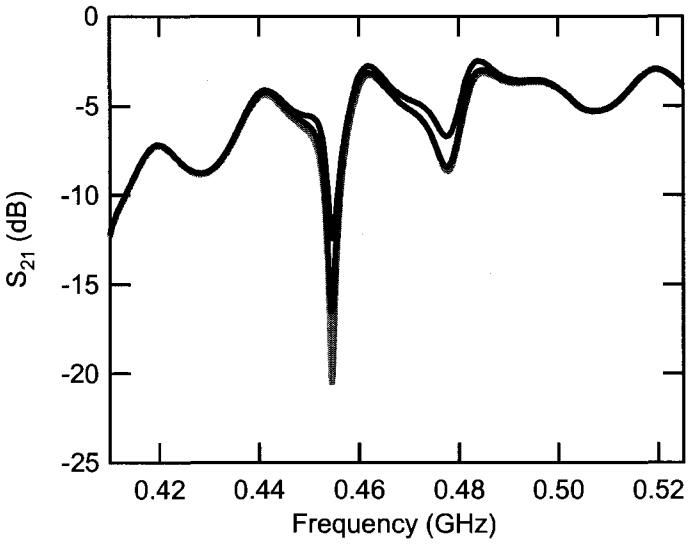

Figure 7.11: This is a measurement of the reflected RF power from two SETs that have been multiplexed in the frequency domain. Each SET has its own DC bias and tank circuit with resonance frequencies of 455 and 480 MHz. Each trace is a different bias point on one of the SETs so that it modulates the reflected power only near its resonance. This is both a demonstration of the multiplexing potential for the RF-SET as well as a useful method to characterize two RF-SETs in a single cryogenic experiment.

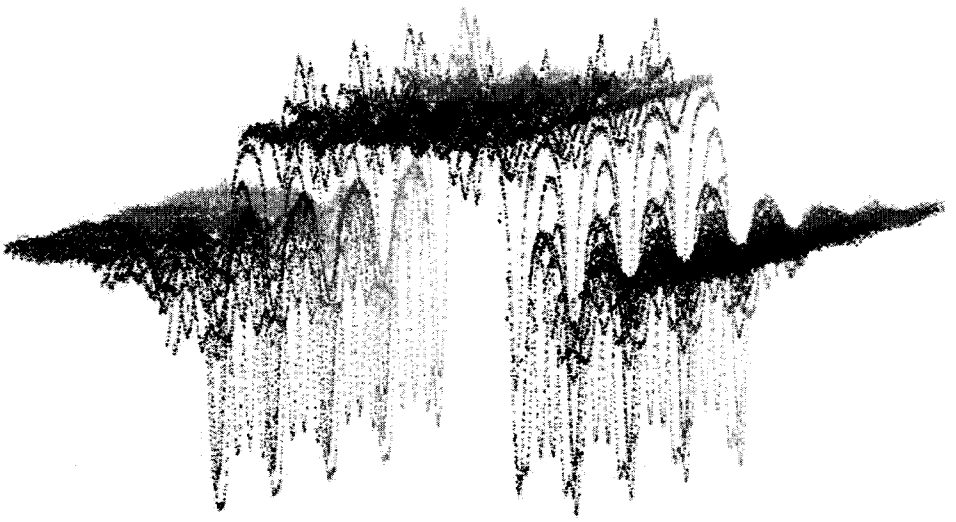

Figure 7.12: This graph shows typical RF-SET charge diamond as a 3-D plot. While the Z-axis is the reflected power, it is a close approximation for the differential resistance of the SET at each bias point.

quantity that is measured is not DC current, voltage or resistance, but the reflected RF voltage. It is this quantity that will plotted and discussed throughout the rest of this chapter. While this could be used to reconstruct the differential resistance and IV characteristic of the SET, it is sufficient to note that it is a quantity that varies monotonically with the dynamic resistance of the SET. Now the transfer function of the SET is from gate charge to RF voltage. This provides a precise look-up table from which one can perfectly quantify the transduction from charge to RF signal of the electrometer. This transfer function is also self-calibrating in that the periodicity is direct measure of one electron coupled to the island of the SET. This allows for precise and accurate characterization of the gain and sensitivity. It is the sensitivity where the RF-SET is superior to its DC counterpart– not because the HEMT amplifier is less noisy than an FET, but because only the RF-SET possesses the necessary bandwidth to measure at frequencies where intrinsic 1/f fluctuations do not dominate the output noise of the electrometer. Finally, for detector readout, the ability to frequency domain multiplex is almost as important as the sensitivity. For all of these reasons, since its invention, the RF-SET has been seen as a natural choice for amplifying the signals from high impedance detectors (Schoelkopf et al., 1999).

Figure 7.9 shows the basic experimental configuration for an RF-SET measurement. With the use of the bias tee, all the usual DC properties of the SET can be measured exactly as outlined in the previous section. The RF characterization begins by using a network analyzer to measure and verify the properties of the resonant circuit. The tank circuit is designed to resonate at a frequency

within the band of the amplifier (300 to 600 MHz) while transforming the impedance of the SET as close to 50 Ω as possible. Because the dielectric properties of the silicon chip as well as the loss of the inductor are quite different at room temperature, the exact resonant frequency is difficult to predict. This is further complicated by the fact that the capacitance of the tank circuit is almost entirely determined by parasitics that can vary from chip to chip. Lastly, the surface mount inductor used are quite close to their self-resonant frequency so that their effective inductance is frequency dependent. Despite all of the factors, one could always design the resonance frequency to be within the octave bandwidth of the amplifier.

Figure 7.10 shows the network analyzer characterization for SET03. The power of the carrier is chosen to be as large as possible without rounding features in the DC IV curve. In this case, the power is on the order of -110 dBm. This corresponds to 700 nV on the 50 Ω side of the transformer. This voltage is transformed up by the tank circuit by a factor of Q resulting in 30 μV across the device. In order to separate which frequency structure is from the SET resonance, the impedance of the SET is varied. This is accomplished simply by biasing at DC on different features within the IV curve. On the gaprise, the impedance is the lowest and usually best matched to 50 Ω. The subgap region has a much higher dynamic resistance that gets over-transformed to well below 50 Ω; this results in almost complete reflection of the carrier even on resonance. The difference between these two curves clearly shows a Lorentzian line shape as expected for the resonance. The center frequency is at the high end of the amplifier band at 580 MHz. The ripple in the spectrum away from resonance is a result of standing waves formed between the SET and the input of the HEMT. Despite the fact that the amplifier is reasonably well input matched, off resonance the impedance of RF-SET has a real component that is untransformed and a large imaginary component due to either the capacitor or inductor, above and below resonance respectively. Fitting to a Lorentzian, this curve shows a loaded Q of 21. From this, one can determine most of the properties of the tank circuit. This loaded Q implies that the inductor and capacitor have an impedance on resonance of Z_{LC}= 2100 Ω. Assuming that the transformation is lossless, this implies that the ideal match would occur when the SET has a differential resistance of ~90 kΩ. The usable bandwidth is the HWHM of the coupling which is about 15 MHz for this device.

Once the resonance frequency is determined that network analyzer can be replaced with a simple signal generator. The reflected signal can then be demodulated either with a mixer or a diode. While the mixer provides more information (both amplitude and phase), usually only the reflected power was measured with either a actual diode or a spectrum analyzer configured to act as one. Figure 7.10 also shows the bias dependence of the reflected power on resonance. This reflected power has all the features that one would see simply by taking the derivative of the IV curve. This is just a reiteration of the fact that the reflected power on resonance is monotonically related to the dynamic resistance. In this way, a charge diamond can be built up by taking a family of reflected power verses voltage curves as a function of gate voltage. This successfully exploits the full bandwidth of the

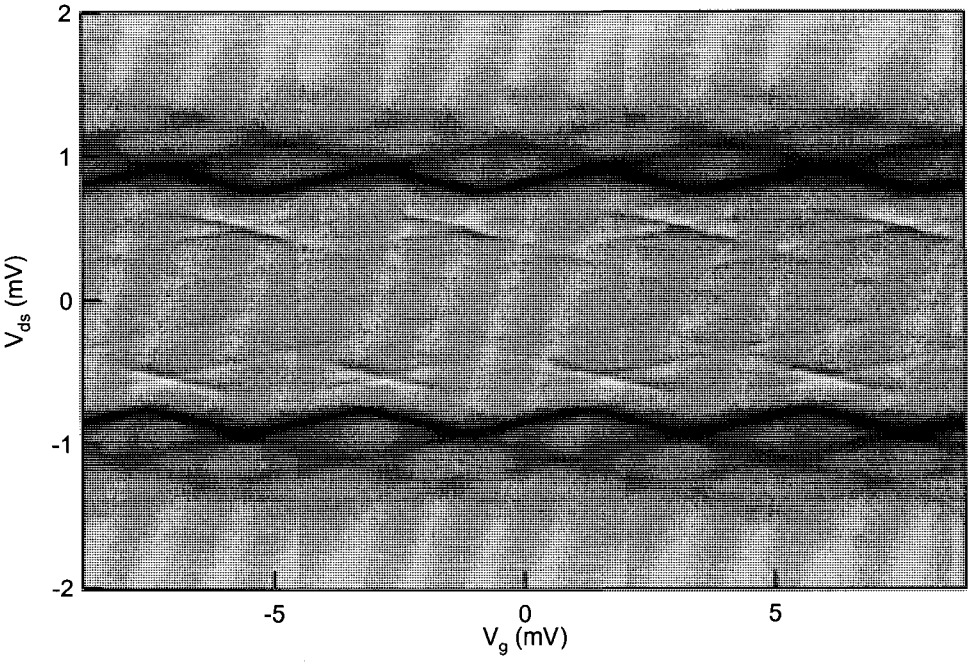

Figure 7.13: Charge diamond of SET13. This data, taken at T=256 mK, shows the reflected RF power as a function of both the drain-source and gate voltages. The darkest lines show the modulation of the gaprise, where the dynamic resistance and hence reflected power are lowest.

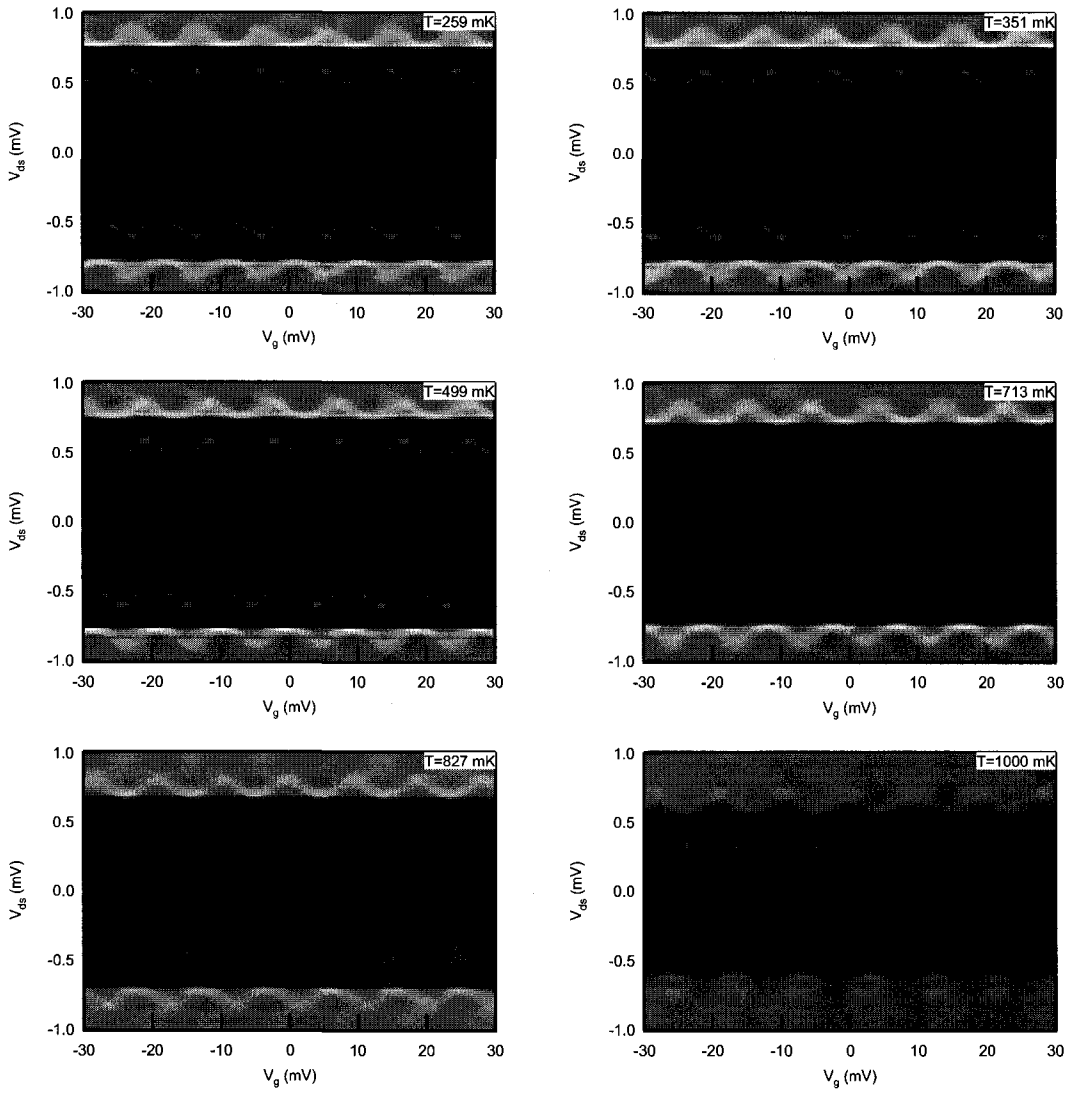

Figure 7.14: These are superconducting, RF charge diamonds for device SET06 from temperatures of 259 mK up to 1 K. Much of the subgap structure is only visible at higher temperatures where there is a sufficient number of quasiparticles to complete the cyclic processes necessary for current flow.

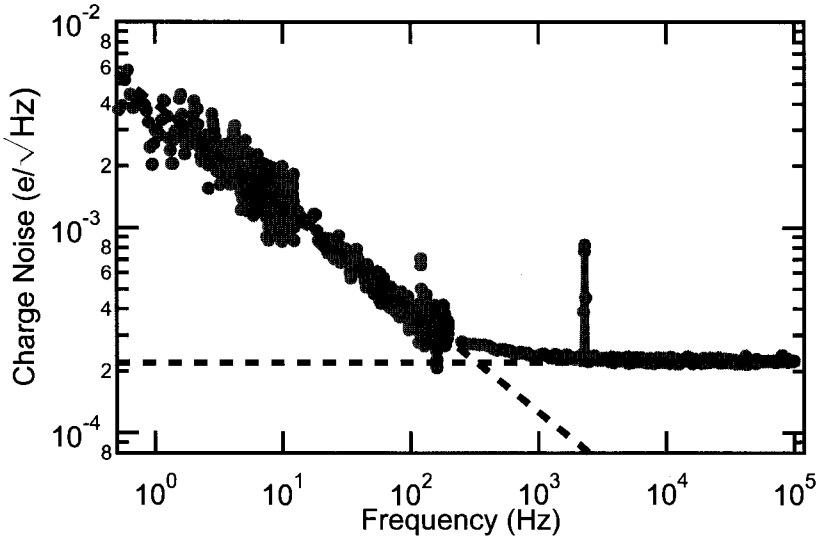

Figure 7.15: Charge sensitivity measured for SET04. The dotted lines are to emphasize the two distinct regions of sensitivity. Below 1 kHz the noise has a characteristic $1/\sqrt{f}$ (1/f in power units) spectrum due to charge fluctuations at the input of the SET. At higher frequencies, the noise is white and dominated by the noise of the HEMT amplifier at the output of the SET. The peak at 2.2 kHz is a calibration tone applied to the gate of the SET with an peak amplitude of 1/80 of an electron.

RF-SET as diamonds with over $>10^4$ independent points can be taken in a matter of minutes, not hours. Figure 7.13 shows a a charge diamond for SET13. The diamonds contain all the information necessary to calculate Δ, E_C and C_g. A horizontal slice is the transfer function for that particular drain-source bias point.

With the exact parameters of the SET determined from the charge diamond, the sensitivity can now be measured. First, the drain-source bias is chosen in order to give the transfer function with sharpest features. The gate voltage is then tuned to this point of maximum slope. The transfer function gives an exact calibration between applied gate voltage and the number of electrons at the SET. Thus, in addition to the DC gate voltage, a small AC signal of known amplitude is applied at the frequency of interest. This signal will in turn amplitude modulate the RF carrier producing sidebands. These sidebands can be measured directly on a spectrum analyzer near the RF carrier frequency or in the audio frequency power spectral density of the demodulated signal. In either case, the size of these peaks relative to the noise floor is a direct measurement of the charge sensitivity of the RF-SET. The sensitivity can now be optimized in real time by maximizing the signal to noise ratio of the calibration peak. This optimization includes iteratively varying the RF carrier power, V_{ds}, and V_g. Figure 7.15 shows a typical noise spectrum from SET 04. In this case carrier signal of -93 dBm is applied at 463 MHz. The reflected signal is amplified and the power is measured in a 1 MHz bandwidth around the carrier frequency. This power level is then fed into an audio frequency spectrum analyzer in order to measure its spectrum. The size of the calibration tone is chosen to be a few percent of an electron so that it is sure not to exceed the linear region of the transfer function. The noise is characterized by two distinct regions: the low frequency pink noise and the higher frequency white noise. The former is the characteristic 1/f noise common to all amplifiers. The exquisite charge sensitivity of the SET unfortunately implies that in addition to measuring the intended signal, the SET is also measuring many uncontrolled charges near its center island. The random motion of all these charges result in a noise spectrum that get progressively worse at low frequency. This corresponds to 1/f dependence in the power spectral density (or $1/\sqrt{f}$ in linear units of $e/\sqrt{Hz}$).

The important aspect to note in the above discussion is that this noise is at the input of the SET, so it cannot be improved by more sensitively amplifying the output of the SET. Eventually, at high enough frequencies, the 1/f noise will fall below the level of the other noise sources in the problem. In the case of the RF-SET, this is typically set by the HEMT's noise temperature. The main advantage of the RF-SET for many applications is not the ability to measure fast dynamics, but rather simply to measure at frequencies high enough so that the noise is no longer dominated by 1/f contributions. In some cases, this does not occur until close to 1 MHz. If the noise temperature of the HEMT could be reduced, the sensitivity would still be limited by the shot noise of the current flowing through the SET. It is only in this limit that the SET could, in principle, achieve true quantum-limited sensitivity (Devoret and Schoelkopf, 2000). Just like the shot noise thermometer

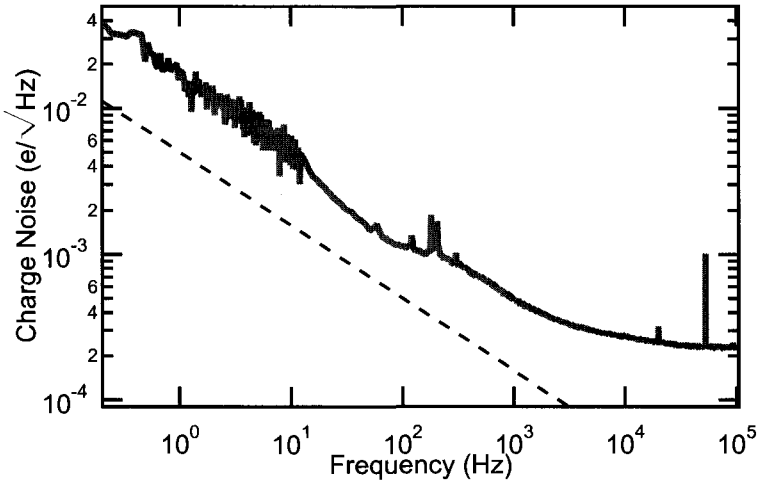

Figure 7.16: Charge sensitivity measured for SET07. The dotted line is for reference and has a frequency dependance of $1/\sqrt{f}$. The spectrum is calibrated by applying a small signal of known amplitude to the gate. This peak can be seen at 53 kHz and corresponds to an AC signal with a peak amplitude of 3% of an electron. While lower temperature amplifiers or better matching circuits can lower the white noise floor, these will never improve the low frequency noise of the SET. In practice, the signal of interest could be modulated at $\sim$ 100 kHz to avoid this 1/f noise.

(Spietz, 2005), any current through the SET (RF or DC) will lead to an increase in the noise. The current noise of a tunnel junction is given by:

$$S_I = 2eI \coth\left(\frac{eV}{2k_BT}\right) \tag{7.7}$$

Here I is understood to be the average current flowing through the junction at a given bias voltage.

The hyperbolic cotangent smoothly interpolates between the two fundamental source of noise: the Johnson noise required by the fluctuation-dissipation theorem for any resistive element at finite temperature and the shot noise arising from the randomness of tunneling events that give rise to the current flow. As will be discussed more in Chapter 8, this noise is white up to frequencies where $h\nu$ becomes comparable to either k_BT or eV. Assuming that the SET is comprised of two identical tunnel junctions in series whose noises are completely uncorrelated, the total noise is reduced by 1/2. Thus, at high bias ($eV \gg k_BT$), the total current noise is given by: $S_I = eI$. This can be used to calibrate the exact noise temperature of the HEMT amplifier.

Figure 7.17 shows such a calibration. Just as with the shot noise thermometer, the vertical axis can be in any units that are proportional to noise power. At low bias, the noise is a complicated function of both the changing impedance (and hence matching to the amplifier) as well as the changing current. But at high bias, where the resistance has reached its asymptotic value and

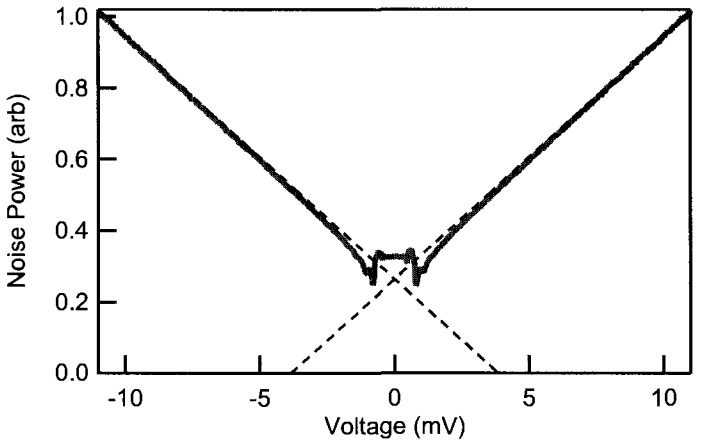

Figure 7.17: Measured noise power in a 1 MHz bandwidth around 454 MHz for SET14. This shot noise calibration demonstrates a noise temperature of 11 K for an impedance of 331 kΩ. In other words, the transformed current noise of the HEMT is <50 fA/$\sqrt{\text{Hz}}$ on resonance.

eV$\gg$k$_B$T, the noise is linear in the bias voltage. The noise temperature can be measured from the x-intercept of this line.

$$T_n = \frac{eV_o}{4k_B} \tag{7.8}$$

where V$_o$ is the voltage intercept.

This noise temperature will be increased by any losses between the SET and HEMT, including that of the tank circuit. It is important to note that a noise temperature is always a function of the load impedance. In this case, T$_n$ is referred to the normal state resistance of the SET, which can be quite different from the dynamic resistance of a chosen bias point. For a superconducting SET, the most sensitive bias points will always be $\lesssim 4\Delta/e$. This implies that in order for the shot noise of SET to dominate, one would require an RF amplifier with a noise temperature less than 1 K. While HEMT amplifiers can approach this, it seems that this will only be achievable with some other preamplifier before the HEMT. The prime candidate is RF SQUID amplifiers (Andre et al., 1999) having demonstrated near quantum limited amplification at 500 MHz. Other forms amplifiers such as a Josephson parametric amplifier could also be a possibility (Movshovich et al., 1990; Castellanos-Beltran and Lehnert, 2007).

Using commercial HEMT amplifiers, charge sensitivities of order a few $\mu e/\sqrt{\text{Hz}}$ have been demonstrated in several group since the invention and original demonstration of the RF-SET here at Yale, for example (Brenning et al., 2006; LaHaye et al., 2004; Thalakulam et al., 2004). The more pertinent figure of merit for our detector readout is the voltage noise. From equation 7.5, it is immediately apparent that size of the gate capacitor is just as important as the charge sensitivity. In most of the

SET	f_o(MHz)	Q_L	Δf(MHz)	C_g(aF)	$q_n(\mu e/\sqrt{Hz})$ @ 10 Hz	$q_n(\mu e/\sqrt{Hz})$ @100 kHz	$v_n(nV/\sqrt{Hz})$ @100 kHz
SET03	577	20	14	320	2500	120	60
SET04	463	15	15	180	1500	200	180
SET05	425	50	4	21	1500	30	230
SET07	389	>100	~2	13	6000	220	2700
SET13	478	53	5	36	900	75	330
SET14	454	230	1	15	900	40	430

Table 7.2: This table summarizes the characteristics of the RF-SETs measured in this thesis.

references for charge sensitivity given above, the gate capacitor was at most only a few attofarads. This implies a voltage noise several hundred $nV/\sqrt{Hz}$. So far the groups that tried to optimize that voltage noise with large coupling capacitors (Zimmerli et al., 1992; Visscher et al., 1995) have only done so with DC SETs so that their charge sensitivity was limited. This work continues measurements in the Schoelkopf lab to optimize the voltage noise of an RF-SET (Segall et al., 2002; Stevenson et al., 2003).

The SETs were designed with large interdigitated finger capacitors as shown in figure 7.4. Several different sizes were measured in order to demonstrate that the large coupling capacitors did not severely reduce the charging energy. Some of these were then measured as RF-SETs in order to directly determine their voltage sensitivity. Table 7.2 summarizes the results that were found. While the charge sensitivity in these devices suffered due to the inability to impedance match to the large SET resistances, the large gate capacitors result in quite good voltage noises.

7.6 RF-SET Configured as a Transimpedance Current Amplifier

With the successful demonstration that SETs can be fabricated and measured to have excellent characteristics when configured as RF-SETs, the next step is to integrate it with an STJ. This is the only way to test that the SET is not only a low-noise readout, but also can faithfully measure current through the detector without causing unwanted effects on the STJ. This section shows the experimental results for a detector with an RF-SET readout measured in the dilution refrigerator. It shows that the RF-SET can be run in feedback in a way that is sensitive, fast, and stable. This represents a record low current noise for an RF-SET in a transimpedance configuration. Furthermore, it also demonstrates that that having the SET on the same chip does not corrupt the ultra-low dark currents of the STJ even at dilution refrigerator temperatures.

As with any amplifier that is optimized for high impedances, a large bias resistor is necessary in order to fully exploit its low-noise characteristics. Almost all commercial current amplifiers implement this bias resistor in feedback. The output of a voltage amplifier is fed back to the load

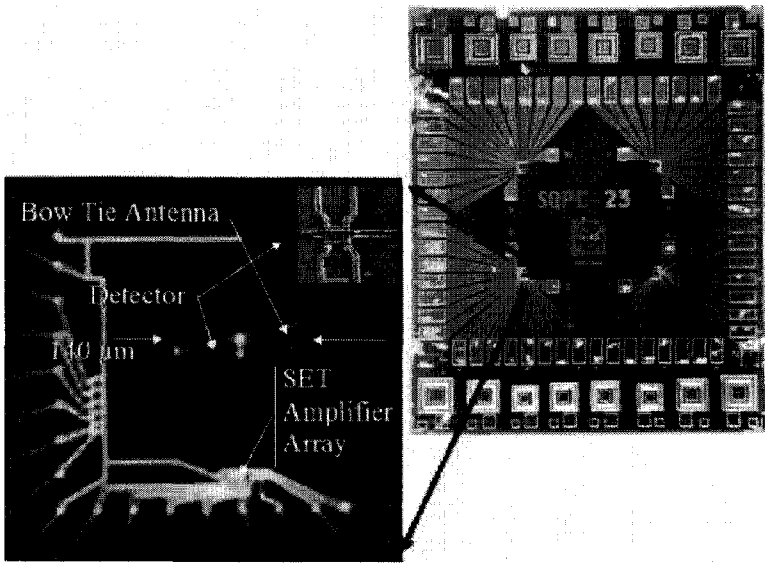

Figure 7.18: These are optical microscope pictures of a typical STJ/SET chip fabricated by NASA Goddard. The spirals visible at the top and bottom of the chip are niobium inductors of varying sizes for multiplexing arrays SETs. These SETS are coupled with large interdigitated-finger capacitors to the detectors. The lower picture also shows the niobium bowtie antenna used to couple submillimeter radiation to the detector.

through the bias resistor as shown in Figure 7.19. This has several advantages over connecting the resistor in series with the load. As the gain of the amplifier is increased, the load become proportionally more voltage biased. In the same way, it also increases the response time of the circuit beyond the RC time one would measure without feedback. What is most important for an amplifier with non-linear transfer function like an SET is that the large gain also greatly increased the linear range of the amplifier. For all of these reasons, the the RF-SET will be run in a transimpedance configuration.

The load impedance at the input of the SET is the parallel combination of the STJ and the bias resistor. Because the dynamic resistance of the STJ is nearly infinite (> 1 GΩ) for this device at low temperatures, this impedance is completely dominated by the the feedback resistor. In order to minimize the total current noise, this resistor should be large impedance, cold, and placed as close to the STJ as possible in order to minimize the capacitance of the load. This was realized in this experiment with resistor fabricated by NASA Goddard by evaporating $\sim 10^4$ squares of NiCr on a quartz chip. This 60 MΩ resistor was placed in the same sample holder as the STJ/SET chip and connected via a wirebond to the device. These chip were enclosed in a light-tight sample holder and mounted on the cold stage of the Kelvinox dilution refrigerator. The device chip was also fabricated at NASA Goddard. The SET was device SET04. They were coupled via an interdigitated finger capacitor of 180 aF. The tank circuit was formed from a Nb planar coil with $\sim$200 nH of inductance

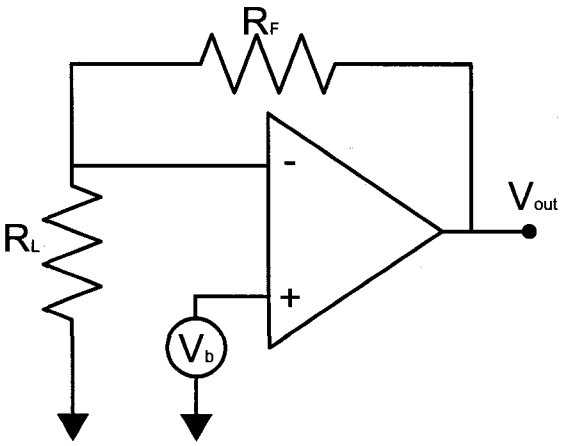

Figure 7.19: General transimpedance amplifier. This diagram shows a typical current amplifier where the output from a voltage amplifier is fedback to the input through a bias resistor. In the limit of large gain, this circuit provides an active voltage bias for the device. As the voltage amplifier draws no current, the output signal is directly proportional to the current through the device.

(also on-chip) and the parasitic capacitance of the bondpads as detailed in (Stevenson et al., 2002). The chip is shown in Figure 7.18.

The bias resistor and the STJ were fully characterized in a previous cooldown. The resistance of the resistor was measured directly, and it was used with a FET at room temperature to measure the temperature dependence of the dark currents of the STJ as shown in Figure 3.2 in Chapter 5. In this way, an explicit comparison can be made between the FET and SET readout. The block diagram of the measurement is shown in Figure 7.20. All "DC" leads are coaxial lines filtered with two stages of powder filters. The RF signal is coupled through a bias tee to an octave-bandwidth, low noise temperature HEMT amplifier operated at 4 K. This signal is further amplified with two room temperature amplifiers and demodulated with a commercial diode. The first measurements were to characterize the properties of the RF-SET. The resonant frequency of the tank circuit is found to be 460 MHz, which corresponds (by design) to the frequency where the HEMT has maximum gain and minimum noise temperature. Unfortunately, the resistances of all devices (SET and STJ) on this chip were much higher than intended. The SET used in this experiment has a resistance of 1.5 MΩ. While this large resistance is helpful in maximizing the charging energy and decreasing the importance of cotunneling to the SET's modulation, it has several drawbacks. Because the energy scales of the SET, Δ and E_C, are voltage scales, a high impedance device has reduced power handling capability. This means that a smaller carrier power must be used, reducing the sensitivity. The most important drawback is that the tank circuit will be unable to impedance match the SET to the HEMT, also degrading the sensitivity. For this experiment, the loaded quality factor of 15 implies that the amplifier is matched to an impedance of 11 kΩ, not 1.5 MΩ. While the tank circuit

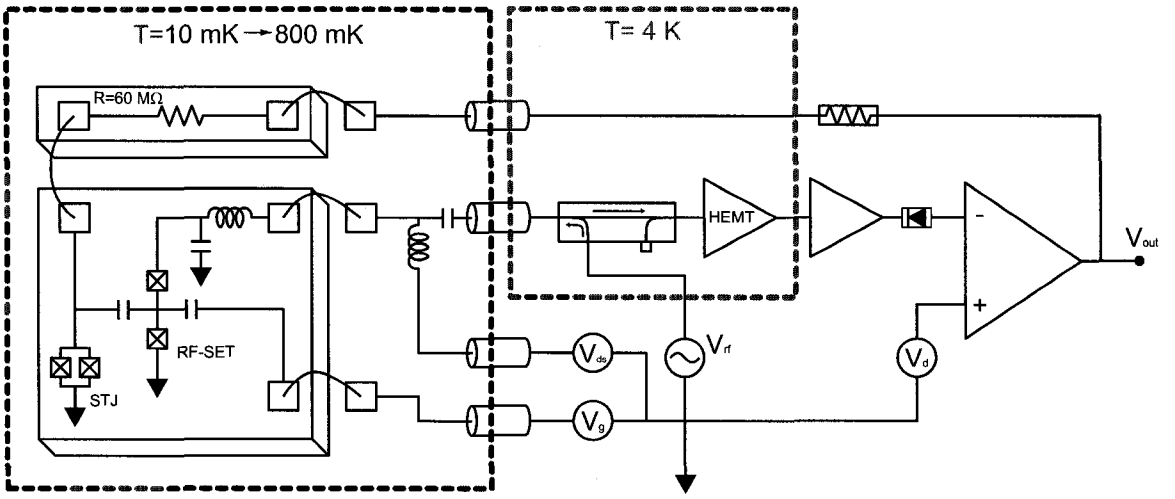

Figure 7.20: This is a detailed circuit diagram showing how the RF-SET can be configured as a current amplifier. The detector, SET and spiral inductor are all fabricated on the same chip. The feedback resistor in fabricated on separate chip by evaporating $\sim 10^4$ squares of NiCr. They are both placed at the cold stage of a dilution refrigerator and connected via aluminum wirebonds. The output signal from the RF-SET is fedback to the detector junction through the cold bias resistor. The bias point of the STJ may be tuned simply by applying a voltage to the gate of the SET.

helps, it over-transforms the impedance of the SET on its quasiparticle branch to $\sim 0.4\ \Omega$. In this way, the 4 K noise temperature of the HEMT is greatly increased when referred to the impedance of the SET. The resulting charge sensitivity is the noise spectrum shown in Figure 7.15. Below frequencies of 1 kHz, the 1/f noise of the SET is dominant. The rest of the spectrum is white at a level of 200 $\mu e/\sqrt{\text{Hz}}$ and is set by the HEMT's noise. The usable bandwidth is limited only by the width of the tank circuit and is >15 MHz. The SET is coupled to the STJ via a interdigitated-finger capacitor of 180 aF. Thus, the voltage noise of the SET is 180 $\text{nV}/\sqrt{\text{Hz}}$. When coupled to a STJ biased with a 60 MΩ bias resistor, the current noise is 3 $\text{fA}/\sqrt{\text{Hz}}$. To our knowledge this is the lowest current noise of an SET used as a voltage amplifier. As mentioned above, in order to be a useful amplifier, with reasonable stability and dynamic range for detector purposes, the SET should be run in feedback. The rest of this section will discuss how the SET is configured in closed-loop operation while preserving the excellent open-loop current sensitivity.

As with any transimpedance amplifier, the feedback is accomplished by using the output of the voltage amplifier to provide the bias current for the device. In this case, the output is the reflected RF carrier power. As shown in Figure 7.20, it is converted to a DC voltage using a microwave diode. This signal is then amplified and low-pass filtered using a commercial voltage preamplifier. In order to avoid applying large voltages to the STJ in the case that the feedback becomes unstable, this signal is resistively divided by a factor of 500 before being applied to the cold feedback resistor. There are three separate DC bias voltages necessary in order to optimize the measurement. First, V_{ds} is chosen

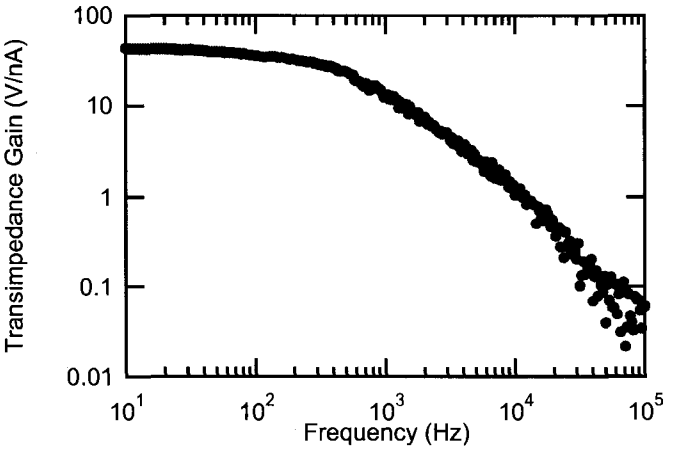

Figure 7.21: Closed-loop gain of the RF-SET as a transimpedance amplifier.

in order to obtain an optimal transfer function of the SET before applying the feedback. This chosen transfer function should possess a bias point with both large gain and reasonable dynamic range. In this case, the gaprise feature provides both of these characteristics. The voltage at the input of the differential amplifier, V_d, provides the reference voltage to which the RF signal is compared. This sets the desired diode voltage which the closed-loop operation should enforce. When the diode voltage is different from V_d, a large output voltage, V_{out} is created, forcing current through the STJ. This bias, in turn, gates the SET until voltages are equalized. Now that the feedback loop is locked to optimal SET operating point, the bias across the STJ can be chosen by applying a third voltage, V_g, to a separate capacitive gate of the SET. As this trim gate voltage tries to change the bias point of the SET, the feedback loop will compensate by imposing a new voltage across the STJ. In the limit of large closed-loop gain, the measured voltage, V_{out} is directly proportional to the current through both the feedback resistor and the STJ. It is in this way that the circuit forms a transimpedance amplifier.

The above discussion demonstrates the basic operating principle, but does not yet consider the dynamics of the feedback system. Stable operation relies on negative feedback to constantly counter any attempted deviation of the system from the chosen operating point. At high enough frequencies, the reactive components in the circuit will cause the feedback signal to be out of phase with the input. If this phase shift exceeds 180° at a frequency where the circuit still have closed-loop gain, the loop will become unstable and oscillate (Horowitz and Hill, 1989). This is the criterion for stable feedback. So while large gain gives the most ideal performance in terms of dynamic range, speed and linearity, it must necessarily be filtered in order to ensure stability. The important reactive components in this circuit are the parasitic capacitances that shunt the feedback resistor and the STJ. With these elements in the circuit, load and feedback impedances become complex quantities.

The load capacitance will shunt the STJ current with its displacement current at frequencies above $1/2\pi$RC. By twice this frequency, the response is sufficiently out of phase to make the system oscillate. Ideally, the remedy to this instability is to intentionally shunt the feedback resistor with the proper amount of capacitance. While introducing this simple pole to the response function limits the performance, it keeps the phase shift under control. In our case, this feedback capacitance could not be adjusted *in situ* so the system was kept stable by rolling-off the gain of the differential amplifier. The parasitic capacitance to ground is due to the parallel-plate capacitance formed by the bond pads between the resistor and the STJ. From phase shift measurements, it was found to be 150 fF. Together with the 60 MΩ feedback resistor, this capacitance implies that the current noise of the SET will begin to increase above ~17 kHz as the impedance at the input of the SET is reduced.

$$i_n = \frac{q_n e}{C_g |Z_F|} \tag{7.9}$$

$$Z_F = \frac{R_F}{1 + i\omega R_F C} \tag{7.10}$$

By twice this frequency, the loop gain must less than unity in order to meet the stability criterion. While this is far below the intrinsic bandwidth of the RF-SET, this is quite close to the intrinsic RC time of the resistor itself. Experimentally, the best stability and performance occurred with the preamplifier gain of 50,000 and a single pole roll-off at 30 Hz. The resulting transimpedance gain in units of [V/A] is shown in Figure 7.21. This is measured with an audio frequency network analyzer. A small test frequency is applied to V_g and the response in V_{out} is measured. This voltage is converted to a current by dividing by the feedback impedance. It should be noted that this has flat gain to frequencies much higher than the 30 Hz of differential amplifier. This is because the available loop gain at DC exceeds the gain demand of the system. It is only at several kHz that this demand is no longer met and the transimpedance gain is reduced. Figure 7.22 demonstrates the bandwidth of the transimpedance amplifier in the time domain. A fast signal applied to the trim gate quickly chances the bias point across the STJ. The current equilibrates on a timescale of 10 μs. While this speed is sufficient for most applications, it is important to note that a smaller feedback resistor could be used in order to trade current sensitivity for more bandwidth.

While the measurements of the transimpedance gain show that the RF-SET is working as a transimpedance amplifier, it is also necessary to show that is is not adversely affecting the STJ it is intended to measure. These effects could include thermal heating of the entire chip from the RF currents through the SET or simply the HEMT coupling high frequency noise into sample holder. This experiment was performed without the use of a circulator. In order to minimize the out of band noise of the HEMT a 700 MHz low pass filter was placed between the SET and the amplifier. The shape features seen in the IV characteristic of the SET show that the coupling to the HEMT was not in fact a problem. The true test is shape and temperature dependence of the dark

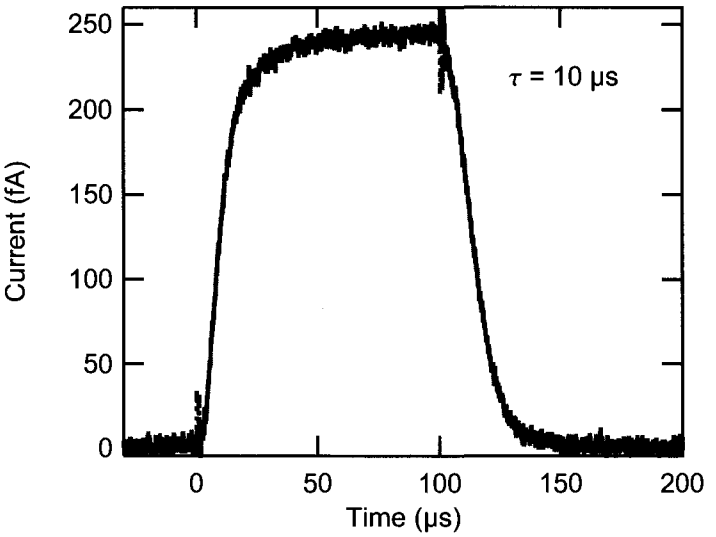

Figure 7.22: Rise time measurement of the RF-SET as a closed-loop transimpedance amplifier. These data show the averaged, closed-loop SET response to a fast current pulse through the STJ. This 10 μs rise time is consistent with the frequency dependence of the transimpedance gain. While the RF-SET itself has more than 20 MHz of bandwidth, the stability conditions of the feedback circuit limit the speed of the closed-loop operation.

current of the STJ. Just as in the previous experiment where the STJ was measured with a room temperature FET. Detailed IV curves of the STJ were taken as a function of temperature using the SET transimpedance amplification. In order to good signal to noise, the IV many IV curves were taken at each temperature with any drifts and offsets subtracted digitally. These curve were then averaged to obtain the dark current measurements of the STJ. The data, in fact, exactly reproduced the previous measurements both in magnitude of the dark current and shape as seen in Figure 7.23. The data taken with the SET and FET agree both with each other and BCS theory. As a function of temperature, there was no indication of of a minimum in the dark current, however below 150 mK the dark current became immeasurably small. This measurement shows that the RF-SET can be integrated with the STJ and faithfully measure its current.

The next property of the closed-loop operation to verify is the current sensitivity. The open-loop measurements of charge sensitivity show that the amplifier should have a current sensitivity of 3 fA/$\sqrt{\text{Hz}}$, but it is nontrivial to ensure that the sensitivity will remain unchanged once the feedback loop is closed. While in principle, the a calibrated pulsed signal like Figure 7.22 could be used to measure the signal to noise ratio of the current measurement, it does not allow one to deconvolve the frequency dependence of the noise. For this, the voltage spectral density of the signal voltage, V_{out}, is measured with a commercial FFT spectrum analyzer. This voltage spectral density can be converted to a current spectral density by dividing by the measured transimpedance gain. The

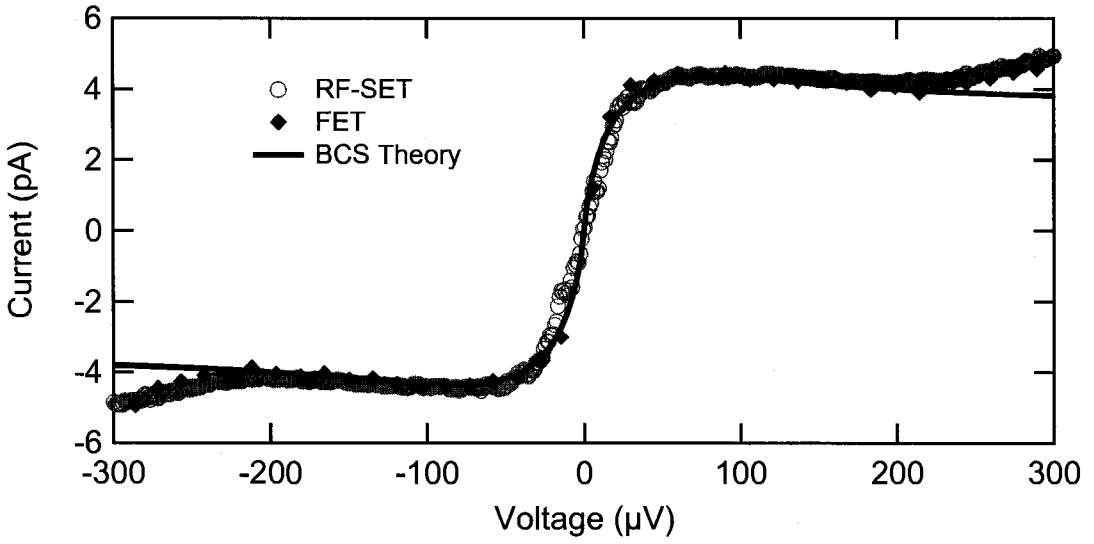

Figure 7.23: This is the dark current of an STJ measured in two separate cooldowns: one is measured with a room temperature FET, the other with an on-chip RF-SET in closed-loop, transimpedance configuration. There excellent agreement with each other as well as with BCS theory demonstrates that the SET measurement is faithful and does not detrimentally act back on the STJ.

result is shown in Figure 7.24. The graphs shows both the current noise measured with and without feedback and show good agreement. The slight discrepancy at higher frequencies is most likely due to the feedback circuit locking to a bias point with slightly less sensitive bias point. The closed loop circuit demonstrates a sensitivity of <5 fA/$\sqrt{\text{Hz}}$ at 500 Hz. This measured current noise includes all contributions including the amplifier, the shot noise of the STJ, and the Johnson noise of the feedback resistor. The latter two contribution are negligible in comparison to the amplifier noise. Even if the STJ had 1 pA of current, the shot noise is 0.6 fA/$\sqrt{\text{Hz}}$. The dark currents in this experiment are up to 1000 smaller than this level. The Johnson noise of the 60 MΩ feedback resistor at 50 mK is also only 0.2 fA/$\sqrt{\text{Hz}}$. As these noise sources are uncorrelated, they could be subtracted in quadrature resulting in a completely negligible contribution. Thus, the current represents that on the RF-SET itself. The noise temperature of the RF-SET transimpedance amplifier is 10 K for this 60 MΩ load. This is far from the optimum noise impedance of the SET which expected to be roughly given by the impedance of the gate capacitor at the relevant audio frequencies (Devoret and Schoelkopf, 2000). For this device this corresponds to an impedance of greater than 1 TΩ at 1 kHz.

Despite the fact that the charge sensitivity of this RF-SET could be improved by an order of magnitude with better impedance matching to the HEMT, this would only lower current noise at frequencies above the 1/f noise. Likewise, using a larger bias resistor would lower the overall current noise, but it would lower the frequency where the current noise begins to increase due to the

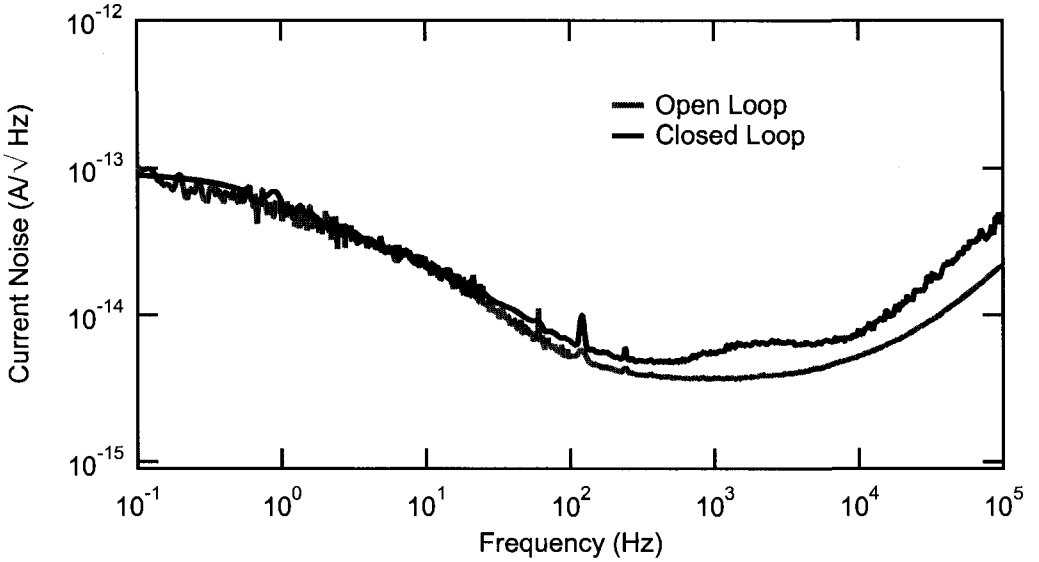

Figure 7.24: This is the measures current sensitivity of an RF-SET in a transimpedance configuration, demonstrating i_n <5 fA/$\sqrt{\text{Hz}}$ at 500 Hz. At frequencies above ~10 kHz, the noise increases as the capacitance of the circuit decreases the impedance of the feedback resistor.

parasitic capacitance. The most dramatic improvement could be made by further increasing the gate capacitor in order to lower the voltage noise. From a detector stand point, it is important to consider to what NEP this current noise would correspond. Assuming a reasonable responsivity for the STJ of 1000 A/W, this implies a measured electrical NEP of 5 10^{-18} W/$\sqrt{Hz}$. Such a sensitivity would already be background limited in any ground-based submillimeter telescope. As emphasized in the beginning of this chapter, the sensitivity is only one of the many attractive qualities of the RF-SET readout. The main benefit is that it possesses the qualities necessary to readout large format arrays: cryogenic, low power dissipation, on-chip, with natural wavelength division multiplexing.

It should also be noted that a feedback circuit is not the only option for stable operation of an amplifier with a periodic transfer function. Recent work with SQUIDs multiplexed in the frequency domain have a shown a flux ramp modulation scheme (Hahn et al., 2006; Lehnert et al., 2007; Mates et al., 2008). Several multiplexed SQUIDs are operated without feedback and a flux ramp is applied to all SQUIDs with a common flux bias line. As the flux ramp has an amplitude of many flux quanta, each SQUID feels a periodic flux modulation sampling all points on the transfer function. A signal coupled to the SQUID then appears as phase modulation of this ramp. An exactly analogous scheme could be implemented for the SET by applying a charge ramp. The advantages are several fold. First, there is only one gate bias line for all the SETs. Secondly, there are no feedback loops to maintain. Lastly, this method naturally modulates a baseband signal at a frequency set by the ramp modulation rate. Thus, while the signal to be detected may only occur at less than 1 Hz, where the

1/f noise of the SET is quite large, this method moves the signal to higher frequencies where this is no longer an issue. While there is a small penalty in sensitivity because the operating point of the SET is time averaged over all points on the transfer function, this is only a factor of $\sqrt{2}$ for a purely sinusoidal transfer function.

In conclusion, these SET experiment demonstrate the capabilities and drawbacks of single electron transistors. These data represent a proof of concept measurement for almost all of the aspects required for an RF-SET as current amplifier. The RF-SET can be configured as a low voltage noise amplifier suitable for high impedance detectors. With feedback, the SET can possess the stability, dynamic range, and speed to successfully amplify photocurrents from an STJ. It is clear that further improvements to the sensitivity and progress toward multiplexing could be made; however some issues such as the 1/f noise and the overall complexity are serious concerns for pursuing this as a viable technology for this application. In the next chapter, the SET readout will be contrasted with the novel readout of the RF-STJ: a method that, at its heart, uses all the principles of the RF-SET applied directly to the detector itself. Although this new method lacks the intrinsic gain and potentially quantum-limited sensitivity that the SET might hope to achieve, the ease of use and overall simplification of the readout made it an attractive option.

Chapter 8

Radio Frequency Superconducting Tunnel Junction

"Science is built up of facts, as a house is with stones. But a collection of facts is no more a science than a heap of stones is a house."

–Henri Poincaré

The previous chapter discussed the advantages and drawbacks of the single electron transistor for amplifying the current through a detector junction. While radio frequency techniques greatly enhanced both the performance and usability of the SET, its use in this application remains limited by many technical issues. Like any true electrometer, the SET becomes a maximally sensitive current amplifier only with integration with a large bias resistor, large coupling capacitor, and a quiet charge environment. In other words, the optimum noise impedance on the input of an SET is much larger than is practically realizable. It is only when the impedance of the input capacitor at the readout frequency becomes comparable to the other impedances in the circuit that the SET could approach quantum limited sensitivity (Devoret and Schoelkopf, 2000). These other impedances are comprised of the output impedance of the STJ as well as that of the resistor used to bias the STJ. As seen from the DC IV characteristics measured in chapter 6, the dynamic resistance of the STJ in the subgap

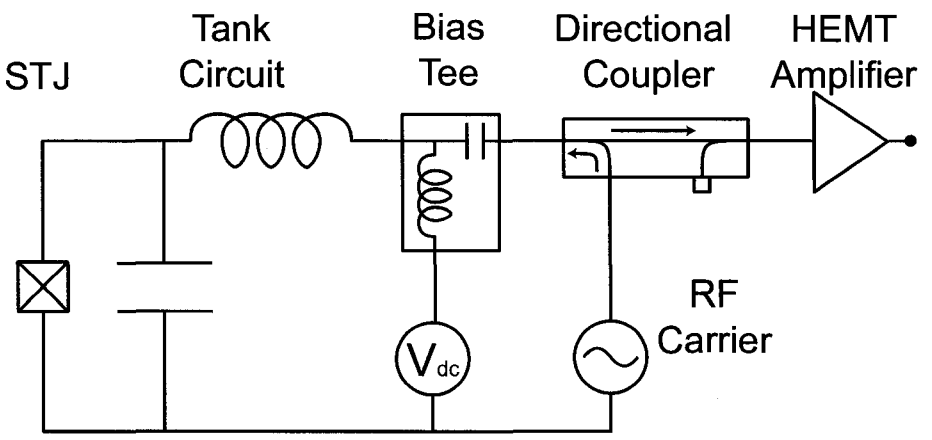

Figure 8.1: The block diagram shows how the STJ can be measured with RF reflectometry in a way exactly analogous to the RF-SET.

can be nearly infinite. Nonetheless, cryogenic bias resistors will always be limited in a practical sense to values of order 100 MΩ. Beyond these limitations, the 1/f noise and overall complexity of the SET are practical issues that will always accompany its use. It is in this light that the role of the SET in this work was re-examined. Its primary role in this detection scheme is to actively transform the large output impedance of the STJ from ~ GΩ to ~50 kΩ. While this impedance is still large, a tank circuit with a modest Q can passively transform this down to match a 50 Ω HEMT amplifier at RF frequencies. The logical question becomes "why not readout the STJ directly with the HEMT amplifier?" This direct readout of the STJ with RF reflectometry constitutes the so-called RF-STJ. This chapter will quantitatively compare its performance with both FET and RF-SET readout schemes and show how its use is ideally suited for submillimeter photon detection.

8.1 RF-STJ: Readout Concept

In principle, the RF-STJ is exactly analogous to an RF-SET. As shown in Figure 8.1, the device is embedded in an LC resonant circuit as the damping element. In lieu of measuring the DC photocurrent, one can monitor its effect on the loading of the resonance. Additional photocurrent through the STJ lowers its resistive impedance at RF frequencies, which in turn, affects how much incident RF power is absorbed or reflected. Thus, the photoresponse of the detector junction is encoded as amplitude modulation of an RF or microwave carrier tone. This carrier is reflected off the tank circuit, amplified with a cryogenic, HEMT amplifier and then demodulated at room temperature with either a diode or a mixer.

Just as with the RF-SET, the series inductor exactly compensates the capacitive reactance on resonance, resulting in an impedance that is purely real. This real impedance seen by the RF carrier is equivalent to the differential resistance of the junction that is ideally transformed down by a factor

of Q^2 to 50 Ω. The device is no longer affected by the additional capacitance of the cables required to take this signal to the amplifier at 4 K and then on to room temperature. This is because the capacitance of the SMA cables ($\sim$100 pF/m) is again compensated by its inductance per unit length to form a transmission line whose characteristic impedance is purely real. Unlike measuring with a high-impedance FET, it does not matter is the amplifier is centimeters or meters away from the device. The only important capacitance is that which shunts the device before the inductor. It is this capacitance that will ultimately set the limit on both the obtainable bandwidth as well as the transformation ratio for a single stage tank circuit. By transforming as physically close to the device as possible (either with a planar inductor on the chip or with a surface mount inductor only millimeters away), the parasitic capacitance can be minimized. This results in a transformation that is limited only by the unavoidable, intrinsic capacitance of the junction itself. Unlike the SET, where there are two ultra-small junctions in series, the capacitance of the STJ itself can dominate over the parasitics. It is in this sense that the tank circuits in this work reach the Bode-Fano limit for optimal matching. Another difference between matching to STJ's and SET's, is that the while the SET has a higher normal state resistance, the STJ can actually have a higher impedance in the region of interest. A superconducting SET is typically biased either on the gaprise or JQP feature; both cases represent points of increased conductance due to the enhanced tunneling matrix elements at those particular bias points. Conversely, the only part of the IV of the STJ that sensitively depends on photocurrent is the subgap region which has the largest resistance. So while most published RF-SET's are embedded in tank circuits with a loaded Q between 5 and 25, this work would ideally want to increase this by more than an order of magnitude. Given that this can be accomplished, there many clear advantages in circumventing the SET and probing the detector directly with RF.

8.2 Advantages of Direct RF Readout

The primary advantage of a direct RF readout scheme would be its simplicity. A fully integrated STJ and RF-SET, even if multiplexed in the frequency domain, still requires at least three DC bias lines per pixel. Furthermore, a feedback loop must be implemented at room temperature in order to maintain maximal sensitivity. In contrast, the RF-STJ could bias the detector purely with an RF carrier and eliminate all DC wires from the system. This would greatly reduce not only the complexity of the wiring scheme, but more importantly it vastly lowers the overall heatload to the cold stage of refrigerator. While this heatload is negligible for single or few pixel characterization in a laboratory setting, it is a crucial consideration for large format arrays intended for use in space-based missions. Many of the the other technical issues that are intrinsic to high impedance measurements are avoided with this RF scheme. For example, high impedance circuits become sensitive to microphonic noise when the RC times of the system do not allow the voltages in the circuit to equilibrate on the timescale of of the vibrations. In contrast, the only bias resistor in this

scheme is the 50 Ω input resistance of the HEMT. It only looks like high impedance in a very narrow window of frequency space near the resonance of the matching circuit. This nearly perfect voltage bias at low frequencies makes the circuit impervious to audio frequency vibrations.

Yet another advantage is that direct reflectometry avoids one of the biggest problems with SET measurements–the 1/f noise. The fact that the 1/f noise of an SET can extend out to >100 kHz is tribute to its extreme sensitivity, not only to the charge that one intensionally couples, but to any charged motion on or near the chip. Even if an application did not require the ability to resolve fast dynamics, the electrical bandwidth becomes necessary in order to measure at frequencies where the 1/f noise is no longer dominant. In the SET transimpedance scheme, a large feedback resistor reduces the overall scale of the current noise, but it also limits the bandwidth so that the 1/f noise can no longer be avoided. No such compromise exists with the direct reflectometry. As will be shown later in this chapter, the output noise spectrum is completely white down to frequencies of order 1 Hz.

One final advantage to emphasize in this section is the readout bandwidth. This method has the ability to access all the speed of the microwave readout without being limited by feedback loop or biasing circuit. As shown in chapter 7, despite the fact that the RF-SET's used had in excess of 10 MHz of electrical bandwidth, its speed as a current amplifier was limited to ~20 kHz, by the parasitic capacitance of the bias resistor. As dictated by the Bode-Fano limit, directly matching the HEMT to the larger impedances of the STJ will necessarily come at the cost of bandwidth. But even if the Q's necessary are 50 times larger than with the SET (*i.e.* matching to 2500 times higher impedance), the readout bandwidth of the RF-STJ would still allow it to resolve microsecond dynamics.

8.3 Impedance Matching to Subgap Currents

As discussed above, reflectometry uses a RF or microwave probe signal to infer the impedance of the device under test. This section will examine exactly what the impedance of the STJ is at RF frequencies and how it is modified when detecting photons. Having already verified that the subgap currents of the detector junctions are in excellent agreement with BCS theory, we can use these theoretical predictions to determine what the optimal bias conditions in terms of both DC voltage across the STJ as well the amplitude of the RF carrier. Furthermore, knowing the exact functional form of the impedance of the STJ, we can also determine the level of impedance matching that is necessary. Thus, an optimal tank circuit can be designed that balances these impedance requirements with practical considerations.

Figure 8.2 shows the subgap currents for an STJ as predicted by BCS theory for three different temperatures. These three temperatures represent different quasiparticle densities analogous to the non-equilibrium situation that occurs when the junction is detecting submillimeter photons. In the

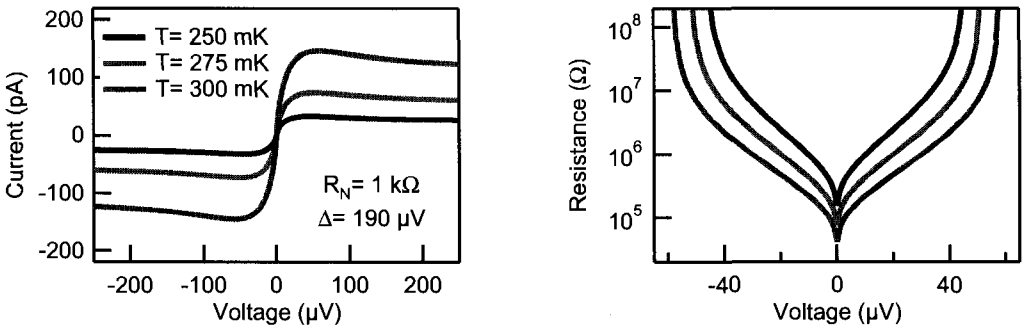

Figure 8.2: Theoretical curves showing the subgap current for three different quasiparticle temperatures. The differential resistance shows that the STJ has the lowest impedance near zero bias voltage, and that its resistance there is a sensitive function of the number of quasiparticles.

traditional measurement, the STJ is biased at around 100 μV and change in DC current is measured as a function of photon flux. It is important to note that there is no fundamental difference from the perspective of the junction between a voltage that is applied at DC or one applied at the RF frequencies that we will use. Its RF impedance is precisely the resistance that one would measure with a lock-in style measurement at audio frequencies or infer from the DC IV curve. This is because the reactive component of the impedance has been resonated out with the tank circuit. Just as the audio bandwidth is limited by the RC time junction itself, the bandwidth of the matching circuit cannot exceed this constraint. For typical junctions parameters, the normal state resistance-area product is $\sim$500 $\Omega - \mu m^2$. Assuming a specific capacitance of $\sim$50 fF/μm^2, this implies a normal state RC time of 25 ps. In the subgap, this resistance greater by a factor of order 10^4, making the RC time $\sim$250 ns. These typical RF frequencies of 300-500 MHz are chosen as a compromise between several factors. This frequency range simultaneously allows good impedance matching, low noise amplifiers, and large readout bandwidth.

To be more precise, the subgap resistance should be increased from the normal state resistance by a factor of order e^{Δ/k_BT}. But because the density of states also has a singularity just above the gap, there is more structure to the subgap conductance than this naive expectation. Formally, it implies a logarithmic singularity in the conductance at zero bias and even causes negative differential resistance (NDR) for voltages between k_BT/e and $2\Delta/e$ (Tinkham, 1996). From an experimental standpoint, these divergent effects are ameliorated by non-idealities such as the fact that the gap of aluminum varies within the sample on the microvolt scale. The negative differential resistance can actually cause a reflection coefficient that is greater than unity (*i.e.*, amplification) as has been on several occasions. In practice, this is only seen to be an appreciable effect in situations where unsuppressed supercurrent causes sharp NDR features. The slight predicted decrease in current at increasing voltage due to quasiparticle effects is small and not readily distinguishable from an open

circuit.

It is clear from Figure 8.2 that the resistance is lower at zero bias than anywhere else in the subgap. Despite the fact that the dynamic resistance at a typical DC STJ bias point of 100 μV is of order 1 GΩ, near zero bias it becomes a much more manageable value, closer to 1 MΩ. It is only here that a tank circuit can feasibly transform the impedance down to 50 Ω. In other words, the ideal bias point for the RF-STJ is to have no DC bias at all. So while throughout this thesis work a bias tee is used to vary the DC voltage across the junction, this would not be required or desired for an actual detector application. It merely provides a way to verify the relation between DC IV characteristics and reflected RF power.

Given this choice of bias point, the next bias condition to determine is the optimum amplitude of the RF carrier. For an ohmic resistor, the signal to noise ratio of a reflection measurement increases linearly with the RF power. But just as with an audio lock-in measurement, the impedance seen by the probe will average over any impedance changes within the amplitude of oscillation–resulting in an effective resistance. So despite the singularity in conductance near zero bias, a carrier of amplitude $\sim k_B T/e$ averages to give an effective impedance that is well approximated by $R_N e^{\Delta/k_B T}$. Assuming a typical gap for aluminum of 190 μV and a normal state resistance of 1 kΩ, this implies a zero-bias resistance of 1 MΩ at 300 mK. As the amplitude is increased beyond this range, the current does not increase. This means that the effective resistance seen by the carrier begins to scale linearly with the voltage until the gaprise is reached. Because the resistance is non-linear, there will power lost to higher order harmonics. Despite this, the impedance seen by the carrier in a vector network analyzer measurement clearly depends on the carrier amplitude. If the tank circuit is under-coupled, this effect may be exploited to use a larger carrier in order to provide a better impedance match. Because the impedance near zero is already at or above the impedance which can be matched to 50 Ω with typical tank circuits, there is little improvement in signal to noise ratio with increasing amplitude. Experimentally, for temperatures below 300 mK, the subgap current above Δ/e is dominated by higher order tunneling processes, not quasiparticle density (see Figure 6.6). This means that the conductance ceases to depend on photon flux for voltages beyond this point. Thus, the carrier amplitudes used in this work will typically be on the order of 20 to 200 μV. Assuming an effective resistance of 1 MΩ, the joule power of the bias is only $\sim$10 fW. While this power seems experimentally insignificant, minimizing the total power dissipated at the cold stage of the cryostat is a necessary requirement for scaling a single detector to a many pixel camera.

8.4 Noise and Sensitivity

With the simplicity of the RF readout, the most important issue to address is whether it can also achieve the sensitivity necessary for future applications. While any signal amplification process must add noise, the goal is to make this added noise negligible compared to the intrinsic noise of the

device. For photon counters, the intrinsic noise is the shot noise of the incoming photons. Expressed in terms of noise equivalent power, the shot noise limit is given by:

$$NEP = \sqrt{2h\nu P} \tag{8.1}$$

where P is the photon power and hν is the energy per photon.

Assuming an ideal responsivity of the STJ of two electrons per photon (each photon breaks one Cooper piar), these photon statistics will imply a current noise of:

$$i_n = \frac{2e}{h\nu}\sqrt{2h\nu P} = \sqrt{8eI} \tag{8.2}$$

where I is the current flowing through the STJ.

Not surprisingly, this noise has the same form as the electrical shot noise of the current itself, but is a factor of two larger because each photon creates two quasiparticles. In the case of non-ideal quantum efficiency, the current noise of the STJ itself will limit the sensitivity. This is the relevant benchmark to which to compare the current noise of the readout. These are the noise processes that will set the output noise temperature of the STJ as a detector. To be more rigorous, the current noise of tunnel junction at frequencies much less than k_BT or eV is given by (Rogovin and Scalapino, 1974):

$$S_I = i_n^2 = 2eI\,(V)\coth\left(\frac{eV}{2k_BT}\right) \tag{8.3}$$

In the limit of small bias voltage, this reduces to the Johnson noise required by the fluctuation dissipation theorem; for large bias, it becomes the usual shot noise formula. In order to best understand the noise in terms of power, it is more convenient to express this as a noise temperature. This is difficult because the STJ resistance is non-linear and changes as a function of bias point or carrier amplitude. A good approximation is to assume that the carrier see an ohmic real impedance for a given carrier power. We can further assume that this impedance is exactly the impedance that is matched to 50 Ω, by the tank circuit. With these assumptions, this current noise can be expressed in terms of an output noise temperature of the STJ as:

$$T_N = \frac{S_I R}{4k_B} = T\left(\frac{x}{2}\coth\left(\frac{x}{2}\right)\right) \tag{8.4}$$

where T is the quasiparticle temperature, $x = \frac{eV}{k_BT}$, and R is understood to be the effective impedance seen by the RF carrier. This equation assumes that the tank circuit has perfectly matched the device impedance to the amplifier.

The total noise at the output of the detector is a combination of three sources. First, there is the shot noise of the incident photons. The next noise source is the current noise from the tunneling current that is not due to photons. This is simply shot noise of the dark current. The last source

of noise is that of the readout. For a traditional current measurement with an FET, this is simply the current noise of the amplifier. For the reflection technique, this is the current noise of the RF amplifier transformed by the tank circuit. Assuming an ideal responsivity of two electrons per photon implies that the photocurrent, I_γ, is given by $\frac{2e}{h\nu}P$. The total NEP is then:

$$NEP = \sqrt{2h\nu P + \left(\frac{h\nu}{2e}\right)^2 (2eI_d) + \left(\frac{h\nu}{2e}\right)^2 (S_I^{amp})} \tag{8.5}$$

$$= \left(\frac{h\nu}{2e}\right)\sqrt{8eI_\gamma + 2eI_d + S_I^{amp}} \tag{8.6}$$

$$= \sqrt{2h\nu P}\sqrt{1 + \frac{I_d}{4I_\gamma} + \frac{4k_BT_N}{8eI_\gamma R_d}} \tag{8.7}$$

$$= \sqrt{2h\nu P}\sqrt{1 + \frac{I_d}{4I_\gamma} + \frac{k_BT_N}{2eV_{RF}}} \tag{8.8}$$

In general, reflectometry can add gain to the measurement if the carrier can be made large enough. Equation 8.4 explicitly shows the power gain that is possible when $eV > k_BT$. In this case the output noise temperature can be much larger than T. Unfortunately for the STJ, the size of the carrier is limited by the energy scales of the STJ itself. It is only over a range of $V_{RF} \approx k_BT/e$ that the impedance is roughly linear and small enough to match to 50 Ω. The carrier can be increased beyond this point with diminishing improvement due to the impedance mismatch and the non-linearity of the STJ. By the time the carrier voltage is comparable to the superconducting gap, the subgap current is no longer a function of quasiparticle density. This means that beyond this point, there will be no improvement in sensitivity. Combining these bias limitations with equation 8.4, determines the ultimate output noise temperature of the STJ. For RF bias voltages comparable or less than k_BT/e, the output noise temperature of the STJ is merely the quasiparticle temperature. The fact that the current through the STJ does not increase as the bias voltage is increased from k_BT/e to Δ/e means that neither does the output noise temperature of the detector. Thus, the reflectometry in this application can, at best preserve the noise temperature of the HEMT as the limiting factor in the measurement, but it cannot improve upon it. This differs from the case of an FET or SET, where the measurement of the STJ's current is simultaneously transforming the impedance and amplifying the signal. Both of these amplifiers can have a noise temperature that is much lower than either their physical temperature or that of the STJ . Omitting this first stage of amplification, and passively impedance transforming to match to a HEMT amplifier implies that the limiting factor becomes the noise temperature of the HEMT. In other words, even with perfect matching, RF-STJ constitutes transduction rather than amplification. Given that commercial HEMT amplifiers can have noise temperatures of ~ 1 K, this readout does not miss the shot noise limit by much, but will necessarily remain a fixed factor above this limit. The advent of other lower noise microwave amplifiers could provide a path to true photon-shot-noise limited sensitivity for the RF-STJ.

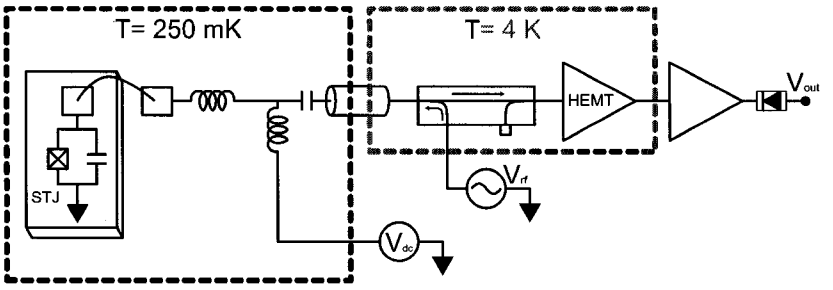

Figure 8.3: The above circuit diagram shows how the RF reflection measurements are performed. While this circuit is already much simpler than that of the STJ with and RF-SET readout (see Figure 7.20, it is important to note that the DC bias shown above is merely for characterization and would not be required in actual applications.

In terms of pure current or photon sensitivity, the RF-STJ can always be made lower noise by using small junctions and higher Q transformers. But as seen from the above equations, the shot noise limit will also be reduced by the same amount. Thus, the primary drawback of this passive readout is that the system can be optimized for any given photon power, but can never beat the shot noise limit without a lower noise microwave amplifier. While being within a factor of two of the shot noise limit is unimpressive for high photon power, ground based applications; it could be state of the art for ultra-low power spaced-based applications where other methods are not yet at this limit.

8.5 Characterization of RF Readout

One the many advantages of this new readout is that the Schoelkopf lab is the ideal place to test such an idea. All the infrastructure integrating sensitive microwave measurements into a cryostat was already in place for RF-SET measurements. In order to test the RF-STJ, all that needed to be done was to omit the SET. With the first measurements, the goal was both to demonstrate that the RF measurement did not corrupt the DC characteristics of the STJ and to show the dependence of the reflected power on the subgap current. To accomplish this, a high impedance SQUID with an R_n of 25 kΩ was chosen in order to ensure good supercurrent suppression. This implies that the zero-bias resistance at 250 mK should be greater than 100 MΩ. Ideally, this impedance would be transformed to 50 Ω using a tank circuit with a single stage Q of 1500. This is unrealistic in two respects. First, using commercial surface mount inductors, conductor losses will limit their internal Q to ~500. Even if the inductor were superconducting, the fact that it would connect to the junction via a wirebond implies that the parasitic capacitance must be at least 50 fF from the bondpad itself. This capacitance would then have an impedance on resonance of only a factor 200 above 50 Ω. Both of these issues could be improved by having a lithographically fabricated inductor directly wired to the junction on the chip; but for initial measurements, simple surface mount technology was used.

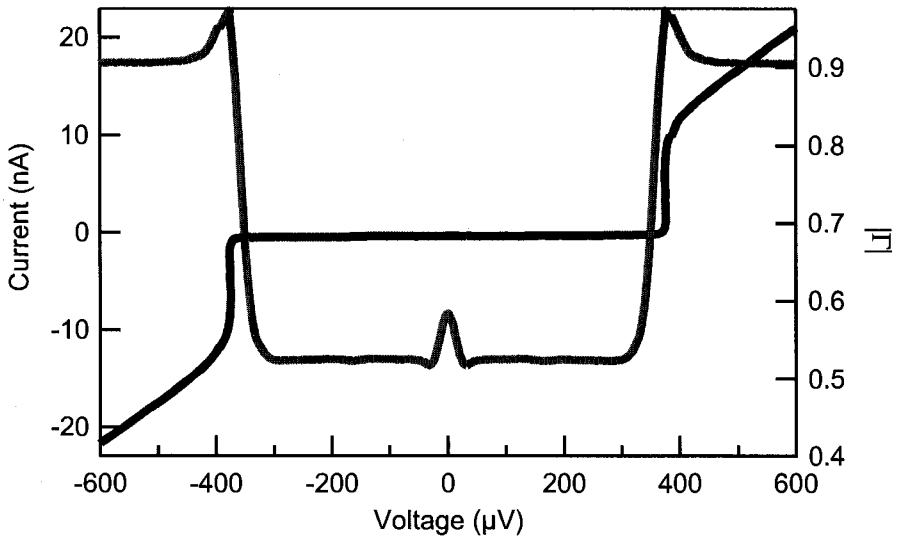

Figure 8.4: Simultaneous measurement of the DC current and the reflection coefficient as a function of bias voltage at T=300 mK. The height of the feature at zero bias voltage is a measure of the number of quasiparticle in the absorber.

The capacitance was minimized by placing the chip and the inductor on several FR-4 dielectric circuit boards and using a tall lid for the sample holder. The inductor was a coilcraft 0805-CS-471 surface mount inductor, whose nominal low frequency inductance is 470 nH. Since its self-resonant frequency is nominally 550 MHz, the effective inductance will be much higher as it is used close to (but less than) this frequency.

Upon mounting in the ^{3}He cryostat and cooling to 270 mK, the resonance frequency was found to be 350 MHz. By varying the bias point of the STJ in order to change is RF impedance, the tank circuit can be fully characterized. Just as a vector network analyzer can be calibrated by placing a short, open, and load on its input, the same can be accomplished *in situ* with the STJ. The supercurrent (before suppression) provides a short circuit, the subgap region gives the "open", and finally, at high bias, the quasiparticle branch is a calibrated load. It was found that the magnitude of the impedance of the inductor or capacitor on resonance was 6500 Ω. In other words, the effective inductance of the surface mount component is 3 μH and the capacitance is only 70 fF. This implies a Q of 130 and an optimal matching impedance of close to 1 MΩ.

Figure 8.4 shows the simultaneous measurements of the DC current-voltage characteristic and the reflected RF voltage. In this measurement the RF carrier is applied at 350 MHz. Using a spectrum analyzer, the reflected carrier voltage was inferred from the total power in a narrow frequency window. It should be noted that this method of demodulation is susceptible to excess noise when the reflected carrier is very small and the resolution bandwidth of the measurement is large. In later

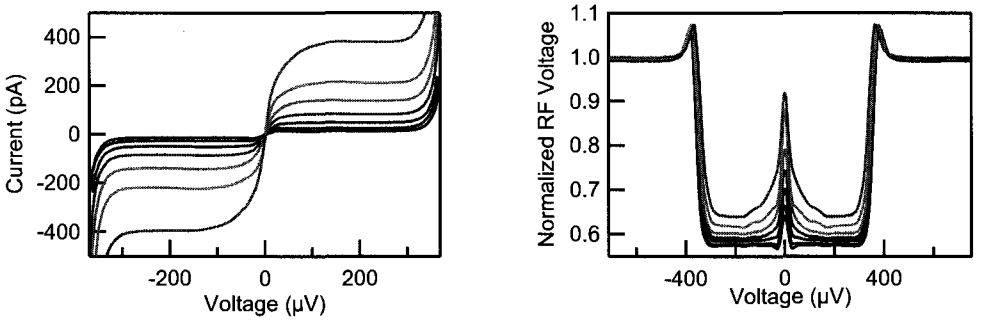

Figure 8.5: DC and RF "IV" curves measured as a function of temperature. The cryostat temperature is varied from 300 to 600 mK. The RF bias power is -120 dBm, which corresponds to $\sim$10 μV across the device.

measurements, a mixer was used to measure the amplitude and phase of the carrier in order to avoid this issue. From Figure 8.4, one can clearly see that the RF reflection measurement closely tracks the differential resistance. Furthermore, the small reflection coefficient in the subgap region implies that the tank circuit matches the large subgap resistance to the 50 Ω amplifier. The height of the feature near zero bias should be a direct measure the quasiparticle density. In lieu of an actual photon source, the quasiparticle density can be changed by simply varying the cryostat temperature. While there can be subtle differences between higher temperatures and the non-equilibrium conditions created via a photon measurement, this method allows us to verify the expected behavior of the STJ and the RF readout. The results of this measurement are shown in Figure 8.5. The cryostat was heated from 300 to 600 mK resulting in an increase in the subgap current from 10 to 400 pA. More importantly, the dynamic resistance near zero bias voltage changed from $>$ 1 MΩ to $<$ 100 kΩ. This impedance change meant that the carrier went from being mostly absorbed by the tank circuit to being mostly reflected.

These measurements demonstrate the basic principle of the RF-STJ readout. These results also show that coupling the STJ directly to the amplifier does not corrupt the low dark currents that of the detector, at least at ^{3}He temperatures. A 550 MHz, multipole, low pass filter was used between the HEMT and the device to limit high frequency noise from affecting the device. In future incarnations, a cryogenic circulator may be used provide in band isolation as well. This work also shows that even without the added complexity of an on-chip inductor, single-stage tank circuits can match to impedances on the order of 1 MΩ. The next section will discuss in more detail the measured current sensitivity.

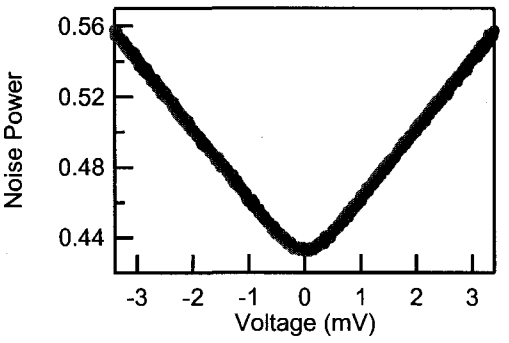

Figure 8.6: Using the shot noise of the STJ, the noise temperature of the amplifier can be measured directly. This data is taken at T=1.5 K, which is above the T_C of the aluminum. Thus the STJ is completely ohmic with a resistance of 25 kΩ. The black line is a fit to Equation 8.3, which gives an electron temperature 1.53 K and an amplifier noise temperature of 61 K for this impedance of the STJ. Because the tank circuit is designed to match to a much higher impedance of 845 kΩ, this measurement implies that the system noise temperature when biased in the subgap is 6 K.

8.6 Characterization of Sensitivity

This section shows the measurements that can be performed to characterize *in situ* the sensitivity and noise performance of the RF-STJ. Given that the sensitivity of the RF-STJ is limited by the HEMT amplifier, it is crucial to minimize losses and maximize power matching in order to keep the system noise temperature as low as possible. While the reflection technique cannot improve the system noise temperature, it can certainly make it worse. The first check to make is to determine exactly to what impedance the tank circuit is optimally matched. This can be done in two ways. Measuring the width of the tank circuit resonance is a direct measure of the loaded quality factor, Q_L. For a lossless, single stage transformer, this quality factor completely determines the matching circuit. Knowing the resistance of both the STJ (R_d) and amplifier (R_o), one can solve for the impedance of the tank circuit on resonance, Z_{LC}.

$$Q_L = \left(\frac{Z_{LC}}{R_d} + \frac{R_o}{Z_{LC}} \right) \tag{8.9}$$

The optimum noise impedance is when power matching occurs and the resonance is equally loaded by the STJ and the amplifier.

$$R_{opt} = \frac{Z_{LC}^2}{R_o} \tag{8.10}$$

If there is a bias point of the STJ where the dynamic resistance takes on this value, it can also be seen directly because this will be the point of minimum reflected power. This is actually the most precise way to determine the properties of the tank circuit. It is only at this impedance that the

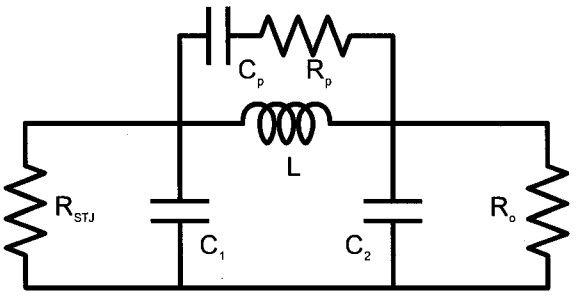

Figure 8.7: Two stage tank circuit used for matching to 2 MΩ. C_1 is merely the capacitance of the bondpad, while C_2 comes from a surface mount capacitor. The inductor used here is an on-chip spiral inductor, with its parasitic self resonance and loss modelled as a series RC shunt.

noise temperature of the amplifier will be preserved; at all other impedances it will necessarily be increased.

Knowing this optimum impedance, the system noise temperature can be measured at any dynamic resistance and the optimum noise temperature may be inferred. Typically, this is easiest at large bias or high temperature where the STJ is ohmic, with a dynamic resistance equal to its normal state resistance, R_N. This measurement can be done with a traditional Y-factor (i.e. varying the physical temperature of the load) or using the shot noise as a calibrated noise source. Just as with the shot noise thermometer (Spietz, 2005) the measurement of the noise power gives a primary measurement of both the physical temperature and the noise temperature of the system. Figure 8.6 shows such a measurement. It was taken at 1.5 K where the STJ is completely normal with a resistance of 25 kΩ. When fit to equation 8.3, it gives an electron temperature of 1.53 K and a noise temperature of 62 K. While this seems quite high, it is mostly due to the fact that the tank circuit is designed to match to the large subgap resistance, not the 25 kΩ R_N of the junction. Taking into account the known impedance mismatch between R_N and R_{opt}= 845 kΩ gives a system noise temperature of 6 K on match. This implies that the current noise of the HEMT is only 20 fA/$\sqrt{Hz}$. Assuming a reasonable responsivity for an STJ at 100 GHz of 3000 A/W implies an electrical NEP of less than 10^{-17} W/$\sqrt{Hz}$.

This current sensitivity can also be obtained directly by measuring how much the reflected power changes for a given change in the subgap current. Because the change in current can be measured directly, the voltage noise of the RF readout can be converted to current noise units. In a separate device that was also measured in the ^{3}He cryostat, this method was employed. An STJ with an R_N of 92 kΩ was cooled to 275 mK. The tank circuit was configured as shown in Figure 8.7 with a two-stage, "pi" network to match to an STJ resistance of 2 MΩ. A 75 pF surface mount capacitor shunted the 50 Ω side of the matching circuit; while the capacitance across the STJ of 375 fF arose primarily from the bondpad. The inductor was an on-chip spiral inductor as designed and fabricated

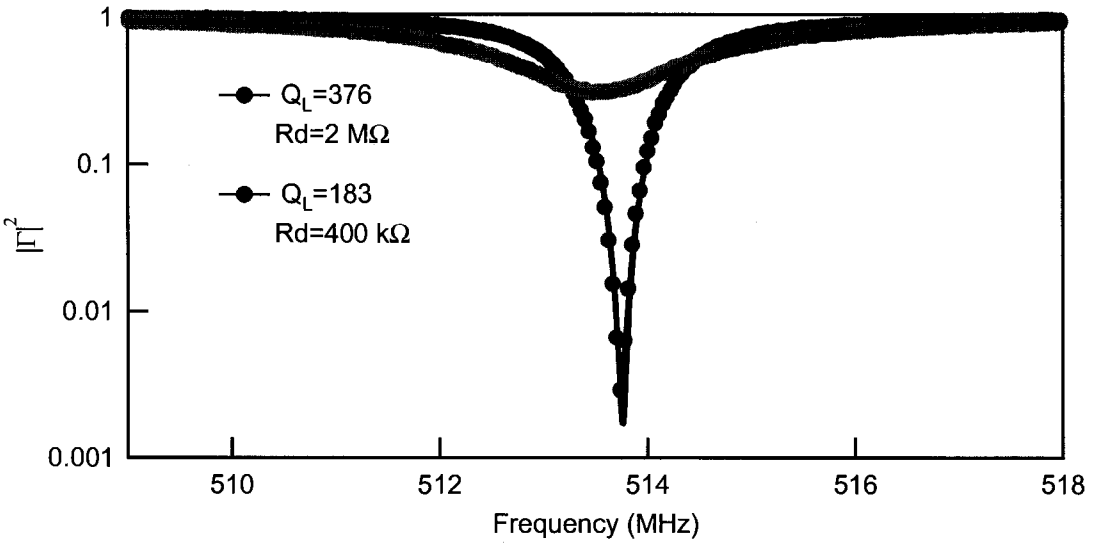

Figure 8.8: Measured reflection coefficient and Lorentzian fits for two different dynamic resistances of the STJ. By changing the bias point of the STJ, a full calibration of the resonance is possible. This circuit shows loaded quality factors as high as 400, but is limited by the internal Q of the matching network.

by NASA Goddard. The details of the inductor can be found in reference (Stevenson et al., 2002). This specific inductor has an inductance of 256 nH at low frequencies. The parasitic capacitance shunting the inductor is less that 100 fF and does not affect its performance at 500 MHz.

This tank circuit in the C-L-C configuration allows one to match to high impedances, but only at the cost of drastically increasing the necessary quality factor of the circuit. It was ambitiously designed have a loaded Q of 2500 on match. Because the inductor in the this case is a bilayer of Au and superconducting Nb, the conductor losses that usually limit the internal quality factor of inductors need not be the dominant loss mechanism. The ability to tune the dynamic resistance of the STJ meant that the tank circuit could be completely characterized, including any internal loss. Figure 8.8 shows data measuring the reflection coefficient at two different STJ resistances. The resonance frequency of 513.6 MHz lies well within the optimal frequency range for the HEMT amplifier. While the data clearly shows that the circuit is best matched to a resistance of 2 MΩ, the width implies an internal quality factor for this circuit of 560. While this necessarily implies that some of the signal from the junction is lost, effectively increasing the noise temperature of the amplifier, the overall circuit still shows a very low current noise.

Again, the noise temperature of the amplifier can be measured directly just above T_C using shot noise as a calibration. For this device the measured noise temperature was 22 K when the device resistance was 92 kΩ. Because the tank circuit is designed to match to 2 MΩ, this noise

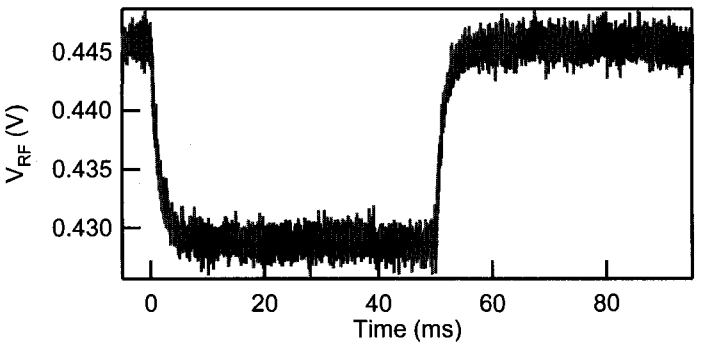

Figure 8.9: This graphs shows the response of the RF readout to a heat pulse. The heat pulse was applied to the chip and gave rise to a 1.8 pA change in the subgap current. This change is easily resolved with good signal to noise. The rise and decay time of the signal is give by the thermal time constant of the chip; in this case, it is 2 ms.

includes a known reflection coefficient of 0.913. Accounting for this, the system noise temperature when referred to match is 3.7 K. This closely reproduces the known system noise temperature of the HEMT with a 50 Ω load. This extrapolation of the matched noise temperature does not account for the internal loss of the tank circuit, which becomes increasingly important as the device resistance is increased. Analysis of the lossy circuit model suggests that this effect will roughly double the noise temperature when the device resistance is 2 MΩ. While further studies would be required to determine the source of this loss, possible explanations include: resistive losses in the gold part of the inductor, a poor loss tangent of the surface mount capacitor, or simply radiation from the circuit.

This current noise can be measured directly by changing the subgap current by a known amount and measuring the signal to noise with which the RF technique can resolve it. By pulsing current through a separate tunnel junction that is on the same chip (but not electrically connected), the chip and the device under test can be heated by ∼1-100 mK on short timescales. As has been shown throughout this thesis, the subgap current of the STJ is an extremely sensitive thermometer. It was found that applying 80 nW of Joule power to the chip increased the temperature from 300 mK to 335 mK as measured from the quasiparticle currents. This corresponds to a thermal conductivity of order 1 μW/K between the chip and the rest of the cryostat. The timescale of the cooling was 2 ms which further implies the heat capacity of the entire chip is roughly 2 nJ/K. Figure 8.9 shows the response of the the RF readout of the STJ to a much smaller heat pulse that corresponded to a 1.8 pA increase in the subgap current. The measured signal to noise ratio of the pulse height to the RMS voltage noise is 22. Given that the the bandwidth of the detection was 10 kHz and that this trace is averaged 500 times, this shows a subgap current sensitivity of 20 fA/$\sqrt{\text{Hz}}$.

The former paragraph uses only the total RMS fluctuations and assumes that the noise is white

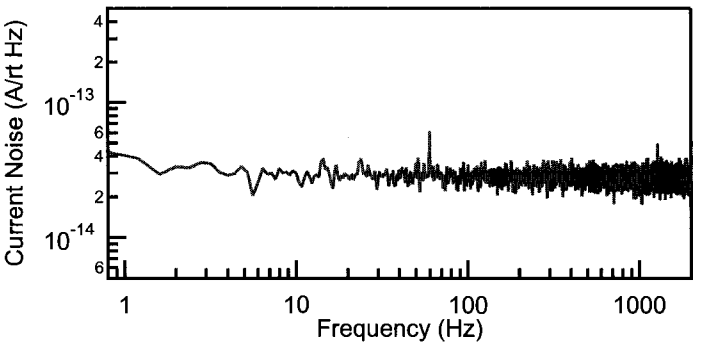

Figure 8.10: Measured current noise of RF-STJ readout. The spectrum is completely white over this frequency range showing no signs of excess noise, 1/f noise, or pickup.

across the measurement band. A better measurement would be to measure the noise spectrum directly to ensure that the RMS noise is not dominated by individual noise peaks or 1/f noise. This spectrum can be converted to a current noise using the same calibration factor found in the the previous measurement. Figure 8.10 shows the result of this measurement for the same parameters. While this tank circuit allows measurement out to 1 MHz, this spectrum shows the low frequency noise in order to emphasize the lack of 1/f noise in the measurement. The noise is in fact white, and appears to be completely HEMT limited. This spectrum is in stark contrast to the noise of the SET, where charge fluctuations dominate the overall noise out to high frequencies (1 kHz-1 MHz depending on the device). This also shows that other sources of noise, including gain instability of the amplifier, RF pickup, and vibrational noise, are not an issue for this technique. While the current sensitivity is still not quite as low as a well-designed FET, it already implies an electrical NEP of less than 10^{-17} W/$\sqrt{\text{Hz}}$.

8.7 Readout Timescales

One final aspect of the RF readout that may be characterized is the readout bandwidth. In the frequency domain, this is measured directly from the FWHM of the loaded resonance. All tank circuits in this thesis work have resonant frequencies between 350 and 550 MHz and loaded quality factors ranging from 20 to 400. This implies all of the matching networks would allow measurements on the sub-microsecond timescale. While this readout speed is not required for most applications, ideally the readout bandwidth should be faster than the response time of the detector itself. For an STJ, this timescale is given by whatever the dominant mechanism is for non-equilibrium quasiparticles in the absorber to return equilibrium. For an ideal detector, the timescale is set by the tunneling time. This is the timescale for non-equilibrium quasiparticles to tunnel across the detector junction out of

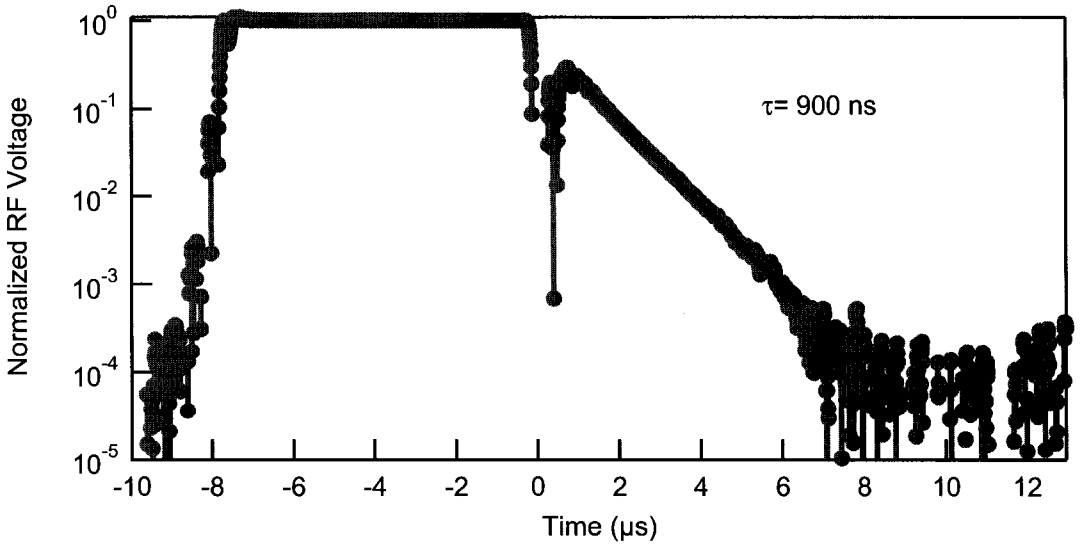

Figure 8.11: The decay time of the STJ detector measured by pulsing the STJ bias voltage and using the RF readout. This device shows a quasiparticle equilibration time of 900 ns, much slower than the readout response time of 50 ns. In chapter 10, this method will be used to determine if the non-equilibrium quasiparticle lifetime is limited by the tunneling or recombination time.

the absorber. If the quasiparticle confinement is not perfect, it is possible for the quasiparticles to scatter into the the large Nb leads and never be measured. Even if the confinement were perfect, if the tunneling time is too slow two quasiparticles can eventually recombine into a Cooper pair. While this recombination time can also limit the quantum efficiency of the STJ, it can be made negligible by either reducing the number of quasiparticles or decreasing the tunneling time. Thus, an important characterization for the detector is demonstrating that the tunneling time is, in fact, setting the detector response time.

In lieu of a photon source that can be pulsed on or off very quickly, this timescale can be measured by pulsing a large current (at DC or RF) through the detector junction itself. Once the bias voltage exceeds 2Δ, many quasiparticles will be generated. By pulsing back down to the subgap region and measuring the decay of the quasiparticle currents, one has a direct measure of the timescale of the detector. Although the timescales are given by completely different physics, this is the same method that has been used to characterize SINIS bolometers (Schmidt et al., 2005). While this technique will be used in later chapters to directly measure the tunneling and recombination time, it is presented here to demonstrate one of the advantages of the RF readout. Figure 8.11 shows the the result of pulsing the DC bias across the tunnel junction to 2 mV and then back down the zero. The RF voltage rings on short timescales, but there is a clear exponential tail showing the quasiparticle lifetime of the device. In this particular measurement the readout bandwidth was 3 MHz and it

could easily resolve the 900 ns decay time of the device.

8.8 Conclusions

This chapter demonstrates the basic principles and methods for using radio frequency reflectometry to measure the state of the detector. The readout possesses all the attributes necessary for sensitive readout of large format arrays. It is simple; with no DC wires required for operation. It successfully exploits the excellent bandwidth, noise temperature, dynamic range and stability of cryogenic HEMT amplifiers in way amenable to frequency domain multiplexing. While the readout does rely on dissipating power on the chip, the small carrier powers necessary imply that the bias Joule heating is of order 1-10 fW per pixel. The sensitivity has been shown to be limited by the noise temperature of the HEMT amplifier. This demonstrates that the noise has not yet reached a fundamental limit and there is room for improvement as lower noise microwave amplifiers based on Josephson junction technology become available. The microwave readout also possesses flexibility to optimize the speed or sensitivity of the detector depending on the application. While this thesis work concentrated on the RF-STJ for submillimeter photon detection, its use is equally applicable to both the optical and X-ray bands.

Chapter 9

Submillimeter Photon Sources

"The thing to do is to supply light and not heat."

–Woodrow T. Wilson

In order to fully understand the performance of any photon detector, it is important to study its response under illumination. This chapter details the various experimental methods for providing an STJ with a predictable amount of submillimeter wave radiation. This region of the electromagnetic spectrum is difficult to work with for several reasons. The losses, both conductor and dielectric, are much greater than with microwave signals. These intermediate wavelengths are too long for many optical techniques; yet too to short for coaxial transmission lines. Even generating coherent signals in this spectrum is difficult. It can be accomplished using nonlinear media to either up-convert microwave signals or down-convert optical or infrared lasers. Further difficulties arise when trying to couple to a sensitive detector. Thermal radiation from room temperature objects provide more than enough radiation to completely saturate the detector. For this reason, the detector and the cryostat have been designed with extensive filtering in order to block or attenuate this ubiquitous room temperature radiation. In providing a way to intentionally couple light from room temperature into the cryostat, one must be certain that light source can be completely turned off. In other words, the setup must ensure that opening this frequency window in the filtering does not allow the detector

to be overwhelmed simply by thermal radiation. This necessary attenuation must then be fully calibrated up to the detector in order to allow quantitative measurement of the properties of the detector. It is for all of these reasons that we decided to pursue the idea of generating the photons from within the cryostat and coupling them to the detector. This chapter will explain the ways in which submillimeter and millimeter wave radiation can be created and detected all at cryogenic temperatures as well as show measurements demonstrating this is possible.

9.1 Requirements for Photon Sources

There are many requirements for the ideal photon source. The source must be capable of producing radiation at frequencies of at least 100 GHz. Unlike a bolometer that may be calibrated with photon power from lower frequency radiation or even DC Joule power, the STJ is a photoconductor that only responds to photons with $h\nu > 2\Delta$. This source should also be tunable in both power and frequency. As mentioned above, it is necessary that when the source is not on, that the detector does not see any excess radiation. It is also desirable that this source can be turned on and off quickly. If the time constants of the source are faster than the detector itself, this provides a method for directly measuring the speed of the STJ and its readout. Beyond this, simply being able to chop the signal at audio frequencies gives a differential measurement that is less subject to many systematics or drifts in the measurement.

One of the most difficult requirements is that the source be efficiently coupled to the detector. Assuming that the source can provide enough power, the absolute coupling efficiency is not a limitation. What is more important is that the coupling be precisely calibrated and reproducible so that the power at the detector can be known. Unlike microwave frequencies where commercial sources can be easily coupled with coaxial cables with little distortion or loss, this becomes much more difficult as the signals of interest exceed ~50 GHz. The physical dimensions of SMA cables imply that they will necessarily become overmoded at these frequencies. These higher order TE and TM modes lead to changes in the impedance, phase velocity, and dispersion at different frequencies. In addition, the losses from both the physical length of the transmission line and the connectors prevent them from being a viable option for submillimeter or even millimeter waves. This leaves two options for transmitting signals: waveguide or quasi-optics. Waveguide technology is designed to support a TE mode. For example, WR-5 rectangular waveguide is designed with an inner cross-section of 1.3 mm by 0.65 mm. It can be used from 140 to 220 GHz. Stainless steel waveguide would be necessary to transmit a signal from room temperature to ^{3}He temperatures. The electrical loss of the stainless steel provides both the thermal isolation to span the temperature gradient and simultaneously attenuates the unwanted blackbody radiation. In order to then couple from the waveguide to the detector, the signal would be sent quasi-optically from a waveguide feedhorn to an on-chip planar antenna terminated with the STJ. These are the methods used in many actual telescope applica-

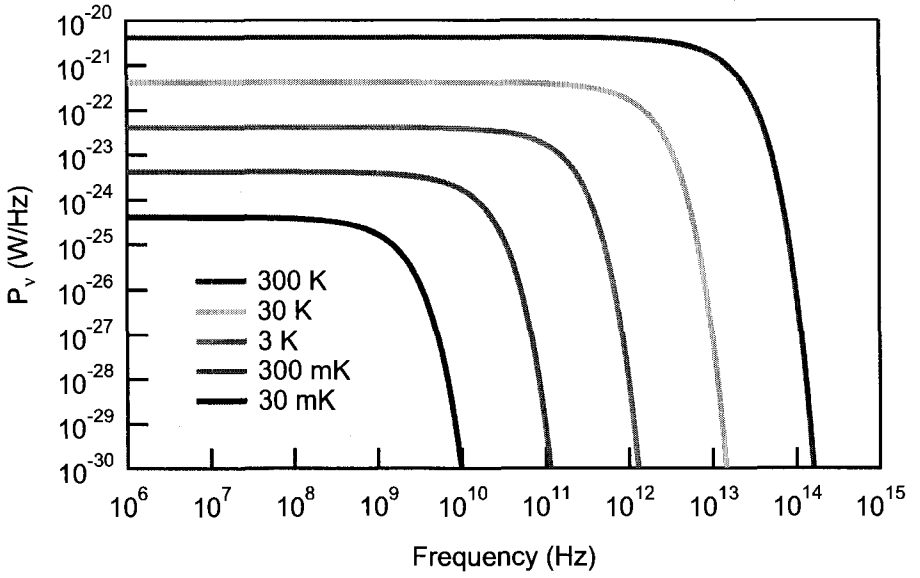

Figure 9.1: The power radiated by a 1-D blackbody as a function of frequency. These spectra clearly show the transition from the Rayleigh-Jeans limit where the noise is while (independent of frequency) to the Wien limit where it is exponentially falling. As the universe is a nearly ideal blackbody with a temperature of 2.735 K, the curve at 3 K is a good approximation of the power seen by an antenna-coupled detector in space-based applications.

tions for calibration. In general, quasi-optical coupling is difficult to precisely calibrate from a room temperature source completely onto the chip. This motivated the idea of using a cryogenic source as an illumination method.

9.2 Cryogenic Blackbody as a Calibration Source

One traditional way that engineers and astronomers have calibrated their measurements is to use thermal radiation as a calibrated source. By monitoring the response of a detector to a hot and then a cold load of known temperatures, the gain and sensitivity may be directly measured. In optics, this is accomplished by aiming the detector at a black surface (unity emissivity); while in the microwave, this is usually done with a transmission line terminated in its characteristic impedance. What is important is that these are completely equivalent. In both cases, the photon power seen by the detector is simply the one dimensional blackbody radiation of the thermal source. In other words, this radiation is nothing more than the Johnson noise required by the Fluctuation-Dissipation theorem for a resistive element at finite temperature. The radiated power per unit bandwidth at a given frequency is given by:

$$P_\nu = \frac{h\,(\nu/c)^d}{e^x - 1} \tag{9.1}$$

where $x = \frac{h\nu}{k_B T}$ and d is the dimensionality of the system.

For a three dimensional system whose size is much larger than the relevant photon wavelengths, this equation gives the familiar Stephan-Boltzmann relation. There is a peak in the blackbody spectrum when $\nu \approx 3k_B T/h$, and for higher frequencies, the power falls off exponentially. The total radiated power, found by integrating over all frequencies, is proportional to T^4. In 1-D, however, there is no peak in the spectrum, as shown in Figure 9.1. At low frequencies, when $h\nu \ll k_B T$, it is completely white. This is the Rayleigh-Jeans limit, and here the noise power per unit frequency is simply $k_B T$. This is nothing more than the usual Johnson noise formula and is applicable for calculating the noise power of a resistor for most situations. However, once in the limit of cryogenic temperatures and microwave frequencies, the effect of the Bose-Einstein occupation factor may become significant. At room temperature, this transition occurs at ~6 THz. But for a resistor at 1 K, the quantum effects are important above ~20 GHz. Above this frequency, the number of photons per mode begins to drop exponentially. This is known as the Wien limit, and it is precisely in this regime that a direct detector can significantly outperform even a quantum-limited, phase-preserving amplifier.

By design, all resistive bolometers that are used to detect a particular wavelength radiation are also well suited for emitting it. That they are impedance matched to absorb submillimeter waves necessarily implies that they also efficiently radiate. Some part of the bolometer must be thermally isolated so that its temperature can decouple from environment as it detects photons. This temperature rise is normally detected as a charge in resistance. Conversely, DC bias current can Joule heat the bolometer so that its blackbody radiation will increase. This temperature can be measured directly from the DC resistance. The small thermal conductance that gives it a large temperature rise for a given amount of absorbed energy, requires a small heat capacity in order to keep the thermal time constant of the circuit fast. This means that the source can be heated and cooled with small amounts of power on a fast timescale. For all of these reason, the use of a submillimeter bolometer as an emitter is a good candidate for illuminating the STJ from within the cryostat.

9.3 Quasi-Optically Coupling to a Macroscopic Bolometer

Our collaboration with NASA Goddard Space Flight Center in fabrication and design of the STJ detectors also provided valuable access to other current bolometer technology. Their HAWC (High-resolution Airborne Wideband Camera) detectors were designed for ground-based large format of arrays for submillimeter wavelengths (Stahle et al., 1999; Voellmer et al., 2004). These detectors are cryogenic bolometers based on hopping conduction thermistors. By properly doping the semiconductors, they are designed to have an exponentially temperature dependent resistance that is ~100 MΩ at the operating temperature of 300 mK. The thermal isolation is provided by suspending

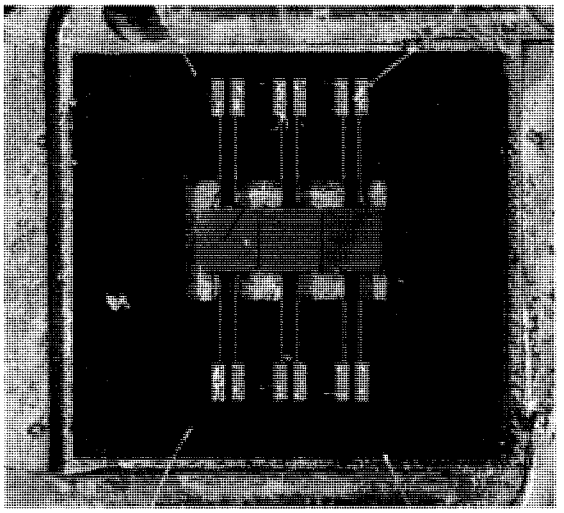

Figure 9.2: This is a photograph a HAWC bolometer used by NASA as a submillimeter wave direct detector. The transport through the properly doped semiconductor gives its resistance an exponential temperature dependence. The large black region is a thin silicon membrane mounted on a copper block. This silicon is micro-machined and suspended in order to provide the required thermal isolation. The three silver-colored squares in the center are three pixels wired in series. The silver color arises from a bismuth coating that ensures good emissivity at the appropriate frequencies. The two sets of gold wirebonds allow independent bias and measurement of resistance of the bolometer. For scale, each square pixel has an area of 1 mm^2. In this work, the bolometer will be used in reverse to emit, not absorber radiation.

the bolometer from thin, micro-machined silicon legs. As shown in Figure 9.2, three 1 mm^2 pixels are mounted in a copper block. The absorber is coated with bismuth in order to ensure efficient absorption of radiation. The match is further improved by adjusting the distance from the ground plane behind the detector so that the backshort properly tunes the impedance. The thermistors themselves have a temperature dependence that obeys the following form:

$$R(T) = R_o e^{\sqrt{\frac{T_o}{T}}} \tag{9.2}$$

When in use as an actual detector, it is current biased through a large (400 MΩ) resistor and its resistance is measured with a JFET. The radiation is coupled quasi-optically. The copper mount can be coupled to waveguide components and eventually feedhorn antennas. In our case, the idea is to exploit this well-establish infrastructure to have a calibrated source for our detector. DC biasing the bolometer means that its increased thermal radiation will be efficiently coupled to the feedhorn. This may then be focused onto an antenna-coupled STJ. The natural thermal isolation of the bolometer means that only the small absorber needs to become hot. Ideally, the bolometer's temperature can be raised to $\sim$10 K, without raising the temperature of the cryostat. The advantages of this scheme are that both the source and the detector are enclosed in a light-tight copper housing at the base temperature of the cryostat. This ensures that the detector (or the source) will not be subject to

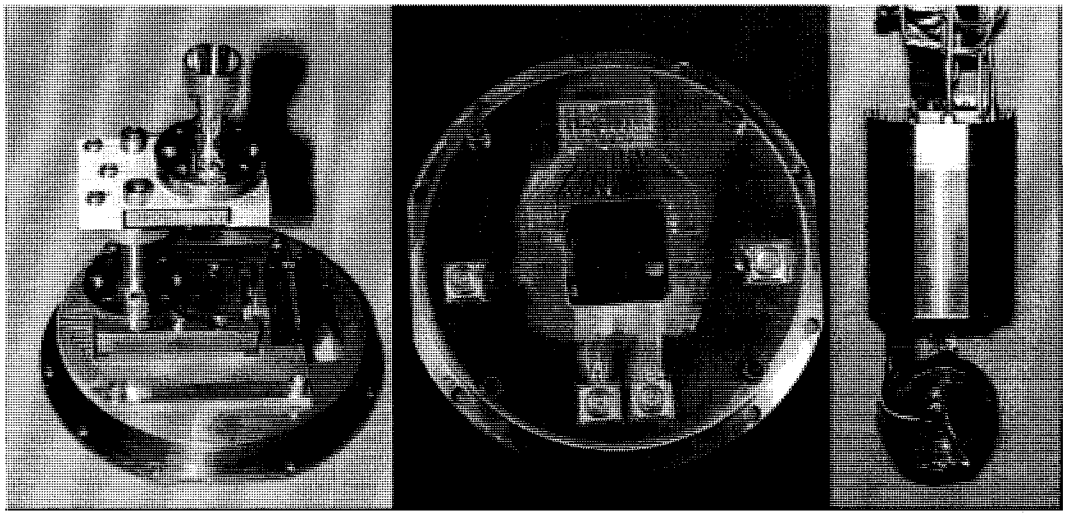

Figure 9.3: These three photographs show how the bolometer is used to quasi-optically illuminate the antenna-coupled STJ. Shown on the left is the bolometer to feedhorn coupling. The bolometer radiates into a waveguide, through a bandpass filter centered at 200 GHz, then out of the feedhorn. The center picture shows the chip with the STJ sitting on a quartz window that will be placed just above the feedhorn. Finally, the righthand picture shows the final assembly. Both the source and the detector are enclosed in a light-tight housing and mounted on the ^{3}He stage of the Heliox cryostat. The role of copper ribbon hanging from the bottom of the fixture is a lossy, transmission line filter for 20 twisted pair lines. The RF measurements are performed using the four SMA cables that enter the top of the sample holder. For scale, the diameter of the cylindrical enclosure is about 7 cm.

extraneous noise or unintended terahertz radiation. While the thermal time constant of this source is much slower than the STJ, it does allow the signal to be chopped on and off rates of roughly 100 Hz.

Figure 9.3 shows how this source was incorporated with the STJ detector. The bolometer is located at the bottom and is coupled to a round waveguide segment. The waveguide is then connected to a commercial bandpass filter from Pacific Millimeter. It has a 30 GHz bandpass centered around 200 GHz and is known to work at cryogenic temperatures. The signal then is radiated toward the detector with a feedhorn. Above the feedhorn, the chip with the antenna coupled STJ sits on a quartz window. The STJ is illuminated through the back of the silicon substrate in order to maximize the coupling. An antenna on a dielectric half-space will always preferentially radiate into the region of higher dielectric constant. The high dielectric constant of silicon (11.9) also implies that there will necessarily be a reflection between free space and the substrate. The quartz window is designed to be $\lambda/4$ thick so that it serves as an antireflection coating at 200 GHz. This impedance transformation occurs because the dielectric constant of the quartz window is roughly the geometric mean of silicon and vacuum. The antenna is a bowtie design that is 140 μm long. This is in the short dipole limit but can still effectively couple 200 GHz radiation. While there are many other

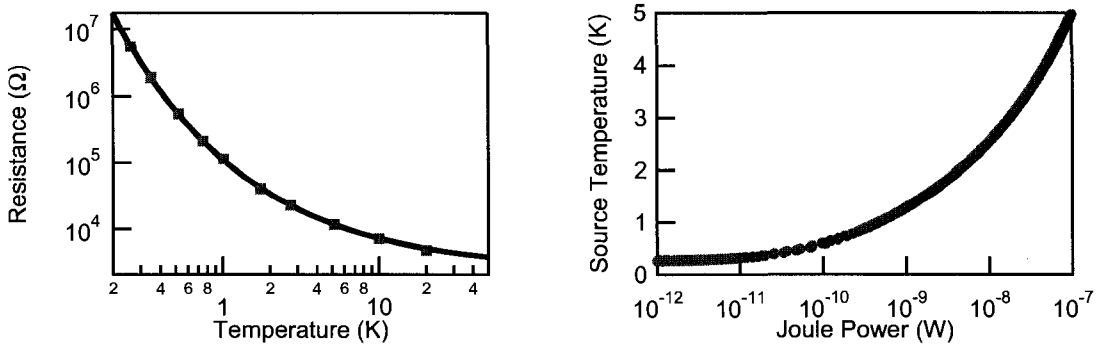

Figure 9.4: These data show the thermal characterization of the bolometer source. The temperature dependent resistance of this thermistor has a functional form of: $R(T) = R_o e^{\sqrt{T_o/T}}$. In the left graph, the square points are the data and the solid black line is a fit to this form with R_o=1880 Ω and T_o=16.7 K. The right graph shows the bolometer temperature (determined from the resistance) as a function of DC applied Joule power. This shows that 1 nW is required to achieve a source temperature of 1 K and 100 nW to reach 5 K.

antenna designs that can couple more efficiently or over a broader band (slotline or log-periodic spirals), this design was chosen as a simple proof of concept. The antenna itself is niobium so that is superconducting at these frequencies. Thus, it can focus the radiation into the aluminum absorber while confining the quasiparticles.

The entre setup described above is enclosed in a sealed copper housing and it placed at the cold stage of the ^{3}He cryostat. There are four SMA lines for RF signals that are filtered with the standard powder filters. There are also 20 DC lines that are used to bias the source as well as other thermometry on the detector circuit board. These lines are filtered with the "tapeworm" design (Spietz et al., 2004) and can be seen in figure 9.3 hanging from the bottom of the enclosure.

The first measurements are to characterize the properties of the bolometer. In the absence of self-heating under bias, the resistance of the bolometer is completely ohmic. However, once the dissipated Joule power begins to heat the thermistor, the resistance will drop. In order to prevent self-heating during characterization a bias voltage of 100 μV was used to measure the resistance as a function of the cryostat temperature. The left-hand graph in Figure 9.4 shows the results. The data fit well to the form of equation 9.2 with R_o=1880 Ω and T_o=16.6 K. The next step is to measure the non-ohmic IV curve of the bolometer in the presence of self-heating. Starting at a cryostat temperature of 260 mK, figure 9.4 shows the measured bolometer temperature as a function of bias Joule power. The 100 nW necessary to raise the temperature to 5 K represents a power level that begins to affect the base temperature of the cryostat at the milli-Kelvin level. For powers beyond this, quasiparticles in the STJ absorber can be broken both by the radiated photons and by phonons associated with the simple heating. This is the fundamental issue with using a cryogenic blackbody

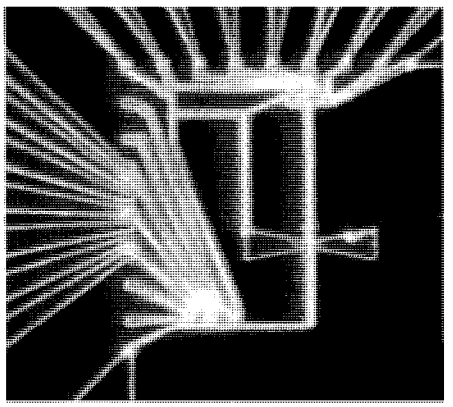

Figure 9.5: Optical microscope picture of the antenna-coupled STJ. The niobium bowtie antenna is 140 μm long and is terminated in 5 μm long aluminum absorber. Broken quasiparticles in the absorber are confined to a small volume by the higher-gap niobium and tunnel on a short timescale through the detector SQUID.

source, both in this incarnation and later with the on-chip photon source.

For this experiment, the detector used was SQPC-D1-60, which was fabricated at NASA Goddard. The detector is configured as an RF-STJ using a surface mount inductor whose nominal inductance is 500 nH. The measured RF and DC properties are shown in figure 9.6. The normal state resistance of the SQUID is 4.3 kΩ and the gap is 195 μV. In this device, the dark current is 25 pA at 260 mK for voltages less than 150 μV. The RF readout shows a resonance centered at 404 MHz with a Q of 36. This implies an impedance match to a dynamic resistance of 65 kΩ. The effective current noise of the RF readout was measured to be 60 fA/$\sqrt{Hz}$ while operating with no DC voltage bias and -110 dBm of RF carrier power on resonance.

In order to calculate the expected photon response, the 1-D blackbody spectrum (given by equation 9.1)can be integrated over the bandpass of the filter. This power can then be converted to a current via the responsivity. For a 200 GHz photon, $\mathcal{R}$=2400 A/W. The 200 GHz detection frequency implies that the radiated power will be only from the Wien side of the spectrum until the temperature reaches $\sim$ 10 K. Assuming unity coupling from source to detector over the 30 GHz bandpass, a bolometer temperature of 2 K would yield 10 pA of photocurrent. This increases to 5 nA by the time the source is 10 K. While this would be more than enough signal to saturate the detector, there are many non-idealities in the actual coupling. The biggest loss in this initial design was the disparity between the effective area of the feedhorn and that of the detector antenna. Even an ideal bowtie would have an effective area of $\lambda/8$=0.28 mm^2 (Friis, 1946). This is only 0.6% of the area into which the feedhorn radiates. The fact that the antenna is less than half a wave length implies that there will also be an appreciable reactive component to the impedance further reducing this coupling. Given all the known losses in the system the overall coupling is estimate to

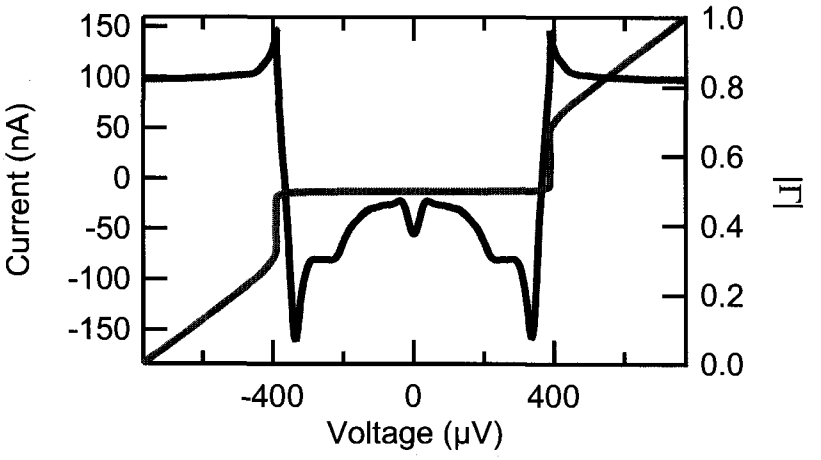

Figure 9.6: This graphs shows the detector squid DC current and RF reflection coefficient, Γ, as a function of voltage for the RF-STJ used for the bolometer photoresponse measurement. The normal state resistance is 4.3 kΩ, and it has a dark current of 25 pA at 260 mK. The RF reflection measurement is performed at 404 MHz where the tank circuit resonantly transforms the 50 Ω amplifier to 65 kΩ.

be 10^{-4}. In practice this means, that the source will need to be heated to roughly 50 K in order to get photocurrent of order 1 pA. Unfortunately, the large Joule power required for this bolometer temperature affects the base temperature of the cryostat, making it difficult to interpret the signal. By pulsing the signal on for a short amount of time, the response can be measured while keeping the duty cycle low enough to maintain the base temperature.

The response could be measured both in the DC current of the detector and using the RF readout. Pulsing the bolometer to 50 K showed an increase in the the detector current of 700 fA. Figure 9.7 shows the response to this same pulse in the RF readout. This current level increase is completely consistent with the calculated radiated power of 20 pW, assuming that only 0.1% of this power couples to the detector. The large uncertainties in the overall coupling relegate the conclusions of this measurement to the proof-of-principle level. Clearly, the biggest improvement to be made would be to better focus the radiation from source to the detector by using a lens or a smaller aperture feedhorn. This could easily improve the coupling by a factor of 10, but would also increase the importance of proper alignment. If such large source temperature are required, further improvement could be made by tying it thermally to the 1 K pot instead of the ^{3}He stage.

9.4 Mesoscopic Resistor as a Photon Source

Given the difficulties of macroscopic bolometer source, it was at this time that we decided to pursue an on-chip photon source. By placing both the source and the detector on the same chip, the

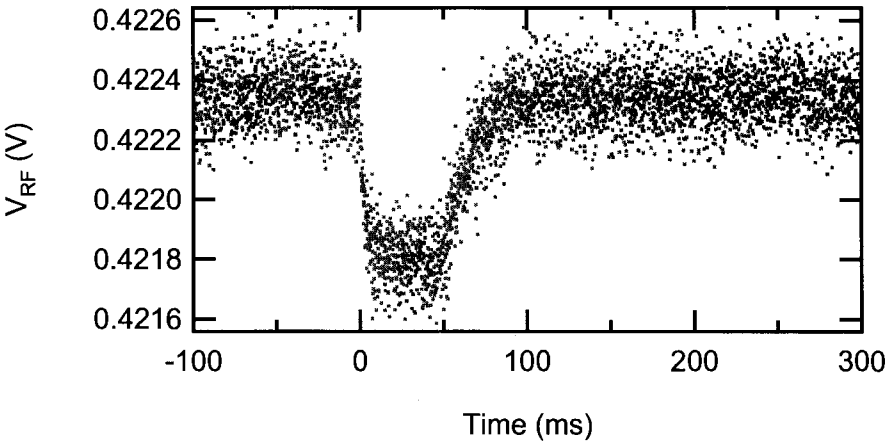

Figure 9.7: The RF response of the the detector while pulsing the bolometer source to a temperature of 50 K for 50 ms. This signal corresponds to a current change of 700 fA. The risetime of 5 ms is the thermal time constant of the bolometer at low temperatures. The longer fall time is probably due to residual heating in the bolometer support structure. Both of these time scales are much slower than that of the detector ($\sim$5 μs) or the readout ($\sim$20 ns).

coupling can be made near unity. While antenna coupling is important for eventual applications, using a short transmission line provides the highest possible efficiency coupling. This would allow for the best determination of the detector characteristics. The transmission line coupling also lends itself to on-chip filtering. On-chip filtering is desirable in future applications because it would allow a single broadband antenna to send signals of different frequencies to different detectors. Another advantage of an on-chip source is that the source can be made to have a very fast time constant. This provides a way to experimentally measure the speed of the detector itself. Because the time constant of the detector is essential in ensuring that the quasiparticles are not being lost to recombination, the fast photon source is invaluable for determining the quantum efficiency of the detector. Since the designed response time of the STJ is roughly 1 μs, the ideal source would have a thermal time constant much shorter than this.

There are many options for a photon source. A Josephson junction could be used to provide a coherent photon source via the AC Josephson effect. Unfortunately, the large specific capacitance of a traditional tunnel junction will filter the signal. The RC time constant of a junction can be varied some by changing the oxidation parameters, but it is independent of the area of the junction. For a typical resistance-area product of 500 $\Omega - \mu m^2$, the 3 dB frequency is of order 10 GHz. For this same reason, the shot noise of a $Al/Al_2O_3/Al$ tunnel junction will also be attenuated by this same time constant. While shot noise is usually associated with a circuit element the involve tunneling, a metallic resistor of mesoscopic length scales can also exhibit noise that is proportional to the bias current. Figure 9.8 is excerpted from reference by steinbach *et al* (Steinbach et al., 1996). It

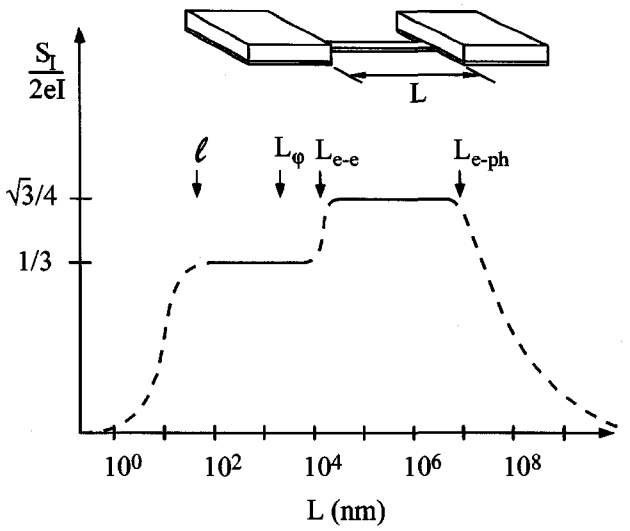

Figure 9.8: This figure is adapted from Steinbach *et al* (Steinbach et al., 1996). It shows the shot noise from a resistor with mesoscopic length scales. The length scales mentioned above in order from shortest to longest are: the mean free path, the phase coherence length, the electron-electron inelastic scattering length, and the electron-phonon scattering length. By properly engineering the length of the resistor to be greater than the mean free path, yet smaller than L_{e-ph}, resistor will have shot noise that can be used as a photon source. Whether the length is longer or shorter than L_{e-e} determines the Fano factor for this noise as well as its high frequency behavior.

schematically shows the magnitude of the shot noise as the length, L, of the resistor transitions past various important length scales. At the shortest length scale, where L is less than the mean free path, ℓ, the transport is completely ballistic and the noise becomes independent of bias (assuming a fully transmitting channel). Likewise, at very large length scales, there is little evidence for the discrete charge carriers, and the current noise is small. In between these two extremes, there are two distinct types of noise that could be used as a photon source.

9.4.1 Hot Electron Regime

First, consider the case where the length of the resistor is longer than the inelastic electron scattering length, L_{e-e}, yet shorter than the electron-phonon interaction length, L_{e-ph}. L_{e-e-} represents the distance over which electrons can exchange energy with each other. Over an even longer length scale, L_{e-ph}, the electron can exchange energy with the phonons in the system. So in this situation, as an applied bias current dissipates Joule power directly into the electrons, diffusion is the dominant mechanism for the electrons to cool. The hottest electrons in the center of the bridge can diffuse out toward the cooler reservoirs that are assumed to remain a the cryostat temperature. Thus, an equilibrium temperature profile, $T_e(x)$, is established over the length of the microbridge. While the dissipated Joule power is proportional to the bias voltage squared, the one-dimension diffusion

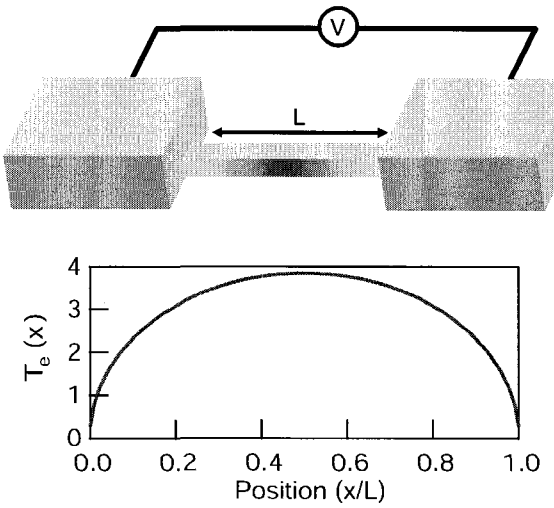

Figure 9.9: This cartoon shows the basic picture of a microbridge bounded by two thick reservoirs. As a bias is placed across the resistor whose length given by $L_{e-e}<L<L_{e-ph}$, the electrons decouple from the phonons and only cool by diffusion to the reservoirs. This diffusion combined with the inelastic electron-electron scattering results in a calculable temperature profile over the length of the bridge. The righthand graph shows the temperature profile for T_o=260 mK and V=1.2 mV. While the average bridge temperature is 3.0 K, the electrons in the center reach temperatures of 3.8 K. Knowing the exact electron temperature of the resistor as a function of bias makes this device a calibrated photon source for illuminating the STJ.

implies that the average bridge temperature will be only be linearly proportional to the bias current. Neglecting any electron-phonon interaction, the temperature profile is (de Jong, 1995; Burke, 1997):

$$T_e(x) = T_o\sqrt{1+\frac{x}{L}\left(1-\frac{x}{L}\right)\frac{V^2}{T_o^2\mathscr{L}}} \tag{9.3}$$

where x is the position along the wire, T_o is the bath temperature, and $\mathscr{L}$ is the Lorenz number ($\mathscr{L}=\pi^2k_B^2/3e^2$ for a free electron metal). The average bridge temperature may be obtained by integrating over the length of the bridge:

$$\langle T_e\rangle = \frac{1}{L}\int_0^L T_e(x)dx = \frac{T_o}{2}\left[1+\left(v+\frac{1}{v}\right)\arctan(v)\right] \tag{9.4}$$

where

$$v = \sqrt{\frac{V^2}{4\mathscr{L}T_o^2}} = \frac{\sqrt{3}}{2\pi}\frac{eV}{k_BT_o} \tag{9.5}$$

This average temperature can be used to calculate the current noise at low frequencies:

$$S_I = \frac{4k_B\langle T_e\rangle}{R} = \frac{2k_BT_o}{R}\left[1+\left(v+\frac{1}{v}\right)\arctan(v)\right] \tag{9.6}$$

In the limit of high bias, ($eV \gg k_BT_o$), the average temperature is linear in the voltage with a slope of $\approx$2.5 K/mV. This then implies that the current spectral density is also linear in the voltage.

$$\langle T_e\rangle \simeq \frac{\sqrt{3}eV}{8k_B} \Rightarrow S_I \simeq \frac{\sqrt{3}}{4}2eI \tag{9.7}$$

Thus, in this hot electron regime, there is noise power that is proportional to current, just as with a vacuum diode, but with a different prefactor. This Fano factor (defined as the ratio of S_I to 2eI) is $\sqrt{3}/4$ in this regime.

These calculations have derived the noise at low frequencies ($h\nu \ll k_BT,eV$). The full frequency dependence can be calculated, just as with any resistor, by accounting for the Bose-Einstein occupation factor. In this case, because the electron temperature is a function of the position along the bridge, the spectrum must be integrated over this length. The frequency dependent noise power in the hot electron regime is:

$$S_I(\nu) = \frac{4}{RL}\int_0^L\left(\frac{h\nu}{e^{\frac{h\nu}{k_BT_e(x)}}-1}\right)dx \tag{9.8}$$

where $T_e(x)$ is given by equation 9.3.

9.4.2 Non-interacting Electron Regime

The next case to consider is when the length of the microbridge is shorter than the electron-electron inelastic scattering length, L_{e-e}. In this regime, the electrons do not thermalize with each other. The electrons are still hot, in that they possess bias energy, but without interacting with each

other they no longer have a Fermi distribution. The only true temperature scale in the problem is that of the reservoir from which they left. In this regime, the noise is calculated by treating the wire a diffusive electronic waveguide, where each mode has a specific transmission probability, D_n. Channels possessing near unity transmission probability contribute little to the overall noise. The full expression for the noise as a function of voltage, temperature, and frequency is given by (Beenakker and Büttiker, 1992; Schoelkopf et al., 1997):

$$S_I(\nu) = \sum_{n=1}^{N} D_n(1-D_n)\frac{2e^2}{h}\left[(eV+h\nu)\coth\left(\frac{eV+h\nu}{2k_BT}\right)+(eV-h\nu)\coth\left(\frac{eV-h\nu}{2k_BT}\right)\right] \quad (9.9)$$
$$+\sum_{n=1}^{N} D_n^2\frac{2e^2}{h}\left[2h\nu\coth\left(\frac{h\nu}{2k_BT}\right)\right]$$

Further simplification can be made by noting that:

$$\eta = \frac{\sum D_n(1-D_n)}{\sum D_n} = \frac{1}{3} \quad (9.10)$$

$$R = \left(\frac{2e^2}{h}\sum D_n\right)^{-1} \quad (9.11)$$

Here, η is the Fano factor, which characterizes the correlations in the current. For a diffusive metallic wire, $\eta = 1/3$. R is the resistance of the wire. The full quantum expression for the noise of a diffusive wire then becomes:

$$S_I(\nu) = \frac{1}{3R}\left[(eV+h\nu)\coth\left(\frac{eV+h\nu}{2k_BT}\right)+(eV-h\nu)\coth\left(\frac{eV-h\nu}{2k_BT}\right)+4h\nu\coth\left(\frac{h\nu}{2k_BT}\right)\right] \quad (9.12)$$

$$S_I \to \begin{cases} \frac{4k_BT}{R} & \text{if } k_BT \gg h\nu, eV \text{ (Johnson Noise)} \\ \frac{1}{3}2eI & \text{if } eV \gg h\nu, k_BT \text{ (Shot Noise)} \\ \frac{2h\nu}{R} & \text{if } h\nu \gg k_BT, eV \text{ (“Quantum” Noise)} \end{cases}$$

This expression can be understood by examining its value in the appropriate limits. When thermal energy is the dominant energy scale ($k_BT \gg eV, h\nu$), this reduces to Johnson noise: $S_I \to \frac{4k_BT}{R}$. Then as the bias voltage is increased and it becomes the dominant energy scale ($eV \gg k_BT, h\nu$), this expression reduces to shot noise: $S_I \to \frac{1}{3}(2eI)$. Lastly, in the situation when the photon energy is the dominant energy scale ($h\nu \gg k_BT, eV$), the noise becomes just “Quantum” noise: $S_I \to \frac{2h\nu}{R}$.

In the low frequency limit, this expression take the more familiar form of:

$$S_I = \frac{2eI}{3}\coth\left(\frac{eV}{2k_BT}\right)+\frac{2}{3}\frac{4k_BT}{R} \quad (9.13)$$

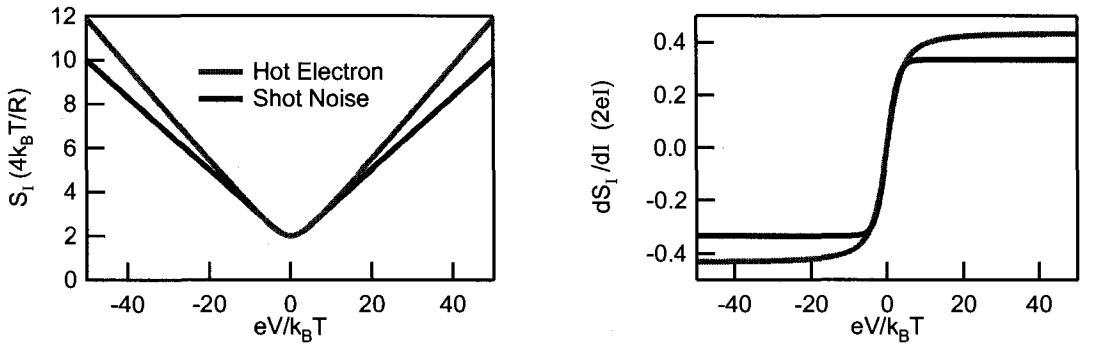

Figure 9.10: These graphs show the predicted current noise that would be measured at frequencies much less than k_BT/h and eV/h for the hot electron and shot noise regimes. These graphs assume that the physical temperature and the noise temperature of the amplifier are each 1 K . The units are normalized to the the Johnson noise and shot noise in the left and right graphs respectively. The derivative clearly shows both a different asymptotic value (1/3 for interacting electrons and $\sqrt{3}/4$ for non-interacting electrons) as well as the differing voltage scale over which they approach this asymptote.

Where the hyperbolic cotangent smoothly interpolates between the zero-bias Johnson noise and the high bias shot noise. This shot noise is reduced by a factor of 1/3 from Poison shot noise as was measured in several experiments (Steinbach et al., 1996; Schoelkopf et al., 1997).

At zero temperature, this resistor cannot emit any photons with $h\nu$ >eV. But the finite temperature of the reservoirs implies that there is some power emitted above this threshold due to the Wien tail of the thermal distribution.

9.4.3 Comparison of the Two Regimes

While the detailed physics of how the noise arises in the two regimes is quite different, the differences in the resulting noise power is actually quite subtle. This can be seen by comparing two resistors of the same resistance, but whose lengths are greater or less than L_{e-e}. At zero bias, their noise is identical as imposed by the Fluctuation-Dissipation theorem. At low frequency, as the bias voltage is increased, both transition to noise that is proportional to voltage. The Fano of factor in these two regimes only differ by 30%, between the hot electron ($\eta = \sqrt{3}/4$) and the shot noise ($\eta = 1/3$) regimes. Even the curvature of S_I with respect to voltage is remarkably similar between the hyperbolic cotangent and the arc cosine functions as they only differ by 10%. These differences are plotted in Figure 9.10. This figure shows the excess noise that would be measured with an amplifier with a noise temperature of 1 K as a function of voltage. There is both a difference in the absolute slope that can be measured if the gain of the system is entirely calibrated. Even without this calibration, there is a measurable difference in the voltage scale over which the noise becomes linear in the voltage. The righthand graph of Figure 9.10 shows the derivative of the curves both

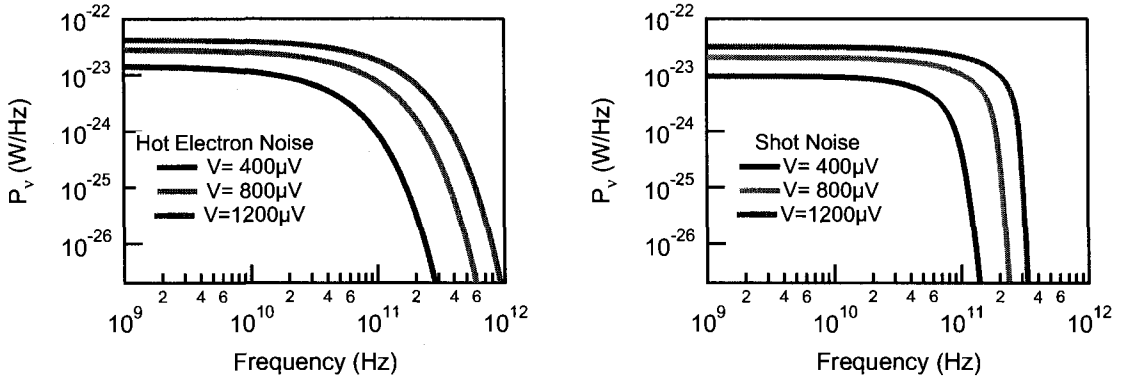

Figure 9.11: The radiated one dimensional power density is shown for the two mesoscopic regimes. When the length of the resistor is greater than L_{e-e}, this is the "hot electron" regime shown on the left. When the length is less than L_{e-e}, the electron do not thermalize with each other. They still have shot noise as shown on the right. The plots assume a bath temperature of 260 mK. The bias voltages of 400 μV, 800 μV, and 1.2 mV correspond to an average electron temperature in the hot electron regime of 1,2, and 3 K, respectively. While the two regimes differ only by 30% at low frequencies, the shot noise has a much sharper cutoff at high frequencies. In this case, the only photons produced with $h\nu > eV$ are due to the finite temperature of the reservoirs.

at a bath temperature of 1 K. The hot electron curve has a distinct shape that does not reach its asymptotic value as quickly. While these differences are small, they are measurable as will be shown in the next section.

The important difference between these two noise sources in this work, is their high frequency limits. As explained above, the hot electron regime has the same Wien tail as any resistor at finite temperature. In the shot noise regime, the bias voltage set the threshold above which the noise is no longer white. Beyond this frequency, it is only the few number of thermal photons for the cold reservoirs that contributes. So in comparing the high frequency noise of a mesoscopic resistor in the hot electron and shot noise regimes, the later has a much sharper cutoff. This is shown in Figure 9.11. The plots are for a bath temperature of 260 mK and three different bias voltages of 400, 800, and 1200 μV. The hot electron regime is preferable as a noise source for several reasons. First, it produces more 100 GHz photons for the the same bias voltage. This is important because too much Joule power can lead to unwanted heating of the detector. As shown in the previous chapters, the STJ is an exponentially sensitive thermometer, so keeping the phonons at the bath temperature is essential. The next reason that the hot electron regime is preferable is that it is less sensitive to slight increases in the temperature of the reservoirs. As detailed in the next section, it is in this hot electron regime that the noise source is designed.

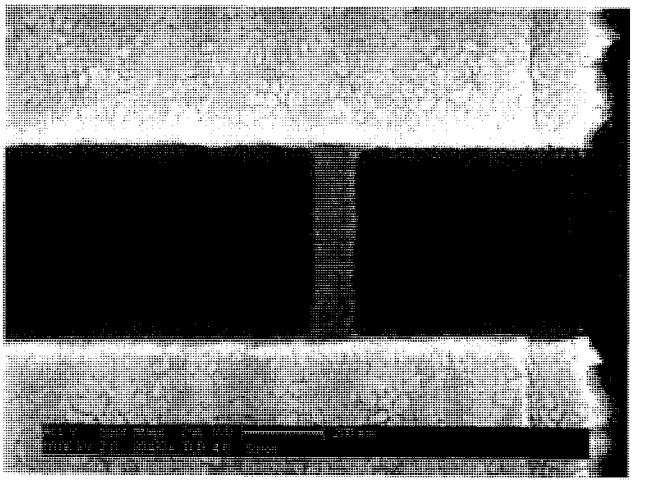

Figure 9.12: The gold microbridge is 10 nm thick, 100 nm wide, and 500 nm long. The reservoirs are 40 nm thick and form the start a coplanar strip line for coupling to the detector.

9.5 Design and Layout of Gold Microbridge

Now that is it clear that a diffusion cooled resistor in the hot electron regime is a good choice for a photon source, this section will discuss the actual implementation. The resistance needs to be matched to the impedances of the transmission line and the aluminum absorber at 100 GHz. Choosing 50 Ω for these impedances implies that this source will also lend itself to direct noise thermometry with the HEMT amplifier. Gold is chosen because it is a metal that does not superconduct, and its mesoscopic properties are known. A 10 nm thick film has a sheet resistance of ~10 Ω/□ that is independent of temperature. Choosing a lithographically reliable width of 100 nm implies a length of 500 nm to obtain a 50 Ω impedance. Figure 9.12 shows an SEM picture of the device that was made using double angle evaporation to have reservoirs that are 4 times thicker than the bridge. A 2 nm thick titanium layer is evaporated under the gold to promote good adhesion to the substrate.

In order to ensure that this length is in the hot electron regime, we can calculate theoretical predictions for the various length scales. The wire is considered to be a quasi-1D diffusive wire. The scattering lengths can be calculated from the scattering rates that are given in literature (Altshuler et al., 1982).

$$L_x = \sqrt{D\tau_x} \tag{9.14}$$

where x is a generic subscript that could apply to electron-electron or electron-phonon and D is the diffusion constant of the film which is 30 cm^2/s for this device. The electron-phonon rate is given as (Echternach et al., 1992): $\tau_{e-ph}^{-1} \approx 130\ MHz/K^3T^3$. This implies that L_{e-ph} is 5 μm at 1 K. Thus, phonon cooling will not become a consideration for this device until the temperature is above

5 K. As for the electron-electron inelastic scattering rate, it is calculated (Altshuler et al., 1982) and measured (Wind et al., 1986) to be:

$$\tau_{e-e}^{-1} = \left[\frac{R_\square}{\sqrt{2}(\hbar/e^2)} \frac{k_B}{\hbar} \frac{\sqrt{D}}{W} \right]^{2/3} T^{2/3} \tag{9.15}$$

This means that at 1 K, L_{e-e} is 1 μm. This is close to, but larger than the length of the resistor used in this work. So it is not clear *a priori* that this device should be in the hot electron regime. Unfortunately, all of these length scale are not merely temperature dependent, but bias dependent as well. There is no complete theoretical prediction for these length scales as a function of bias and temperature. For these reasons, it is necessary to verify using direct noise thermometry (at $\sim$ 1 GHz) that the microbridge is in the hot electron regime in order to calculate the noise power at 100 GHz.

Another important parameter of the source is its thermal time constant. Because the only thing the becomes hot are the electrons in the microbridge, the device can still have a fast time constant despite its weak thermal conductance. The only cooling mechanisms are diffusion and radiation. The radiation, even if it were perfectly coupled to a cold environment, can only contribute a thermal conductance quantum, $G_o = \frac{\pi^2 k_B^2 T}{3h}$, which is roughly 1 pW/K at 1 K (Schmidt et al., 2004). This can be seen by integrating the 1-D blackbody spectrum over all frequencies and differentiating with respect to temperature to obtain a thermal conductance. While cooling from radiation can become important when the other conductances are made extremely small; in this work, its effect is negligible. Thus, the thermal conductance and the time constant are determined by the diffusion properties of the wire. The time constant is given by: $\tau^{-1} \approx \frac{\pi^2 D}{L^2}$. The source can heat and cool on the 10 ps time scale, which is many orders of magnitude faster than any time constant in the detector. This means that this source can be used to directly measure the speed of the detector.

9.6 Calibration of Microbridge Noise at RF Frequencies

In the work of Stienbach *et al.*, the noise was measured with a SQUID amplifier with T_n= 175 mK from 10 to 50 kHz (Steinbach et al., 1996). In the work of Schoelkopf *et al.*, a HEMT amplifier was used to measure over a much large bandwidth (Schoelkopf et al., 1997). Despite the higher noise temperature of a HEMT compared to a SQUID, the large bandwidth allows for similar temperature sensitivity, t_n, measured in K/$\sqrt{\text{Hz}}$. Applying the Dicke radiometer formula to compute the fluctuations (Dicke, 1946):

$$t_n = \frac{T + T_N}{\sqrt{B}} \tag{9.16}$$

where T is the temperature of the noise under test, T_n is the noise temperature of the amplifier, and B is the bandwidth over which the noise is measured. Using our cryogenic, HEMT amplifiers

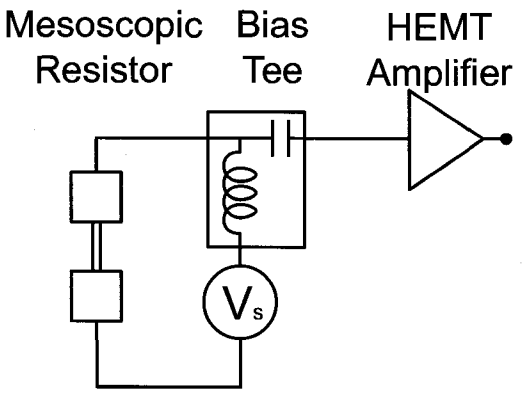

Figure 9.13: In order to verify the noise power of the photon source, it can be measured with noise thermometry at microwave frequencies as a function of DC bias voltage. The noise power at 500 MHz is well in the Rayleigh-Jeans limit and can directly measure whether the resistor is in the hot electron or non-interacting electron regime. The low noise temperature and large bandwidth of the HEMT amplifiers mean that this thermometry can have a temperature sensitivity less than 1 mK/$\sqrt{\text{Hz}}$.

with T_n= 4 K and B= 200 MHz centered at 500 MHz, the shot noise can be measured with $t_n \approx$ 300 μK/$\sqrt{\text{Hz}}$. This method, as shown in Figure 9.13, has been used in the Schoelkopf lab both for primary thermometry (Spietz, 2005) and for characterization of phonon cooled microbridges (Shen, 2005). 500 MHz is well in the low frequency limit for temperatures (~250 mK) used in this work.

The measured resistance of the gold microbridge is 26 Ω at 260 mK. The noise power from the source is amplified at first at 4 K and then again at room temperature. The signal is bandpass filtered from 300 to 600 MHz and rectified with a commercial diode. The system gain and noise temperature are calibrated *in situ* by varying the temperature of the cryostat. The system noise temperature is 4.25 K and the noise power continues to drop linearly down to the base temperature of the cryostat (260 mK). With this information, the noise may be measured as a function of bias voltage. Figure 9.14 shows this measurement. The data is fit over low voltages ($\pm$100 μV) and constrained to the the measured zero bias temperature and noise temperature as measured in the calibration. The results of the fits to the hot electron theory and shot noise theory are shown. As is clear from the graph, the hot electron theory reproduces the data over the range of the graph, whereas the shot noise shows a significant deviation. In order to make the shot noise theory fit the data, the fit temperature would have to be over 500 mK. This clearly indicates that the resistors used in this work are in the hot electron regime with L>L_{e-e}. Given this information, the photon power at 100 GHz may be calculated from equation 9.8.

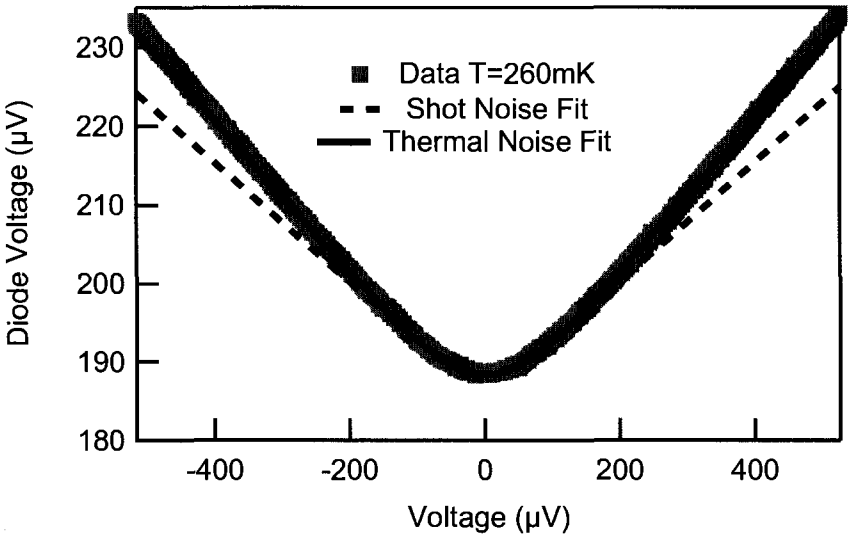

Figure 9.14: The measured noise power of the gold microbridge as a function of bias voltage. The electron temperature and system noise temperature were independently calibrated *in situ* by varying the cryostat temperature. The data is fit in the range below 100 μV using both the hot electron and the non-interacting electron theory. These data clearly show that the noise power follows the hot electron theory indicating that $L<L_{e-e}$ for the devices used in this thesis work.

9.7 Conclusions

This chapter has discussed several types of bolometers that could be used in reverse to be a submillimeter photon source. The reciprocity between absorbing and emitting radiation can be exploited to use existing bolometer technology to create high frequency photons. The emitted radiation may then be used to calibrate a sensitive detector like an STJ. This was done first with a hopping-conduction thermistor quasi-optically illuminating an antenna-coupled STJ. This proof-of-principle demonstration of quasi-optical coupling shows that the bolometer source is feasible and that the STJ is amenable to antenna coupling. For more efficient coupling, the idea of an on-chip blackbody source was used. This source takes the form on a gold microbridge whose electron temperature can be controlled with a DC bias voltage. This source requires low power, has a fast time constant, and is easily coupled to a transmission line geometry. Its low frequency performance was measured and calibrated at 500 MHz showing that it is, in fact, in the hot electron regime. The next chapter will discuss the exact design of the on-chip coupling between this source and the RF-STJ, as well as show the experimental results obtained with its use.

Chapter 10

Detector Characterization with Photon Source

"It is better to light a candle than to curse the darkness."

–Chinese proverb

With thorough independent characterization of both the STJ and the source properties, the final experiments measure their interaction. This chapter describes the experimental results from using an on-chip, mesoscopic resistor to illuminate the detector with submillimeter radiation. This allows for quantitative determination of the relevant detector properties, including the responsivity, sensitivity, and response time. The measurements performed in this chapter involve two separate designs. The first design which used a single junction with a relatively low normal state resistance as the detector showed very promising results. It was characterized in both the ^{3}He and dilution cryostats. In order to optimize the sensitivity and implement several other improvements, a new chip was fabricated with a variety of smaller area detector junctions. This chapter will discuss the design, fabrication and characterization of each of these detectors.

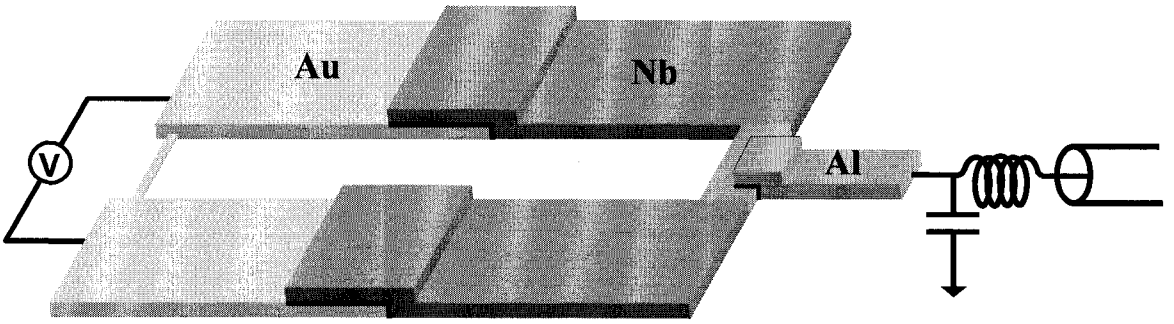

Figure 10.1: Cartoon representation of the general layout of the source and detector structure. A DC bias voltage across the gold source Joule heats the electrons in the microbridge. These hot electrons emit excess Johnson noise that is coupled via a short coplanar strip line to an aluminum absorber. The radiation with $h\nu > 2\Delta$ breaks Cooper pairs in the absorber and creates excess quasiparticles. These quasiparticles are confined to a small volume by the niobium contacts and are forced to tunnel through the detector junction. This results in an increased current through the junction and corresponding decrease in its RF impedance. In this way, the response can be monitored by a DC current measurement or RF reflectometry.

10.1 Design Principles

As discussed in chapter 9, the main advantage of the on-chip source is that the coupling from source to detector is calculable, reproducible, and most importantly efficient. The near unity coupling implies maximal number of photons for a given amount of joule power dissipated on the chip. The basic geometry employed is to use a balanced transmission line in the form of coplanar strip line (CPS) (Wadell, 1991). This lends itself to propagating the differential, quasi-TEM mode that can be excited or absorbed by a thin strip of metal. This is exactly the geometry of the source and the STJ absorber. The impedances of both the source and detector are matched to each other as well as the impedance of the transmission line. This ensures maximum power transfer. Because the source is made of a thin normal metal, the real part of the impedance is essentially constant up to the plasma frequency of the metal. Thus, its impedance at 100 GHz may be extracted from the DC resistance. The skin depth would also increase the resistance at high frequencies, but the thickness used in this work (10 nm) is less than the skin depth, even at submillimeter frequencies. The other important issue is to consider any reactive component of the impedance given from the geometry. In this case, one would need to ensure that the inductance does not dominate the impedance. This argues for achieving the resistance with as few squares of metal as possible. The gold sources are chosen to be ~500 nm long, so that their inductance is less than 1 pH. This implies that at 100 GHz the reactance is <1 Ω and negligible compared to the 50 Ω of real impedance. For the absorber, all the same issues apply. It is more complicated because the absorber is comprised of superconducting aluminum. At frequencies well below $2\Delta/h$, the Cooper pairs completely short circuit the impedance. The only appreciable impedance is reactive and arises from both kinetic and geometric inductance. As

described in Chapter 2, Mattis-Bardeen theory shows that at frequencies above $2\Delta/h$, the impedance of the superconducting metal asymptotically approaches its value in the normal state. As must be expected from Kramers-Kronig relations, this sharp change in the real part of the impedance with frequency is necessarily accompanied by a change in the imaginary part. In fact, right at $2\Delta/h$ there is an appreciable inductance of the metal, but this quickly becomes negligible for higher frequencies. The design of the absorber is then essentially the same as for the source; a strip a metal that has a DC resistance (in the normal state) of the desired impedance. There is the additional constraint of optimizing the volume of the absorber. This volume sets the overall scale for the tunneling time, and a smaller volume always implies a faster detector. As the actual speed of the detector is rarely the important parameter in submillimeter applications, the main consideration is to keep the tunneling time short compared to the recombination time for good efficiency. Ideally, for maximum sensitivity, the absorber volume would be made as small as possible, and then the R_n of the detector would be increased to keep the tunneling time a few percent of the recombination time even in the presence of photon-excited quasiparticles. As with any detector, this sensitivity comes at the cost of earlier saturation. If the absorber volume is too small the number of quasiparticles created by the photons can quickly reduce the recombination time or even drive the absorber normal. For our purposes, the design goal was to have a tunneling time of order 1 μs with as small of an absorber volume as is feasible from the geometry. This implies a volume of approximately 1 μm^3 for an STJ with 1 kΩ normal state resistance.

The next design consideration is the actual transmission line itself. It needs to be low loss, have a controlled characteristic impedance at 100 GHz and also must include a DC block so that the source and the detector can be independently biased. A CPS structure with 3 μm gap will have a characteristic impedance of 50 Ω on a silicon dielectric half-space. Making the transmission line out of superconducting metal that has $2\Delta/h>100$ GHz, would imply negligible conductor losses. In practice, because the length of transmission line is short ($\sim$100 μm), a clean normal metal at cryogenic temperature also would have sufficiently low losses. The compromise is to use gold for the part of the transmission line near the photon source, and to use niobium for the part that contacts the aluminum absorber. The niobium provides a way for the absorber to make good ohmic contact with transmission line without allowing the quasiparticles to escape into this large metallic volume. The larger gap of niobium means that quasiparticles created just above the gap of aluminum lack the energy necessary to escape in the the niobium. Formally, this is to say that a quasiparticles in the aluminum will be Andreev reflected at the Al/Nb interface (Andreev, 1964). Hence, excess quasiparticles generated by absorption of radiation are confined in the absorber until they either recombine with other quasiparticles or tunnel through the detector junction. Once the quasiparticles tunnel into the aluminum counter-electrode, they should not be allowed to back-tunnel. While back-tunneling may be exploited to provide signal gain (Wilson, 2002; Savu, 2007), in this work it is avoided so that the decay time of the detector will be set by the tunneling time.

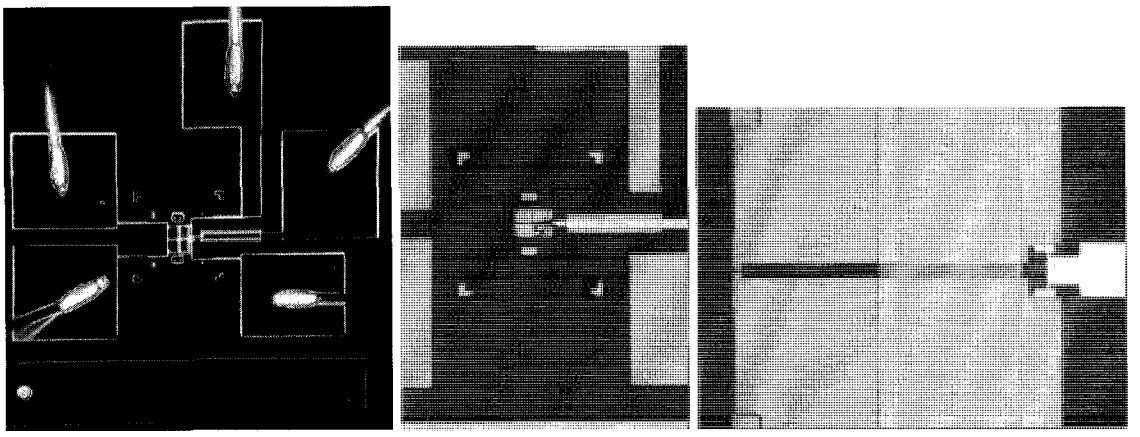

Figure 10.2: Photograph of one of the devices on chip "submm7." On the left, the aluminum wirebonds (25 μm diameter) can be seen contacting the niobium bond pads. The left two wires are for the DC bias of the gold source. The other three wires contact the detector junction and the two sides of the aluminum absorber. The center picture shows the narrow bias leads for all contacts that help prevent leakage of the submillimeter radiation into the bias leads. It also shows the gold that contacts the counter electrode of the detector junction in order to prevent back-tunneling. The right hand picture shows the CPS transmission line that is terminated with a gold microbridge on the left and the aluminum absorber on the right. The gold and niobium parts of the transmission line are separated by a 100 nm thick layer of evaporated silicon oxide so that the source and detector can have independent DC bias voltages.

Back-tunneling is prevented by making ohmic contact between the aluminum counter electrode and a gold quasiparticle trap. Once the quasiparticles enter the normal metal of the trap, they quickly lose energy to the other electrons and can no longer reenter the aluminum. This ensures that each quasiparticle tunnels only once and that its excess energy is dissipated away from the junction.

In order to separate the source from the detector at DC, a blocking capacitor is fabricated between them. This is accomplished by making an overlap capacitor out of the gold and the niobium portions of the transmission line with evaporated silicon oxide between them as the dielectric. This capacitance must be sufficiently large so that its impedance at 100 GHz is much less than the 50 Ω characteristic impedance of the line. To keep the reactive impedance less than 1 Ω, the capacitors must be at least 1 pF each.

Another consideration is to ensure that none of the radiation is inadvertently allowed to propagate out through the DC bias leads. This can be accomplished with a choke structure whose impedance looks much greater or less than 50 Ω at the relevant frequencies. While the inductance of the wirebonds ($\sim$1 nH) alone would sufficiently block submillimeter radiation, it is difficult to control the parasitic capacitances to ensure there are not any resonances over the band of interest. In practice, narrow lithographic wires connecting the transmission line to the bondpads provide the necessary isolation. These are made out of superconducting metal so that these long bias wires do

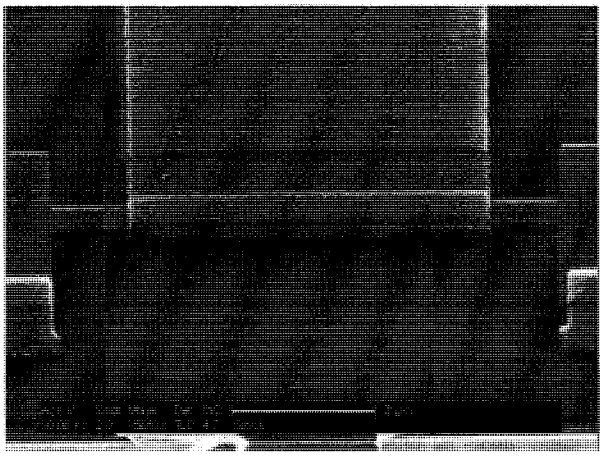

Figure 10.3: Scanning electron microscope image of the detector junction and absorber from chip "submm7." The junction is 5 μm long by 0.5 μm wide to give a normal state resistance of 200 Ω. The supercurrent is suppressed by applying a parallel magnetic field through the junction. In this chip, the absorber is made by evaporating 40 nm of aluminum in an intentionally oxygen-rich environment so that it has both a large sheet resistance and larger superconducting gap. This allows the absorber to achieve a real impedance of 50 Ω (when $T>T_c$ or $h\nu > 2\Delta$) with only 7 μm of length. The counter electrode is comprised of 60 nm of "clean" aluminum evaporated without excess oxygen in the chamber.

not dissipate power when biasing the source.

Combining all these considerations, a final design was implemented. Figure 10.1 shows the general design concept. The next section will give the details of the exact geometry and fabrication for the first devices of this style.

10.2 Fabrication

In order to fabricate the devices as outlined above four separate layers of lithography are necessary. For all layers, the lithography is patterned with e-beam lithography as outlined in chapter 4. This section gives the details for the first chip (submm7) that was designed and fabricated by Chris Wilson and Luigi Frunzio. The substrate is high resistivity silicon with a thermally grown oxide. The high resistivity ensures that the dielectric will not be lossy at high frequencies and the oxide allows the devices to be probed at room temperature without any DC leakage. The first deposited layer is the gold. The gold layer defines the general alignment marks, part of the transmission line, the microbridge source, and the quasiparticle trap for the detector. First, a 2 nm titanium layer is evaporated to ensure good adhesion between the gold and the substrate. Then a double angle evaporation of gold allows the microbridge to have a 10 nm thickness, while everywhere else a second 40 nm thick layer is evaporated on top. The microbridge itself is 100 nm wide and 500 nm long. The next layer is 100 nm of thermally evaporated silicon oxide which will form the dielectric for the

blocking capacitors between the gold and the niobium electrodes. The total overlap area for each capacitor is 1200 μm^2 in order to yield 1 pF of capacitance. The next layer is the aluminum. Again, a double angle evaporation will define the detector junction. The first layer is the absorber and is evaporated in an oxygen-rich atmosphere in order to increase the resistivity and the T_c of the film. The absorber is 40 nm thick, 500 nm wide and 7 μm long. There is an additional 24 μm^2 of area that will be covered by the niobium. This gives a total absorber volume of 1.4 μm^3. The junction itself is 5 μm by 0.5 μm. It is a single junction (not a SQUID) with a normal state resistance of 200 Ω. The top layer of aluminum is 60 nm thick and is not evaporated with oxygen in the chamber. This implies that the junction will be an SIS′ structure with two different superconducting gaps. The last layer is the niobium. For this step, the resist is baked at a much lower temperature in order to ensure that the junctions are not damaged. The surface is ion cleaned before the niobium is then sputtered in order to ensure ohmic contact at the Al/Nb and Au/Nb interfaces. The niobium forms the second half of the CPS structure as well as the bondpads and bias leads for the source and absorber. The resulting structure is shown is figure 10.2. Further detail of the detector junction is shown in figure 10.3. An SEM of the source is shown in the previous chapter in figure 9.12. On this chip, there are 15 separate devices that are nominally identical to the one shown in the figure. This chip had 100% yield with the resistance of the junctions varying by less than 10% over the chip.

10.3 Detector Characterization

The initial characterization is performed in the pumped ^{3}He cryostat. The chip is mounted in the standard "jellyhog" sample holder and is oriented vertically so that the magnet on the outside of the IVC can apply a field parallel to the junction. The chip is attached to the circuit board using vacuum grease and all wirebonds are aluminum. A 270 nH surface mount inductor resonates with the junction and parasitic capacitance to form the tank circuit for the RF readout. The gold microbridge uses the twisted-pair, "DC" lines for biasing.

The first step is to measure the resistances of the source, the junction and the absorber. For the absorber the important measurement is just above T_c. The T_c of the absorber is 1.8 K with a resistance just above T_c of 47 Ω. While this value for T_c is much higher than the bulk value of 1.1 K, it is consistent with previous measurements of "dirty" aluminum. This can be further confirmed by measuring the IV curve of the junction in the superconducting state. There should be a peak in the current at a voltage that corresponds to the difference between the two superconducting gaps. At the base temperature of 256 mK, the IV curve shows a peak in the current at 80 μV. Given that the clean aluminum has a T_c of 1.2 K and Δ=190 μeV.

This indicates that the gap of the absorber is 270 μeV. This implies that the absorber will only couple to radiation above 130 GHz. At this frequency, the ideal responsivity would 3700 A/W. The junction has a normal state resistance of 220 Ω, which is very close to the designed value. The first

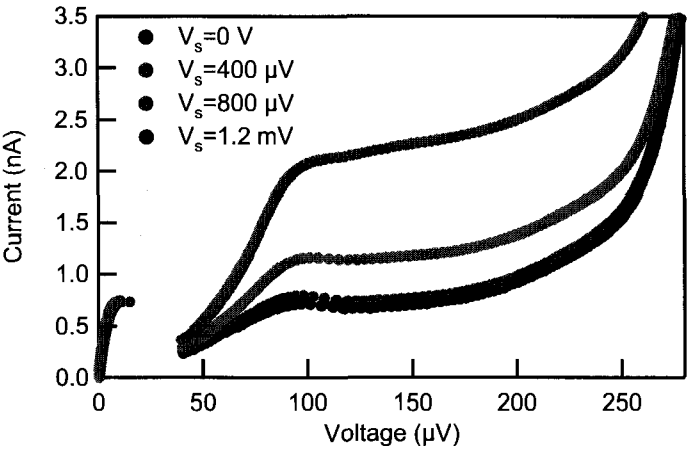

Figure 10.4: The DC current-voltage characteristic of the detector junction is dramatically affected by the biasing of the coupled source. Ideally, this steady-state increase in the subgap current is solely due to the Johnson noise of the hot electron source constantly breaking Cooper pairs in the absorber of the STJ. In practice, the increased detector current is a result of both of coupled radiation and trivial heating of the chip. While these effects are indistinguishable in this DC characterization, they may be separated by looking at the timescale of the response.

null in the supercurrent occurs at an applied magnetic field of 75 G. For this device the supercurrent has a minimum value of 700 pA.

The resistance of the source for this particular device is much lower than the others on this chip and has a value of 15.4 Ω. This implies that there will be an impedance mismatch between the source and the absorber. This effect only gives a 30% reduction in coupled power, but it is a known loss that may be accounted for. The other disadvantage of the lower source resistance is increased Joule heating. Since the average electron temperature in the microbridge is proportional to the voltage across the resistor, lower resistance gives more Joule heating for a given bridge temperature.

The next step is to examine the effect of the source on the detector. The DC IV curves clearly show an increase subgap current with increased source bias. As shown in figure 10.4, the current at 120 μV increases from 600 pA to 2.2 nA by biasing the source to 1.2 mV. The source bias corresponds to an average electron temperature in the microbridge of 3 K. It is important to note that for all source temperatures used in this work, the radiation coupled to the detector at frequencies above 130 GHz is still well in the Wien limit. In order to determine the coupled power from the source to the detector, several steps are required. First, for a given bias voltage, there is a known temperature profile of microbridge that can be integrated numerically over the length of the resistor. This give the emitted power spectrum. The fraction of the emitted power that is coupled can be determined from the complex (frequency-dependent) impedance of the absorber as given by Mattis-Bardeen theory. This coupled power is then integrated over all frequencies to give the total coupled power.

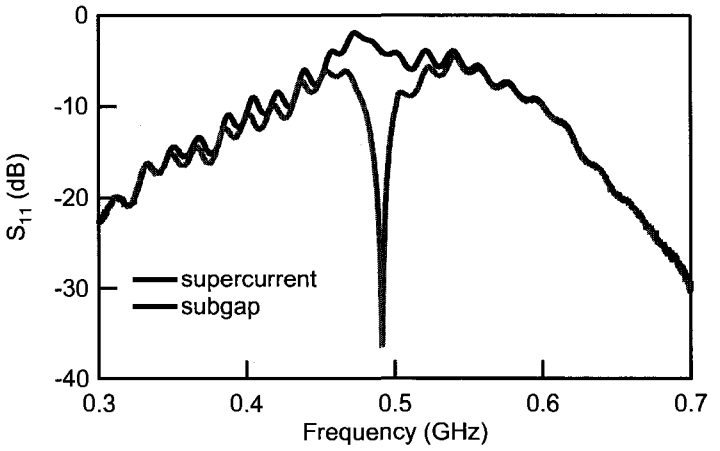

Figure 10.5: The resonance of the tank circuit at 490 MHz is measured using a vector network analyzer. This resonance has a Q of 23 and matches the amplifier to an impedance of 26 kΩ. When the bias of point of the STJ is tuned to a feature in the subgap with this dynamic resistance, the RF reflection is reduced by more than 30 dB on resonance.

Performing this calculation for the parameters of this device yields a coupled power of 10 fW, 300 fW, and 1400 fW for average source temperatures of 1, 2, and 3 K, respectively. Because the source temperature is always in the Wien limit for the frequencies of interest, the dominant uncertainty in this calculation is the exact value of the spectroscopic gap of the absorber. While it can be independently measured from the T_c and the IV curve, the coupled power in exponentially sensitive to both this quantity and the temperature of the source.

10.4 RF Characterization

The DC IV curves show the steady-state response of the detector to the source, but one of the main advantages of the mesoscopic source is its fast thermal time constant. By pulsing the source, one can measure the dynamic response of the detector. In this heavily filtered cryostat, the bandwidth of the current measurement is less than 100 Hz. The RF readout, on the other hand, has more than enough bandwidth to measure the $\sim \mu$s time constant of the detector. For this device, network analyzer measurements show a strong resonance in the RF reflected power at 490 MHz. As seen in figure 10.5, the reflected power modulates by over 30 dB as the bias point (and hence dynamic resistance) of the junction changes. The Q of this circuit is 23 and it matches the amplifier to an impedance of 26 kΩ over 20 MHz of bandwidth. For the RF readout, a carrier tone is applied at the resonance frequency with an amplitude corresponding to 200 μV on the device and no DC applied voltage. While the residual supercurrent makes the dynamic resistance of the junction non-linear, the reflection technique with large carrier amplitude averages over the structured IV characteristic.

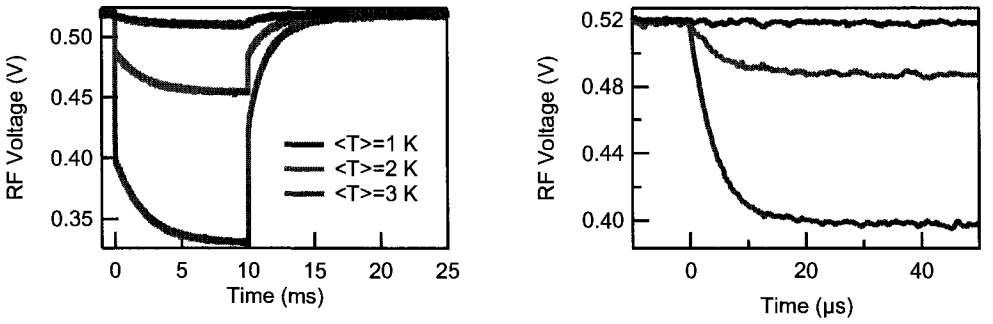

Figure 10.6: The time domain response to pulsing the source to 1,2, and 3 K reveals the presence of two distinct timescales. The fast timescale is presumable due the the photon response, and the slow one due to phonons. The ability to clearly resolve the distinct responses in the time domain allows the phonon effect to be accurately subtracted in the determination of the photon response of the detector.

The effective impedance seen by the carrier still depends sensitively on the subgap current and hence constitutes a robust readout. By comparing the change in reflected RF voltage to a known change in subgap current, the sensitivity of the RF readout can be directly measured. In this case, the measured current noise is 140 $fA/\sqrt{Hz}$. Despite the structured IV curve, this sensitivity is consistent with the noise temperature of the amplifier and the Q of the matching circuit.

With the RF measurement calibrated, the dynamic response of the detector may be examined. Figure 10.6 shows the response of the RF voltage to a square pulse on the source. It is immediately apparent that there are actually two time scales in the response. The first has a time constant of 2 μs, and the second a time constant of 2 ms. The fast time constant is on par with the expected tunnel time of the detector. It is also, however, about the same as the rise time of the twisted-pair leads used to bias the source. This shows that the detector can respond at a fast timescale, but it will require further measurements to verify this is in fact the tunneling time of the detector junction. The slower time constant can plausibly be attributed to a thermal time constant in the cryostat. As the subgap current is an extremely sensitive thermometer, even small changes in the temperature of the chip can be easily resolved with the junction. Since this chip is only connected electrically through superconducting wirebonds, there is little electronic thermal conductance to keep the chip from heating as Joule power is dissipated on the chip. In order to check that this time constant is in fact the thermal time scale of the chip itself, another device elsewhere on the chip may be biased. Figure 10.7 shows the result of this measurement. The response of the coupled source show both the fast and slow time constants. The response to the other "blind" source only show a response on the millisecond timescale. When the same Joule power is dissipated in the blind or coupled source, the slow detector response is the same. The blind source is a different gold microbridge, several hundred microns away. Given this interpretation of the data, this implies that only about half of the current

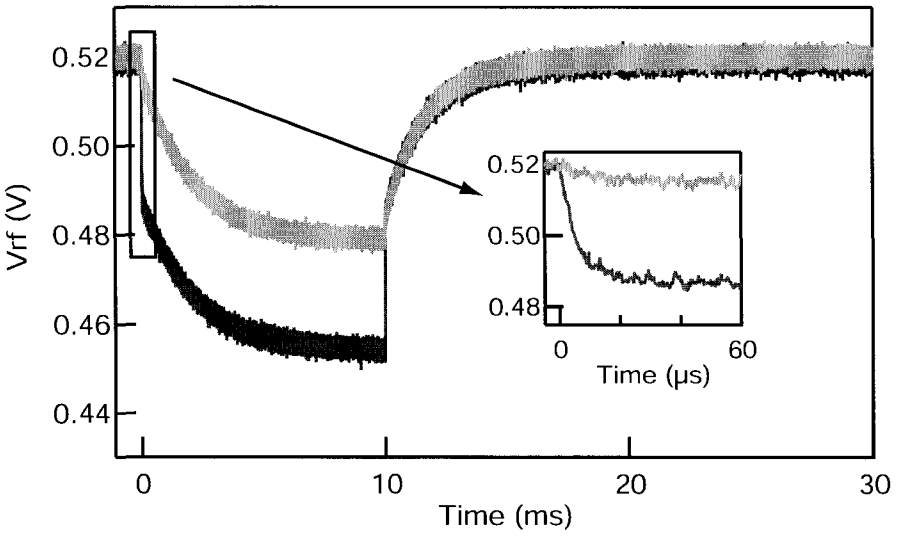

Figure 10.7: In order to verify that the slow timescale is due to gross macroscopic heating of the entire chip, the dynamical response to a coupled and uncoupled source was measured. When biasing the coupled source, the detector show a fast (μs) response as well as a slow (ms) response. The other source is not electromagnetically coupled to the detector and only shows the slow response. In future experiments, better heat sinking of the chip reduces unwanted response to a negligible effect.

is due to photons. The exact fraction of the current change seen in the IV curve that is due to the photons can be calculated from the pulsed response. The ratio of the pulse height after 10 μs to the height after 10 ms determines this value. Plotting the resulting photo-current verses the calculated couple submillimeter power gives a measurement of the responsivity.

Figure 10.8 shows this calculation. The slope of this line gives a measured responsivity of 1700 A/W. The theoretical value for the responsivity for 130 GHz radiation is 3700 A/W. This agreement within a factor of two is an encouraging first result that seems to indicate the detector is performing as expected. In this measurement, there is no way to separate the coupling efficiency from the quantum efficiency of the detector. So it is unclear if the discrepancy is due to less radiation coupling into the absorber or from broken quasiparticles being lost before they tunnel through the detector.

Combining the measured current sensitivity with measured responsivity gives a determination of the "optical" NEP of the detector. Figure 10.9 show the measured NEP. There are several important characteristics of this spectrum. The detector noise is shown to be completely white from 1 Hz to 1 MHz. The readout bandwidth is, in fact, much greater than is shown in this graph (~20 MHz). Most importantly, for submillimeter applications, the low frequency noise is not dominated by 1/f noise. This is in stark contrast to the SET measurements. The noise spectrum is completely limited by the noise temperature of the HEMT. This implies that it is understood, and could be improved upon with amplifier technology continues to improve. Even with this amplifier, the current and

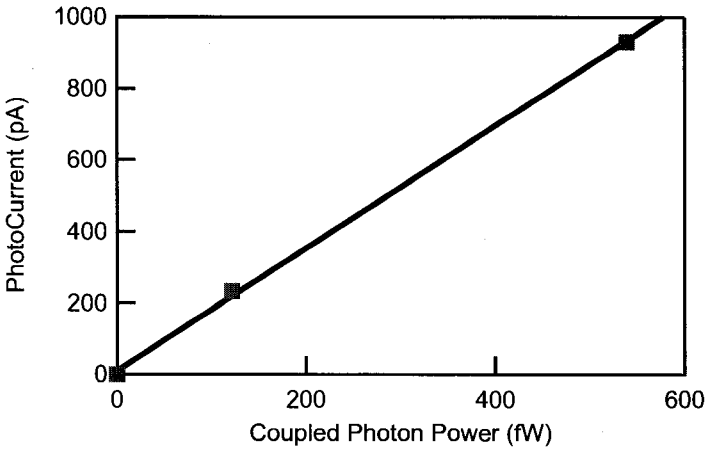

Figure 10.8: Using the dynamical response to deduce the current resulting from coupled photons allows for direct measurement of the responsivity of the detector. The x-axis is the calculated photon power that couples to the absorber for a given bias voltage of the source. The slope of this line gives a responsivity of 1700 A/W for this device.

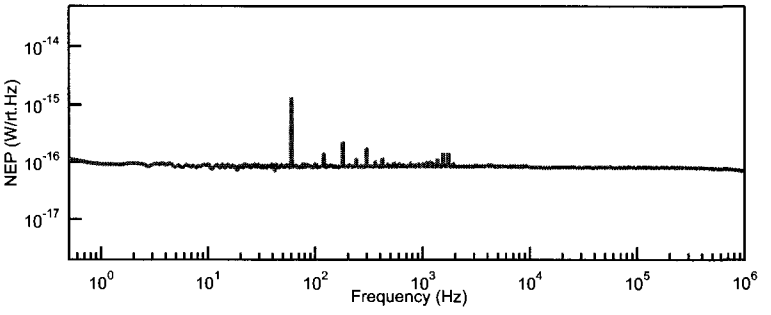

Figure 10.9: Measurement of the current noise of the RF-STJ in conjunction with the responsivity allows for direct verification of the "optical" NEP of the detector. The spectrum is white from 1 Hz to over 1 MHz. The lack of 1/f noise and the large readout bandwidth make this an attractive readout option for any STJ application. This level of sensitivity is already low enough for many ground-based applications where large background levels limit the overall NEP.

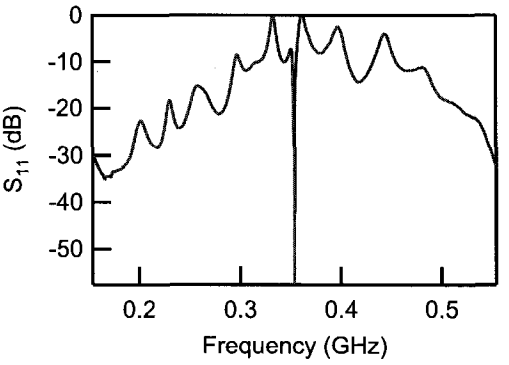

Figure 10.10: This tank circuit shows a resonance at 394 MHz with a Q of 60. On resonance, this circuit transforms the 180 kΩ dynamic resistance of the detector junction to 50 Ω over a 6 MHz span.

power sensitivity can be improved by using smaller area junctions and higher Q tank circuits.

10.5 Dilution Refrigerator Measurements

The next set of experiments is to measure a similar device from the same chip in the Cryoconcept dilution refrigerator. These additional measurements serve several purposes. In general, they provide confirmation for the previous measurements in the ^{3}He cryostat. Secondly, the colder temperatures will drastically reduce the number of thermal quasiparticles in the absorber. Ideally, this both lowers the dark current and increases the thermal recombination time of the detector. Several other aspects of the experimental setup could also be implemented. These include better thermal heat-sinking of the chip, improved tank circuit for better sensitivity of the RF readout, and biasing the source with a coaxial line in order to apply fast pulses.

The device (stj008) is coupled source and detector fabricated on the same chip as the device described in the last section. The R_n of the 2.5 μm^2 area detector junction is 205 Ω. The coupled, microbridge source has a resistance of 41 Ω. As a control experiment, a second source from a separate e-beam field on the same chip is also connected; its resistance is 29 Ω.. Both sources are biased through coaxial lines with a risetime of less than 10 ns for a 50 Ω load. This will allow clear determination of the intrinsic time constants of the detector.

In order to keep the temperature of the chip from decoupling from the cryostat when biasing the source, special care was taken in the heat sinking of the chip. The chip itself sits directly on the gold-plated copper sample holder with a thin layer of Apiezon cryogenic vacuum grease. This provides a large area over which the phonons in the substrate can equilibrate with the phonons in the copper. As the thermal conductance of the phonons drop as the cube of the temperature, at dilution refrigerator temperatures it is necessary to provide cooling through the electrons in the

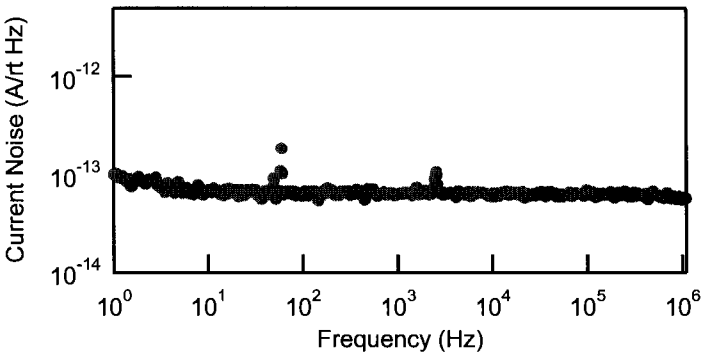

Figure 10.11: The effective current noise of the RF readout. By increasing the Q of the tank circuit to 60, the current noise of the HEMT is transformed down to 66 fA/$\sqrt{\text{Hz}}$. Given the measured responsivity of 1700 A/W, this demonstrates an "optical" NEP of 4×10^{-17} W/$\sqrt{\text{Hz}}$.

metal as well. For a normal metal, the Wiediman-Frantz law says that the thermal conductivity is proportional to the electrical conductance.

$$G = \frac{\mathscr{L}T}{R} \tag{10.1}$$

where G is the thermal conductivity, R is the electrical resistance, and $\mathscr{L}$ is the Lorentz number (24.4 nWΩ/K^2). In a superconductor, however, the Cooper pairs do not contribute at all to the thermal conductance. It is only the vanishingly small number of quasiparticles that allow for any electronic cooling. As the number of quasiparticles is exponentially suppressed at low temperature, using a normal metal provides far superior electronic cooling compared to a superconducting wire. For all experiments, thus far, the wirebonds used to connect devices have been aluminum. In this cooldown, as well as all subsequent measurements, both aluminum and gold wire bonds are used. This parallel combination of a superconducting and normal metal gives both lossless electrical connections as well as good thermal heat sinking. In addition to bonding the actual devices, the large gold alignment marks on the chip are bonded to give maximal cooling for the entire chip. As the electrical resistance of each gold wirebond is of order 1 mΩ, this implies a thermal conductance of 250 nW/K per bond at 10 mK. For this and all subsequent experiment measurements, the chip is bonded with many (~50) gold and aluminum wirebonds.

The tank circuit for this measurements uses a nominally 390 nH surface mount inductor (Coilcraft 0805-cs-391). It is placed upside-down on the silicon chip and wirebonded to the both the leads and the detector junction. As with all surface mount inductors used in this work, the self-resonance of the inductor greatly increases its effective inductance. The resulting matching circuit has a resonance at 354 MHz, which is the optimal frequency for the 350 MHz cryogenic HEMT amplifier that is used. The circuit has a Q of 60. This implies a Z_{LC} of 6 kΩ and an impedance match to 180 kΩ over a 6 MHz span. Figure 10.10 shows the over 50 dB of carrier modulation as the bias point of the

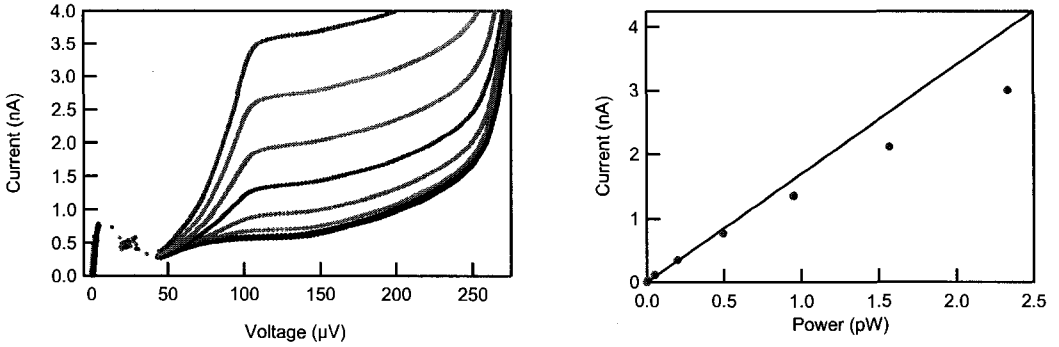

Figure 10.12: This is the DC response of the detector junction while biasing the coupled source at a cryostat temperature of 11 mK. In the left graph, the nine IV curves correspond to source voltages from 0 to 1.6 mV in 200 μV steps. The right graph plots the increase in current at an STJ bias point of 120 μV verses the calculated submillimeter photon power for these source voltages. The black line is a fit to the low power data giving a responsivity of 1700 A/W. The mild saturation for larger powers is to be expected as the increased number of quasiparticles decreases the recombination time until it is comparable or less than the tunneling time.

STJ is tunes the dynamic resistance loading the circuit. This higher Q matching circuit improves the current noise (and hence NEP) by further transforming the HEMT's current noise down to 66 fA/$\sqrt{\text{Hz}}$.

Repeating the measurements taking in the Heliox, the DC IV curve versus source voltage is measured. The results are shown in Figure 10.12. There are several features to note. Despite the fact that this data is taken at a cryostat temperature of 11 mK, the dark current is comparable to what was measured at 250 mK. This alone does not indicate a high quasiparticle temperature. On the contrary, it most likely implies that the dark current is set by other mechanisms such as inelastic Cooper pair tunneling resulting from unsuppressed supercurrent. The change in DC current is less than the steady-state increase in current measured before for a similar source temperature. This is not because the responsivity is less, but merely because the substrate heating is now negligible. Measuring the response to the blind source in fact shows a current change roughly 1% of that of the coupled source. Thus, the responsivity may be calculated directly from the DC measurements. The result is a responsivity just as measured before (1700 A/W). The data also shows the onset of mild saturation as the source temperature is increased past 3 K. This is consistent with the expected reduction in quantum efficiency as the recombination time become comparable to the tunneling time of the detector.

With the large bandwidth leads biasing the gold source, a conclusive measurement of the time constant of the detector can be made. The tunneling time for this device is 2.2 μs. There is also a 1 ms tail that can be seen in the data. Pulsing the blind source confirms that this is the thermal time constant of the chip. That the thermal time constant of the chip has improved by a factor of

two despite the factor of 20 reduction in temperature indicates a drastic improvement in the overall heat sinking.

While this device did not show improvement with colder temperatures of the dilution refrigerator, the set of measurements clearly confirm the device performances that were previously measured. The improvement in the RF readout also lower the demonstrate NEP to 4×10^{-17} W/$\sqrt{\text{Hz}}$. The fact the time constant of the detector did not increase also shows that the previous measurement were not limited by thermal recombination times.

The success of these measurements seemed to indicate an even more sensitive detector could be made simply by using smaller area junctions and higher Q tank circuit. As will be described in the next section, a new chip was designed and fabricated implementing several other improvements as well as varying the R_n of the junctions.

10.6 Redesign of Chip Layout

Given the effects of improper heat sinking of the chip, it is important to consider if the reservoirs of the gold microbridge also remain at the cryostat temperature. All of the calculations for the noise power of the source given in Chapter 9 assume that the reservoirs remain cold and that it is only electrons in the bridge that have excess energy. In practice this is accomplished by having thick, large area pads at the boundaries of the bridge. This ensures that the electrons in the metallic reservoirs do not decouple from the phonons in the metal. The large area also helps enforce that the phonons in the metal remain strongly tied to the phonons in the silicon substrate. At the interface of any two materials, there is a thermal Kapitza resistance that quantifies the acoustic mismatch between phonons in the two solids (Kapitza, 1941; Gray, 1981). The thermal conductance is given by:

$$G = \frac{dP}{dT} = 4\sigma A T^3 \tag{10.2}$$

where σ is a constant measured to be 12.5 $\frac{mW}{K^4 cm^2}$ in these references (Roukes et al., 1985; Mees et al., 1991). This implies that at 260 mK, the thermal conductance is $\sim$10 μW/K for every square millimeter of area. As heating the noise source to 3 K requires 1.2 mV across the 50 Ω resistor, the Joule power is 30 nW. Keeping the reservoirs within 10 mK of 260 mK implies that area should be at least 0.3 mm^2.

One possible source of inefficiency in the detector is if the niobium does not provide lossless confinement of the quasiparticles. In some STJ work, niobium has been seen to be a source of quasiparticle loss (Verhoeve et al., 2004). This could be due to low lying states in the superconducting gap of niobium or due to the formation of metallic, but not superconducting, niobium oxide. One way to protect against this loss is not to contact the aluminum with the niobium directly. Instead of making ohmic contact between the niobium transmission line and the aluminum absorber, in the redesigned chip, this contact is a Nb\Al_2O_3\Al junction. The small transmission probability

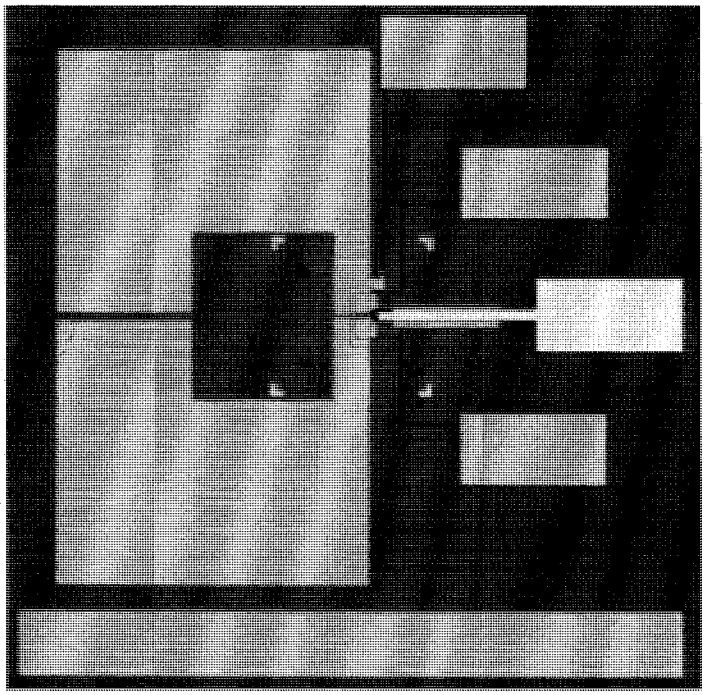

Figure 10.13: Optical microscope picture of the redesigned layout of the devices on chip BC05-4. One major difference from previous devices is that shape of the gold electrodes. Instead of biasing with narrow niobium wires, the wide gold leads provide submillimeter isolation by having the impedance much less than 50 Ω. The large area ensures that the temperature gold reservoirs remains close to the cryostat temperature. There is also a "blind" source that is connected to the same reservoir, but whose radiation should not couple to the detector. This provides a control experiment to help separate the effect of phonons and photons. The detector junctions are in a SQUID geometry with varied junction areas of 0.1, 0.25, or 0.75 μm^2. For scale, the gold bar along the bottom of the picture is 90 μm long.

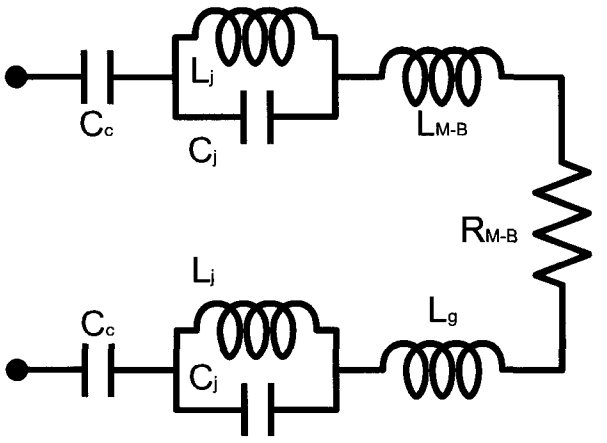

Figure 10.14: The total complex impedance seen by the photon source can be modelled as a combination of several lumped circuit elements. The DC blocking capacitors, C_c, are formed by the silicon oxide between the gold and niobium parts of the transmission line. L_J and C_J are the Josephson inductance and geometric capacitance of the Nb\$Al_2O_3$\Al junctions. L_g is the geometric inductance of the absorber strip. R_{M-B} and L_{M-B} represent the frequency-dependent resistive and inductive parts of the impedance of the superconducting absorber given by Mattis-Bardeen theory. This entire circuit is designed to be weakly resonant around the detection frequencies, so that impedance is real with a value close to that of the source for maximal power coupling. The Al\$Al_2O_3$\Al detector junction is not shown in this diagram.

of a quasiparticle through the oxide layer implies that any loss into the niobium will be greatly reduced. The Cooper pairs, however, provides a short at DC and RF for biasing the detector. Most importantly, the 100 GHz radiation is well above the plasma resonance of the junction, which implies its impedance looks capacitive. This reactive impedance can be made much less than the real impedance so that it has a negligible effect on the coupling. In practice, this capacitance can be used to resonate with the geometric and kinetic inductance of the absorber to result in conjugate matching between the source and the detector at the detection frequencies.

The total complex impedance seen by the photon source can be modelled as a combination of several lumped circuit elements as seen in Figure 10.14. The DC blocking capacitors, C_c, formed by the silicon oxide between the gold and niobium parts of the transmission line have a value of 2 pF. L_J and C_J are the Josephson inductance and geometric capacitance of the Nb\Al_2O_3\Al junctions. The plasma frequency is the frequency at which the Josephson inductance resonates with the geometric capacitance of the junction.

$$\omega_p = \frac{1}{\sqrt{L_J C_J}} \tag{10.3}$$

While both L_J and C_J depend on the area of the junction, their product does not. Thus, the plasma frequency is independent of junction area and depends only of the current density of the junction. This current density depends on the thickness of the oxide as well as the superconducting gap of

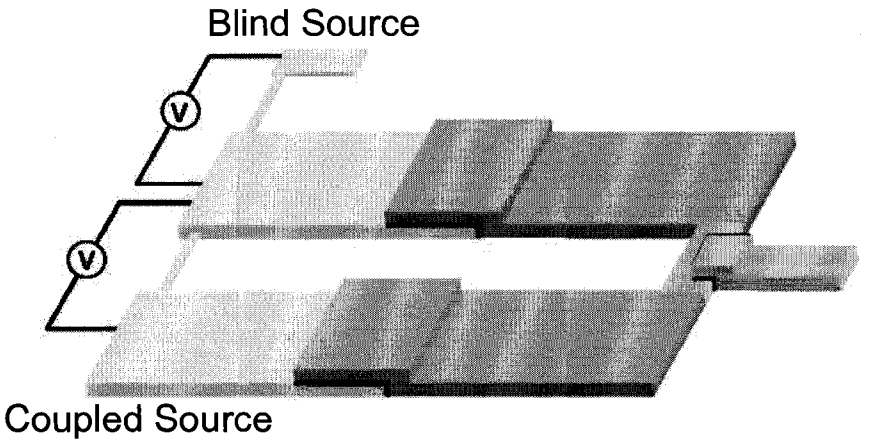

Figure 10.15: In the redesigned layout, a blind source is fabricated in metallic contact with the device. Ideally, the radiation from this source should not couple to the detector. In this way, it serves as a more stringent control experiment than biasing a source elsewhere on the chip.

both the niobium and aluminum. The Ambegoakar-Baratoff value for the critical current of an SIS′ junction is given by (Ambegaokar and Baratoff, 1963):

$$I_c = \frac{\Delta_1}{eR_n} K\left[\sqrt{1-\frac{\Delta_1}{\Delta_2}}\right] \tag{10.4}$$

where Δ_1 is the smaller of the two gaps and K is the complete elliptic integral of the first kind. As K(0)=$\pi/2$, this reduces to the usual Ambegaokar-Baratoff relation when Δ_1=Δ_2. While Nb\$Al_2O_3$\Nb junctions typically have a plasma resonance at 90 GHz, and Al\$Al_2O_3$\Al junctions at 30 GHz, these Nb\$Al_2O_3$\Al junctions should have there plasma resonance at 45 GHz. Thus, by 100 GHz, the impedance is purely capacitive and is within 10% of its high frequency asymptotic value. The area of the coupling junction is chosen to be 4 μm^2 so that C_J is 200 fF and L_J is 60 pH.

The absorber itself has a complex, frequency-dependent impedance given by Mattis-Bardeen theory as discussed in Chapter 2. While this impedance asymptotically approaches the resistance in the normal state at high frequency, near $2\Delta/h$ the absorber looks quite inductive. As seen in Figure 2.4 from Chapter 2, the reactance reaches a maximum value of $i|R_N|\sqrt{2}$ at a frequency of $2.4\Delta/h$. In addition to this kinetic inductance, there is also the geometric inductance, L_g, that is always present from storing energy in magnetic fields around the metal. The inductance per unit length of a narrow wire is roughly given by the permeability of free space, $\mu_0 \simeq 1$ pH/μm. For a rectangular thin film, the inductance is better approximated by the formula (Wadell, 1991):

$$L_g[nH] = 200\ell \ln\left[\frac{2\ell}{w+t}+\frac{1}{2}\right] \tag{10.5}$$

where ℓ, w, and t are the length, width and thickness of the film, respectively. For the aluminum absorbers in the redesigned chip with ℓ=16 μm, w=200 nm, and t=30 nm, the geometric inductance

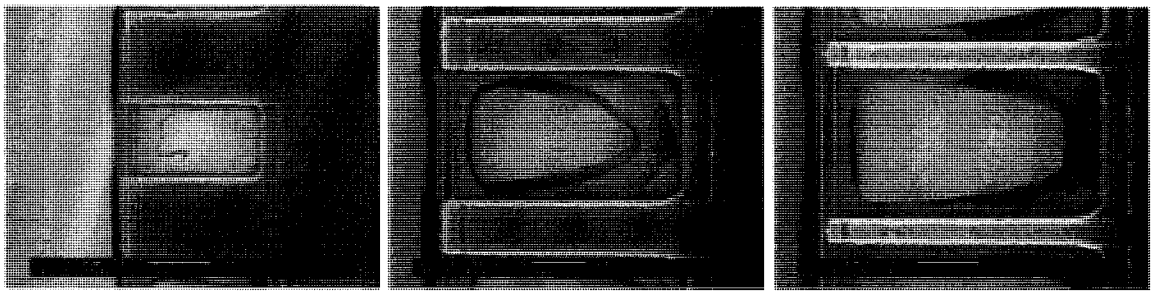

Figure 10.16: SEM images of the three types of detector junctions from the final measurements. All are SQUID geometries with loop areas of 10 μm^2. The target SQUID resistances are 300, 1500, 4000 Ω. All three have the same absorber volume; so their tunneling time should scale directly with the R_n.

is 16 pH. The combination of this inductance with that arising from the Mattis-Bardeen implies a reactive impedance that is not negligible compared to the real 50 Ω impedance. However, the 100 fF of junction capacitance in series cancels much of this reactance at the detection frequencies. As the reactances are close in magnitude to the resistance of the absorber, the resulting resonance is very low Q, providing conjugate matching over a broad band.

One last change is the addition of a control source fabricated in the same e-beam field as each detector. This source is connected to the same gold reservoirs as the coupled source but does not terminate the differential electromagnetic mode of the transmission line. In this way, this source should not not couple photons, but would rule out the local phonon, or phonons that coupled directly across the metallic layer without entering the substrate. Its effect could also be compared (as before) with the response to a source elsewhere on the chip.

With all of these considerations in mind, the final design is as shown in Figures 10.13 and 10.16. There are 15 sets of coupled source and detectors. There are three different junction designs so that the dependence on R_n may be measured. As all devices have the same absorber volume ($\sim$0.35 mum^3), a linear dependence of tunneling time on the R_n would rule out other loss mechanisms. These devices should also attain much lower dark currents and better NEP's.

10.7 Measurements of Redesigned Source and Detectors

This sections describes a series of three measurements–one for each style of detector SQUID. Each device is measured in the ^{3}He cryostat with the ability to bias the detector, the coupled source, the new control source, and a blind source elsewhere on the chip. All of these are connected with coaxial leads so that the dynamics of each situation may be accurately measured. The readout for the detector is both a DC current measurement and RF reflectometry is a high Q two stage 450 MHz tank circuit. These device are made with clean aluminum. Thus, the lower superconducting gap of the

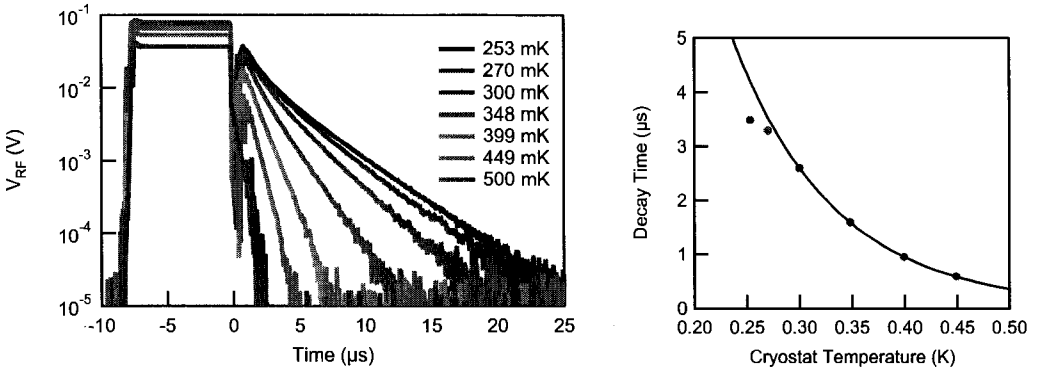

Figure 10.17: One way to measure the time constant of the detector is to put a large voltage bias across the detector itself for a short time in order to generate quasiparticles. This is the response of the 4.75 kΩ detector. After the pulse, the bias point quickly settles back to zero bias on the 10 ns time scale, but the quasiparticle density only relaxes on the μs timescale. This decay time is measured as a function of temperature. The graph on the right shows this temperature dependence. The black curve is a fit to the expected recombination time that should be exponential in temperature. It seems to show that at low temperatures, it is deviating from this behavior as one would expect when the tunneling time becomes the fastest time scale. It is also clear however, the the decay time has not completely reached its low temperature asymptote even at the lowest cryostat temperature. This means that some quasiparticles are being lost to recombination for this high resistance device.

clean aluminum absorber implies that the detector should absorb photons above 90 GHz (compared to 130 GHz for the original devices). This means that a given source temperature should give rise to a much bigger current. Furthermore, because the photocurrent in the STJ is proportional to the number of absorbed photons (whether they are 90 GHz or 130 GHz), the expected responsivity is now greater. When combined with expected improvements in current sensitivity, these device should demonstrate the full potential of the RF-STJ.

The first device (BCO5-4-8) has an R_n of 4.75 kΩ. The dark current of 20 pA is slightly higher than the expected quasiparticle current at 260 mK, but is more than 25 times lower than the dark current of the 200 Ωjunction from the last chip. The two stage tank circuit optimally matches to a dynamic resistance of 300 kΩ over 4 MHz of bandwidth. This is almost precisely the differential resistance near zero bias voltage. The coupled source for this device has a resistance of 36 Ω. The DC IV curve shows a clear increase is subgap current when biasing the source, but not nearly as much as expected. For example, heating the source to 2 K gives rise to only 80 pA of additional current. This corresponds to a responsivity of 230 A/W. This is much less than in the previous device and more than a factor of ten lower than expected. One possibility is that this power is already saturating the detector. But measurement at much lower power, whose photocurrent is comparable or less than the dark current also shows the same poor response.

The next check is to measure the time constant of the detector directly to ensure that its tunneling

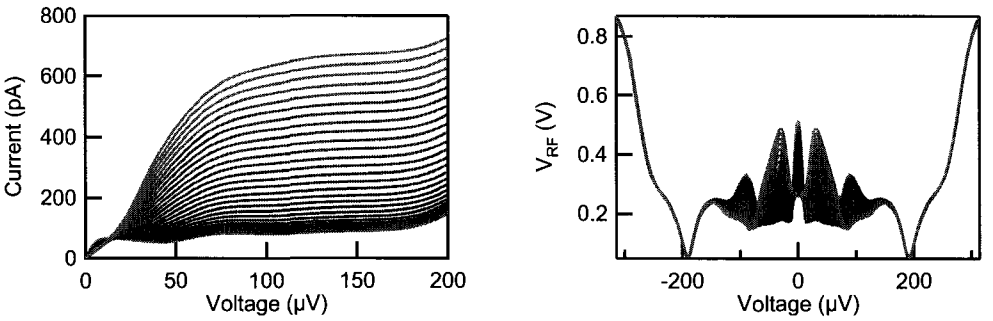

Figure 10.18: The steady-state response of the detector to increasing source bias voltage for device BC05-4-15. This response can be seen both in the DC current through the STJ as well as the reflected RF voltage.

time, in the absence of photons, is at least faster than the recombination time. The time constant is measured two different ways. One method is to pulse the coupled source on and off as has been done in previous measurements. The other method is to pulse a larger DC or RF bias on the detector junction, creating excess quasiparticles in both the absorber and the counter electrode. While the quasiparticles in the counter electrode quick diffuse and scatter in the the normal metal quasiparticle trap, those in the absorber can only decay by tunneling. Thus, the decay time is a direct measure of the time constant of the detector. This can be done as a function of cryostat temperature in order to see the effect of thermal recombination. At high temperature, the data follows an exponential dependence that is expected for a time constant that is limited by quasiparticle recombination. At low temperature, there is some indication that the tunneling time is becoming the dominant timescale. Unfortunately, the data shows that the time constant of the detector is still increasing with decreasing temperature. This means that the recombination time is not yet negligible, and thus, quasiparticles are being lost. The remedy is simply to use a lower resistance detector junction that will have a faster tunneling time. In this way, the recombination loss can be avoided. Unfortunately, this device died to an open circuit before further measurements could be made to study the effects of the two blind sources. However, given the low responsivity, it is clear that this is not an optimal device. Experimentally, the next step is to measure the response for detectors with a lower normal state resistance.

The next device (BC05-4-15) under test is a detector comprised of the medium size junctions. The R_n is 1250 Ω. It is nominally identical to the previous device except for the larger area junctions. The dark current is again low (50 pA), but slightly above the BCS theory for the measured values of the R_n and Δ. The RF matching and readout is nearly optimal again giving a measured current noise of 10 $fA/\sqrt{Hz}$ as shown in Figure 10.20. Figure 10.18 shows the response in the DC IV curve and the RF reflected power to the source. This source has a resistance of 36 Ω, and it is

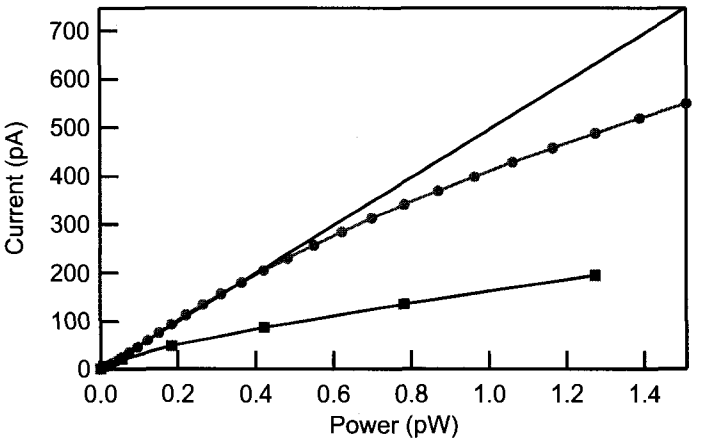

Figure 10.19: The current response of device BC05-4-15 while voltage biased at 100 μV as a function of the inferred submillimeter radiation. The red circles show the response to the coupled source, while the blue squares are the response the control "blind" source. The black line is a linear fit to the response for low incident power. This fit gives a $\mathcal{R}$=500 A/W. The blind source shows response that is roughly 40% of the coupled.

voltage biased from 0 to 1.2 mV. This monotonically increases the average electron temperature in the source up to 3 K. The DC IV curve of the STJ shows a superconducting gap of 190 μV, which implies the detector begins absorbing radiation above 92 GHz. Numerically integrating the radiation spectrum of the source gives a coupled power up to 1.5 pW for a 3 K source temperature. Figure 10.19 shows the STJ current as a function of this calculated power. The response is linear for low powers (<500 fW) and fits to $\mathcal{R}$=500 A/W. This is only 15% of the expected responsivity at these frequencies. Without an independent method for calibration it is unclear if this discrepancy is due to poor detector conversion efficiency or poor photon coupling. Figure 10.19 also shows the response to the "blind" source. This source is fabricated in metallic contact with the same gold reservoirs of the coupled source (as depicted in Figure 10.15), but is located such that it should not couple its radiation. The large measurable response to the control source could arise from several effects. If this response were attributed solely to phonons, then the actual photon response should be difference between the coupled and blind source. From the standpoint of the detector performance, this represents a worst-case scenario in which the responsivity would be 300 A/W. Another possible explanation is that Johnson noise of the blind source does couple to the detector. While the blind source ideally should not excite the differential quasi-TEM mode that couples to the detector, it is to be expected that radiation will couple through other modes at some level.

With previous devices, the time dependence of the response provided valuable information in separating the the photon response from trivial heating. For this device, both the blind and coupled source show the same constant. The detector response time to pulses on the source is 1.3 μs. This

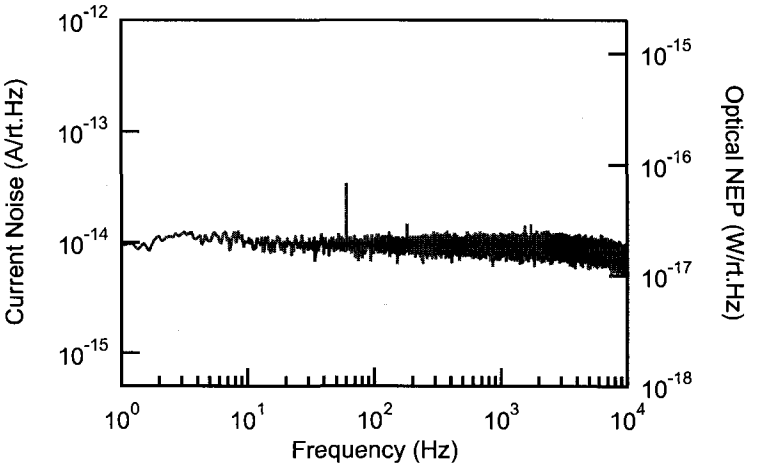

Figure 10.20: The current noise spectrum of the RF readout for 1250 Ω STJ. Using the measured responsivity of 500 A/W, this gives an optical NEP of 2×10^{-17} W/$\sqrt{\text{Hz}}$.

response time is independent of cryostat temperatures for T<350 mK. By 400 mK, the decay time is 860 ns. This indicates that the thermal recombination time is not affecting the measurements at base temperature. As both sources show a similar time constant, this indicates that the blind source is either creating photons or phonons on a timescale faster than the tunneling time of the STJ.

In order to obtain the most information, one would like the time constant of the detector to be faster than all other timescales. The last measurements focus on one of the large area detector SQUIDs. This device (BC05-4-14) has a normal state resistance of 285 Ω. While this device will not have the lowest dark current or current noise, it should have the fastest tunneling time. This should make this device least susceptible to saturation and fast enough to temporally resolve all of the relevant time constants.

In this device, the supercurrent of the detector could not be suppressed completely. The resulting IV curve shows a minimum I_c of 2.5 nA and a minimum dark current of 1 nA at bias point of 50 μV. The tank circuit has a resonance at 433 MHz and a Q of 28. This provides an impedance match to roughly 40 kΩ over 15 MHz of bandwidth. In other words, the time constant of the RF readout is 10 ns and will easily resolve the expected detector response time, which should be several hundred nanoseconds. The current noise of the RF measurement is consistent with the lower Q impedance transform and is 30 fA/$\sqrt{\text{Hz}}$.

For this measurement, there are three separate sources: a coupled source (source 1), a blind source as described above (source 2), and a source located in a separate e-beam field $\sim$ 1 mm away (source 3). These measurements seek to compare both the magnitude and timescale of the detector response to each of these sources. Figure 10.21 demonstrates the steady-state response to the coupled source. Despite the visible structure in the subgap current, the response is roughly constant over

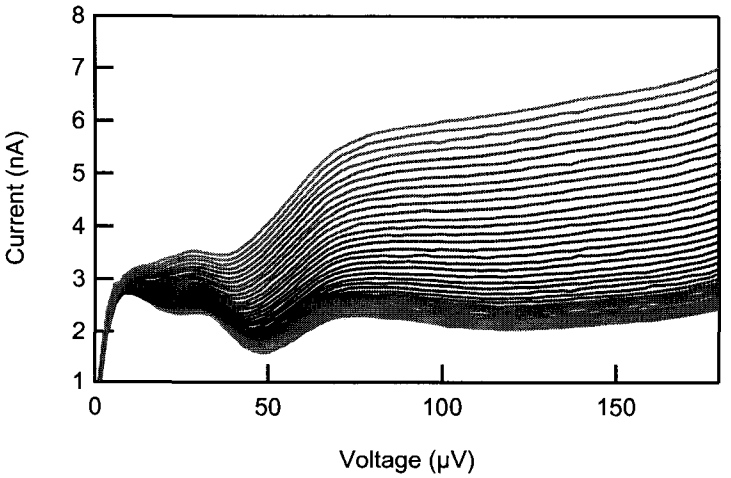

Figure 10.21: DC characterization of device BC05-4-14. This family of curves shows the increasing subgap current as the coupled source bias is increased.

the entire subgap region. A similar family of IV curves is measured for each of three sources. The results are shown in Figure 10.22. As with the previous device, the coupled source does in fact give the largest response. The magnitude of the response is again disappointing as it is only a fraction of ideal calculated response. Furthermore, the large response of blind source indicates that ~50% of this response is present in the control experiment. The markedly different response to the two types of blind sources also indicates that source 2 couples in some way other than simple macroscopic heating of the entire chip.

Figure 10.23 shows the temporal response of the detector to a 800 μV pulse on the source. In the first graph, a 2 ms pulse is used to measure the slowest timescales. All three sources show a slow decay time of 0.8 ms. This is presumably the the thermal time constant of the chip. The magnitude of the response reproduces the levels seen in the DC IV curves. The small response seen in the source 3 is consistent with heating on the order of 10 mK. All three source also show some response on a much faster time scale. The right graph looks at pulses that are 100 times faster. Unlike previous measurements there several "fast" timescales that may be resolved. The coupled source shows the fastest response, with an initial decay time of 300 ns. This is precisely the tunneling time that one would predict by scaling from the previous device. There is subsequently a second decay time of 2.7 μs. This is approximately the same time constant that is seen in response to source 2. This is fast enough that it would not have been resolvable in any of the previous devices. Finally, source three shows a small response with a decay time 5 μs. In order to precisely identify the origin of each of these timescales much further experiment would be required. Even without a definitive identification, there are several conclusion that can be drawn. First, as only the coupled source shows a response at 300 ns, it seems to rule out the possibility that sources 2 or 3 are coupling

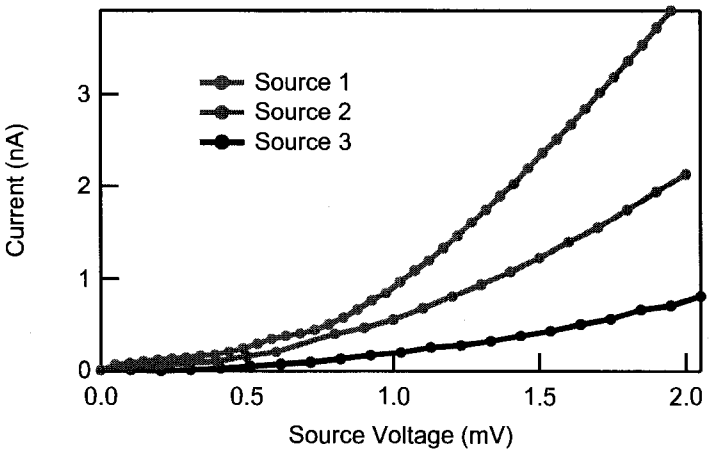

Figure 10.22: For the lowest normal state resistance device (BC05-4-14), the steady-state current response is measured for the three different sources. As expected, the coupled source (source 1) gives the largest response. The two types of blind source give differing levels of response. This indicates that the blind source fabricated in metallic contact with the device (source 2)is affecting the detector in some manner other than simple heating of the entire chip. While these measurements cannot definitively explain the origin of this response, assuming the entire response of source 2 is not from photons gives a worst-case-scenario for responsivity of the detector.

photons to the detector. This then implies that there are important thermal dynamics occurring on microsecond timescale. One possibility is the the STJ is detecting athermal phonons prior to their equilibration. While the timescale for a ballistic phonon to spectrally reflect off the opposite face of the chip and arrive at the detector in much faster than 1 μs, this could correspond to the time for hot phonons to diffuse outward toward the absorber. In this way, the source represents a "hot spot" on the chip whose radius propagates at a rate of roughly 10 μm/μs. It is unclear the degree to which these effects were present in the original measurement.

In summarizing the results from the redesigned chip, it is clear that the detector response is much less than with the original design. The dependence of the detector response time on the normal state resistance of the detector junction indicates that it cannot merely be attributed to quasiparticle recombination. Figure 10.24 shows that the tunneling time of the two lowest resistance devices seem to scale as expected. It is only the highest resistance device that recombination plays a significant role. It also indicates that the any other quasiparticle loss mechanism is slower than a few microseconds, and hence should not significantly affect a detector with a 300 ns tunneling time. The likeliest explanation for the low responsivity is the actual photon coupling. The coupled power is calculated from DC bias voltage of the source based on many assumptions. Because there were many changes that were implemented in the redesigned chip, it is difficult to determine which changes might have degraded the coupling. One large difference, for example, is that the original

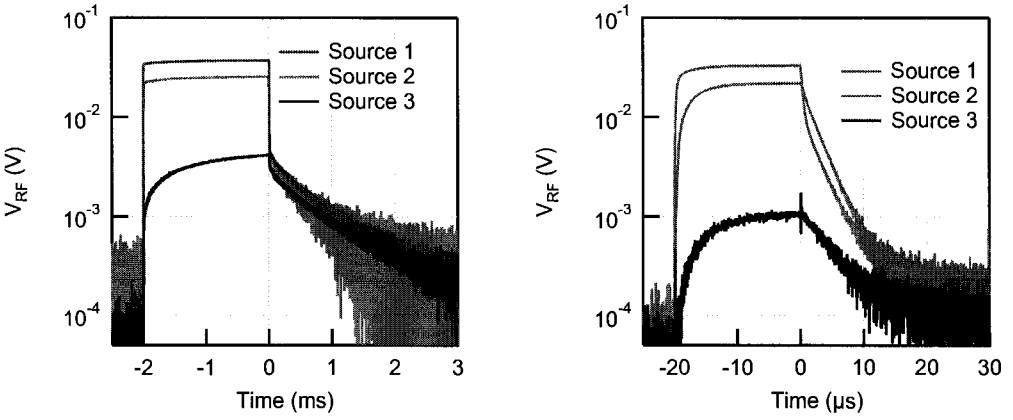

Figure 10.23: The dynamic response of the detector (BC05-4-14) to pulses on the three sources shows several different relevant timescales. The graph on the left shows the response of the RF readout on the millisecond time scale. All three sources show a slow response at 0.8 ms; presumably due to uniform heating of the chip at the 10 mK level. The right graph shows the response to a pulse on the microsecond timescale. Only the coupled source shows the fastest time constant of 300 ns. There is also a second slower time constant of 2.7 μs. This is the same decay that is seen in response to source 2. The response to source 3 is a order of magnitude smaller and has a decay time of 5 μs. In both graphs, the source is pulsed to a voltage of 800 μV corresponding to an average electron temperature of 2 K in the source.

chip had a larger superconducting gap. This implies it is detecting at a different frequency and has a much lower expected response for a given source temperature. Another important possibly important difference is the Nb\Al_2O_3\Al junctions that were introduced between the absorber and the transmission line. It is assumed that the plasma resonance of this junction is 45 GHz based on the geometry and the superconducting gaps of Al and Nb. However, if the plasma resonance is actually higher, this could affect the coupling. In other word, if the plasma frequency were 90 GHz, these junctions would become a bandstop filter at exactly the frequency over which we are trying to couple. These are the types of issues that could be systematically ruled out with further measurements beyond the scope of this thesis work. While much has been learned from the use of the on-chip source, it has also let us discover many of the important technical issues that require detailed understanding as well.

10.8 Conclusions

This chapter has demonstrated the ability to measure the blackbody radiation from a cryogenic source in the Wien limit with an RF-STJ. The integration of a mesoscopic source on-chip allows the STJ to be illuminated with submillimeter radiation from within the cryostat. The intensity of the radiation can be calculated from first principles and used to measure many of the important figures

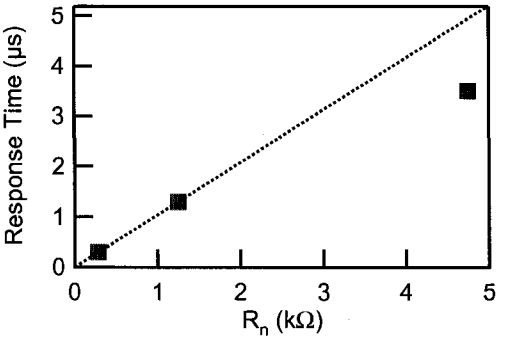

Figure 10.24: As all devices on the redesigned chip BC05-4 have the same nominal absorber volume, the tunneling time should scale linearly with the $R_n$of the detector. These data assume that the fastest measured timescale for each size detector is intrinsic detector response time. The highest resistance STJ clearly shows a faster response than expected. This would seem to indicate that the response time is set by a combination of tunnelling and quasiparticle recombination.

of merit for the detector. These include the response time, the responsivity, and the sensitivity.

The original design successfully shows the proof of concept measurements. The parameters of the detector were chosen to measure up to ~pW of power at frequencies above 130 GHz. The measured responsivity of 1700 A/W is within a factor of two of the ideal response. The large readout bandwidth and fast thermal time constant of the source allows for the direct measurement of the dynamics of the detector. The microsecond response time of the STJ shows that the detector can be simultaneously fast and sensitive. The low current noise corresponds to a demonstrated "optical" NEP of 4×10^{-17} W/$\sqrt{\text{Hz}}$.

Ideally, using a higher resistance detector junction should allow the design to be optimized for even more sensitive measurements. A new chip was designed and fabricated with several modifications. This new chip had three different size junctions in order to study the dependence of the responsivity, sensitivity, and saturation on this parameter. These new devices also include a control experiment in the form of a blind source that is as physically close to the detector as the coupled source. These higher resistance devices integrated well with higher Q tank circuits for the RF-STJ readout. This gave the lowest current noise measurements to date of 10 fA/$\sqrt{\text{Hz}}$. Unfortunately, the overall responsivity of these devices was unexpectedly low, even with the lowest resistance junctions. Furthermore, the new control experiment showed that the local blind source could give rise to a response on the few microsecond timescale. While this does not necessarily invalidate the previous measurements, it opens that possibility that the favorable responsivity in the previous measurements is an over estimate. Ultimately, definitive conclusions about the exact photon coupling and hence responsivity will require further measurements beyond this thesis work.

The overall results of the characterization of the the RF-STJ with on-chip source is summarized

Device	$R_n(\Omega)$	$\Delta(\mu eV)$	Vol(μm^3)	$\tau(\mu s)$	$\mathcal{R}$(A/W)	$i_n(fA/\sqrt{Hz})$	NEP($W/\sqrt{Hz}$)
Submil7-7	220	270	1.4	2.0	1700	140	8×10^{-17}
Submil7-8	205	270	1.4	2.2	1700	66	4×10^{-17}
BC05-4-14	285	190	0.35	0.3	800	30	4×10^{-17}
BC05-4-15	1250	190	0.35	1.3	500	10	2×10^{-17}
BC05-4-08	4750	190	0.35	3.5	200	10	5×10^{-17}

Table 10.1: This table summarizes the results of 5 separate measurements of coupled source and detectors.

in Table 10.1. The original chip showed very promising performance consistent with expectations. The apparent responsivity is within a factor of 2 of the ideal response. The redesigned chip, however, showed a responsivity that is at best 1/6 of the expected value. The uncertainty in the actual coupled photon power places a large uncertainty on an absolute number for the responsivity or optical NEP. Even assuming the worst-case scenario for the detector responsivity, the low current noise still implies an NEP of 10's of $aW/\sqrt{Hz}$.

If the small response is simply due to less photon power on the device than calculated and not detector loss, this would correspond to improvement of almost an order of magnitude in both the responsivity and hence the NEP. Thus, the demonstrated current noise of 10 $fA/\sqrt{Hz}$ corresponds to an ideal electrical NEP of 1×10^{-18}. This NEP is with a readout that is naturally scalable to frequency domain multiplexing of large format arrays. Furthermore, this sensitivity is completely limited by the HEMT amplifier. This implies that it will continue to improve as even lower noise microwave amplifiers become available. While the motivation for this work has been to explore the ultimate performance limits for an STJ as a photon detector for astrophysical applications, the array techniques and methods demonstrated are equally applicable to many other areas of condensed matter physics ranging from sensitive phonon detection to mesoscopic shot noise measurements.

Chapter 11

Conclusions

"Work. Finish. Publish."

–Michael Faraday

As with most research, this thesis work has made great experimental progress, but also revealed areas that require further research. The work achieved its overall goal of characterizing and optimizing the performance of the STJ as a submillimeter photon detector. To this end several novel approaches and experimental techniques were implemented. These include demonstration of a current amplifier based on an RF-SET, the invention and characterization of the RF-STJ readout and the novel integration of an on-chip noise source for calibration.

11.1 Review of Conclusions Drawn from this Work

The focus of the initial measurements was to quantify the subgap leakage currents of small-area SQUID junctions as this sets the ultimate limit on the intrinsic sensitivity of the detectors. The measurements performed on junctions fabricated at NASA/GSFC showed excellent subgap currents. These SQUIDS closely followed the exponential temperature dependance predicted by BCS theory. The only deviation arose in lower resistance devices in which the supercurrent could not be fully suppressed. One device was measured in the dilution refrigerator and followed BCS theory to a

current level of $\lesssim$1 fA, for temperatures below 150 mK. For lower temperatures, the subgap current was no longer measurable. This is a factor of 10^6 reduction from the current in the normal state. Other more typical devices demonstrated that subgap currents of order 1 pA can routinely be achieved at ^{3}He temperatures in devices where the supercurrent can be sufficiently suppressed. This implies a detector shot noise limited NEP of 10^{-19} W/$\sqrt{\text{Hz}}$.

The next measurements sought to characterize RF-SETs so that they might be configured as a sensitive current amplifier for the detector. The general measurements showed that good charge sensitivity $\sim 100\mu e/\sqrt{\text{Hz}}$ was achievable even with large-gate SETs. These large ($\sim$0.1–1 fF) interdigitated-finger, gate capacitors are necessary to optimize the voltage or current noise of the SET as amplifier. These measurements culminated in an experiment in which an RF-SET was configured in a charge-locked loop and used to measure the subgap current of an STJ. This experiment demonstrated the speed, faithfulness, and sensitivity of the RF-SET. The total current noise of this RF-SET transimpedance amplifier was 5 fA/$\sqrt{\text{Hz}}$ at 1 kHz. This is the lowest current noise of all readout methods used in this thesis work. While this is comparable to the current noise of a state of the art FET operated at room temperature, RF-SET possess many of the characteristic necessary for the readout of large arrays of cryogenic detectors. These attributes include the ability to operate at cryogenic temperatures with low power dissipation and to be multiplexed in the frequency domain.

Simultaneous with the SET characterization were measurements using a microscopic bolometer to illuminate an antenna-coupled detector. These experiments clearly showed a response in the STJ, but the poor overall coupling efficiency between the hot bolometer source and the detector made the experiments hard to quantify. These results did demonstrate the general principles of antenna coupling 200 GHz radiation to the detector, as well as the likely usefulness of a bolometer as a photon source.

It was at this time that RF-STJ was invented. The experimental focus shifted from the RF-SET readout to monitoring the response of the detector directly with an RF probe signal. While the advantages of RF reflectometry were clear, many aspects needed to be experimentally developed before this could be considered as a potential readout. The initial, proof-of-concept measurements showed that the performance was exactly as expected. The RF readout successfully transduced a change in detector impedance to the modulation of the amplitude of an RF carrier. This method did not corrupt or distort the BCS-like dark currents of the detector junction. Furthermore, this method is robust in that it still works well in the non-ideal case where the supercurrent of the detector junction cannot be fully suppressed. As with the readout of the RF-SET, the readout bandwidth is limited only by the RF matching circuit. Unlike the RF-SET, this readout of the STJ does not require any DC wires, feedback loops nor a large bias resistor. The most important measurement was the sensitivity. The effective current noise of the readout was seen to be white from less than 1 Hz to over 1 MHz and completely limited by the noise of a cryogenic RF HEMT amplifier. The importance of this is threefold. First, it shows that at this level, there are not any unknown noise

sources. Second, the lack of any appreciable 1/f noise is in stark contrast to almost all low noise current amplifiers, especially the SET. Finally, this measurement shows that the sensitivity will likely continue to improve as even lower noise RF amplifiers become available. Preliminary measurements showed current noise levels of order 100 fA/$\sqrt{\text{Hz}}$. As the effective current noise of the RF readout scales with the quality factor of the tank circuit, efforts were made to optimize the matching circuit to create the largest possible transformation. The best circuits have a quality factor of ~200 and lowest measured effective current noise of this method is 10 fA/$\sqrt{\text{Hz}}$. This represents the practical limits of using a HEMT amplifier and a surface mount inductor for the transformer. While this is still not as sensitive as state of the art FET amplifiers, the numerous other advantages continue to make this an attractive option.

The final thrust of this research was to quantify the detector performance by illuminating it with an on-chip source. To this end, this work merged with the research of a fellow graduate student, Minghao Shen, who has been using RF techniques to characterize the noise from mesoscopic resistors. A chip was designed wherein the 130 GHz Johnson noise from a hot electron source (a gold resistor) was coupled via an on-chip transmission line to the absorber of an RF-STJ detector. The first device showed very promising results, with a responsivity of 1700 A/W, NEP of 4×10^{-17} W/$\sqrt{\text{Hz}}$, and a detector response time of 2 μs.

With these results, the chip was redesigned with the hope of improved the sensitivity and verifying the previous measurements. While these measurement clearly improved sensitivity of the RF readout, the poor responsivity prevented these devices from achieving better NEPs. Furthermore, these measurements also showed a fast and sizable response from "blind" photon sources that were not coupled to the device. While this effect is presumable due to creations of phonons, further measurements will be necessary to separate this from the photon response, and to determine the level at which this may have affected the original measurements. The most likely explanation for the poor responsivity is that the high frequency coupling between the source and the detector is not the ideal calculated coupling. These calculations rely of electromagnetic simulations and several assumptions about the circuit parameters in order to infer the actual power at the device. Furthermore, the detected photons are in the Wien limit, which implies that the total power is exponentially sensitive to the exact frequency. One important change between the two incarnations of these measurements was the inclusion of a Nb/AlO_x/Al tunnel junction between the transmission line and the absorber. It was designed to operate well above its plasma resonance, as a capacitive element. However, if the thin aluminum were proximitized by the Nb, the plasma resonance would be pulled exactly into the frequency range of detection and reduce the power coupled to the aluminum absorber. If, instead, the low responsivity is not due to the coupling inefficiency, we would conclude that the intrinsic detector efficiency is low due to some form of unknown quasiparticle loss. The fact that the detector response times scale with the R_n of the detectors,for a fixed absorber volume, seems to contradict this hypothesis. A third possibility is that photon power emitted by the gold microbridge is less than

is calculated in Chapter 9. If the the photon source were in the non-interacting electron regime, the emitted noise power at 100 GHz would be markedly reduced. While the noise measurements made at 1 GHz indicate this is not the case, a systematic measurement of the noise power as a function of microbridge length would conclusively determine the electron-electron inelastic scattering length and hence the functional form of the high frequency radiation.

A conclusive answer to these questions could only come from further measurements in which a new chip was designed to systematically test each possibility. Ideally, the noise source could be calibrated by measuring with a known detector, or the detector could be illuminated with a known source. In spite of these uncertainties, the overall goal of demonstrating the performance of the RF-STJ with a cryogenic noise source was quite successful.

11.2 Relevance of this Work to the Detector Community

This thesis work has not only quantified some important figures of merit related to the detector, but it has also implemented several novel techniques and experimental methods that are more broadly applicable. While at this time the RF readout is not as sensitive measuring DC current with a FET amplifier, the FET is not a viable option for reading out large format arrays. The sheer number of wires and heat load on the cold stage implies that some form of cryogenic readout must be implemented. The current detector state-of-the-art is to use a TES with a SQUID readout. These have already been integrated into arrays with time domain multiplexed readouts and readily demonstrate photon background limited sensitivities for most applications. Unlike the RF-STJ, the additional gain of the SQUID means that the sensitivity is limited only by intrinsic noise of the TES. At this point in time, the RF-STJ is a detector with comparable potential, but is a much less mature technology. There are several aspects in which the RF-STJ could potentially excel. In the TES, operating at lower temperature gives more sensitivity, but also reduces the speed of the detector as thermal time constants become quite long. In contrast, both the STJ and the RF readout have the potential of 1 μs to 100 ns response times, independent of operation temperature. The ultimate sensitivity of the detector will only be realized with the advent of lower noise RF amplifiers. Recently, several research areas, including quantum computing and dark matter searches, have brought renewed interest to low noise amplifiers base on Josephson junctions. The 2 K noise temperature of HEMT amplifiers at 500 MHz is still two orders of magnitude above the quantum limit, so there is significant room for improvement. There are also potential gains to be made by integrating an on-chip, superconducting tank circuit. Quality factors in excess of 10^5 are routinely demonstrated with superconducting transmission line resonators. A transformer with a Q of 5000 would reduce the current noise of a HEMT amplifier to less than 1 fA/$\sqrt{\text{Hz}}$. It is with these types of improvements that the sensitivity could reach the level of 10^{-19} W/$\sqrt{\text{Hz}}$.

11.3 Possible Future Applications

One straightforward application of this technology is to apply the RF readout to current STJ research. Primarily, these detectors are used in the x-ray and visible frequency ranges. The RF readout could either be used to conveniently multiplex or simply to realize a fast readout. While the large detector junctions in these devices imply a large capacitance and low Q matching circuits for the RF readout, a multi-stage tank circuit could provide a high Q resonance that offers a good impedance match over a bandwidth sufficiently narrow for multiplexing. Alternatively, a low Q matching circuit could be coupled to a detector with a fast tunneling time in order to realize a detector capable of fast reset and high count rates.

Recent research with TES and NIS bolometers have developed methods for doping aluminum with manganese in order to lowest the T_c of the film. The result is that quality aluminum tunnel junctions can be fabricated with arbitrarily small superconducting gaps. Unlike a bolometer which simply measures power, a photoconductor (like the STJ) measure the number of quanta of light. Thus, the responsivity is inversely proportional to the size of the spectroscopic energy gap. This implies that both the NEP and frequency of operation could be reduced by lowering the gap. Implicit in the successful operation of a lower gap detector is that it must be operated at an analogously lower temperature. For example, a device with a gap of 20 μeV operated in a dilution refrigerator at 25 mK would have quasiparticle densities similar to current devices at 250 mK. Thus, the dark current and self-recombination times would remain similar to the present measurements at 250 mK. The responsivity would increase by a factor of 10 and this detector could operate as a photon counter for photons as low in frequency as 10 GHz. Such a detector might have applications in quantum computing, quantum communication, or the emerging field of microwave quantum optics.

References

Aassime, A., Johansson, G., Wendin, G., Schoelkopf, R. J., and Delsing, P. Radio-frequency single-electron transistor as readout device for qubits: Charge sensitivity and backaction. *Physical Review Letters*, 86(15):3376–, 2001. URL: http://link.aps.org/abstract/PRL/v86/p3376.

Altshuler, B., Aronov, A., and Khmelnitsky, D. Effects of electron-electron collisions with small energy transfers on quantum localisation. *Journal of Physics C: Solid State Physics*, 15(36):7367–7386, 1982. doi:10.1088/0022-3719/15/36/018. URL: http://stacks.iop.org/0022-3719/15/7367.

Ambegaokar, V. and Baratoff, A. Tunneling between superconductors. *Physical Review Letters*, 10(11):456–459, 1963. URL: http://prola.aps.org/abstract/PRL/v10/i11/p486_1.

Andre, M., Muck, M., Clarke, J., Gail, J., and Heiden, C. Radio-frequency amplifier with tenth-kelvin noise temperature based on a microstrip direct current superconducting quantum interference device. *Applied Physics Letters*, 75(5):698–700, 1999. doi:10.1063/1.124486. URL: http://link.aip.org/link/?APL/75/698/1.

Andreev, A. The thermal conductivity of the intermediate state in superconductors. *Sov. Phys. JETP*, 19:1228, 1964.

Averin, D. V., Korotkov, A. N., Manninen, A. J., and Pekola, J. P. Resonant tunneling through a macroscopic charge state in a superconducting single electron transistor. *Phys. Rev. Lett.*, 78(25):4821–4824, 1997. doi:10.1103/PhysRevLett.78.4821. URL: http://link.aps.org/abstract/PRL/v78/p4821.

Averin, D. V. and Likharev, K. K. *Mesoscopic Phenomena in Solids*. Elsevier, 1990.

Bardeen, J., Cooper, L. N., and Schrieffer, J. R. Theory of superconductivity. *Physical Review*, 108(5):1175–1204, 1957. doi:10.1103/PhysRev.108.1175. URL: http://link.aps.org/abstract/PR/v108/p1175.

Baselmans, J., Yates, S. J. C., Barends, R., Lankwarden, Y. J. Y., Gao, J. R., Hoevers, H., and Klapwijk, T. M. Noise and sensitivity of aluminum kinetic inductance detec-

tors for sub-mm astronomy. *Journal of Low Temperature Physics*, 151:524, 2008. URL: http://www.springerlink.com/content/958t38200823qj3t.

Beenakker, C. W. J. and Büttiker, M. Suppression of shot noise in metallic diffusive conductors. *Phys. Rev. B*, 46(3):1889–1892, 1992. doi:10.1103/PhysRevB.46.1889. URL: http://link.aps.org/abstract/PRB/v46/p1889.

Bladh, K., Gunnarsson, D., Hurfeld, E., Devi, S., Kristoffersson, C., Smalander, B., Pehrson, S., Claeson, T., Delsing, P., and Taslakov, M. Comparison of cryogenic filters for use in single electronics experiments. *Review of Scientific Instruments*, 74(3):1323–1327, 2003. doi:10.1063/1.1540721. URL: http://link.aip.org/link/?RSI/74/1323/1.

Bode, H. W. *Network Analysis and Feedback Amplifier Design.* D. Van Nostrand company, inc, 1945.

Bradley, R., Clarke, J., Kinion, D., Rosenberg, L., van Bibber, K., Matsuki, S., Muck, M., and Sikivie, P. Microwave cavity searches for dark-matter axions. *Rev. Mod. Phys.*, 75(3):777–817, 2003. doi:10.1103/RevModPhys.75.777. URL: http://link.aps.org/abstract/RMP/v75/p777.

Bradley, R. F. Cryogenic, low-noise, balanced amplifiers for the 300-1200 mhz band using heterostructure field-effect transistors. *Nuclear Physics B*, 72:137–144, 1999. URL: http://dx.doi.org/10.1016/S0920-5632(98)00516-7.

Brenning, H., Kafanov, S., Duty, T., Kubatkin, S., and Delsing, P. An ultrasensitive radio-frequency single-electron transistor working up to 4.2 k. *Journal of Applied Physics*, 100(11):114321, 2006. URL: http://link.aip.org/link/?JAP/100/114321/1.

Burke, P. J. *High Frequency Electron Dynamics in Thin Film Superconductors and Applications to Fast Sensitive THz Detectors.* Ph.D. thesis, Yale University, 1997. URL: http://www.yale.edu/proberlab/.

Cassidy, M. C., Dzurak, A. S., Clark, R. G., Petersson, K. D., Farrer, I., Ritchie, D. A., and Smith, C. G. Single shot charge detection using a radio-frequency quantum point contact. *Applied Physics Letters*, 91(22):222104, 2007. doi:10.1063/1.2809370. URL: http://link.aip.org/link/?APL/91/222104/1.

Castellanos-Beltran, M. A. and Lehnert, K. W. Widely tunable parametric amplifier based on a superconducting quantum interference device array resonator. *Applied Physics Letters*, 91(8):083509, 2007. doi:10.1063/1.2773988. URL: http://link.aip.org/link/?APL/91/083509/1.

Caves, C. M. Quantum limits on noise in linear amplifiers. *Physical Review D*, 26(8):1817–, 1982. URL: http://link.aps.org/abstract/PRD/v26/p1817.

Clarke, J. and Braginski, A. I. *The SQUID Handbook: Fundamentals and Technology of SQUIDs and SQUID Systems*. Wiley-VCH, Winheim, 2004.

Day, P. K., LeDuc, H. G., Mazin, B. A., Vayonakis, A., and Zmuidzinas, J. A broadband superconducting detector suitable for use in large arrays. *Nature*, 425:817–821, 2003. doi: 10.1038/nature02037. URL: http://dx.doi.org/10.1038/nature02037.

de Jong, M. J. *Shot Noise and Electrical Conduction in Mesoscopic Systems*. Ph.D. thesis, Leiden University, 1995.

Devoret, M. and Schoelkopf, R. Amplifying quantum signals with the single-electron transistor. *Nature*, 406(6799):1039–46, 2000. ISSN 0028-0836. URL: http://www.eng.yale.edu/rslab/papers/Nature_SET_amplifier.pdf.

Dicke, R. H. The measurement of thermal radiation at microwave frequencies. *Review of Scientific Instruments*, 17(7):268–275, 1946. doi:10.1063/1.1770483. URL: http://link.aip.org/link/?RSINAK/17/268/1.

Dicke, R. H., Beringer, R., Kyhl, R., and Vane, A. Atmospheric absorption measurements with a microwave radiometer. *Physical Review*, 70:340, 1946. doi:10.1103/PhysRev.70.340. URL: http://link.aps.org/abstract/PR/v70/p340.

Dolan, G. J. Offset masks for lift-off photoprocessing. *Applied Physics Letters*, 31(5):337–339, 1977. doi:10.1063/1.89690. URL: http://link.aip.org/link/?APL/31/337/1.

Echternach, P. M., Thoman, M. R., Gould, C. M., and Bozler, H. M. Electron-phonon scattering rates in disordered metallic films below 1 k. *Phys. Rev. B*, 46(16):10339–10344, 1992. doi: 10.1103/PhysRevB.46.10339. URL: http://link.aps.org/abstract/PRB/v46/p10339.

Face, D. W., Prober, D. E., McGrath, W. R., and Richards, P. L. High quality tantalum superconducting tunnel junctions for microwave mixing in the quantum limit. *Applied Physics Letters*, 48(16):1098–1100, 1986. doi:10.1063/1.96610. URL: http://link.aip.org/link/?APL/48/1098/1.

Fano, R. M. Theoretical limitations on the broadband matching of arbitrary impedances. *MIT technical report*, 41, 1950.

Fiske, M. D. Temperature and magnetic field dependences of the josephson tunneling current. *Rev. Mod. Phys.*, 36(1):221–222, 1964. doi:10.1103/RevModPhys.36.221. URL: http://link.aps.org/abstract/RMP/v36/p221.

Fixsen, D. J., Cheng, E. S., Gales, J. M., Mather, J. C., Shafer, R. A., and Wright, E. L. The cosmic microwave background spectrum from the full cobe firas data set. *Astrophysical Journal*, 473:576, 1996. doi:10.1086/178173. URL: http://www.journals.uchicago.edu/doi/abs/10.1086/178173.

Flowers-Jacobs, N. E., Schmidt, D. R., and Lehnert, K. W. Intrinsic noise properties of atomic point contact displacement detectors. *Physical Review Letters*, 98(9):096804, 2007. doi:10.1103/PhysRevLett.98.096804. URL: http://link.aps.org/abstract/PRL/v98/e096804.

Friis, H. T. A note on a simple transmission formula. *Proc. IRE*, 34(5):254–256, 1946. URL: http://ieeexplore.ieee.org/xpls/abs_all.jsp?arnumber=1697062.

Fujisawa, T. and Hirayama, Y. Charge noise analysis of an algaas/gaas quantum dot using transmission-type radio-frequency single-electron transistor technique. *Applied Physics Letters*, 77(4):543–545, 2000. doi:10.1063/1.127038. URL: http://link.aip.org/link/?APL/77/543/1.

Fukushima, A., Sato, A., Iwasa, A., Nakamura, Y., Komatsuzaki, T., and Sakamoto, Y. Attenuation of microwave filters for single-electron tunneling experiments. *Instrumentation and Measurement, IEEE Transactions on*, 46(2):289–293, 1997. ISSN 0018-9456. URL: http://dx.doi.org/10.1109/19.571834.

Fulton, T. A. and Dolan, G. J. Observation of single-electron charging effects in small tunnel junctions. *Physical Review Letters*, 59(1):109–, 1987. URL: http://link.aps.org/abstract/PRL/v59/p109.

Gaier, T., Lawrence, C. R., Seiffert, M. D., Wells, M. M., Kangaslahti, P., and Dawson, D. Amplifier arrays for cmb polarization. *Proceedings of the Workshop on The Cosmic Microwave Background Radiation and its Polarization*, 47:1167–1171, 2003. doi:doi:10.1016/j.newar.2003.09.010. URL: http://dx.doi.org/10.1016/j.newar.2003.09.010.

Giazotto, F., Heikkila, T. T., Luukanen, A., Savin, A. M., and Pekola, J. P. Opportunities for mesoscopics in thermometry and refrigeration: Physics and applications. *Reviews of Modern Physics*, 78(1):217, 2006. doi:10.1103/RevModPhys.78.217. URL: http://link.aps.org/abstract/RMP/v78/p217.

Glattli, D. C., Jacques, P., Kumar, A., Pari, P., and Saminadayar, L. A noise detection scheme with 10 mk noise temperature resolution for semiconductor single electron tunneling devices. *Journal of Applied Physics*, 81(11):7350–7356, 1997. doi:10.1063/1.365332. URL: http://link.aip.org/link/?JAP/81/7350/1.

Glover, R. E. and Tinkham, M. Conductivity of superconducting films for photon energies between 0.3 and $40kt_c$. *Phys. Rev.*, 108(2):243–256, 1957. doi:10.1103/PhysRev.108.243. URL: `http://link.aps.org/abstract/PR/v108/p243`.

Gorter, C. A possible explanation of the increase of the electrical resistance of thin metal films at low temperatures and small field strengths. *Physica*, 17(5367):777–780, 1951. URL: `http://dx.doi.org/10.1016/0031-8914(51)90098-52`.

Grabert, H. and Devoret, M. H. *Single Charge Tunneling: Coulomb Blockade Phenomena in Nanostructures*, volume 294 of *NATO ASI Series*. Plenum Press, 1992. Proceedings of a NATO Advance Study Institute on Signle Charge Tunneling held March, 1991 in Les Houches, France.

Gray, K. E. *Nonequilibrium Superconductivity, Phonons, and Kapitza Boundaries*, volume 65. Plenum, 1981.

Hahn, I., Bumble, B., LeDuc, H. G., Weilert, M., and Day, P. An x-band squid multiplexer. *AIP Conference Proceedings*, 850(1):1613–1614, 2006. doi:10.1063/1.2355324. URL: `http://link.aip.org/link/?APC/850/1613/1`. Flux Ramp Modulation Scheme.

Hajenius, M., Yang, Z., Gao, J., Baselmans, J., Klapwijk, T., Voronov, B., and Gol'tsman, G. Optimized sensitivity of nbn hot electron bolometer mixers by annealing. *IEEE Transactions on Applied Superconductivity*, 17:399–402, 2007. doi:10.1109/TASC.2007.898064. URL: `http://dx.doi.org/10.1109/TASC.2007.898064`.

Hinshaw, G., Nolta, M. R., Bennett, C. L., Bean, R., Dor, O., Greason, M. R., Halpern, M., Hill, R. S., Jarosik, N., Kogut, A., Komatsu, E., Limon, M., Odegard, N., Meyer, S. S., Page, L., Peiris, H. V., Spergel, D. N., Tucker, G. S., Verde, L., Weiland, J. L., Wollack, E., and Wright, E. L. Three-year wilkinson microwave anisotropy probe (wmap) observations: Temperature analysis. *Astrophysical Journal*, 170:288, 2007. URL: `http://lambda.gsfc.nasa.gov/product/map/dr2/map_bibliography.cfm`.

Holst, T., Esteve, D., Urbina, C., and Devoret, M. Effect of a transmission line resonator on a small capacitance tunnel junction. *Physical Review Letters*, 73(25):3455 – 8, 1994. ISSN 0031-9007. URL: `http://dx.doi.org/10.1103/PhysRevLett.73.3455`.

Horowitz, P. and Hill, W. *The Art of Electronics*. Cambridge University Press, second edition, 1989.

Irwin, K. D. and Hilton, G. C. *Cryogenic Particle Detection*, chapter Transition-Edge Sensors, pages 63–149. Springer-Verlag Berlin Heidelberg, 2005. URL: `http://qdev.boulder.nist.gov/817.03/pubs/downloads/qsensors/TESIrwinHilton.pdf`.

Irwin, K. D. and Lehnert, K. W. Microwave squid multiplexer. *Applied Physics Letters*, 85(11):2107–2109, 2004. URL: `http://link.aip.org/link/?APL/85/2107/1`.

Josephson, B. Possible new effects in superconductive tunnelling. *Physics Letters*, 1(7):251 – 253, 1962. URL: http://dx.doi.org/10.1016/0031-9163(62)91369-0.

Kapitza, P. *J. Phys. (Moscow)*, 4:181, 1941.

Kaplan, S. B., Chi, C. C., Langenberg, D. N., Chang, J. J., Jafarey, S., and Scalapino, D. J. Quasiparticle and phonon lifetimes in superconductors. *Physical Review B*, 14(11):4854–4873, 1976. doi:10.1103/PhysRevB.14.4854. URL: http://link.aps.org/abstract/PRB/v14/p4854.

Kenyon, M., Day, P., Bradford, C., Bock, J., and Leduc, H. Background-limited membrane-isolated tes bolometers for far-ir/submillimeter direct-detection spectroscopy. *Nuclear Instruments and Methods in Physics Research A*, 559:456–458, 2006. doi:doi:10.1016/j.nima.2005.12.036. URL: http://dx.doi.org/10.1016/j.nima.2005.12.036.

Kittel, P. Comment on the equivalent noise bandwidth approximation. *Review of Scientific Instruments*, 48(9):1214–1215, 1977. doi:10.1063/1.1135225. URL: http://link.aip.org/link/?RSI/48/1214/1.

Krauss, H., Gutsche, M., Hettl, P., Jochum, J., and Kemmather, B. Measurement of the tunnel rate in sis' tunnel junctions as a function of bias voltage. *Journal of Superconductivity*, 9:245–252, 1996.

LaHaye, M. D., Buu, O., Camarota, B., and Schwab, K. C. Approaching the Quantum Limit of a Nanomechanical Resonator. *Science*, 304(5667):74–77, 2004. doi:10.1126/science.1094419. URL: http://www.sciencemag.org/cgi/content/abstract/304/5667/74.

Lehnert, K., Irwin, K., Castellanos-Beltran, M., Mates, J., and Vale, L. Evaluation of a microwave squid multiplexer prototype. *Applied Superconductivity, IEEE Transactions on*, 17(2):705–709, 2007. ISSN 1051-8223. URL: http://dx.doi.org/10.1109/TASC.2007.898118.

Lehnert, K. W., Bladh, K., Spietz, L. F., Gunnarsson, D., Schuster, D. I., Delsing, P., and Schoelkopf, R. J. Measurement of the excited-state lifetime of a microelectronic circuit. *Physical Review Letters*, 90(2):027002, 2003. URL: http://link.aps.org/abstract/PRL/v90/e027002.

Lerch, P. and Zehnder, A. *Cryogenic Particle Detection*, chapter Quantum Giaever Detectors: STJs, pages 217–266. Springer-Verlag Berlin Heidelberg, 2005. doi:10.1007/10933596_5. URL: http://www.springerlink.com/content/60bve6c977u2nq1r.

Li, L. *X-ray Single Photon Imaging Detectors Using Superconducting Tunnel Junctions.* Ph.D. thesis, Yale University, 2003. URL: http://www.yale.edu/proberlab/.

Love, J. H. *Resolved Dynamics of Single Electron Tunneling Using the RF-SET.* Ph.D. thesis, Yale University, 2007. URL: http://www.eng.yale.edu/rslab.

Martinis, J. M., Devoret, M. H., and Clarke, J. Experimental tests for the quantum behavior of a macroscopic degree of freedom: The phase difference across a josephson junction. *Physical Review B*, 35(10):4682–4698, 1987. doi:10.1103/PhysRevB.35.4682. URL: `http://prola.aps.org/abstract/PRB/v35/i10/p4682_1`.

Mates, J., Hilton, G., Irwin, K., Vale, L., and Lehnert, K. Demonstration of a multiplexer of dissipationless squids. *Applied Physics Letters*, 92:023514, 2008. URL: `http://link.aip.org/link/?APL/92/023514/1`.

Mather, J., Moseley, S., Leisawitz, D., Dwek, E., Hacking, P., Harwit, M., Mundy, L., Mushotzky, R., Neufeld, D., Spergel, D., and Wright, E. The submillimeter frontier: A space science imperative. *astro-ph/9812454v1*, 1996. URL: `http://xxx.lanl.gov/abs/astro-ph/9812454v1`.

Mattis, D. C. and Bardeen, J. Theory of the anomalous skin effect in normal and superconducting metals. *Physical Review*, 111(2):412–417, 1958. doi:10.1103/PhysRev.111.412. URL: `http://link.aps.org/abstract/PR/v111/p412`.

Mazin, B. A. *Microwave Kinetic Inductance Detectors*. Ph.D. thesis, California Institute of Technology, 2004. URL: `http://etd.caltech.edu/etd/available/etd-10042004-120707/`.

McMillan, W. L. Transition temperature of strong-coupled superconductors. *Physical Review*, 167(2):331–344, 1968. doi:10.1103/PhysRev.167.331. URL: `http://link.aps.org/abstract/PR/v167/p331`.

Mees, J., Nahum, M., and Richards, P. L. New designs for antenna-coupled superconducting bolometers. *Applied Physics Letters*, 59(18):2329–2331, 1991. doi:10.1063/1.106059. URL: `http://link.aip.org/link/?APL/59/2329/1`.

Movshovich, R., Yurke, B., Kaminsky, P. G., Smith, A. D., Silver, A. H., Simon, R. W., and Schneider, M. V. Observation of zero-point noise squeezing via a josephson-parametric amplifier. *Phys. Rev. Lett.*, 65(12):1419–1422, 1990. doi:10.1103/PhysRevLett.65.1419. URL: `http://link.aps.org/abstract/PRL/v65/p1419`.

Muck, M., Andre, M.-O., Clarke, J., Gail, J., and Heiden, C. Radio-frequency amplifier based on a niobium dc superconducting quantum interference device with microstrip input coupling. *Applied Physics Letters*, 72(22):2885–2887, 1998. doi:10.1063/1.121490. URL: `http://link.aip.org/link/?APL/72/2885/1`.

Muck, M., Andre, M.-O., Clarke, J., Gail, J., and Heiden, C. Microstrip superconducting quantum interference device radio-frequency amplifier: Tuning and cascading. *Applied Physics Letters*, 75(22):3545–3547, 1999. doi:10.1063/1.125383. URL: `http://link.aip.org/link/?APL/75/3545/1`.

Muck, M., Kycia, J. B., and Clarke, J. Superconducting quantum interference device as a near-quantum-limited amplifier at 0.5 ghz. *Applied Physics Letters*, 78(7):967–969, 2001. doi:10.1063/1.1347384. URL: `http://link.aip.org/link/?APL/78/967/1`.

Nahum, M. and Martinis, J. M. Ultrasensitive-hot-electron microbolometer. *Applied Physics Letters*, 63:3075, 1993. URL: `http://link.aip.org/link/?APPLAB/63/3075/1`.

Onnes, H. K. The superconductivity of mercury. *Comm. Phys. Lab. Univ. Leiden*, 12:120, 1911.

Pohlen, S. L. *The Superconducting Single Electron Transistor.* Ph.D. thesis, Harvard University, 1999.

Porter, F. S., Audley, M. D., Brekosky, R. P., Derro, R. J., DiPirro, M. J., Gendreau, K. C., Gygax, J. D., Kelley, R. L., McCammon, D., Morrell, A., Murphy, S. D., Paulos, R. J., Pham, T., Stahle, C. K., Szymkowiak, A. E., and Tuttle, J. G. Detector assembly and the ultralow-temperature refrigerator for xrs. volume 3765, pages 729–740. SPIE, 1999. doi:10.1117/12.366556. URL: `http://link.aip.org/link/?PSI/3765/729/1`.

Pozar, D. M. *Microwave Engineering.* John Wiley & Sons, Inc., 3rd edition, 2005.

Qin, H. and Williams, D. A. Radio-frequency point-contact electrometer. *Applied Physics Letters*, 88(20):203506, 2006. doi:10.1063/1.2205159. URL: `http://link.aip.org/link/?APL/88/203506/1`.

Rogovin, D. and Scalapino, D. Fluctuation phenomena in tunnel junctions. *Annals of Physics*, 86(1):1 – 90, 1974. ISSN 0003-4916. URL: `http://dx.doi.org/10.1016/0003-4916(74)90430-8`.

Roukes, M. L., Freeman, M. R., Germain, R. S., Richardson, R. C., and Ketchen, M. B. Hot electrons and energy transport in metals at millikelvin temperatures. *Physical Review Letters*, 55(4):422–425, 1985. doi:10.1103/PhysRevLett.55.422. URL: `http://link.aps.org/abstract/PRL/v55/p422`.

Savu, V. A. *The Light at the End of the Tunnel Junction - Improving the Energy Resolution of UV Single-Photon Spectrometers using Diffusion Engineering.* Ph.D. thesis, Yale University, 2007. URL: `http://www.yale.edu/proberlab/`.

Schmidt, D., Schoelkopf, R., and Cleland, A. Photon-mediated thermal relaxation of electrons in nanostructures. *Physical Review Letters*, 93:045901, 2004. doi:10.1103/PhysRevLett.93.045901. URL: `http://link.aps.org/abstract/PRL/v93/e045901`.

Schmidt, D. R., Lehnert, K. W., Clark, A. M., Duncan, W. D., Irwin, K. D., Miller, N., and Ullom, J. N. A superconductor–insulator–normal metal bolometer with microwave readout suitable for large-format arrays. *Applied Physics Letters*, 86(5):053505, 2005. URL: http://link.aip.org/link/?APL/86/053505/1.

Schmidt, D. R., Yung, C. S., and Cleland, A. N. Nanoscale radio-frequency thermometry. *Applied Physics Letters*, 83(5):1002–1004, 2003. doi:10.1063/1.1597983. URL: http://link.aip.org/link/?APL/83/1002/1.

Schoelkopf, R., Burke, P., Kozhevnikov, A., Prober, D., and Rooks, M. Frequency dependence of shot noise in a diffusive mesoscopic conductor. *Physical Review Letters*, 78(17):3370 – 3, 1997. ISSN 0031-9007. URL: http://dx.doi.org/10.1103/PhysRevLett.78.3370.

Schoelkopf, R., Wahlgren, P., Kozhevnikov, A., Delsing, P., and Prober, D. The radio-frequency single-electron transistor (rf-set): a fast and ultrasensitive electrometer. *Science*, 280(5367):1238–42, 1998. ISSN 0036-8075. URL: http://www.eng.yale.edu/rslab/papers/RFSETScience.pdf.

Schoelkopf, R. J., Moesley, S. H., Stahle, C. M., Wahlgren, P., and Delsing, P. A concept for a submillimeter-wave single-photon counter. *Applied Superconductivity, IEEE Transactions on*, 9(2):2935–2939, 1999. URL: http://dx.doi.org/10.1109/77.783645.

Segall, K., Lehnert, K. W., Stevenson, T. R., Schoelkopf, R. J., Wahlgren, P., Aassime, A., and Delsing, P. A high-performance cryogenic amplifier based on a radio-frequency single electron transistor. *Applied Physics Letters*, 81(25):4859–4861, 2002. URL: http://link.aip.org/link/?APL/81/4859/1.

Shapiro, S. Josephson currents in superconducting tunneling: The effect of microwaves and other observations. *Physical Review Letters*, 11(2):80–82, 1963. doi:10.1103/PhysRevLett.11.80. URL: http://prola.aps.org/abstract/PRL/v11/i2/p80_1.

Shen, M. *Low Temperature Electron-Phonon Interaction in Disordered Metal Thin Films and Applications to Fast, Sensitive Sub-Millimeter Photon Sources and Detectors.* Ph.D. thesis, Yale University, 2005. URL: http://www.eng.yale.edu/rslab.

Spergel, D. N., Bean, R., Dor, O., Nolta, M. R., Bennett, C. L., Dunkley, J., Hinshaw, G., Jarosik, N., Komatsu, E., Page, L., Peiris, H. V., Verde, L., Halpern, M., Hill, R. S., Kogut, A., Limon, M., Meyer, S. S., Odegard, N., Tucker, G. S., Weiland, J. L., Wollack, E., and Wright, E. L. Wilkinson microwave anisotropy probe (wmap) three year results: Implications for cosmology. *Astrophysical Journal*, 170:377, 2007. URL: http://lambda.gsfc.nasa.gov/product/map/dr2/map_bibliography.cfm.

Spietz, L., Teufel, J. D., and Schoelkopf, R. J. A twisted pair cryogenic filter. *cond-mat/0601316*, 2004. URL: `http://arxiv.org/abs/cond-mat/0601316`.

Spietz, L. F. *The Shot Noise Thermometer.* Ph.D. thesis, Yale University, 2005. URL: `http://www.eng.yale.edu/rslab`.

Stahle, C. K., McCammon, D., and Irwin, K. D. Quantum calorimetry. *Physics Today*, 52:32–72, 1999. URL: `http://phonon.gsfc.nasa.gov/qcal/qcal.html`.

Steinbach, A. H., Martinis, J. M., and Devoret, M. H. Observation of hot-electron shot noise in a metallic resistor. *Physical Review Letters*, 76(20):3806–3809, 1996. doi:10.1103/PhysRevLett.76.3806. URL: `http://link.aps.org/abstract/PRL/v76/p3806`.

Stevenson, T. R., Aassime, A., Delsing, P., Schoelkopf, R. J., Segall, K., and C.M.Stahle. Rf single electron transistor readout amplifiers for superconducting astronomical detectors of x-ray to sub-mm wavelengths. *Applied Superconductivity, IEEE Transactions on*, 11(1):692–695, 2001. ISSN 1051-8223. URL: `http://dx.doi.org/10.1109/77.919439`.

Stevenson, T. R., Hsieh, W.-T., Li, M. J., Rhee, K. W., Schoelkopf, R. J., Stahle, C. M., and Teufel, J. Fabrication of tunnel junctions for direct detector arrays with single-electron transistor readout using electron-beam lithography. *Applied Superconductivity, IEEE Transactions on*, 13(2):1139–1142, 2003. ISSN 1051-8223. URL: `http://dx.doi.org/10.1109/TASC.2003.814175`.

Stevenson, T. R., Pellerano, F. A., Stahle, C. M., Aidala, K., and Schoelkopf, R. J. Multiplexing of radio-frequency single-electron transistors. *Applied Physics Letters*, 80(16):3012–3014, 2002. doi:10.1063/1.1472472. URL: `http://link.aip.org/link/?APL/80/3012/1`.

Thalakulam, M., Ji, Z., and Rimberg, A. J. Sensitivity and linearity of superconducting radio-frequency single-electron transistors: Effects of quantum charge fluctuations. *Physical Review Letters*, 93(6):066804, 2004. doi:10.1103/PhysRevLett.93.066804. URL: `http://link.aps.org/abstract/PRL/v93/e066804`.

Tinkham, M. *Superconductivity.* Gordon and Breach, 1965.

Tinkham, M. *Introduction to Superconductivity.* Dover Publications, Inc., 1996.

Turek, B. A. *Precision Measurements with the Single Electron Transistor: Noise and Backaction in the Normal and Superconducting State.* Ph.D. thesis, Yale University, 2007. URL: `http://www.eng.yale.edu/rslab`.

Twerenbold, D. Cryogenic particle detectors. *Reports on Progress in Physics*, 59(3):349–426, 1996. URL: `http://stacks.iop.org/0034-4885/59/349`.

Van Duzer, T. and Turner, C. *Principles of superfconductive devices and circuits (2nd Edition).* Prentice Hall, 1998.

Verhoeve, P., Brammertz, G., Martin, D., and Peacock, A. Quasiparticle loss rates in ta-based superconducting tunnel junctions. *Nuclear Instruments and Methods in Physics Research Section A: Accelerators, Spectrometers, Detectors and Associated Equipment*, 520:246–249, 2004. doi:10.1016/j.nima.2003.11.335. URL: `http://dx.doi.org/10.1016/j.nima.2003.11.335`.

Vion, D., Orfila, P. F., Joyez, P., Esteve, D., and Devoret, M. H. Miniature electrical filters for single electron devices. *Journal of Applied Physics*, 77(6):2519–2524, 1995. doi:10.1063/1.358781. URL: `http://link.aip.org/link/?JAP/77/2519/1`.

Visscher, E. H., Verbrugh, S. M., Lindeman, J., Hadley, P., and Mooij, J. E. Fabrication of multilayer single-electron tunneling devices. *Applied Physics Letters*, 66(3):305–307, 1995. URL: `http://link.aip.org/link/?APL/66/305/1`.

Voellmer, G. M., Allen, C. A., Babu, S. R., Bartels, A. E., Dowell, C. D., Dotson, J. L., Harper, D. A., Moseley, S. H., Jr., Rennick, T., Shirron, P. J., Smith, W. W., and Wollack, E. J. A two-dimensional semiconducting bolometer array for hawc. In C. M. Bradford, P. A. R. Ade, J. E. Aguirre, J. J. Bock, M. Dragovan, L. Duband, L. Earle, J. Glenn, H. Matsuhara, B. J. Naylor, H. T. Nguyen, M. Yun, and J. Zmuidzinas, editors, *Millimeter and Submillimeter Detectors for Astronomy II. Edited by Jonas Zmuidzinas, Wayne S. Holland and Stafford Withington Proceedings of the SPIE, Volume 5498, pp. 428-437 (2004).*, volume 5498 of *Presented at the Society of Photo-Optical Instrumentation Engineers (SPIE) Conference*, pages 428–437. 2004. doi:10.1117/12.552016. URL: `http://adsabs.harvard.edu/abs/2004SPIE.5498..428V`.

Wadell, B. C. *Transmission Line Design Handbook.* Artech House Publishers, 1991.

Wilson, C. M. *Optical/UV Single-Photon Spectrometers Using Superconducting Tunnel Junctions.* Ph.D. thesis, Yale University, 2002. URL: `http://www.yale.edu/proberlab/`.

Wind, S., Rooks, M. J., Chandrasekhar, V., and Prober, D. E. One-dimensional electron-electron scattering with small energy transfers. *Phys. Rev. Lett.*, 57(5):633–636, 1986. doi:10.1103/PhysRevLett.57.633. URL: `http://link.aps.org/abstract/PRL/v57/p633`.

Woodcraft, A. L., Ade, P. A. R., Bintley, D., House, J. S., Hunt, C. L., Sudiwala, R. V., Doriese, W. B., Duncan, W. D., Hilton, G. C., Irwin, K. D., Reintsema, C. D., Ullom, J. N., Audley, M. D., Ellis, M. A., Holland, W. S., MacIntosh, M., Dunare, C. C., Parkes, W., Walton, A. J., Kycia, J. B., Halpern, M., and Schulte, E. Electrical and optical measurements on the first scuba-2 prototype 1280 pixel submillimeter superconducting bolometer array. *Review of Scientific Instruments*, 78(2):024502, 2007. doi:10.1063/1.2436839. URL: `http://link.aip.org/link/?RSI/78/024502/1`.

Zimmerli, G., Kautz, R. L., and Martinis, J. M. Voltage gain in the single-electron transistor. *Applied Physics Letters*, 61(21):2616–2618, 1992. URL: `http://link.aip.org/link/?APL/61/2616/1`.

Zorin, A. B. The thermocoax cable as the microwave frequency filter for single electron circuits. *Review of Scientific Instruments*, 66(8):4296–4300, 1995. doi:10.1063/1.1145385. URL: `http://link.aip.org/link/?RSI/66/4296/1`.